the Larsen B embayment recorded still higher values briefly, at +18.7°C on the 24th, and several other weather stations in the region surpassed +17°C on 23 and 24 March.

Temperatures at the AWS locations provide a broader view of weather records and trends for the continent. For the Ross sector, Possession Island (not shown) reported a record low temperature of −21.9°C (greater than 2 standard deviations from the 1981–2010 mean) in September and then tied its record high mean temperature of 1.7°C in December. Otherwise, temperatures at Possession Island were above normal for February, August, October, November, and December and below normal for the rest of the months (no report for July). The Ross Ice Shelf region (e.g., Gill AWS, Fig. 6.4f) had generally above-normal temperatures from January through March and again in August, but these warm periods were interspersed by colder-than-normal temperatures, especially in April, July, and September. In West Antarctica, Byrd AWS (Fig. 6.4e) was colder than normal for March–April, June–August, and November–December and was warmer than normal otherwise. At Relay Station (not shown) on the Polar Plateau, temperatures were above normal through May, below normal for June–September, and then 5°C above normal in October. On the other side of the Polar Plateau, Dome C II (not shown) did not operate from May through part of September, but October and November had above-normal temperatures.

While stations over Antarctica generally did not report record temperature anomalies, many staffed and unstaffed stations reported record low pressure anomalies in at least one month. The pressure data from all staffed stations showed lower-than-average pressures for all months except October (Figs. 6.4a–d) and January at the Bellingshausen station (Fig. 6.4a). On the Ross Ice Shelf, almost every month had below-normal pressure with a record low anomaly reported for February for Possession Island (−6.7 hPa), Marble Point (−9.2 hPa, greater than 2 standard deviations below normal), Ferrell (−9.9 hPa, about 2 standard deviations below normal), and Gill AWS (−10.5 hPa, greater than 2 standard deviations below normal; the latter shown in Fig. 6.4f). The record low pressure anomalies ranged from −6.7 to −10.5 hPa. Possession Island was only above normal for May, and Marble Point had slightly above-normal pressure for October. Relay Station also had a record low pressure anomaly in February (−5.1 hPa), and pressures were below normal through the whole year until October. The record low pressure anomalies observed in February on both the Ross Ice Shelf and at Relay Station also coincided with the record high SAM index value (Fig. 6.2c). Byrd AWS (Fig. 6.4e) in West Antarctica reported record low pressures in March and November (803.7 and 799.8 hPa, respectively), with only four other months reporting pressure anomalies less than 6 hPa below normal. There were also a few reported wind speed records (not shown), but most stations generally reported only slightly above or below normal wind speeds over the course of the year. Marble Point had a record low monthly mean wind speed of 2.4 m s^{-1} in March, and Gill reported a record low wind speed of 1.5 m s^{-1} in April (both more than 2 standard deviations below normal). Relay Station had a record high monthly mean wind speed of 9.1 m s^{-1} in April (greater than 2 standard deviations above normal).

d. Net precipitation (P−E)—D. H. Bromwich and S.-H. Wang

Precipitation minus evaporation/sublimation (P − E) closely approximates the surface mass balance over Antarctica, except for the steep coastal slopes (e.g., Bromwich et al. 2011; Lenaerts and van den Broeke 2012). Precipitation variability is the dominant term for P − E changes at regional and larger scales over the Antarctic continent. There are few precipitation gauge measurements for Antarctica, and those are compromised by blowing snow. In addition, over the interior Antarctic plateau, snowfall amounts are often less than the minimum gauge resolution. As a result, precipitation and evaporation fields from the Japanese 55-year Reanalysis (JRA-55; Kobayashi et al. 2015) were examined to assess Antarctic net precipitation (P − E) behavior for 2015. JRA-55, the second generation of JRA, is produced with a low-resolution version of the Japan Meteorological Agency's (JMA) operational data assimilation system as of December 2009, which incorporated many improvements achieved since JRA-25 (Onogi et al. 2007), including a revised longwave radiation scheme, four-dimensional data assimilation, bias correction for satellite radiances, and assimilation of newly available homogenized observations. These improvements have resulted in better fits to observations, reduced analysis increments and improved forecast results (Kobayashi et al. 2015). The model is run at a spatial resolution of TL319 (~0.5625° or 55 km) and at 60 vertical levels from the surface up to 0.1 hPa. In comparison to other long-term global reanalyses (e.g., NCEP1 and NCEP2), JRA has higher horizontal and vertical model resolution, uses a greater number of observations, and has a more advanced model configuration (e.g., Bromwich et al. 2007; Kang and Ahn 2015).

Figure 6.5 shows the JRA-55 2015 and 2014 annual anomalies of $P - E$ and mean sea level pressure

(MSLP) departures from the 1981–2010 average. In general, annual $P-E$ anomalies (Figs. 6.5a,b) over the high interior of the continent are small (within ±50 mm yr^{-1}), but larger anomalies can be observed along the coast, consistent with the low and high snow accumulation in these regions. At higher latitudes (> 60°S) JRA-55 is quantitatively similar to JRA-25 and ERA-I (European Centre for Medium-Range Weather Forecasts Interim reanalysis) $P-E$ results (Bromwich and Wang 2014, 2015). The excessively high positive anomalies of JRA-25 over the Southern Ocean north of 60°S (that were noted in last year's report) are not present in JRA-55. JRA-55 also shows better overall agreement with ERA-I than JRA-25 during 2013 and 2014.

Based on JRA-55, the 2014 negative anomalies located at eastern Queen Maud Land (between 15° and 80°E) are weaker in 2015, and positive anomalies are observed over Enderby Land and the Amery Ice Shelf. The strong negative features between American Highland and Wilkes Land (between 80° and 150°E) observed in 2014 were replaced by weak positive anomalies in 2015, except near the Budd Coast region (near 115°E) where negative anomalies were observed again. The George V Coast and Ross Sea had positive anomalies in 2015, in contrast to 2014 conditions. The small positive anomalies over the western Ross Sea seen in 2014 were replaced by negative anomalies in 2015. Strong positive anomalies over the Amundsen and Bellingshausen Seas (between 150° and 75°W) in 2014 were weaker but remained positive in 2015. Small negative anomaly centers were present along the West Antarctic coastline in 2015. Both sides of the Antarctic Peninsula have similar anomaly patterns to 2014, but were weaker. The negative $P-E$ anomaly center over the Weddell Sea in 2014 was replaced by a positive one in 2015.

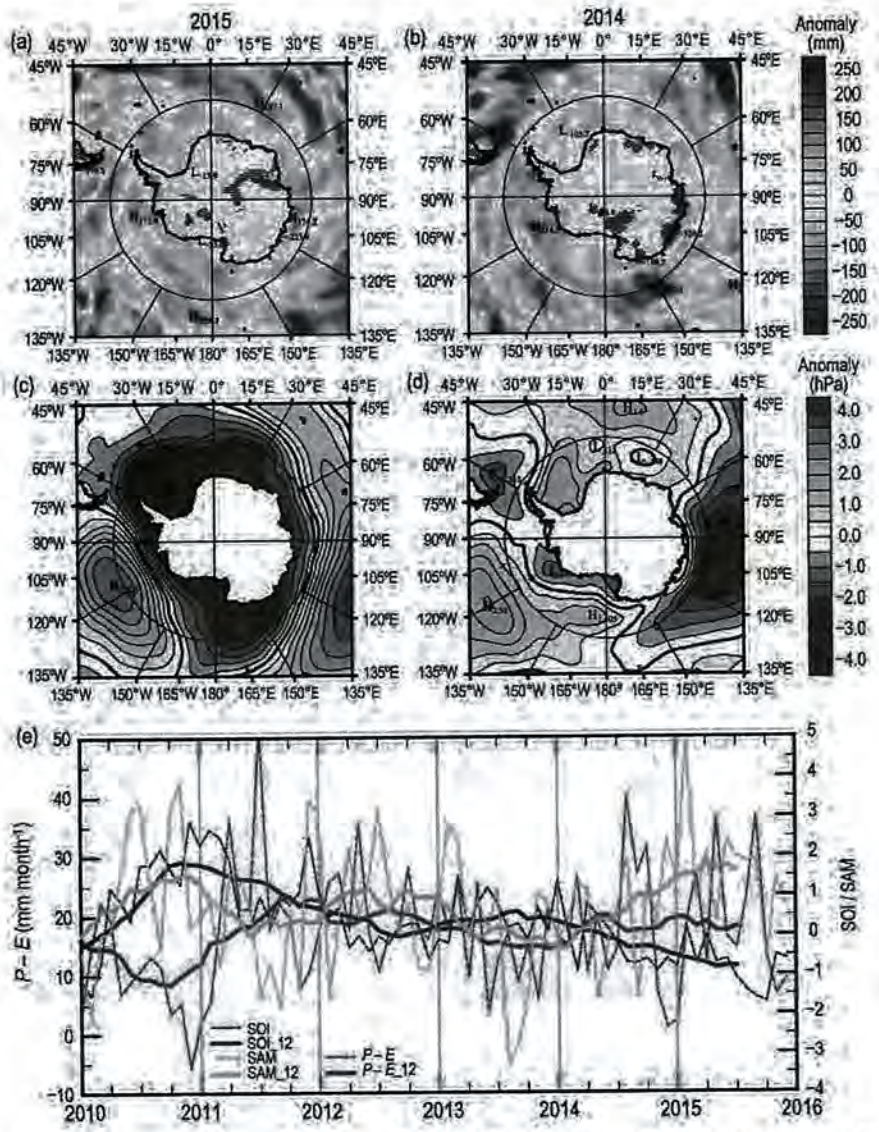

FIG. 6.5. JRA-55 (a–d) annual $P-E$ and MSLP anomalies: (a) 2015 $P-E$ anomalies (mm month^{-1}); (b) 2014 $P-E$ anomalies (mm month^{-1}); (c) 2015 MSLP anomalies (hPa); and (d) 2014 MSLP anomalies (hPa). All anomalies are departures from the 1981–2010 mean. (e) Monthly total $P-E$ (mm; dashed green) for the West Antarctic sector bounded by 75°–90°S, 120°W–180°, along with the SOI (dashed dark blue, from NOAA Climate Prediction Center) and SAM [dashed light blue, from Marshall (2003)] indices since 2010. In (a) and (b), Antarctic regions with greater than ±30% change are hatched; sloping denotes negative values and horizontal denotes positive. Centered annual running means are plotted as solid lines.

These annual $P-E$ anomaly features were generally consistent with the mean atmospheric circulation implied by the MSLP anomalies (Figs. 6.5c,d). In 2015 the MSLP anomalies surrounding Antarctica were less localized than in 2014 (Figs. 6.5c,d). The MSLP

pattern in 2015 consisted of large negative pressure anomalies over Antarctica (or high latitudes) and a ring of positive pressure anomalies at midlatitudes, which resulted in positive SAM index values recorded for most of 2015 (Figs. 6.2c, 6.5e). This MSLP pattern tended to induce higher precipitation from the Southern Ocean into Antarctica. The positive MSLP anomaly over the Ronne Ice Shelf and the Weddell Sea in 2014 was replaced by a strong negative anomaly center at the tip of the Antarctic Peninsula in 2015. Enhanced cyclonic flows induced more inflow from the ocean and resulted in higher precipitation anomalies into the Weddell Sea and Queen Maud Land. A strong negative anomaly center at the southern Indian Ocean (near 105°E) in 2014 was replaced by large positive anomalies, with weak negative anomalies along the coast of East Antarctica. Combined with cyclonic flow produced by negative anomalies over Weddell Sea, it produced higher precipitation along Queen Mary Coast (between 60° and 125°E) in 2015. The large positive anomaly center in 2014 over the South Pacific Ocean (near 120°W) was enhanced in 2015. In combination with the expanded and strengthened negative anomalies over the western Ross Sea region, above-normal precipitation was observed in the Ross Sea and Amundsen Sea regions (Fig. 6.5a).

Earlier studies show that almost half of the moisture transport into Antarctica occurs in the West Antarctic sector. Here, there is also large interannual variability in moisture transport in response to atmospheric circulation patterns associated with extreme ENSO events (e.g., Bromwich et al. 2004) and high SAM index values (e.g., Fogt et al. 2011). As the seasons progressed from 2014 to 2015, the negative MSLP anomalies over the Ross Sea weakened (Figs. 6.3a,c, 6.5d), while a positive MSLP anomaly deepened offshore of 60°S (Figs. 6.5c,d). A positive anomaly then appeared in the Bellingshausen Sea and strengthened in later months of 2015 (Figs. 6.3e,g). These anomaly features are consistent with a simultaneously strong El Niño event and a positive SAM index. Figure 6.5e shows the time series of average monthly total $P-E$ over Marie Byrd Land–Ross Ice Shelf (75°–90°S, 120°W–180°) and the monthly Southern Oscillation index (SOI) and SAM indices (with 12-month running means). It is clear that the SOI and SAM index were positively associated with each other, but negatively associated with $P-E$, in most months from 2010 to mid-2011. From then on, the SOI and SAM index were negatively associated through 2015. From 2014 into 2015, the SOI became more negative (indicating El Niño conditions in the tropical Pacific), while the SAM index became more positive. The atmospheric circulation pattern associated with a positive SAM index modulated the high latitude response to El Niño, and the associated MSLP anomalies were located farther north than normal (Sidebar 6.1). The end result was near-normal precipitation over Marie Byrd Land–Ross Ice Shelf (Fig. 6.5e), in contrast to higher-than-normal precipitation during previous El Niño events (e.g., Bromwich et al. 2004).

e. *Seasonal melt extent and duration*—L. Wang and H. Liu

Seasonal surface melt on the Antarctic continent during 2014/15 was estimated from daily measurements of passive microwave brightness temperature using data acquired by the Special Sensor Microwave–Imager Sounder (SSMIS) onboard the Defense Meteorological Satellite Program (DMSP) *F17* satellite. The data were preprocessed and provided by the U.S. National Snow and Ice Data Center (NSIDC) in level-3 EASE-Grid format (Armstrong et al. 1994) and were analyzed using a wavelet transform-based edge

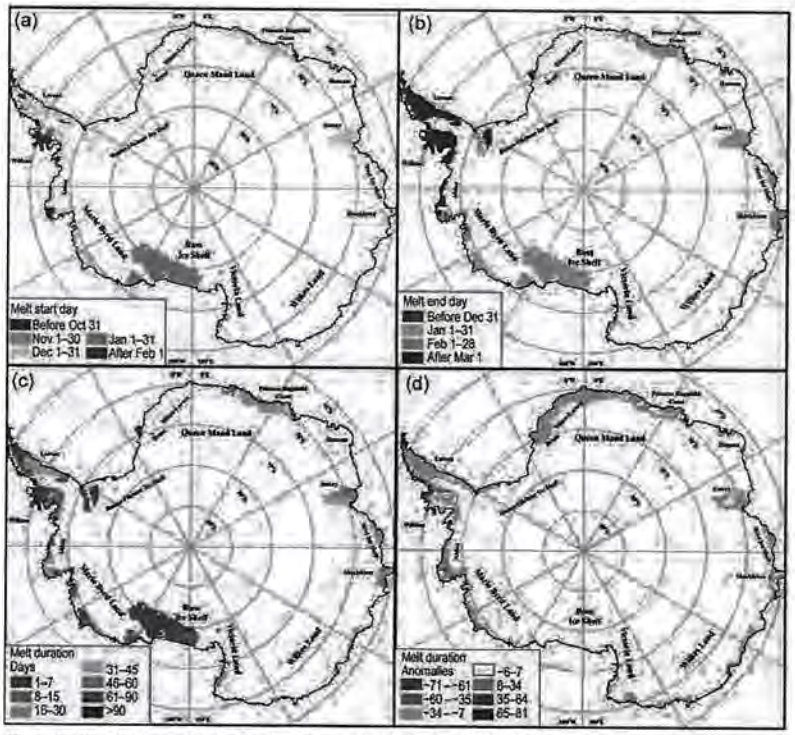

FIG. 6.6. Estimated surface melt for the 2014/15 austral summer (a) melt start day, (b) melt end day, (c) melt duration (days), and (d) melt duration anomalies (days) relative to 1981–2010. (Data source: DMSP SSMIS daily brightness temperature observations.)

SIDEBAR 6.1: EL NIÑO AND ANTARCTICA—R. L. FOGT

During 2015, a strong El Niño developed and intensified in the tropical Pacific. Like much of the globe, Antarctica is influenced during ENSO events by a series of atmospheric Rossby waves emanating from the tropical Pacific, extending to high latitudes over the South Pacific Ocean near West Antarctica (Turner 2004). This pattern has been widely referred to as the Pacific South American pattern, and during an El Niño event, positive pressure anomalies are typical off the coast of West Antarctica (Mo and Ghil 1987; Karoly 1989).

Despite the 2015/16 El Niño's emergence as a strong event in the Pacific by midyear, its impact near Antarctica was not at all typical. However, true to form, in September–December (SOND) 2015, the high-latitude South Pacific was marked by a strong positive pressure anomaly and associated counterclockwise near-surface flow (Figs. SB6.1a, 6.3g). The southerly flow in the vicinity of the Antarctic Peninsula partially explains the persistence of below-average temperatures across the Antarctic Peninsula in the latter half of 2015 (compare Figs. 6.3f,h with Fig. 6.4a). Elsewhere, the pattern of response was quite different from recent strong El Niño events (Fig. SB6.1b). The southern Pacific positive pressure anomaly, although much stronger than the El Niño average, was displaced northward. While this had consistent temperature and wind impacts across the Antarctic Peninsula and the South Pacific, much of the rest of West Antarctica was not strongly impacted in 2015 as is typical during other strong El Niño events (compare Fig. SB6.1b with Fig. 6.3e,g and Byrd AWS data in Fig. 6.4e). The northward displacement of the high pressure anomaly in 2015 is most likely due to the fact that much of 2015, with the exception of October, was marked by a positive SAM index (compare Fig. 6.2c). Because the SAM index monitors the strength and/or position of the circumpolar jet, which is known to influence extratropical Rossby wave propagation and breaking (L'Heureux and Thompson 2006; Fogt et al. 2011; Gong et al. 2010, 2013), the strengthened jet in 2015 was not so favorable for Rossby wave propagation into the higher (>60°) southern latitudes. Thus, the South Pacific teleconnection was displaced farther north than normal (based on Fig. SB6.1b). Historically, many of the strongest El Niño events occurred during negative SAM index values (Fogt et al. 2011) in contrast to the 2015 El Niño event. Nonetheless, because of its influence on meridional flow over the ice edge at the time of maximum sea ice extent (Figs. SB6.1a, 6.8c), the end of 2015 was marked by strong regional sea ice extent anomalies in the West Antarctic sector (Figs. 6.8c,d, 6.9c–e), which were opposite in sign to the long-term trends in sea ice extent in that region (Fig. 6.8e).

In summary, the 2015 El Niño indeed produced strong atmospheric circulation impacts in the South Pacific, which are consistent with the below-average temperatures across the Antarctic Peninsula and sea ice extent anomalies in the Bellingshausen, Amundsen, and Ross Seas. However, because the teleconnection was displaced farther north than normal, its impact across the rest of Antarctica was much weaker than was the case for previous strong El Niño events.

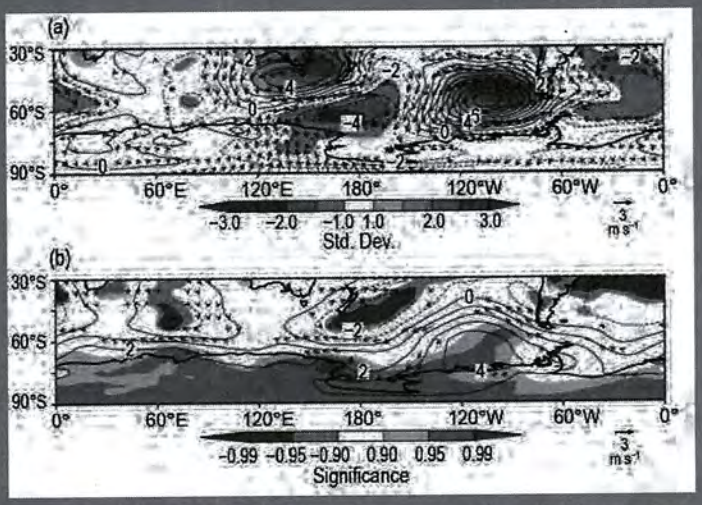

FIG. SB6.1. (a) SOND MSLP (contoured) and 10-m wind anomalies (vectors) from the 1981–2010 climatological mean. Shading represents the number of standard deviations the 2015 SOND MSLP anomalies were from the climatological mean; wind vectors are only shown if at least one component was a standard deviation outside the climatological mean. (b) MSLP (contoured) and 10-m wind (vectors) anomaly composite for the six strongest El Niño events in SOND since 1979 (in rank order: 1997, 1982, 1987, 2002, 2009, 1991), with shading (from lightest to darkest shades) indicating composite mean anomalies (of MSLP and winds) significantly different from zero at $p < 0.10$, $p < 0.05$, $p < 0.01$, respectively, based on a two-tailed Student's t test. The shading therefore indicates where the El Niño composite mean is significantly different from the 1981–2010 climatology. (Source: ERA-Interim reanalysis.)

detection method (Liu et al. 2005). The algorithm delineates each melt event in the time series by tracking its onset and end dates, with the onset day of the first melt event being the start day of the melt season (Fig. 6.6a) and the end day of the last melt event being the end day of the melt season (Fig. 6.6b). The melt duration is then the total number of melting days per pixel during the defined melt season (excluding any refreezing events that may have occurred during this period; Fig. 6.6c). The melt extent and melt index are metrics useful for quantifying the interannual variability in surface melt (Zwally and Fiegles 1994; Liu et al. 2006). Melt extent (km^2) is the total area that experienced surface melt for at least one day, while the melt index ($day \cdot km^2$) is the product of duration and melt extent and describes the spatiotemporal variability of surface melting. The anomaly map (Fig. 6.6d) was created by referencing the mean melt duration computed over 1981–2010 (see also Fig. 3 in Liu et al. 2006).

The spatial pattern of the melt duration map in austral summer 2014/15 (Fig. 6.6c) was similar to previous years (Wang et al. 2014). Areas with extended melt duration (>45 day duration in orange-red) were the Antarctic Peninsula area, including the Larsen and Wilkins ice shelves, and parts of coastal East Antarctica, including the Shackleton ice shelf and other smaller ice shelves east of there. Areas with moderate melt duration (16–45 day duration in green-yellow) included much of coastal Queen Maud Land and the Amery, West, and Abbot ice shelves; short-term melt (<16 day duration in blues) occurred on the coast of Marie Byrd Land, including Ross ice shelf and portions of Queen Maud Land near the Filchner Ice Shelf.

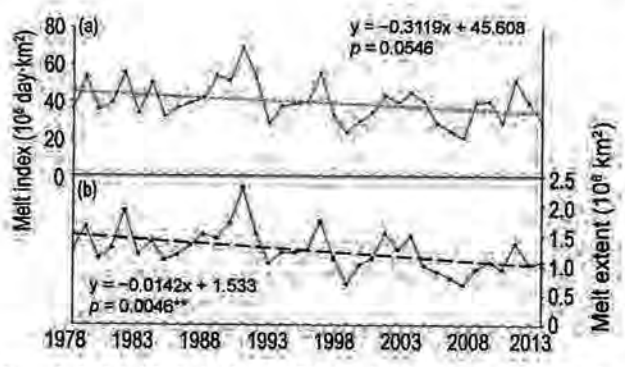

FIG. 6.7. (a) Melt index (10^6 day·km^2) from 1978/79 to 2014/15, showing a slight negative trend (p not significant at 95%). (b) Melt extent (10^6 km^2) from 1978/79 to 2014/15, also showing a negative trend (p significant at 99%). A record low melt was observed during 2008/09. The year on the x-axis corresponds to the start of the austral summer melt season, e.g., 2008 corresponds to summer (DFJ) 2008/09.

The melt index for the entire Antarctic continent has continued to drop since the 2012/13 season (Fig. 6.7a; Wang et al. 2014). The estimated melt index of the 2014/15 season is 29 252 500 day·km^2 in comparison to 39 093 125 day·km^2 in 2013/14 and 51 335 000 day·km^2 in the 2012/13 season. The melt extent of the 2014/15 season (Fig. 6.7b), however, is 1 058 750 km^2, slightly greater than last year at 1 043 750 km^2. The melt anomaly map in Fig. 6.6d shows the melt season was generally shorter than the historical average. Therefore, austral summer 2014/15 is classified as a low melt year for Antarctica. The 2014/15 melt extent and index numbers were almost equivalent to those observed during austral summer 2011/12 (944 375 km^2 and 29 006 250 day·km^2, respectively). Figure 6.7 shows a nearly significant ($p = 0.05$) negative trend (311 900 day·km^2 yr^{-1}) in melt index and a significant ($p < 0.01$) negative trend (14 200 km^2 yr^{-1}) in melt extent over 1978/79 to 2014/15, highlighted by the record low melt season observed during austral summer 2008/09. The negative trends in melt index and melt extent are consistent with previous reports (Liu et al. 2006; Tedesco 2009a,b).

f. Sea ice extent, concentration, and duration—P. Reid, R. A. Massom, S. Stammerjohn, S. Barreira, J. L. Lieser, and T. Scambos

Net sea ice areal extent was well above average during the first few months of 2015 (Fig. 6.8a). Monthly record extents were observed in January (7.46×10^6 km^2), April (9.06×10^6 km^2), and May (12.1×10^6 km^2). The January extent marked the highest departure from average for any month since records began in 1979, at 2.39×10^6 km^2 above the 1981–2010 mean of 5.07×10^6 km^2, or nearly 50% greater. These early season records follow on from the record high extent and late retreat of sea ice in 2014 (Reid et al. 2015). During the first half of 2015, there were 65 individual days of record daily sea ice extent, the last occurring on 11 July, and 46 record-breaking days of sea ice area within the first half of the year. However, the expansion of sea ice slowed so dramatically midyear that although sea ice area was at a record high level in May, it was at a record low level in August, just 83 days later (Fig. 6.8a). Close-to-average net sea ice extent levels were then observed in the latter half of 2015.

The record high net sea ice extent in January was dominated by strong positive regional anomalies in sea ice concentration and extent in the Ross and Weddell Seas (Figs. 6.8b, 6.9c,e) and across East Antarctica (~75°–140°E). This was counterbalanced by strong negative ice concentration and extent anomalies that were present in the Bellingshausen–Amundsen Seas (Figs. 6.8b, 6.9d). All three regions

of more extensive sea ice coincided with anomalously cool SSTs adjacent to the sea ice. Low atmospheric pressure anomalies were also present in the Weddell and Ross–Amundsen Seas (Fig. 6.3a). Interestingly, at this time colder-than-normal SSTs were present just to the north of the Bellingshausen–Amundsen Seas, possibly entrained within the ACC but not adjacent to the ice edge itself (and thus removed from the area experiencing below-normal ice extent).

As shown in Fig. 6.8a, there was a substantial and rapid decrease in the net ice extent (and area) anomaly from late January to early February, in large part due to changes in the eastern Ross (reflected in Fig. 6.9c) and western Amundsen (not shown) Seas. This rapid regional "collapse" followed lower-than-normal sea ice concentrations in the central pack ice during the latter part of 2014 (see Reid et al. 2015). In spite of this, net sea ice extent and area continued to track well above average or at record high levels between February and May. The Indian Ocean sector between ~60° and 110°E, the western Ross Sea, and the Weddell Sea showed particularly high or increasing sea ice extents during the February to May period as reflected in the regionwide daily anomaly series (Figs. 6.9a,c,e, respectively), with early-season areal expansion spurred on by colder-than-normal SSTs (not shown) and surface air temperatures (Figs. 6.3b,d).

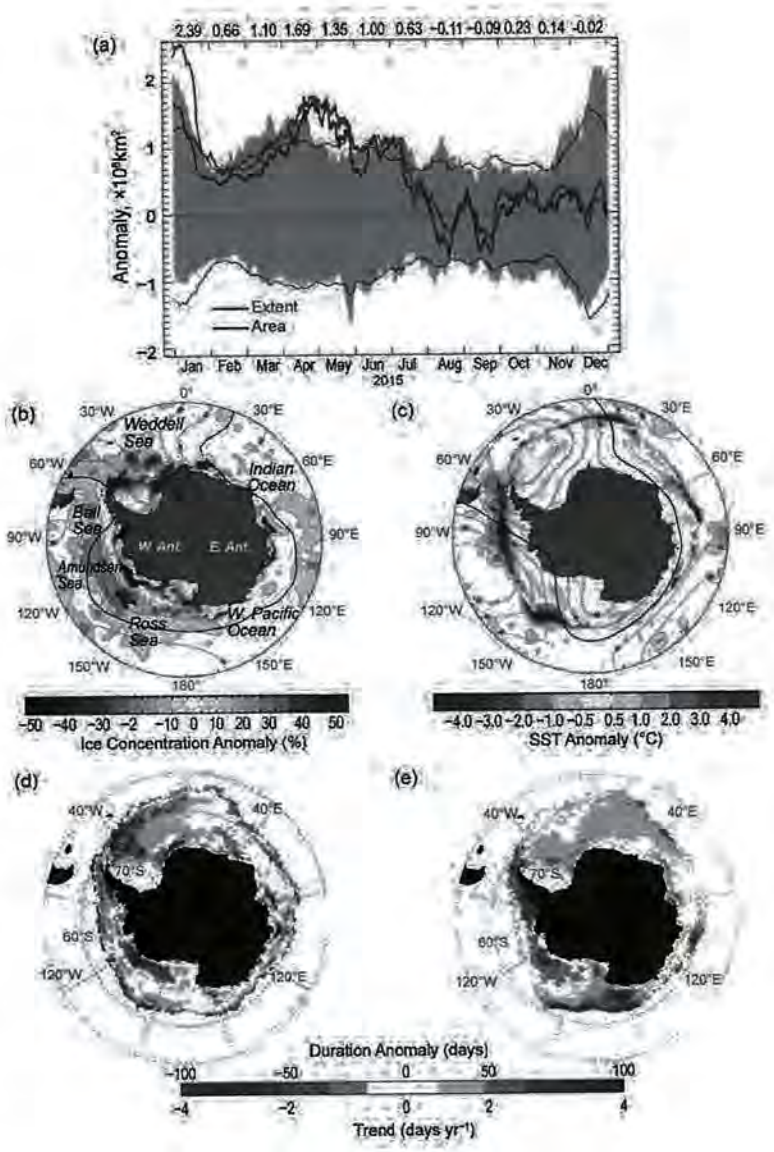

Fig. 6.8. (a) Plot of daily anomalies from the 1981–2010 mean of daily Southern Hemisphere sea ice extent (red line) and area (blue line) for 2015. Blue banding represents the range of daily values of extent for 1981–2010, while the thin black lines represent ±2 standard deviations of extent. Numbers at the top are monthly mean extent anomalies (× 10^6 km^2). Sea ice concentration anomaly (%) maps for (b) Jan and (c) Sep 2015 relative to the monthly means for 1981–2010, along with monthly mean SST anomalies (Reynolds et al. 2002; Smith et al. 2008). These maps are also superimposed with monthly mean contours of 500-hPa geopotential height anomaly (Kalnay et al. 1996; NCEP). Bell is Bellingshausen Sea, AIS is Amery Ice Shelf. (d) Sea ice duration anomaly for 2015/16 and (e) duration trend (Stammerjohn et al. 2008). Both the climatology (for computing the anomaly) and trend are based on 1981/82 to 2010/11 data (Cavalieri et al. 1996, updated yearly), while the 2015/16 duration-year data are from the NASA Team NRTSI dataset (Maslanik and Stroeve 1999).

June saw the beginning of a major change in the large-scale atmospheric pattern at higher southern latitudes, with lower-than-normal atmospheric pressure over the Antarctic continent and a strong atmospheric wave-3 pattern evolving (Fig. 6.3e). This coincided with warmer-than-normal SSTs in lower latitudes of the Indian and Pacific Oceans (the latter associated with the developing El Niño) and their influence on the distribution of atmospheric jets (Yuan 2004) and hence cyclonicity at higher southern latitudes. The abrupt change in hemispheric atmospheric circulation began a regional redistribution of patterns of sea ice areal expansion (Fig. 6.9). On one hand, there was

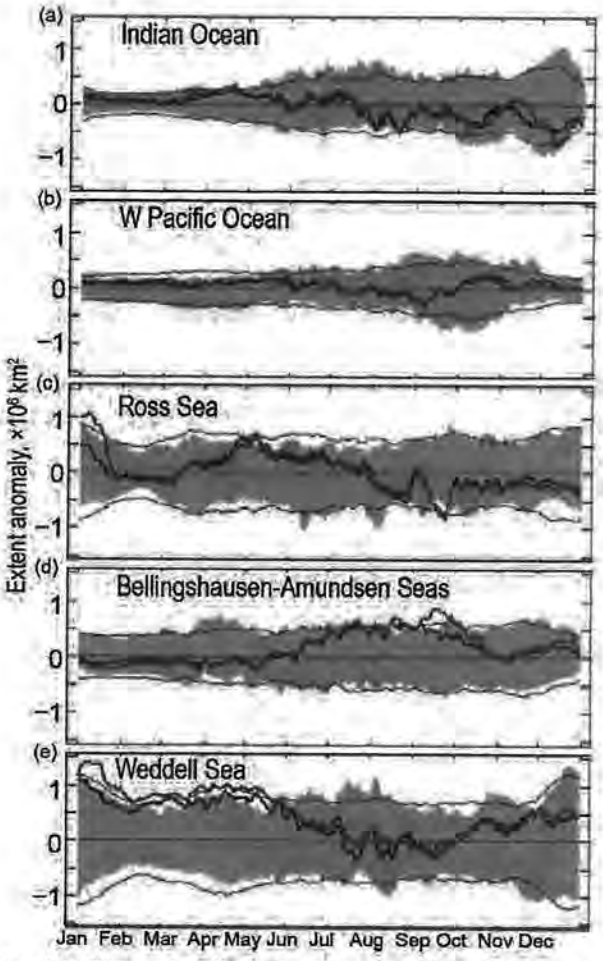

FIG. 6.9. Plots of daily anomalies (× 10^6 km^2) from the 1981–2010 mean of daily Southern Hemisphere sea ice extent (red line) and area (blue line) for 2015 for the sectors: (a) Indian Ocean; (b) western Pacific Ocean; (c) Ross Sea; (d) Bellingshausen–Amundsen Seas; and (e) Weddell Sea. The blue banding represents the range of daily values for 1981–2010 and the thin red line represents ±2 std dev. Based on satellite passive-microwave ice concentration data (Cavalieri et al. 1996, updated yearly).

a reduction in the rate of expansion in the western Weddell and Ross Seas and much of East Antarctica (~30°E–180°). In other regions (i.e., the eastern Weddell and Ross Seas and Bellingshausen and Amundsen Seas), however, a likely combination of wind-driven ice advection and enhanced thermodynamics (colder-than-normal atmospheric temperatures, and in the Bellingshausen and Amundsen Seas region colder-than-normal SSTs) led to strongly positive sea ice extent anomalies. The anomalous ice extent patterns in the Ross Sea and Bellingshausen–Amundsen Seas were opposite to the trends observed over the last few decades of greater/lesser sea ice extent in those two regions respectively (Holland 2014). The net result of this redistribution in regional ice extent anomalies was that net circumpolar sea ice extent and area dropped dramatically at the beginning of July (Fig. 6.8a). This general regional ice anomaly pattern then persisted to the end of September (Fig. 6.8c).

Another switch in large-scale regional sea ice extent anomalies occurred in October in response to the dissipation of the atmospheric wave-3 pattern and subsequent increase in negative pressure anomalies centered on ~0° and ~170°W and a broad ridge of positive pressure anomalies centered on ~55°S, 90°W (Fig. 6.3g). Positive sea ice extent anomalies were associated with a combination of cold SSTs in the Bellingshausen–Amundsen Seas and cool atmospheric temperatures in the western Ross and Weddell Seas and far eastern East Antarctic. Negative anomalies were associated with relatively warm atmospheric temperatures to the east of the low pressure systems (Fig. 6.3h). At the same time, sea ice extent in the far eastern Weddell Sea and Indian Ocean sector (~0° to ~60°E) was well below average (Fig. 6.9a) and remained so for the rest of the year. This is attributable to the very low sea ice extent in the western Weddell Sea in the previous months (July–September as mentioned above), leading to lower-than-normal eastward advection of sea ice in the eastern limb of the Weddell Gyre (see Kimura and Wakatsuchi 2011). Similarly, a lack of eastward zonal advection of sea ice from the western Ross Sea resulted in lower-than-normal sea ice extent in the eastern Ross Sea (~150° to ~120°W). On a smaller scale, in late October through mid-November several intense low pressure systems caused a temporary expansion of the sea ice edge (~50% above the long-term average) between ~60° and 90°E.

The net result of the seasonal sea ice anomalies described is summarized by the anomaly pattern in the annual ice season duration (Fig. 6.8d). The longer-than-normal annual ice season in the outer pack ice of the eastern Amundsen, Bellingshausen, and western Weddell Seas (120°W–0°) was due both to an anomalously early autumn ice-edge advance and later spring ice-edge retreat. In contrast, the longer annual ice season in the inner pack ice zones of the western Weddell Sea and East Antarctic sector (~80°–120°E) was the result of anomalously high summer sea ice concentrations (Fig. 6.8b) that initiated an anomalously early autumn ice edge advance in those two regions. The shorter-than-normal annual ice season in the eastern Ross and western Amundsen Seas (160°–120°W) was mostly due to an anomalously early ice edge retreat in spring associated with the increased negative pressure anomalies centered on 170°W and lack of zonal ice advection from the west. Though of lesser magnitude, similar spring factors

(the low pressure at 0° and lack of zonal ice advection from the west) were also implicated in the shorter-than-normal ice season in the far eastern Weddell Sea and western Indian Ocean sector between 10° and 40°E. The contrast in spring–summer anomaly patterns between the Bellingshausen–Amundsen Seas and eastern Ross Sea (Figs. 6.8c, 6.9c,d) is a somewhat typical response to El Niño and as such is opposite to the sea ice response to the atmospheric circulation pattern associated with a strong positive SAM index (and is also opposite to the long-term trend in annual ice season duration; Fig. 6.8e). However, and as described in Sidebar 6.1, the high-latitude response to this year's El Niño was spatially muted relative to past El Niños due to the damping effect of the circulation anomalies associated with a mostly positive SAM index during this time.

g. Southern Ocean—J.-B. Sallée, M. Mazloff, M. P. Meredith, C. W. Hughes, S. Rintoul, R. Gomez, N. Metzl, C. Lo Monaco, S. Schmidtko, M. M. Mata, A. Wåhlin, S. Swart, M. J. M. Williams, A. C. Naveira-Garabata, and P. Monteiro

The horizontal circulation of the Southern Ocean, which allows climate signals to propagate across the major ocean basins, is marked by eddies and the meandering fronts of the Antarctic Circumpolar Current (ACC). In 2015, large observed anomalies of sea surface height (SSH; Fig. 6.10a) contributed to variations in the horizontal ocean circulation. While many of these anomalies are typical of interannual variability, there were several regions where the 2015 anomaly was noteworthy due either to its extreme magnitude or its spatial coherence: north of the ACC in the Southwest Indian Ocean (~20°–90°E); in the entire South Pacific (~150°E–60°W), specifically the mid-Pacific basin around 120°W; and the anomalous negative SSH anomalies stretching around much of the Antarctic south of the ACC, especially over the Weddell Sea (0°–60°W). A large part of the 2015 SSH anomalies in the mid-Pacific, around Australia, and around South America was likely attributable to the strong El Niño event in 2015, though the low around Antarctica appears unrelated to ENSO variations (Sallée et al. 2008).

It is not straightforward to convert these large-scale SSH anomalies into anomalies of circumpolar volume transport. The best indicator of such variations is bottom pressure averaged on the Antarctic continental slope (Hughes et al. 2014), but such observations on the narrow slope regions are not available. Instead, the focus is on sea level averaged over this strip (Hogg et al. 2015). Figure 6.10d reveals that recent years have shown a resumption of the steady rise in sea level in this region. A slight sea level fall in 2015 compared to 2014 remains consistent with this trend given the increase from 2014 to 2015 in eastward winds as represented by the SAM index (Fig. 6.10e), which is known to be associated with a fall in sea level (Aoki 2002; Hughes et al. 2003). A conversion from sea level to zonally averaged circumpolar transport, which is well established for periods of up to five years, is shown in Fig. 6.10e. This confirms the association with the atmospheric structures related to SAM but is suggestive of an additional source of variability associated with major El Niño (e.g., 2009/10, 2015/16) and La Niña (e.g., 1998/99, 1999/2000) events, when zonally averaged circumpolar transport anomalies became more negative (decreased transport) and positive (increased transport), respectively.

The horizontal circulation and vertical water-mass circulation are dynamically linked through a series of processes including surface water-mass transformation associated with air–sea–ice interactions. The characteristics of the lightest and densest of the Southern Ocean water masses are now described to provide an assessment of the vertical circulation and its contribution to ventilating the world's oceans. The ocean surface mixed layer is the gateway for air–sea exchanges and provides a conduit for the sequestration of heat or carbon dioxide from the atmosphere into the ocean's interior, which is ultimately mediated by the physical characteristics of the mixed layer.

The 2015 mixed layer temperature anomaly pattern revealed a distinct north–south dipole delimited by the ACC (Figs. 6.10b,c). Mixed layer conditions in Antarctic waters were very cold, whereas the mixed layers north of the ACC were warmer than average. This pattern persisted throughout both summer and winter, though with a reduced magnitude in winter. While the warm signal in the mid-Pacific was consistent with the influence of the 2015 El Niño event (Vivier et al. 2010), the cold signal south of the ACC was not. It was consistent, however, with the atmospheric circulation pattern associated with a positive SAM index that included increased northward Ekman transport of relatively cool and fresh Antarctic surface waters. In agreement, the southeast Pacific sector was fresher than the climatological average conditions, though other regions showed little homogeneity in salinity anomaly (not shown).

Mixed layer temperatures have a strong influence on air–sea CO_2 fluxes and ocean pH. Overall, the Southern Ocean is a net carbon sink. This sink decreased during the 1990s, but since 2002 has increased, reaching a maximum of about 1.3 Pg C yr^{-1} in 2011 (Pg = 10^{15}g; Landschutzer et al. 2015) and was

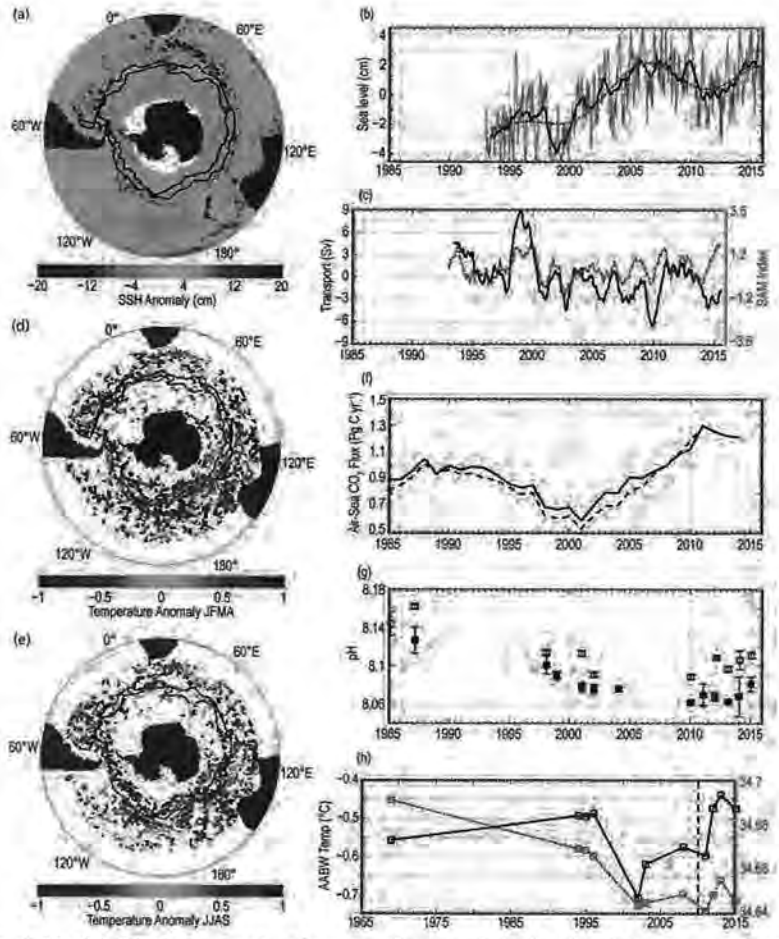

FIG. 6.10. (a) 2015 anomaly of sea surface height (cm) with respect to the 1993–2014 mean (produced from the Aviso SSH merged and gridded product). The trend at each location has been removed. (b) Time series (gray) of sea level anomaly (cm; produced from the Aviso SSH merged and gridded product) representative of a narrow region along the Antarctic coast (see Hogg et al. 2015) smoothed at different time scales. (c) Estimate of annual mean ACC transport anomaly (Sv, black line) derived from sea level (Hogg et al. 2015) with SAM index (Marshall et al. 2003) superimposed (dashed orange line). (d) 2015 anomaly of mixed layer temperature (°C) in summer (Jan–Apr) with respect to the climatological mean (2000–2014; computed from all available Argo observations). (e) Same as (d) but for the winter anomaly (Jul–Sep). In (a, d, e), the two black lines represent the mean location of the two main fronts of the ACC (Orsi et al. 1995). (f) Evolution of the Southern Ocean carbon sink (Pg C yr^{-1}) south of 35°S, showing the flux derived from an interpolation method (Landschutzer et al. 2015) based on surface ocean pCO_2 data from SOCAT-V3 (black solid line) and from SOCAT-V2 (black dotted line; Bakker et al. 2014). Positive values refer to a flux from air to ocean (i.e., ocean acts as a sink). (g) Evolution of pH in the Antarctic surface water (around 56°S, solid square) and subantarctic surface water (around 40°S, hollow square) in the South Indian Ocean; only repeat summer stations are used. (h) Potential temperature (°C, black line) and salinity (dashed orange line) of Antarctic Bottom Water at 140°E for 1969–2015; only repeat summer stations are used. Potential temperature and salinity are averaged over the deepest 100 m of the water column for stations between 63.2° and 64.4°S, in the core of the AABW over the lower continental slope (average pressure of 3690 dbar). The vertical dashed line indicates the date of the calving of the Mertz Glacier Tongue. Note that time axis in (h) is different from (b), (c), (f), and (g).

likely stronger than 1 Pg C yr^{-1} in 2015 (Fig. 6.10f). South of the ACC, the increase of the sink is explained by the cooling of the surface layer in summer (Fig. 6.10b) and the stability of the CO_2 concentrations in winter (Munro et al. 2015). The ocean carbon uptake leads to a decrease in pH, the so-called ocean acidification. A global assessment of surface water pH in 2015 is not possible due to scarcity of observations, so we present the evolution of pH in the South Indian sector, which has been monitored since 1985 (Fig. 6.10g). A rapid pH change was identified in 1985–2001 (−0.03 decade^{-1}) but has stabilized since 2002 (Fig. 6.10g), a signal probably associated with a shift in climate forcing (e.g., neutral state of SAM in 2000s; Fig. 6.10e).

The bottom layers of the Southern Ocean are also undergoing substantial changes. Linear trends of deep ocean change constructed from repeat sections between 1992 and 2005 reveal abyssal warming, with the strongest warming close to Antarctica (Purkey and Johnson 2010; Talley et al. 2016). Antarctic Bottom Water (AABW) is also contracting in volume and freshening (Purkey and Johnson 2012, 2013; Shimada et al. 2012; Jullion et al. 2013; van Wijk and Rintoul 2014; Katsumata et al. 2014; Meredith et al. 2014). These changes reflect the response of AABW source regions to changes in surface climate and ocean–ice shelf interaction and to downstream propagation of the signal by wave and advective processes (Jacobs and Giulivi 2010; van Wijk and Rintoul 2014; Johnson et al. 2014).

As with pH, observations of the deep ocean remain scarce, preventing a global assessment of the state of the abyssal ocean in 2015. However, repeat occupa-

tions of hydrographic sections at 140°E provide a record of variations in AABW properties immediately downstream of a primary source of bottom water (Fig. 6.10h). Potential temperature shows significant variability but no long-term trend between 1969 and 2015. In contrast, the long-term trend in salinity (~ −0.01 decade^{-1}; Fig. 6.10h) exceeds interannual variability. Calving of the Mertz Glacier Tongue in 2010 reduced the area of the Mertz polynya and thereby reduced the amount of sea ice and dense water formed in the polynya (Tamura et al. 2012; Shadwick et al. 2013), which likely contributed to the AABW variations observed after 2010.

h. Antarctic ozone hole—E. R. Nash, S. E. Strahan, N. Kramarova, C. S. Long, M. C. Pitts, P. A. Newman, B. Johnson, M. L. Santee, I. Petropavlovskikh, and G. O. Braathen

The 2015 Antarctic ozone hole was among the largest and most persistent ever observed, based upon the record of ground and satellite measurements starting in the 1970s. Figure 6.11a displays the daily areal coverage of the Antarctic ozone hole during 2015 (blue line) compared to the 1986–2014 climatology (white line). The ozone hole area is defined as the area covered by total column ozone values less than 220 Dobson Units (DU). For 2015, area values greater than 5 million km^2 first appeared in late August, approximately two weeks later than typical. The ozone hole usually reaches its largest size by mid-September, but in 2015 the maximum size occurred on 2 October at 28.2 million km^2. The ozone hole then persisted at this large size (>20 million km^2) until 15 November, setting daily records during much of October and November. The development of ozone depletion over time (daily minimum values; Fig. 6.11b) indicates that the ozone minimum was reached near 2 October; ozone then remained near record low values until early December. The late start, persistent large area, and low ozone minima were caused by unusually weak stratospheric wave dynamics.

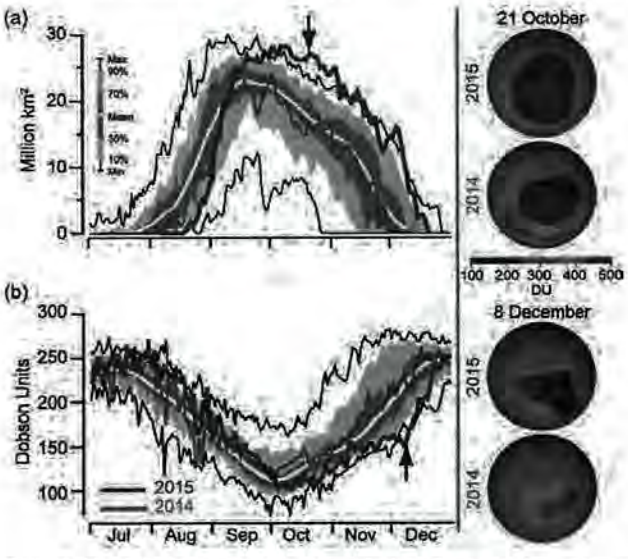

Fig. 6.11. (a) Area coverage of the Antarctic ozone hole as defined by total column ozone values less than 220 DU and (b) daily total column ozone minimum values in the Antarctic region from TOMS/OMI for 2014 (red line) and 2015 (blue line). The average of the daily values (thick white line), the record maximum and minimum sizes (thin black lines), and the percentiles (gray regions and legend in a) are based on a climatology from 1986–2014. The black arrows indicate the dates of the ozone maps on the right side.

NOAA ozonesondes are launched regularly over South Pole station. In early October 2015, the 12–20-km column ozone was close to the long-term mean (Fig. 6.12a), while ozone increases thereafter were delayed compared to the long-term record. The minimum 12–20-km column ozone in 2015 was the fourth lowest at 7.2 DU, measured on 21 October (ozone hole image Fig. 6.11a). The ozonesonde total column minimum was 112 DU on 15 October. The ozonesonde of 8 December 2015 (ozone hole image Fig. 6.11b) showed record low total column ozone for early December, highlighting the abnormally late breakup of the hole.

One of the key factors controlling the severity of the Antarctic ozone hole is stratospheric temperature. Lower temperatures allow more polar stratospheric cloud (PSC) formation, exacerbating ozone depletion. Southern Hemisphere stratospheric dynamical conditions were anomalous in spring 2015. The lower stratospheric polar cap temperatures from the NCEP–DOE Reanalysis 2 for 2015 (Fig. 6.12b, blue line) were near the climatological average through August, but were below climatology during September–November.

The 100-hPa eddy heat flux is a measure of wave propagation into the stratosphere. A smaller (larger) magnitude leads to colder- (warmer-) than-average temperatures. The heat flux was generally below average for July–October (Fig. 6.12c), especially in October. As a result, temperatures warmed at a slower rate in September–October (Fig. 6.12b), and the vortex eroded more slowly than in previous years. Consequently, the ozone hole was persistent, and stratospheric ozone levels at South Pole remained below average during October–November (Fig. 6.12a).

The 2015 ozone hole broke up on 21 December, about two weeks later than average. The breakup is identified as the date when total ozone values below 220 DU disappear (see Fig. 6.11). Ozone hole breakup is tightly correlated with the stratospheric polar vor-

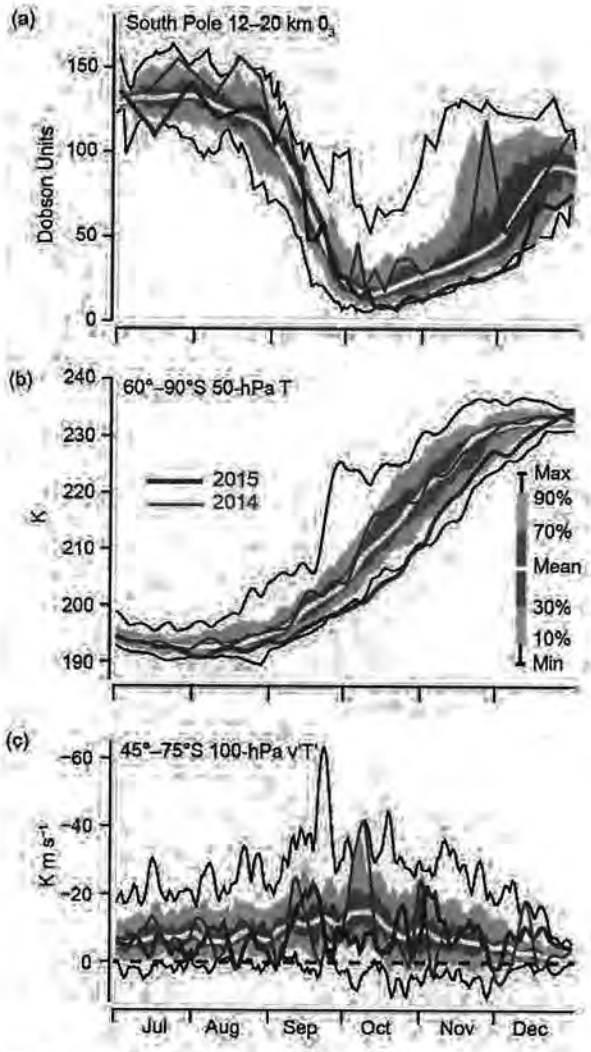

FIG. 6.12. (a) Column ozone from NOAA South Pole ozonesondes measured over the 12–20-km (~160–40-hPa) range. (b) NCEP–DOE Reanalysis 2 of lower stratospheric temperature (60°–90°S, 50-hPa). (c) NCEP–DOE Reanalysis 2 of zonal mean eddy heat flux (45°–75°S, 100 hPa). The blue lines show the 2015 values and the red lines show 2014. The average of the daily values (thick white line), the record maximum and minimum sizes (thin black lines), and the percentiles [(gray regions and legend in (b)] are based on a climatology from (a) 1986–2014 and (b), (c) 1979–2014.

tex breakup, which is driven by wave events propagating upward into the stratosphere, thus enabling transport of ozone-rich air from midlatitudes. The 2015 ozone hole broke up late because of weak wave driving in October–November (Fig. 6.12c).

Levels of chlorine and bromine continue to decline in the stratosphere, and improvement of ozone conditions over Antarctica is expected. Ozone depletion is estimated using equivalent effective stratospheric chlorine (EESC)—a combination of inorganic chlorine (Cl_y) and bromine. Using a mean age of air of 5.2 years, EESC shows a 2000–02 peak of 3.8 ppb, with a projected decrease in 2015 of 9% to 3.45 ppb as a result of the Montreal Protocol. This is a 20% drop towards the 1980 ("pre-ozone hole") level of 2.03 ppb. NASA *Aura* satellite Microwave Limb Sounder (MLS) N_2O measurements can be used to estimate Antarctic stratospheric Cl_y levels (Strahan et al. 2014). Antarctic EESC has a small annual decrease (<1% yr^{-1}), but interannual variations in transport to the Antarctic vortex cause Cl_y to vary by up to ±8% with respect to expected levels. Similar to 2014, the 2015 Antarctic stratospheric Cl_y was higher than recent years and similar to levels found in 2008 and 2010.

MLS lower stratospheric chlorine and ozone observations in the vortex were consistent with the

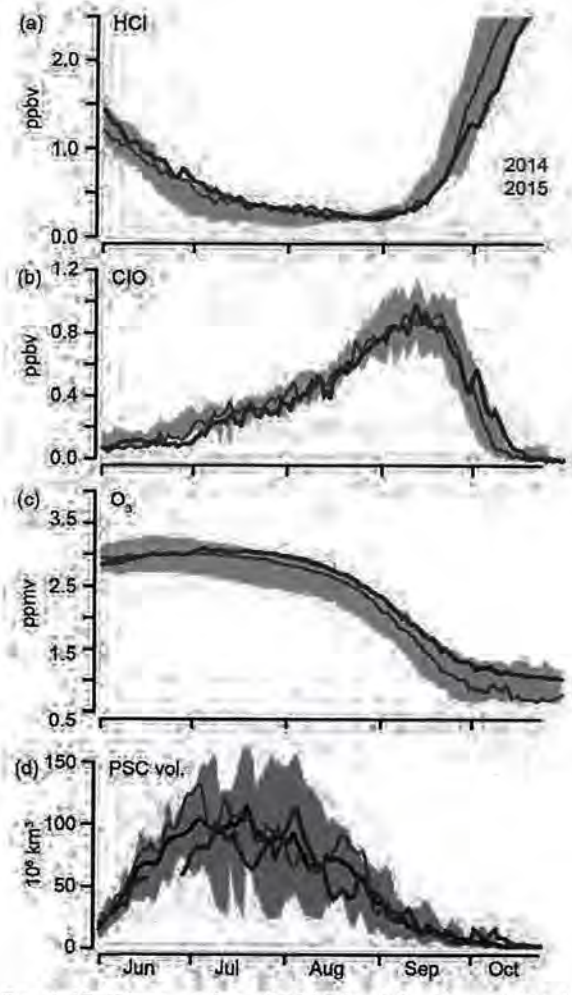

FIG. 6.13. Time series of 2014 (red line) and 2015 (blue line) Antarctic vortex-averaged: (a) HCl, (b) ClO, and (c) ozone from *Aura* MLS (updated from Manney et al. 2011). These MLS averages are made inside the polar vortex on the 440-K isentropic surface (~18 km or 65 hPa). The gray shading shows the range of Antarctic values for 2004–14. (d) Time series of 2014 (red line) and 2015 (blue line) *CALIPSO* PSC volume (updated from Pitts et al. 2009). The gray shading shows the range for 2006–14, and the black line is the average.

SIDEBAR 6.2: POLAR ECOSYSTEMS AND THEIR SENSITIVITY TO CLIMATE PERTURBATION—H. DUCKLOW AND A. FOUNTAIN

Ice exerts a dominant control on the function and structure of polar ecosystems. Depending on the organism, it provides habitat and foraging platforms, or serves as a barrier to food and the flow of nutrients (Fountain et al. 2012). Polar ecosystems, both terrestrial and marine, have evolved and adapted to pervasive ice conditions, so when air temperatures rise above the melting threshold, the normal balance of water and ice shifts dramatically, resulting in a series of cascading effects that propagate through the entire ecosystem. The effects may persist for years to decades (J. Priscu 2016, manuscript submitted to *BioScience*).

In Antarctica, the differences between marine and terrestrial ecosystems could not be more extreme. These two biomes are the focus of two NSF-funded Long Term Ecological Research (LTER) programs: the Palmer LTER (or PAL), which is studying the rapidly changing marine ecosystem west of the Antarctic Peninsula (Ducklow et al. 2013), and the McMurdo Dry Valleys LTER (or MCM), which is studying the terrestrial ecosystem in the Dry Valley polar desert (Freckman and Virginia 1997). Established in the early 1990s, these two Antarctic sites collect baseline measurements to develop process-level understanding, thus providing necessary context for evaluating ecological responses to climate events.

The marine ecosystem surrounding Antarctica includes the coastal and continental shelf region that is influenced by seasonal sea ice cover, as well as the permanently open ocean zone poleward of the Antarctic Circumpolar Current (Treguer and Jacques 1992). Primary production in these regions is dominantly by phytoplankton. Although considerable regional and seasonal variability exists, Antarctic food webs are typically supported by diatoms with variable contributions by other types of phytoplankton. Diatom-based food webs are typically characterized by highly variable but sometimes vast swarms of Antarctic krill. Krill in turn are the principal food for the conspicuous large predators of Antarctic seas, including penguins and other seabirds, seals, and whales (Hardy 1967).

This general picture has served as the paradigm for the Antarctic marine ecosystem for decades, but it appears to be changing, at least in the rapidly warming (Smith et al. 1996) western Antarctic Peninsula region (WAP) of the Bellinsghausen Sea. Ecological change along the WAP was first marked by catastrophic declines in Adélie penguins (Fig. SB6.2a; Fraser and Hofmann 2003; Bestelmeyer et al. 2011). The principal cause of ecological change is decreasing sea ice cover in the WAP and greater Bellingshausen Sea—both its extent and duration (Fig. 6.8e; Stammerjohn et al. 2012). Diatom blooms, krill recruitment, and penguin breeding success are all dependent on the extent of sea ice and the timing of its retreat (Saba et al. 2014; Montes-Hugo et al. 2009). Other changes in the freshwater system are also known to influence the marine ecosystem. Glacial discharge and melt, for example, have the capacity to increase ocean stratification and add bio-available micronutrients, such as iron, to the productive upper

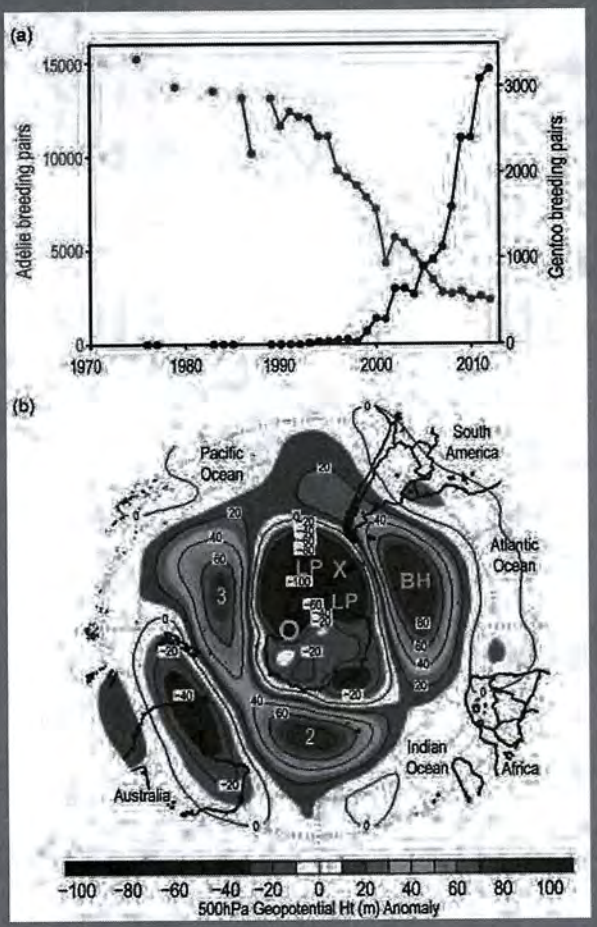

FIG. SB6.2. (a) The number of breeding pairs of Adélie and Gentoo penguins near Palmer Station, 1976–2013. The Gentoo is a subpolar, ice-tolerant invasive species that has colonized the polar region as sea ice cover has declined and water temperatures have increased. The first Gentoo pairs were observed at this location in 1994. (b) Monthly mean composite anomaly map of 500-hPa geopotential height centered over Antarctica for Sep 2001 to Feb 2002 relative to the mean calculated over Sep to Feb 1980–2001. BH and LP denote blocking high pressure and low-pressure anomalies, respectively. The yellow X is close to Palmer Station and the yellow circle is close to McMurdo Station. (From Massom et al. 2006.)

layers (Boyd and Ellwood 2010; Hawkings et al. 2014). Changes in any of these environment variables can lead to functionally extinct species and a reorganization of the marine ecosystem (e.g., Sailley et al. 2013).

Antarctic terrestrial ecosystems, at least those that inhabit the largest ice-free areas of the Antarctic continent, the Dry Valleys (78°S, 162°E), exist in a landscape that includes glaciers, perennially ice-covered lakes, seasonal meltwater streams, and arid soils (Ugolini and Bockhiem 2008). No vascular plants or vertebrates inhabit the region, and food webs are dominated by bacteria, cyanobacteria, fungi, yeasts, protozoa, and a few taxa of metazoan invertebrates (Freckman and Virginia 1997). Glacial meltwater is the primary source of water, which flows in ephemeral streams and conveys water, solutes, sediment, and organic matter to the lakes (Fountain et al. 1998; McKnight et al. 1999). Streams flow for up to 12 weeks in the austral summer providing a habitat for microbial mats abundant in streambeds stabilized by stone pavement (McKnight et al. 1998). Perennial water environments include ice-covered lakes in the Dry Valleys of Antarctica; they maintain biological activity year-round with food webs dominated by phytoplankton and bacteria (Laybourn-Parry 1997).

The two LTER sites are separated by about 3800 km (Fig. 6.1). On annual time scales, air temperatures at these two sites are inversely related (A. Fountain et al. 2016, manuscript submitted to *BioScience*; M. Obryk et al. 2016, manuscript submitted to *BioScience*) due mostly to the circulation anomalies associated with the SAM index (Trenberth et al. 2007). On decadal time scales, the lower-latitude PAL site is also experiencing rising air temperatures (+3°C increase in annual temperatures over 1958–2014), while the higher-latitude MCM site is experiencing a more modest change [+1°C over the same time period; A. Fountain et al. (2016), manuscript submitted to *BioScience*].

However, in the austral spring/summer of 2001/02, a hemisphere-wide atmospheric circulation anomaly caused unusually high temperatures across the entire continent (Fig. SB6.2b; Massom et al. 2006), which had long-lasting impacts.

At MCM, the rapid melting of glacial ice caused streams to flow at record levels, eroding stream banks and rapidly raising lake levels (Foreman et al. 2004). The stream waters transported unusually high concentrations of sediments and nutrients to the ice-covered lakes. Phytoplankton chlorophyll-*a* concentrations reached record high levels that austral summer but also remained at elevated levels for almost a decade. Elevated soil moisture caused a reorganization of species composition in the soils that was still evident seven years later (Barrett et al. 2008).

At PAL, warm, moist northwesterly winds caused a rapid and early ice edge retreat in early spring (September–October 2001) that subsequently compacted and piled the ice against the Peninsula. Snowfall was also anomalously high during this time (Massom et al. 2006). Abundances of krill species were higher than normal, likely due to the high productivity associated with the compacted sea ice inshore (Steinberg et al. 2015). The positive chlorophyll-*a* anomaly in 2001/02 corresponded to a statistically significant krill recruitment event (evidenced in Adélie penguin diet samples) the following year (Saba et al. 2014). However, it was the catastrophic late-season snowfalls and subsequent flooding that caused the largest single-season decline in Adélie penguin breeding success in 30 years (Fraser et al. 2013). There was a devastating loss of an entire breeding cohort, an effect that is still evident 10 years later.

The climate event of 2001/02 illustrates the extreme sensitivity of polar ecosystems and also illustrates how an anomalous event can induce connectivity across different regional climates. As exemplified here, a relatively small but critical change in the temporal and spatial distributions of ice and water exhibited dramatic and persistent ecological responses, the implications of which are still being studied.

late start of the 2015 ozone hole (Fig. 6.11a). The reformation of hydrogen chloride (HCl; Fig. 6.13a) and decrease of chlorine monoxide (ClO; Fig. 6.13b) occurred late in 2015. The 440-K potential temperature ozone levels (Fig. 6.13c) were higher than average in July–September, but declined to very low values by mid-October, consistent with Fig. 6.12a.

Heterogeneous chemical reactions on PSC surfaces convert reservoir chlorine (e.g., HCl) into reactive forms (e.g., ClO) for catalytic ozone loss. The PSC volume (Fig. 6.13d), as measured by the *Cloud-Aerosol Lidar and Infrared Pathfinder Satellite Observation (CALIPSO)*, generally followed the average (black line) for the entire season. However, the October 2015 volume of 5.6 million km^3 ranked highest of all 10 years, consistent with the persistent and large October ozone hole (Fig. 6.11a).

Satellite column observations over Antarctica (not shown) show some indications that ozone loss

has diminished since the late-1990s. Averaged daily minima over 21 September–16 October (ozone hole maximum period) have increased since 1998 at a rate of 1.2 DU yr^{-1} (90% confidence level). The 2015 ozone hole area, averaged over 7 September–13 October, was estimated at 25.6 million km^2, the fourth largest over the 1979–2015 record. Since 1998, this area is decreasing at a rate of −0.09 million km^2 yr^{-1}, but this trend is not statistically significant. The decline of chlorine concentrations should eventually be manifested in smaller and shallower Antarctic ozone holes. However, unambiguous attribution of the ozone hole improvement to the Montreal Protocol cannot yet be made because of relatively large year-to-year transport, wave activity, temperature variability, and observational uncertainty. Further information on the ozone hole, with data from satellites, ground instruments, and balloon instruments, can be found at www.wmo.int/pages/prog/arep/gaw/ozone/index.html.

7. REGIONAL CLIMATES—A. Mekonnen, J. A. Renwick, and A. Sanchez-Lugo, Eds.

a. Overview

This chapter provides summaries of the 2015 temperature and precipitation conditions across seven broad regions: North America, Central America and the Caribbean, South America, Africa, Europe, Asia, and Oceania. In most cases, summaries of notable weather events are also included. Local scientists provided the annual summary for their respective regions and, unless otherwise noted, the source of the data used is typically the agency affiliated with the authors. Please note that different nations, even within the same section, may use unique periods to define their normals. Section introductions will typically define the prevailing practices for that section, and exceptions will be noted within the text. In a similar way, many contributing authors use languages other than English as their primary professional language. To minimize additional loss of fidelity through reinterpretation after translation, editors have been conservative and careful to preserve the voice of the author. In some cases, this may result in abrupt transitions in style from section to section.

b. North America

This section is divided into three subsections: Canada, the United States, and Mexico. Information for each country has been provided by local scientists, and the source of the data is from the agency affiliated with the authors. Where available, anomalies are reported using a 1981–2010 base period; however, due to the different data sources, some anomalies are reported using other base periods. These are noted in the text.

1) Canada—R. Whitewood, L. A. Vincent, and D. Phillips

In Canada, 2015 was characterized by higher-than-average temperatures stretching from the central regions to the Pacific Coast and lower- and drier-than-average temperatures in the northeastern region of the country. Anomalies in this section are reported with respect to the 1961–90 base period.

(i) Temperature

The annual average temperature in 2015 for Canada was 1.3°C above the 1961–90 average, based on preliminary data. This marks the 11th warmest year since nationwide records began in 1948. The warmest year on record for Canada was 2010, at 3.0°C above average, and 4 of the 10 warmest years have occurred during the last decade. The national annual average temperature has increased 1.6°C over the past 68 years (Fig. 7.1). In 2015, annual departures >+2.5°C were recorded in the Yukon and western Northwest Territories, while annual departures <–0.5°C were observed in northern Quebec, Labrador, and Baffin Island (Fig. 7.2a).

Seasonally, winter (December–February) 2014/15 was 1.0°C above average and the 27th warmest since 1948. Warmer-than-average conditions were

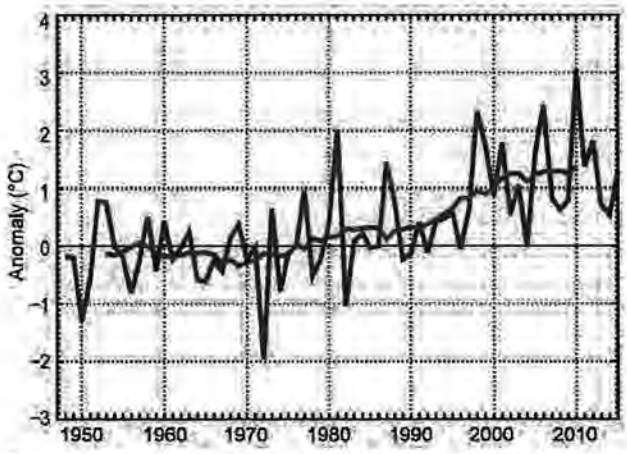

Fig. 7.1. Annual average temperature anomalies (°C) for Canada for 1948–2015 (base period: 1961–90). The red line is the 11-yr running mean. (Source: Environment and Climate Change Canada.)

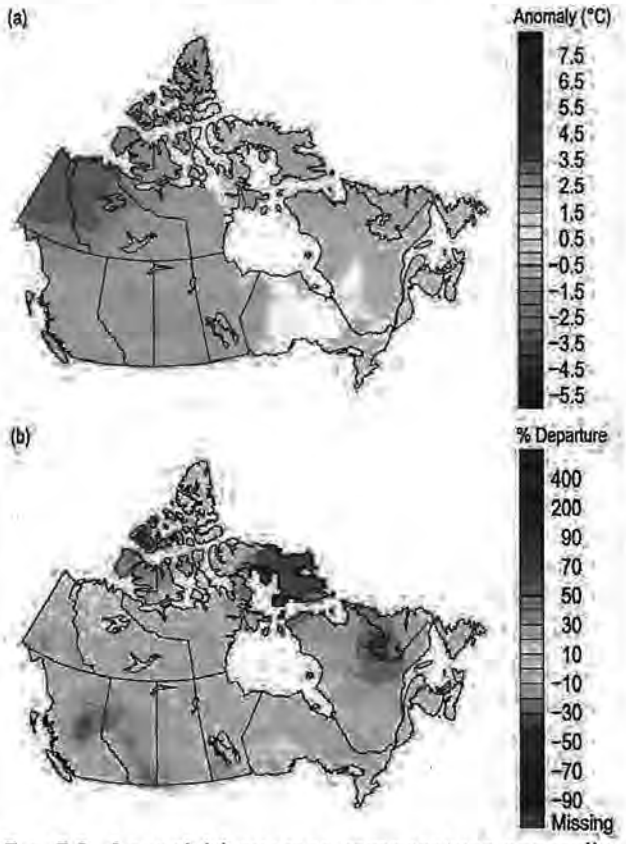

Fig. 7.2. Annual (a) average temperature anomalies (°C) and (b) total precipitation anomalies in Canada (% departure; base period: 1961–90). (Source: Environment and Climate Change Canada.)

observed in Yukon, Northwest Territories, British Columbia, Alberta, and Saskatchewan. Most of Ontario, Quebec, and the Atlantic provinces experienced cooler-than-average conditions. During spring (March–May), the same pattern of warmer-than-average conditions in the western and central regions and cooler-than-average conditions in the eastern regions of the country continued. The nationally averaged temperature for spring 2015 was 1.3°C above the 1961–90 average and the 14th warmest in the 68-year period of record.

Summer (June–August) was 1.0°C above average and the sixth warmest since 1948. British Columbia and northern Nunavut (a territory in the northeast of the country) experienced warmer-than-average conditions. Southern Ontario was the only region with slightly cooler-than-average temperature conditions during summer. Summer temperatures across the remainder of the country were near-average.

During autumn (September–November), the pattern changed with the central regions of the country, from Saskatchewan through the Maritimes, and the northern territories all experiencing warmer-than-average conditions, while British Columbia, Alberta, northern Quebec, and Newfoundland and Labrador experienced near-average conditions. The nationally averaged temperature was 1.7°C above the 1961–90 average; the sixth warmest autumn since 1948.

(ii) Precipitation

Canada as a whole experienced slightly drier-than-average precipitation in 2015. Based on preliminary data, it was the 20th driest year since nationwide records began in 1948, with nationally averaged precipitation 97% of the 1961–90 average. Drier-than-average conditions were observed for eastern Nunavut, northern Quebec and Labrador, in central British Columbia, and Alberta, whereas only the area over the Canadian Arctic Archipelago experienced wetter-than-average conditions (Fig. 7.2b).

Seasonally, winter 2014/15 was the 13th driest since 1948, and nationally averaged precipitation was 90% of the 1961–90 average, with most of the country experiencing drier-than-average conditions. However, wetter-than-average conditions were observed over much of Nunavut and the Atlantic provinces. Spring 2015 was the 10th driest in the 68-year period of record with nationally averaged precipitation 89% of average. Drier-than-average conditions continued across much of the country, with some wetter-than-average conditions in the western Canadian Arctic Archipelago.

Summer 2015 was the 17th wettest since 1948, and national average precipitation was 105% of average. Wetter-than-average conditions were mainly observed in the northwestern regions of the country whereas drier-than-average conditions occurred in British Columbia and Alberta. Autumn 2015 was the 26th wettest since 1948, with nationally averaged precipitation 103% of average. Drier-than-average conditions for the season were experienced in the Yukon, northern British Columbia, most of Quebec, and over Baffin Island in the north. Wetter-than-average conditions were observed in the Prairie Provinces (Alberta, Saskatchewan, and Manitoba) and in the rest of Nunavut for the autumn months.

(iii) Notable events

Winter got off to a slow start for the Maritimes, but conditions changed in January. Snow fell from several storms, often just a few days apart. Atlantic Canada was continually battered through February and March with storm after storm, leaving behind snow amounts not seen in decades. Numerous records were set over the 2014/15 winter in the Maritimes. Halifax International Airport in Nova Scotia recorded total snow accumulation from January to May of 371 cm (normal is 59 cm). The previous snowiest such period at any Halifax station was 330 cm in 1972. Saint John, New Brunswick, received more than double its normal snowfall—495 cm (normal is 240 cm)—its snowiest winter on record. Moncton, New Brunswick, broke the 5-meter level at 507 cm (normal is 325 cm). In Charlottetown, Prince Edward Island, the snowiest city in Canada this winter, an April snowstorm helped set a new record for the most snow in one winter—551 cm—12 cm more than the previous record in 1971/72.

The wildfire season in Canada began early, ended late, and was extremely active, especially in the West. The national wildland fire season was above average for both number of fires and hectares burned, about four times the 15-year average (2001–15) and three times the 25-year average (1991–2015), respectively. Wildfires began in northern Saskatchewan in March. Residents from several communities near La Ronge and La Loche began evacuating to centers in the south. Hot temperatures and dry thunderstorms in May and June contributed to even more volatile fire conditions, with more than 13 000 people evacuated in what was the largest evacuation in Saskatchewan's history. In total, 1.8 million hectares burned in Saskatchewan, six times the provincial average. In Alberta, wildfires burned hot and fast in June when half the province came under a fire advisory. British

Columbia reported more than 1800 wildfires that burned an estimated 300 000 hectares and cost more than 287 million U.S. dollars to fight. The 20-year (1996–2015) average number of fires is about 1050 with an average 43 280 hectares burned. Conditions in British Columbia included extreme heat near 40°C, widespread and persistent dryness, large amounts of dry lightning, and gusty winds, which all contributed to the extreme fire season.

2) United States—J. Crouch, R. R. Heim Jr., and C. Fenimore

The annual average temperature in 2015 for the contiguous United States (CONUS) was 12.4°C, or 0.9°C above the 1981–2010 average—the second warmest year since records began in 1895, behind 2012 (Fig. 7.3). The annual CONUS temperature over the 121-year period of record is increasing at an average rate of 0.1°C per decade. The nationally averaged precipitation total during 2015 was 111% of average, the third wettest year in the 121-year historical record. The annual CONUS precipitation is increasing at an average rate of 4.1 mm per decade. Outside of the CONUS, Alaska had its 2nd warmest and 15th wettest year since records began in 1925. The statewide temperature was 1.6°C above average, while the precipitation total was 108% of average. Complete U.S. temperature and precipitation maps are available at www.ncdc.noaa.gov/cag/.

(i) Temperature

During early 2015, record warmth spanned the western United States with record and near-record cold temperatures in the Midwest and Northeast. The last few months of 2015, particularly December, brought much-above-average temperatures to the East, with near-average temperatures across the West. This pattern resulted in all 48 states in the CONUS observing an above-average annual temperature (Fig. 7.4a). Florida, Montana, Oregon, and Washington (state) each had their warmest year on record. Twenty-three additional states across the West, Great Plains, Gulf Coast, and East Coast each had annual temperatures that ranked in the highest 10th percentile of their historical records.

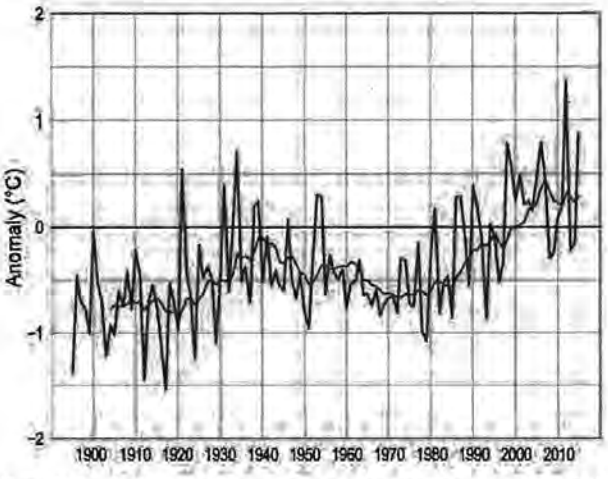

Fig. 7.3. Annual mean temperature anomalies (°C) for the contiguous United States for 1895–2015 based on the 1981–2010 average. The red line is the 10-year running mean. (Source: NOAA/NCEI.)

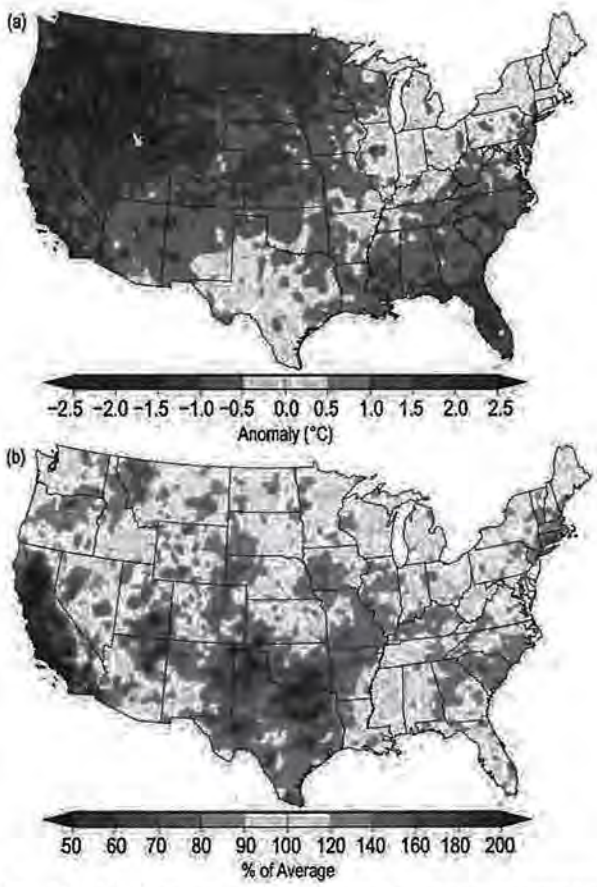

Fig. 7.4. (a) Annual average temperature anomalies (°C) and (b) % of average annual total precipitation in the contiguous United States (base period: 1981–2010). (Source: NOAA/NCEI.)

The winter (December–February) 2014/15 CONUS temperature was 0.4°C above average, ranking in the warmest third of the historical record. Record and near-record warmth were observed in the West, with six states observing record high seasonal temperatures. Below-average temperatures occurred in the East; February was particularly cold, with 24 states observing one of their 10 coldest months on record and numerous cities, including Chicago, Illinois, and Buffalo, New York, being record cold. The CONUS spring (March–May) temperature was 0.7°C above average, the 11th warmest on record. Much-above-average temperatures were observed across the West and Southeast—Florida observed its warmest spring

on record. The summer (June–August) CONUS temperature was 0.5°C above average, the 12th warmest on record. Above-average temperatures continued in the Southeast and West, where California, Oregon, and Washington were record warm, while parts of the Midwest were cooler than average. The autumn (September–November) temperature was 1.5°C above average, the warmest such period on record for the CONUS. Every state had an above-average autumn temperature: 40 states observed one of their 10 warmest on record, with Florida record warm. December ended the year with a record high monthly temperature for the CONUS that was 3.0°C above average. Twenty-nine states across the East were record warm, while near-average temperatures were observed across the West.

(ii) Precipitation

During 2015, much of the central and eastern CONUS were wetter than average, while parts of the West and Northeast were drier than average (Fig. 7.4b). Fourteen states had an annual precipitation total that was within their wettest 10th percentiles. Oklahoma and Texas were both record wet with 145% and 143% of average annual precipitation, respectively. Drought conditions that began in 2010 in both states were eradicated during 2015. California, which was plagued by drought during all of 2015, had its 13th driest year on record; end-of-year precipitation partially erased early year deficits. At the beginning of 2015, the CONUS moderate to exceptional drought footprint was 28.7%; it peaked at 37.8% in May and ended the year at 18.7%. This end-of-year drought footprint was the smallest for the CONUS since December 2010.

The CONUS winter precipitation was 90% of average, ranking in the driest third of the historical record (29th driest). Despite near-average precipitation in the West, record warmth caused much of the high-elevation precipitation to fall as rain and not snow. The below-average mountain snowpack and subsequent below-average spring and summer runoff contributed to near-record low reservoir levels, worsening drought, and a record-breaking wildfire season. Spring was the 10th wettest on record for the CONUS, with 117% of average precipitation. Record and near-record precipitation totals were observed in the southern Great Plains and Central Rockies, with below-average precipitation along both coasts. May was an extraordinarily wet month for the CONUS with 112.8 mm of precipitation, 147% of average, the wettest among all months on record. Much of the precipitation fell across the Southern Plains. The summer precipitation for the CONUS was 108% of average, the 16th wettest on record. Above-average precipitation was observed across the Ohio Valley, where record rain fell during June and July. For autumn, the CONUS precipitation total was 111% of average and the 15th wettest on record. Above-average precipitation was observed across the South and along the East Coast. South Carolina had its wettest autumn on record with 603.5 mm of rainfall, 321% of average. December was record wet for the CONUS, at 160% of average, becoming the only month in the 121-year period of record that was simultaneously wettest and warmest for its respective month.

(iii) Notable events

Tornado activity during 2015 was below average for the fourth consecutive year, with a total of 1177 confirmed tornadoes, compared to the 1991–2010 annual average of 1253. Despite the below-average number of tornadoes, there were 36 tornado-related fatalities, with most occurring during a deadly outbreak in December across the Southern Plains and Lower Mississippi Valley.

Wildfires burned nearly 4.1 million hectares across the United States during 2015, surpassing 2006 for the most acreage burned since record keeping began in 1960. The most costly wildfires occurred in California, where over 2500 structures were destroyed in the Valley and Butte wildfires in September.

Numerous major precipitation events impacted different regions of the CONUS in 2015. Heavy snowfall during late winter and early spring set a new seasonal record for Boston, Massachusetts, with 281 cm of snow. In early October, an upper-level low interacted with moisture from Hurricane Joaquin offshore in the Atlantic to produce rainfall totals exceeding 500 mm in parts of North and South Carolina. In the Southern Plains, late-spring rainfall and summer and autumn rains associated with the remnants of east Pacific tropical cyclones (see section 4e3) caused several significant flooding events. On 30 October, the remnants of Hurricane Patricia dumped 389.7 mm of rain on Austin, Texas, 146.3 mm of which fell in a single hour.

3) MEXICO—R. Pascual Ramírez, A. Albanil Encarnación, and J. L. Rodríguez Solís

In Mexico, the annual temperature for 2015 tied with 2014 as the highest since national temperature records began in 1971. The nationally averaged precipitation total was ninth highest since precipitation records began in 1941, with the most notable accumulations during February and March.

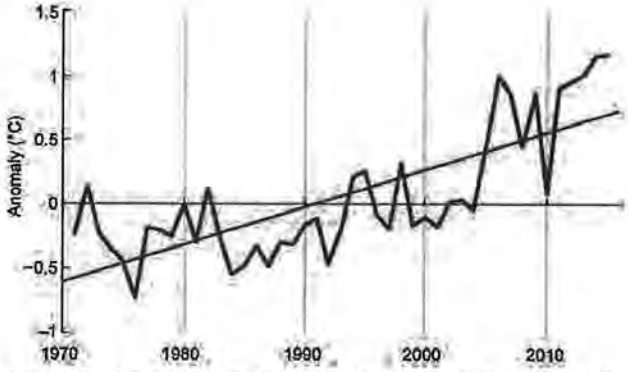

Fig. 7.5. Annual mean temperature anomalies (°C, blue) for Mexico (base period: 1981–2010). A linear trend is depicted by the red line. (Source: National Meteorological Service of Mexico.)

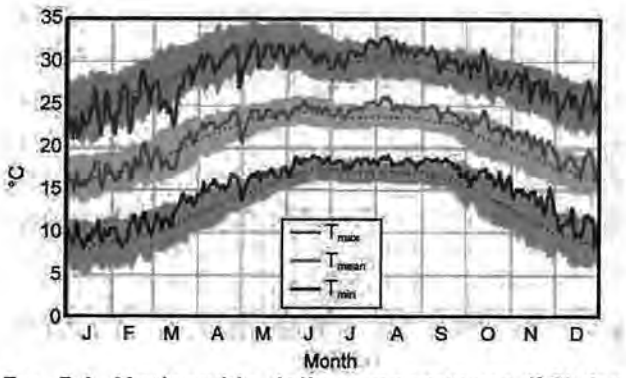

Fig. 7.6. Nationwide daily temperatures (°C) for Mexico. Shaded areas represent the ±2 std. dev. (base period: 1981–2010). Solid lines represent daily values for the three temperature parameters and dotted lines are the climatology. (Source: National Meteorological Service of Mexico.)

(i) Temperature

The 2015 mean temperature for Mexico was 22.1°C, which was 1.1°C above the 1981–2010 average, tying with 2014 as the warmest year since national records began in 1971 and surpassing the previous record of 21.9°C set in 2006 and 2013 (Fig. 7.5). This was also the 12th consecutive year with an above-average annual temperature.

The first three months of the year were near-average; however, the rest of the year was characterized by above-average temperatures and, in some instances, the daily mean, maximum, and minimum temperatures were close to two standard deviations above average (Fig. 7.6). The mean temperature for July–September was 2.3°C above average—the warmest such period on record, surpassing the previous record set in 2013 and 2014 and making the last three years the three warmest for the July–September period on record.

Regionally, the mean temperature in 2015 was below average in northern Baja California, areas of Chihuahua and its borders with Coahuila and Durango, between Colima and Jalisco, the central region (which includes the states of Mexico, Puebla, and Veracruz), and Oaxaca, while the rest of the country observed near-average to above-average temperatures. Eight states had their warmest year since records began in 1971: Campeche, Quintana Roo, and Yucatan in the Yucatan Peninsula; Nayarit, Jalisco, Michoacán, and Guerrero in the west; and Morelos in the central portion of the country. Conversely, the state of Veracruz observed one of its 20 coldest years on record (Fig. 7.7a).

Frost days, defined as daily minimum temperatures ≤0°C, is typical in Mexico during October–March, while hot days—daily maximum temperatures ≥40°C—are typical during April–September. During January–March 2015, only 26.0% of the country, mostly confined to the central region,

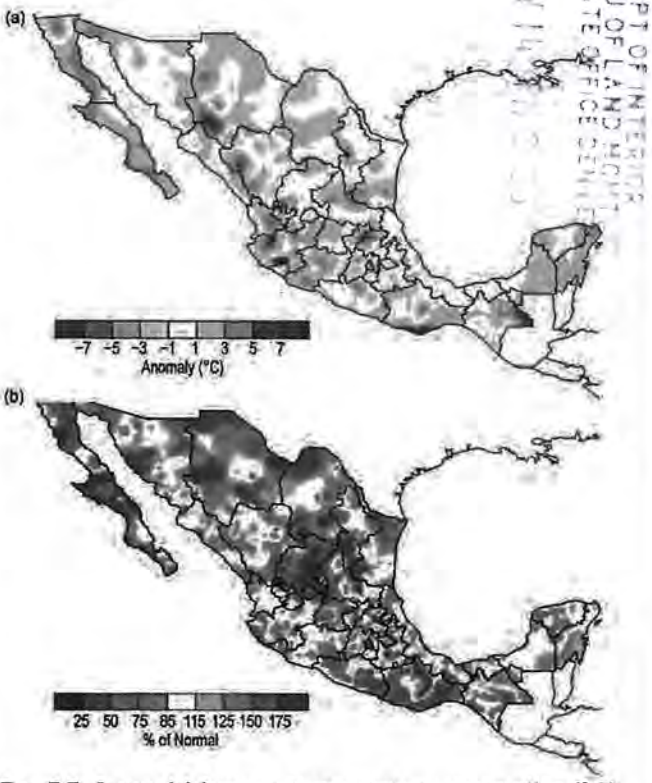

Fig. 7.7. Annual (a) mean temperature anomalies (°C) and (b) precipitation anomalies (% of normal) observed in 2015 over Mexico (base period: 1981–2010). (Source: National Meteorological Service of Mexico.)

experienced frost conditions (compared to the January–March average of 43.3%). Similarly, during October–December 2015, only 28.1% of the country, mainly in the northern areas, observed frost conditions, compared to the October–December average of 38.2%. During April–June, 20.2% of the country, mainly across northwestern and southern Mexico, observed hot days (compared to the average of 41.8%),

while 16.7% of the country, mainly in the northern regions, recorded hot days during July–September (much below the average of 29.6%).

(ii) Precipitation

Above-average rainfall was observed across the north-central region in 2015, while below-average conditions were present across northern Baja California, the South Pacific (coastal areas of Guerrero, Oaxaca, and Chiapas), Veracruz, and the northern Yucatan Peninsula (Fig. 7.7b). The 2015 national rainfall total of 872.0 mm (110.8% of normal) was the ninth highest annual total since national records began in 1941.

March was exceptionally wet. Two winter storms and four frontal passages led to the rainiest March since records began in 1941, with 69.6 mm of rain, providing 8.0% of the annual rainfall for the year compared to a normal contribution (14.7 mm) close to 2.0%. September, which climatologically provides the greatest amount to the annual rainfall total (18.5%), added 132.7 mm in 2015, which represents 15.2% of 2015 annual rainfall.

Nine hurricanes, which all formed in the eastern North Pacific basin (see section 4e3), impacted the nation's western coastal region, leaving, in most cases, significant rainfall. The most activity occurred in September when Tropical Storm Kevin, Hurricane Linda, Hurricane Marty, and Tropical Depression 16-E brought heavy rain to northwestern and southwestern parts of the nation.

Overall, Aguascalientes (central Mexico) and Colima (western Mexico) had their wettest year on record, while Baja California Sur and Chihuahua had their second wettest. Meanwhile, the rainfall deficits were remarkable along the South Pacific coast, with Oaxaca having its second driest year since national records began in 1941.

(iii) Notable events

An EF3 tornado struck Ciudad Acuña, Coahuila, on the morning of 25 May, causing at least 14 deaths and 290 injuries and destroying 750 homes. This was only the second tornado to reach EF3 intensity over the past 15 years, following the tornado in Piedras Negras on 24 April 2007, also in the state of Coahuila.

Hurricane Patricia was the strongest hurricane on record in the eastern North Pacific basin and one of the most intense to strike Mexico. It developed on 20 October and reached Category 5 hurricane strength on the Saffir–Simpson scale, with maximum sustained winds of 174 kt (88 m s^{-1}) and a minimum pressure of 879 mb (see section 3e4). Patricia was only the second tropical cyclone to make landfall in Mexico on the Pacific shores as a Category 5 storm since records began in the Pacific basin in 1949. The previous Category 5 landfall was in October 1959, when Hurricane No. 12 made landfall in the Tenacatita Bay, Jalisco, similar to Patricia's trajectory.

c. Central America and the Caribbean

1) Central America—J. A. Amador, H. G. Hidalgo, E. J. Alfaro, A. M. Durán-Quesada, and B. Calderón

For this region, nine stations from five countries were analyzed (Fig. 7.8). Stations on the Caribbean slope are: Philip Goldson International Airport, Belize; Puerto Barrios, Guatemala; Puerto Lempira, Honduras; and Puerto Limón, Costa Rica. Stations located on the Pacific slope are: Tocumen International Airport and David, Panama; Liberia, Costa Rica; Choluteca, Honduras; and Puerto San Jose, Guatemala. For 2015, the NOAA/NCEI GHCN daily precipitation dataset showed a considerable amount of missing data. For some stations, the daily rainfall amount was incomplete, whereas in other cases the value was flagged because it did not pass a quality control test. Precipitation historical records for the above-mentioned stations were recovered from Central American national weather services (NWS). The station climatology (1981–2010) and anomalies for 2015 were recalculated using NWS data by filling the gaps in the daily data records of the NOAA/NCEI database (especially those considered initially as zero based on the flags listed in the metadata of this database). In some stations (e.g., David and Choluteca), differences in precipitation totals between NWS data and the NOAA/NCEI dataset were as high as 420 and 560 mm, respectively, for 2015. In the station climatology, the largest differences were found in David and Liberia (490 and 820 mm, respectively). Previous years' station climatology from the NOAA/NCEI database and procedures used for all variables can be found in Amador et al. (2011).

(i) Temperature

Mean temperature (Tm) frequency distributions for the nine stations are shown in Fig. 7.8. Most stations, with the exception of Limon and Liberia, experienced a higher frequency of above-average daily mean temperatures in 2015. There was a near-normal negative skewness in Tm at Philip Goldson (Tm1) and Puerto Barrios (Tm2) on the Caribbean slope and a near-average number of cold surges during the winter months. Stations in Panama (Tm5 and Tm6) and Honduras (Tm8) show a shift to the right of the Tm distribution with a higher frequency of warm Tm values during 2015.

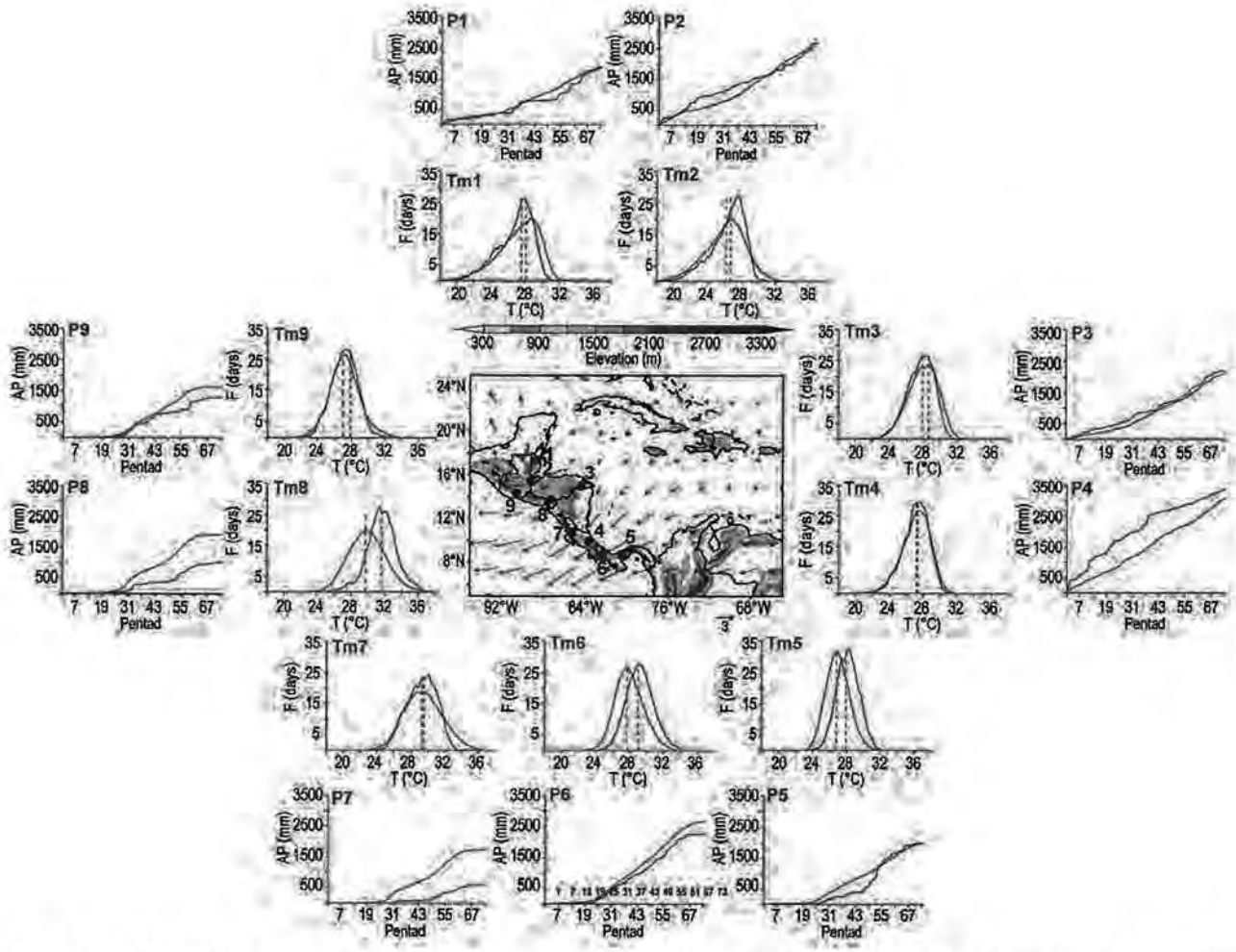

FIG. 7.8. Mean surface temperature (Tm) frequency (F; days) and accumulated pentad precipitation (P; mm) time series are shown for nine stations (blue dots) in Central America: (1) Philip Goldson International Airport, Belize; (2) Puerto Barrios, Guatemala; (3) Puerto Lempira, Honduras; (4) Puerto Limón, Costa Rica; (5) Tocumen International Airport, Panamá; (6) David, Panamá; (7) Liberia, Costa Rica; (8) Choluteca, Honduras; and (9) Puerto San José, Guatemala. The blue solid line represents the 1981–2010 average values and the red solid line shows 2015 values. Vertical dashed lines depict the mean temperature for 2015 (red) and the 1981–2010 period (blue). Vectors indicate July wind anomalies at 925 hPa (1981–2010 base period). Shading depicts regional elevation (m). (Source: NOAA/NCEI and Central American NWS.)

(ii) Precipitation

Annual precipitation totals were below normal at all stations on the Pacific slope (Fig. 7.8). At Liberia and Choluteca, the values were extremely low (in the tail of the distribution at the $p = 0.05$ level), and these areas experienced a long dry spell that extended past pentad 50 (beginning of September). Subsequent rains helped increase the accumulations later in the year, but they were not sufficient to move out of the "extremely dry" classification. A similar type of variation also occurred in Tocumen, where lack of precipitation caused an extremely dry condition until around pentad 47 (third week of August), but subsequent rains led to a close-to-normal annual total. The other stations in the Pacific slope (David and Puerto San Jose) showed no or little indication of this "late-rains" effect. Stations on the Caribbean slope observed relatively normal accumulations at the end of the year. Puerto Limon was extremely wet most of the time from the beginning of the year to pentad 40 (third week of July). A subsequent reduction of rainfall at this station resulted in moderately wetter-than-normal conditions for the year as a whole.

Low-level moisture appeared sensitive to ENSO conditions. Regional rainfall resembled conditions associated with the development of the El Niño event in 2015. Near-surface moisture flux convergence anomalies were computed based on ERA Interim reanalysis data. Results (not shown) reveal that wetter-than-normal conditions in late 2014 evolved into drier-than-normal after spring 2015.

Table 7.1. Summary of events and impacts, including number of fatalities (f), missing people (m), and affected people (a) by country and specific region. [(Sources for the Guatemala landslide in October 2015: www.redhum.org/documento_detail/17300 and the Pacific slope of Cenral America: OCHA-ROLAC (in Spanish: Oficina de Coordinación de Asuntos Humanitarios-Oficina Regional para América Latina y el Caribe, reliefweb.int/sites/reliefweb.int/files/resources/Crisis%20por%20sequia%20en%20America%20Central%20en%202015.pdf)]

Country(ies)	Dates (2015)	Hydrometeorological Conditions	Fatalities (f) Missing People (m) Affected People (a)	Specific Region
Panamá	22 Sep	Extreme below-average rains	Unknown number of affected farmers, 2500 cattle died	Azuero Peninsula
Costa Rica	27–28 Oct	Floods	4f	Central Valley
	19 Nov	Floods	1f	Alajuela and Corredores
Nicaragua	2–14 Jun	Heavy rainfall and floods associated with low pressure systems	6f, 35000a	Managua
El Salvador	15–20 Oct	Floods and landslides	4f, more than 210a	San Cayetano, Zaragoza, San Miguel, Luis de Moscoso
Honduras	07–15 Jun	Heavy rainfall, landslides and floods	2f, 2m, 300a	Tegucigalpa
	16–18 Oct	Floods	8f	Central Honduras
	7–8 Dec	Floods and landslides	3f	Northern Honduras
	15 Dec	Landslides	1f	Cuculmeca
Guatemala	7 Jun	Floods and landslides	8000a	Departments of Guatemala, Sacatepéquez, Santa Inés, and San Miguel Petapa
	8 Aug	Floods associated with a tropical wave	5f	Caribbean slope
	13 Oct	Landslides	274f, 353m	El Cambray II Community, and Santa Catalina Pinula
Pacific Slope of Central America	Up to 6 Oct	Extreme below-average rains	An estimated 3.5 million people affected, with more than 2 million in need of food, medical, and sanitary assistance	Azuero Peninsula, Panama; Guanacaste, Costa Rica; Pacific slopes of Nicaragua, El Salvador, Honduras, and Guatemala

(iii) Notable events

Tropical storm activity during 2015 was below average for the Caribbean basin (6°–24°N, 60°–92°W). There were three named storms: Danny, Erika, and Joaquin. Joaquin became a hurricane and reached major hurricane status in early October. No significant impacts were reported for Central America associated with any of these tropical systems. Stronger-than-average Caribbean low-level jet (CLLJ; Amador 1998), 925-hPa winds during July (vectors in Fig. 7.8) were consistent with El Niño (Amador et al. 2006). Central America experienced contrasting hydrometeorological conditions between the Pacific and Caribbean slopes from January to May. The impacts were severe, but different, across the region (Table 7.1).

2) CARIBBEAN—T. S. Stephenson, M. A. Taylor, A. R. Trotman, S. Etienne–LeBlanc, A. O. Porter, M. Hernández, D. Boudet, C. Fonseca, J. M. Spence, A. Shaw, A. P. Aaron-Morrison, K. Kerr, G. Tamar, D. Destin, C. Van Meerbeeck, V. Marcellin, A. C. Joseph, S. Willie, R. Stennett-Brown, and J. D. Campbell

Prevailing El Niño conditions were associated with below-normal annual rainfall and above-normal annual mean temperatures over much of the region (Fig. 7.9). Abundant dry and dusty air from the Sahara Desert in Africa also contributed to the dry weather for the year, particularly during the first six months. The base period for comparisons is 1981–2010.

(i) Temperature

Some Caribbean countries, including Anguilla, Barbados, Cayman Islands, Cuba, Dominican Republic, St. Kitts and Nevis, St. Maarten, and St. Lucia, experienced above-normal to record temperatures during 2015. The average annual temperatures were the highest on record since 1951 for Cuba (26.6°C) and second highest since 1946 for Piarco, Trinidad (27.4°C). Other temperature extremes for Piarco include the highest mean maximum temperature since 1946 for October (33.6°C) and November (32.7°C) and the second highest for August (33.6°C). V. C. Bird International Airport, Antigua, recorded its second-highest maximum temperature of 34.6°C (on 30 September) since records began in 1971 and observed a high mean minimum temperature of 24.5°C for the year, tying the record set in 2001 and 2002. Sangster International Airport, Jamaica, recorded its highest mean maximum temperature for May (33.0°C) since 1973, and Crown Point, Tobago, set records for August (33.2°C), September (33.9°C), and November (33.0°C) since records began in 1969. During October–December, record high mean maximum temperatures were observed in Freeport, Bahamas (25.3°C), and Grand Cayman (31.3°C) since 1990 and 1971, respectively, and the highest absolute maximum temperature was observed for Dominica (35.5°C) in the 45-year record.

(ii) Precipitation

While annual rainfall for 2015 was below normal for most of the Caribbean, contrasting rainfall anomalies were observed in some territories during the first quarter of the year. The January–March rainfall was above normal for Dominican Republic, Grenada, Aruba, Barbados, and eastern Jamaica, and below normal for Anguilla, Antigua and Barbuda, and St. Maarten. St. Thomas, U.S. Virgin Islands, recorded its wettest February (339.1 mm) since 1953. The transition to drier conditions commenced in the second quarter for Aruba, Dominican Republic, and Jamaica, with Dominica, Guadeloupe, St. Kitts, and St. Lucia also recording very dry conditions.

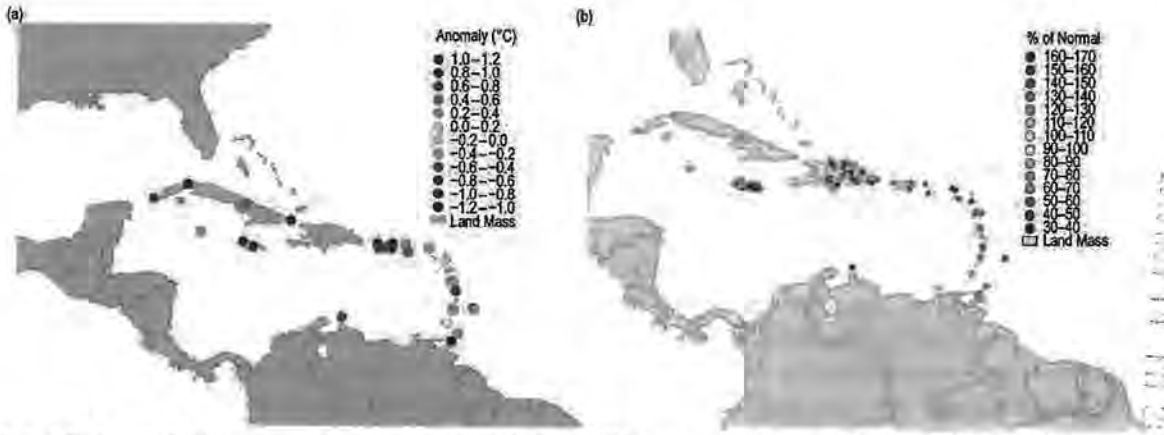

FIG. 7.9. Annual (a) temperature anomalies (°C) and (b) percent of normal (%) rainfall for 2015 across the Caribbean basin with respect to the 1981–2010 annual mean. (Source: Caribbean Institute for Meteorology and Hydrology and the Instituto de Meteorología de la República de Cuba.)

Dry weather persisted from July to September across much of the Caribbean, including Aruba, Barbados, central Cuba, Grand Cayman, Dominica, southern and eastern Dominican Republic, Grenada, western Jamaica, the Leewards, and St. Lucia, though in August, wet conditions were recorded for Dominica and below-normal to near-normal rainfall for Puerto Rico. This is consistent with a below-normal Atlantic hurricane season (see section 4e2) in relation to El Niño that produced strong vertical wind shear, increased atmospheric stability, and subsidence over the Atlantic. July was the driest on record for St. Maarten (8.4 mm) since 1953 and second driest for St. Thomas (5.6 mm). Tobago had its fifth driest August (83.3 mm) since 1969.

For the last quarter, very dry conditions were recorded in Antigua, Aruba, Dominica, and northwestern Dominican Republic, with very wet conditions in northern Dominican Republic and western Puerto Rico. Antigua's all island-averaged rainfall for December was 49.0 mm, its 10th driest on record, and rainfall for the three-month period of October–December was the ninth lowest on record (246.1 mm) since 1928. Record-low October–December rainfall was also observed at a number of stations, including Bowmanston, Barbados, (245.1 mm) since records began in 1981, and Rio San Juan and Villa Vasquez in Dominican Republic (230.7 and 31 mm, respectively) since 1971.

A number of territories and stations recorded their driest year (Table 7.2). The second driest year was observed at Hewanorra, St. Lucia, (1336.6 mm) since 1973 and the third driest for Jamaica (1308.0 mm) since 1881 and St. Croix (586.0 mm) since 1951. Conversely, St. Thomas (1276.4 mm) observed its sixth wettest year on record since 1953.

Table 7.2. List of Caribbean territories and stations that had their driest year in 2015.

Station/Country	Annual rainfall recorded (mm)	Year records began
Antigua	574.5	1928
Aruba	134.2	1971
St. Barths	465.6	1971
St. Maarten	495.4	1953
Tobago	1064.6	1969
Grantley Adams, Barbados	789.5	1979
Santo Domingo, Dominican Republic	813.8	1971
Potsdam, Jamaica	762.0	1971
George F. L. Charles Airport, St. Lucia	1148.6	1967

(iii) Notable events

Several significant events impacted the Caribbean in 2015:

- Prevailing droughts were observed in Anguilla, Antigua, Barbados, Cuba, Dominica, Dominican Republic, Jamaica, Puerto Rico, St. Kitts and Nevis, and St. Lucia, with widespread agricultural losses and/or very low water production and rationed distribution. St. Lucia declared a water emergency for the period May to August amid continuing drought.
- Water shortage was experienced in the eastern half of Puerto Rico, with San Juan (capital of Puerto Rico) having strict water rationing for much of 2015.
- Low rainfall totals in 2015 in Antigua led to Potworks Dam, with a capacity of 1 billion gallons, being completely dry. There were more bushfires than usual, and 65% of farmers were forced out of business. The drought continued throughout 2015 and was deemed the worst on record. The duration of the drought conditions in Antigua was the second longest of any drought on record and, by far, the greatest deficit of rainfall (records date to 1928). The longest drought occurred in 1964–67, lasting 32 months. The return period for 2015 rainfall is 1 in 500 years.
- On 27 August, flash floods from Tropical Storm Erika caused catastrophic damage across Dominica, dumping over 320.5 mm of rain in 12 hours, with 225.0 mm in less than six hours.

d. South America

Positive SST anomalies were present along the tropical equatorial Pacific since the beginning of 2015. With the onset of El Niño, SST anomalies increased and expanded along the southeastern Pacific Ocean during the second half of the year. As is typical, El Niño influenced regional weather conditions in South America during most of 2015 (Fig. 7.10).

The annual temperature and precipitation anomalies were computed using data from 1190 stations provided by national meteorological services from South America and processed by El Centro Internacional para la Investigación del Fenómeno de El Niño (CIIFEN). Air temperature was above normal across most of the continent, with anomalies 0.5°–2.0°C (Fig. 7.11a) above average. El Niño impacts across

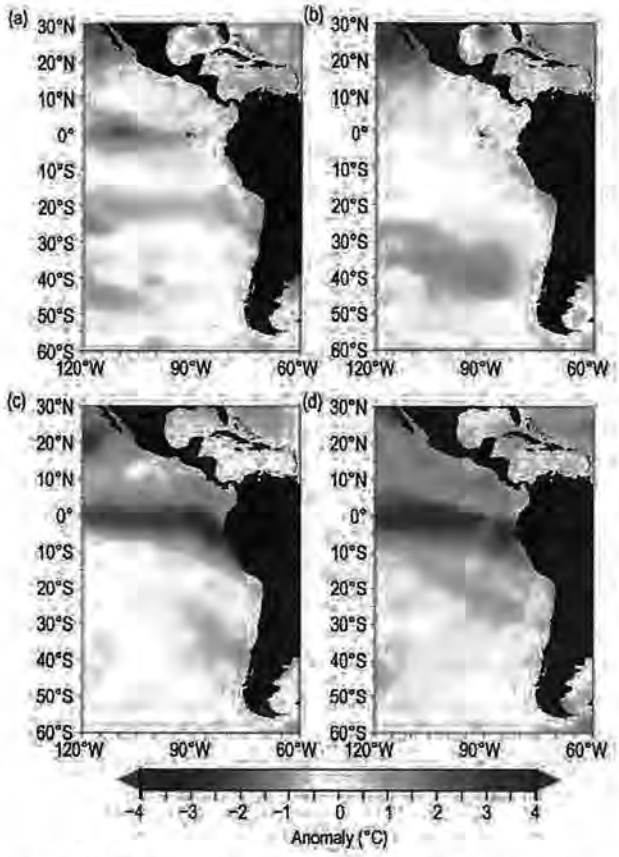

Fig. 7.10. Seasonal mean sea surface temperature anomalies (°C) for 30°N–60°S, 120°–60°W (base period: 1971–2000). Data source: NOAA–NCEP (Processed by CIIFEN, 2016).

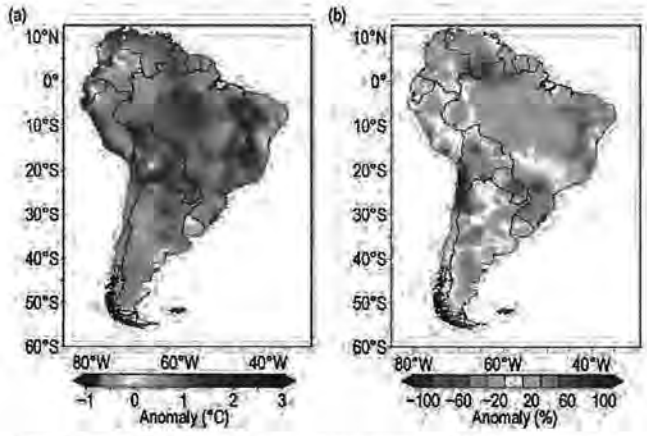

Fig. 7.11. 2015 South American annual (a) temperature anomalies (°C) and (b) precipitation anomalies (%; base period: 1981–2010). (Sources: Data from 1190 stations provided by National Meteorological Services of Argentina, Brazil, Bolivia, Chile, Colombia, Guyanas, Ecuador, Paraguay, Peru, Suriname, Uruguay, and Venezuela. The data were compiled and processed by CIIFEN 2016).

South America generally include, but are not limited to, drier-than-average conditions across northern South America, with wetter-than-average conditions across the southeast. Dry conditions, observed since 2014, persisted and, in some instances, deteriorated during 2015, especially in northern South America. Above-normal precipitation with severe impacts was observed in southeastern South America (Fig. 7.11b). Along the west coast of South America, the El Niño effects during the last quarter of the year were modulated by regional factors such as the persistent positive sea level pressure anomalies in the southeastern Pacific Ocean and strong winds, which reduced convection near Ecuador and northern Peru.

All anomalies in this section are with respect to the 1981–2010 average unless otherwise noted.

1) Northern South America and the tropical Andes—R. Martinez, A. Malheiros, J. Arévalo, G. Carrasco, L. López Álvarez, J. Bazo, J. Nieto, and E. Zambrano

This subsection covers Bolivia, Colombia, Ecuador, Peru, and Venezuela.

(i) Temperature

Above-normal temperatures were predominant across Venezuela throughout the year. In the highlands (Tolima) and Caribbean coast (Cesar) of Colombia, record maximum temperatures were observed in September and December, respectively, with anomalies as high as +5°C. In Ecuador, above-average temperatures were present most of the year, with anomalies of +1.5°C to +2.0°C. Temperatures across Peru were above normal during March–May and June–August. During July and August, above-average temperatures (between +1°C and +4°C) were observed along the coastal zone, in some instances surpassing record high temperatures set in 1998. In Bolivia, temperatures were near- to above normal most of the year. From August to November, at least 12 maximum temperature records were reported at stations in central and eastern Bolivia.

(ii) Precipitation

Venezuela and Colombia experienced drier-than-normal conditions during 2015. During the first half of the year, anomalous subsidence was the main driver for the lack of precipitation in northern and southeastern Venezuela, which was just 40%–60% of normal. On the Caribbean coast of Colombia a slight precipitation deficit was also observed in this period. During the second half of the year, as a consequence of the El Niño onset, precipitation anomalies were 50%–70% of normal across most of Venezuela

and as little as 20% of normal in the Andean region (Departments of Tolima, Huila, Cauca, Valle) and Caribbean (central and northern) regions in Colombia. In Ecuador, precipitation was above normal during the first half of the year, with anomalies up to 200% of normal on the central coast. During the second half of the year, precipitation over the Amazon region was 50%–80% of normal; meanwhile, precipitation was 120%–150% of normal in the northern and central coastal regions during September–November. In Peru, extreme below-normal precipitation was observed in the northwest of the country and in the southern Andes. Above-normal precipitation prevailed during the second half of 2015 in the southern and central Amazon region.

In northern Bolivia, precipitation was above normal from January to August, with anomalies up to 159% of normal during March–May. During September–November, 88% of normal precipitation was observed. Over the Altiplano region (western Bolivia), precipitation was predominately above normal with anomalies ranging from 117% to 149% of normal throughout the year. In central Bolivia, precipitation was near normal. Above-normal precipitation (up to 150% of normal) was recorded in southeastern Bolivia during June–August. Below-normal precipitation (63% of normal) was observed during September–November.

(iii) Notable events

On 24 March, unusually heavy rainfall caused landslides in the District of Lurigancho-Chosica (Lima region), Peru, leading to eight fatalities and destroying over 150 houses.

During April, northwestern Venezuela experienced a week-long heat wave, with some stations registering daily maximum temperatures as high as 40°C (April average maximum temperature is 34.9°C).

Northern Ecuador was affected by flooding during December that caused crop and cattle losses.

Colombia and Venezuela were impacted by a severe drought during most of the year, causing restrictions in water supply for human consumption, agriculture, and hydropower generation.

2) Tropical South America east of the Andes—J. A. Marengo, J. C. Espinoza, J. Ronchail, and L. M. Alves

This region includes Brazil, Paraguay, southern Venezuela, and the Amazon lowland sectors of Peru, Colombia and Bolivia.

(i) Temperature

Monthly mean temperatures across most of the region were about 1°–3°C higher than average most of the year. In São Paulo, Brazil, the January mean temperature was 3.5°C above normal—the second warmest January since 1943. In October, temperatures were about 4°–5°C above normal in southeastern and west central Brazil, with the most notable warmth in Rio de Janeiro, which recorded a maximum temperature of 40°C, compared to the average October maximum temperature of 25°C. Maximum temperatures were slightly above average for autumn (March–May) and winter (June–August), with a mean temperature anomaly of +1.0°C. Notable temperatures of 2.0°–3.0°C above average were observed across Paraguay in June.

Various cold fronts during May–September brought well-below-freezing temperatures, hail, and the highest snowfall in 10 years in the Andean region, located more than 3500 meters a.s.l.

(ii) Precipitation

Below-average rainfall (20%–75% of normal) was observed over southeastern Brazil, eastern Bolivia, and Paraguay during January–March. An atmospheric blocking pattern and a high pressure system over large parts of tropical Brazil and the South Atlantic, together with the absence of the South Atlantic convergence zone during January, were responsible for the lack of precipitation over most of subtropical South America east of the Andes, which lasted through mid-February. Between April and December, rainfall totals of 20%–50% of normal were recorded in northeastern Brazil, north-central Amazonia, eastern Peru, and the Amazon lowland sectors of Colombia and Venezuela. A weak and/or anomalously northward displaced intertropical convergence zone contributed to the below-average precipitation.

(iii) Notable events

Drought conditions in southeastern Brazil that began in January 2014 (Nobre et al. 2016) continued through April 2015, particularly over the Cantareira reservoir system, which supplies water to nearly half of São Paulo's population (about 18 million residents). Summer (December–February 2014/15) rainfall was marginally less than average. However, during November and December 2015, above-average rain (100–150 mm month^{-1} above normal) fell over the region, allowing the Cantareira Reservoir system to recover its volume.

The drought conditions that started in 2012 in northeast Brazil continued to persist in 2015, however, with less severity (Fig. 7.12a). Figure 7.12b shows that very dry conditions were present across the northern

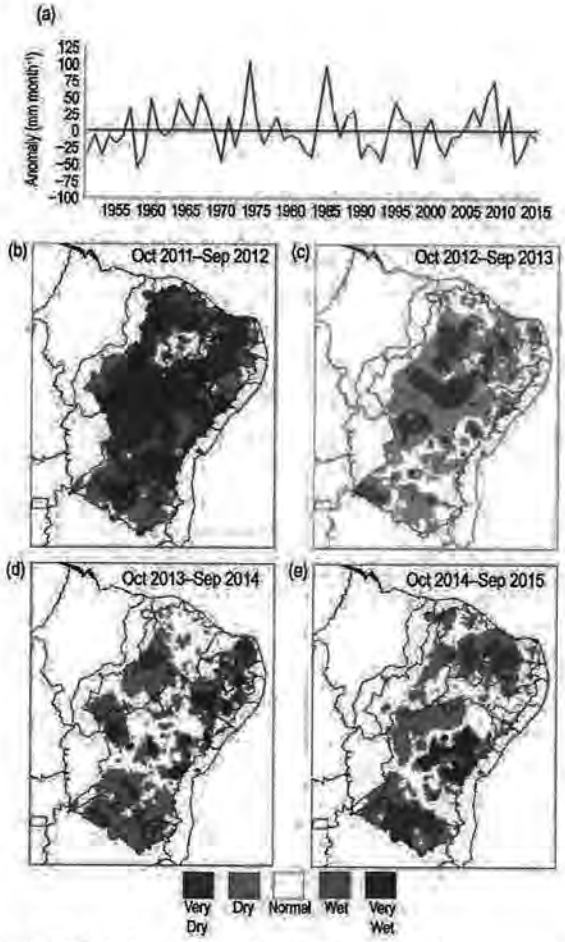

Fig. 7.12. (a) Average rainfall anomalies (mm month^{-1}) during the peak rainy season (Feb–May) in northeast Brazil for 1951–2015. (Source: Global Precipitation Climatology Centre; updates from Marengo et al. 2013.) (b) Categories of observed precipitation based on percentiles for northeast Brazil during the hydrological year Oct–September (b) 2011/12, (c) 2012/13, (d) 2013/14, and (e) 2014/15. (Source: CEMADEN.)

part of the state of Bahia, and particularly in the semiarid region of northern northeast Brazil and the region between southern Bahia and the northern parts of the state of Minas Gerais. The extreme dry conditions observed in this region contributed to an increase in wildfires and damages to crops, with local residents depending on water to be trucked in.

Between January and April, 32 000 families were affected by heavy rains in the lowlands of Bolivia, with the worst impacts occurring on 20 February when the Acre River flooded the city of Cobija, capital of Pando in western Amazonia.

As a result of heavy rains in the northwesternmost Amazonian regions (north of the Peruvian Amazon and western state of Amazonas in Brazil), the Peruvian government declared a state of emergency on 9 April. During March and April, more than 115 000 people were affected by floods. Also, in April, flooding and landslides affected more than 20 000 people in Colombia. On 29 June, heavy rainfall in southern and southwestern Venezuela caused flooding, with more than 40 000 people affected. On 4 April, a severe storm hit several towns in the department of Concepción in northern Paraguay, affecting houses, crops, and farm animals. Authorities estimate that 5000 people were affected. Precipitation patterns shifted in October, as is typical during the presence of El Niño in the tropical Pacific Ocean (see section 4b), resulting in above-average rainfall across the same region. Abundant rainfall over southern Brazil and most of the La Plata basin caused significant floods.

During 8–10 July, minimum temperatures between −18°C and −22°C were measured in high areas of the Arequipa, Moquegua, Tacna, and Puno regions of the Peruvian southern Andes. According to the Empresa de Pesquisa Agropecuaria e de Extensao Rural of the state of Santa Catarina (EPAGRI) in southern Brazil, the same cold spell affected the southern region of Brazil, with minimum temperatures ranging between −3.0°C and 2.0°C in the highland city of São Joaquim on 5 July, compared with the average July minimum temperature of 6.1°C.

The above-normal rainy season in southeastern South America, which typically starts in October and ends in May, was 100–300 mm above normal in December 2015, leading to floods in Paraguay, Bolivia, and southern Brazil due to the overflow of the main rivers. The highest levels in 110 years were recorded along the Paraguay River, which produced slow-onset flooding that forced the evacuation of 18 545 families in the city of Asunción. Four people died and 130 000 were evacuated by the end of the year.

3) Southern South America—M. Bidegain, J. L. Stella, M. L. Bettolli, and J. Quintana

Argentina, Chile, Uruguay, and adjacent areas of southern Brazil are considered here.

(i) Temperature

Above-normal temperatures were observed over most of southern South America (SSA) during 2015, with mean temperature anomalies between +0.5°C and +1.5°C (Fig. 7.11a). According to preliminary analysis of the official data for 2015, the mean temperature anomaly for Argentina and Uruguay was estimated to be +0.71°C and +0.51°C, respectively. Argentina had its second warmest year in the country's 55-year period of record, behind 2012, with the past four years (2012–15) the four warmest on record. The cities of Buenos Aires, Iguazú, Santa Fé, Rosario, and Pehuajó were each record warm in 2015. Chile observed warmer-than-

average monthly temperatures most of the year. The largest positive annual anomalies were observed in the northern (+1.1°C) and central (+1.0°C) regions; however, September and October were cooler than average in the central and southern regions. Above-normal maximum temperatures were observed in Chile, particularly in the central region, with anomalies between +1.0° and +1.5°C.

Summer (December–February) 2014/15 had near-average temperatures, with no significant heat waves observed across Argentina and Uruguay. In Chile, anomalies of −0.8°C were observed across the north coast.

Autumn (March–May) was extremely warm. The most notable warmth was observed during April and May, with mean temperature anomalies as high as +2.0°C and +2.5°C in central Argentina and Uruguay, respectively. Argentina observed its warmest autumn since national records began in 1961, with a mean temperature 1.51°C above average. Chile had above-average temperatures during March–May, with much of the central to northwest regions 1.5°–3.0°C above average.

Above-average temperatures were observed across much of SSA during winter (June–August), with the most notable warmth across northeastern Argentina, Uruguay, southern Brazil, and Chile, where mean temperatures anomalies were as high as +3.0°C. Argentina also had its warmest winter on record. Much warmer-than-average conditions dominated the country during August, with many locations experiencing record high temperatures.

Below-average temperatures were present across Argentina, Uruguay, and Chile during spring (September–November). In Chile and central and southern Argentina, an increase in frequency of frontal systems and abundant cloudiness resulted in the region's coldest October on record. In Argentina, anomalies were 6°–7°C below average in some areas and more than 35% of stations set new daily low temperature records. Extremely cold conditions, including rare snowfalls and late frosts, affected Buenos Aires province during September and the Cuyo region during October.

(ii) Precipitation

Drier-than-average conditions were observed during January–July, especially from March to July, in eastern Argentina (Corrientes, Entre Ríos, and Buenos Aires provinces), northeastern Argentina (Misiones province), Uruguay, and central Chile. During August–December, above-average precipitation fell across central and northeastern Argentina, northern Uruguay, southern Brazil, and central Chile, as is typical during El Niño. The 2015 annual rainfall for Argentina and Uruguay was 109% and 103% of normal, respectively, and marked the second consecutive year since 2013 in which precipitation was above average in Argentina. However, some regions south of 34°S in Uruguay and Buenos Aires province recorded below-normal precipitation in 2015. As a result of severe water deficit, the Minister of Agriculture in Uruguay declared an "agricultural emergency" in May to assist farmers. Santiago, the capital of Chile, had its driest June on record, with no precipitation recorded for the first time since records began in 1866. During the second half of 2015, especially during October–December, some locations in northeastern Argentina and northern Uruguay were severely affected by floods, especially cities located near the Paraná and Uruguay Rivers.

(iii) Notable events

Some areas of southern Chile experienced their driest January in at least 65 years. In northern Chile, unusually heavy rainfall during 24–26 March impacted the extremely dry regions of Atacama and Antofagasta. Some areas received well over their annual rainfall during this event. Antofagasta received 24.4 mm of rainfall in a 24-h period during 25–26 March (normal annual average rainfall for this location is 1.7 mm). Three people were killed by the impacts of the floods in Antofagasta and 23 people perished in Atacama.

Heavy precipitation fell across parts of northeastern Argentina in August. The downpours overflowed rivers and produced floods. The highest rainfall totals during August were in eastern Argentina, mainly in the south of the province of Corrientes, Entre Ríos, and northeast of Santa Fé, where values reached 300 mm. There was also significant precipitation in the province of Buenos Aires, with 200–250 mm recorded in August. Many other locations set new August precipitation total records (Table 7.3).

During December, abundant precipitation fell over northeastern Argentina and Uruguay, with several locations setting new records for the month (Table 7.4). Heavy rainfall mainly affected Corrientes and Misiones provinces in Argentina, with thousands of people forced to evacuate.

Above-normal temperatures and below-normal rainfall at the beginning of 2015 in Patagonia (southern Argentina) favored the development of one of the largest wildfires in the history of Argentina. The fire lasted nearly two months and burned 41 000 hectares of native forests.

Table 7.3. Locations in Argentina that set new August precipitation totals (mm) in 2015.

Locations	2015 Record (mm)	Previous Record (mm)
Reconquista	330.2	138.8 (1956)
Mercedes Aero	170.0	134.3 (1975)
Paso de los Libres Aero	188.0	182.9 (1971)
Monte Caseros Aero	262.6	218.0 (1972)
Concordia Aero	358.8	198.0 (2012)
Junin Aero	201.0	151.4 (1976)
San Fernando	252.1	237.1 (2012)

Table 7.4. Locations in Argentina that set new December precipitation totals (mm) in 2015.

Locations	2015 Record (mm)	Previous Record (mm)
Formosa	425.3	357.5 set in 1979
Posadas Aero	466.9	416.1 set in 2012
Oberá	477.0	447.5 set in 2012
Mercedes Aero	458.1	337.0 set in 1968
El Calafate	42.2	30.5 set in 2012

e. *Africa*

In 2015, most of Africa experienced above-average temperatures and below-average precipitation. Extreme weather caused loss of life and property damage in many parts of the continent. This extreme weather included torrential rains across western Africa and heavy rainfall related to a tropical storm over western Indian Ocean island countries. In contrast, eastern African countries, including Ethiopia, Somalia, and parts of Kenya, were impacted by drought. The drought in Ethiopia, the worst in several decades, was associated with the El Niño that developed early in the year. Extreme high temperatures were observed over northern, southern, and southwestern parts of Africa.

The 2015 climate assessment for Africa is based on the 1981–2010 reference period. Both observed and reanalysis datasets are presented for analysis.

1) Northern Africa—K. Kabidi, A. Sayouri, M. ElKharrim, A. Ebrahim, and A. Mekonnen

Countries considered in this region are Morocco, Algeria, and Egypt. Overall, below-normal precipitation and above-normal temperature conditions dominated during 2015. The annual temperature was the warmest since 1960 over Morocco, and successive heat waves were observed both during winter and summer in Egypt. Heavy downpours were reported in May and August 2015 in Morocco.

(i) Temperature

The annual mean maximum temperature over northwestern Morocco was about 1°C higher than normal. However, temperatures during January and February were markedly below average in association with a cold air surge from the Black Sea to the Maghreb (northwestern African countries). In January, temperatures were 2.4°C below normal in northeastern Morocco. In February they were 2.7°C below normal in southern Morocco. Generally, the winter (December–February 2014/15) mean surface seasonal temperatures over Algeria and Morocco were about 1°C below normal (Fig. 7.13), while winter surface temperatures over Egypt were mainly above normal. However, minimum temperatures as low as 1°C were observed in January in northeastern Egypt.

Temperatures during spring, summer, and autumn were all above normal in Morocco and Algeria. The average mean monthly temperature in Morocco and Algeria was 3°C above normal in May (Fig. 7.14). Overall, summer temperatures in Egypt were above normal, while isolated locations recorded below-average temperatures.

(ii) Precipitation

Annual precipitation was marked by deficits over southern Egypt and surpluses over the northern regions. Winter precipitation was about 50% of normal over western Egypt, while heavy rainfall events

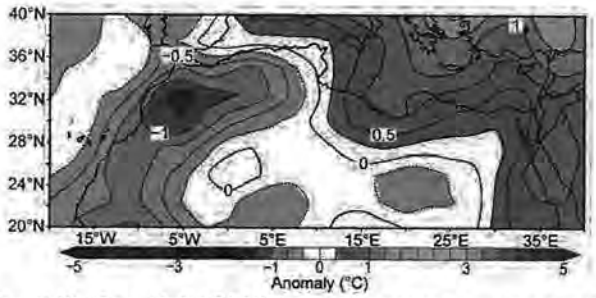

Fig. 7.13. Dec–Feb 2014/15 mean temperature anomaly (°C; base period 1981–2010). (Source: NCEP–NCAR reanalysis.)

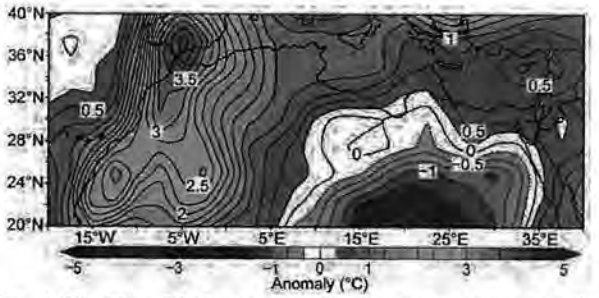

Fig. 7.14. May 2015 mean temperature anomaly (°C; base period 1981–2010). (Source: NCEP–NCAR reanalysis.)

were observed in January. Winter precipitation over Morocco was also highly variable. The average deficit in Morocco was about 89% of normal in January and 71% of normal in February (Fig. 7.15). Lack of rainfall was associated with dominant atmospheric high pressure conditions on the Moroccan Atlantic coast and in western Europe.

Monthly precipitation in spring was generally below normal in Morocco. However, above-normal rainfall ranging between 145% and 230% of normal was observed in March across central Morocco. New 24-h rainfall records ranging between 20 and 55 mm were observed during 23–25 May at various places in Morocco.

Convective precipitation brought extreme weather conditions in summer, especially during July and August, leading to excess rainfall, with an average amount of around 158% of normal over Morocco. Total precipitation received during August was well above normal (e.g., 45 mm at Marrakech compared to the normal of 2.7 mm; 23.2 mm at Sidi Ifni compared to the normal of 2.1 mm).

Unlike the recent autumns of 2013 and 2014, which were marked by a series of above-normal rainy conditions, autumn precipitation in 2015 was generally below normal over most of Morocco. Monthly rainfall ranged from 7% of normal at Casablanca to about 86% of normal at Midelt.

(iii) Notable events

During January and February, a series of cold spells affected the region, resulting in heavy snow. Three meters of snow fell over northeastern Morocco during February, the highest total for February in the past 30 years. In Egypt, Alexandria received much-above-normal rainfall in October (238% of normal). A record rainfall of 127 mm was observed on 6 October 2015 at Alexandria.

Conversely, May, July, and August were marked by several heat waves (defined as daily maximum temperatures much higher than the daily mean), resulting in high maximum temperatures. These heat waves were associated with continental dry air intrusions from the intense heat source in the Sahara. The heat waves, associated with an east wind, caused several forest fires, which devastated hundreds of hectares of forest, especially in northern Morocco. In Luxor, Egypt, a record temperature of 48°C was observed on 28 May.

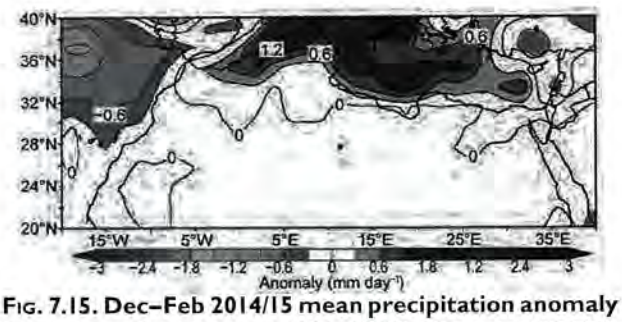

FIG. 7.15. Dec–Feb 2014/15 mean precipitation anomaly (mm day^{-1}; base period 1981–2010). (Source: NCEP–NCAR reanalysis.)

2) WEST AFRICA—S. Hagos, I. A. Ijampy, F. Sima, S. D. Francis, and Z. Feng

West Africa refers to the region between 17.5°W (eastern Atlantic coast) and approximately 15°E (along the western border of Chad) and north of the equator (near Guinea coast) to about 20°N. Countries included are Senegal, the Gambia, Guinea-Bissau, Guinea, Sierra Leonne, Liberia, southern regions of Mali and Niger, Burkina-Faso, Côte d'Ivoire, Ghana, Togo, Benin, Cameroon, and Nigeria. It is often divided into two climatically distinct sub regions: the semiarid Sahel region (north of about 12°N) and the relatively wet coast of Guinea region to the south.

(i) Temperature

The annual mean temperature over West Africa was slightly above the 1981–2010 average with much of the northwestern Sahel region about 0.5°C above average. In May, much warmer-than-average conditions were reported over the region, with record warmth observed in Togo, Benin, and Burkina Faso. The majority of northern cities in Nigeria experienced above-average mean temperatures. Minna, Yelwa, Zaria, Katsina, and Kano experienced the highest annual mean temperature departures for 2015, as did Benin, Ikom, Ondo, and Warri in the South. Similarly, record high temperatures were observed across eastern Senegal in June, while Sierra Leone, central Mauritania, and eastern Nigeria recorded temperatures up to 3°C above normal in July (Fig. 7.16). The maximum temperature over the western part of The Gambia was higher than normal (by 3%–6%), while the minimum temperature increased by 5%–8% compared with normal in the central and eastern part of the country. Warmer-than-average conditions persisted over most of West Africa during August and September.

(ii) Precipitation

Wetter-than-average conditions persisted over most of the Sahel region. Rainfall totals for June–September, during which time the West African monsoon provides much of the annual precipitation, are shown in Fig. 7.17a. Relatively dry conditions prevailed over most of the coast of the Gulf of Guinea

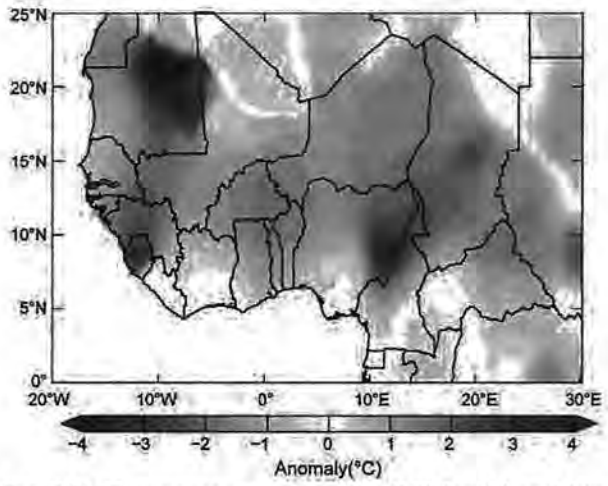

Fig. 7.16. Temperature anomalies (°C) for West Africa in Jul 2015 (base period: 1981–2010). (Source: NOAA–NCEP reanalysis.)

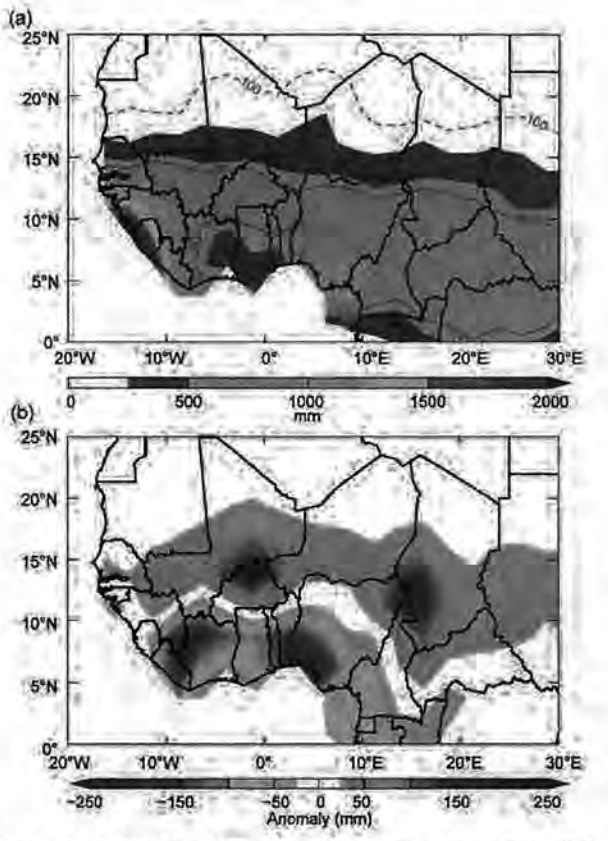

Fig. 7.17. (a) Jun–Sep 2015 precipitation (mm) for West Africa as total accumulated precipitation. The red dashed and solid lines mark 100 mm and 600 mm isohyets. (b) Jun–Sep 2015 precipitation anomaly, departure from 1981–2010 normal. (Source: NOAA–NCEP Reanalysis.)

region from Liberia to Cameroon. Specifically, much drier-than-normal conditions over the Niger Delta and wetter-than-normal conditions in the Lake Chad region were observed during summer. Rainfall over most parts of Nigeria was near normal. However, wetter-than-normal conditions were experienced over parts of central and northern Nigeria and drier conditions over pockets in the southwestern and eastern parts. The Gambia experienced a late onset of rains with late withdrawal and, overall, received above-normal rainfall for the season. Significant rainfall amounts prevailed during July–September, with the highest amounts, between 275 and 475 mm, recorded in August. The greater part of The Gambia experienced significant annual rainfall, ranging from 750 mm to more than 1000 mm. The country average seasonal rainfall during 2015 stood at 960.5 mm, 136% of the 1981–2010 mean (705.1 mm). The above-average rainfall over much of West Africa resulted in an above-average harvest according to the Famine Early Warning Systems Network. The dipole-like precipitation with a dry Guinean coast and wet Sahel region (Fig. 7.17b) often occurs as the intertropical convergence zone (ITCZ) precipitation is shifted farther north due to warmer SSTs over northeastern subtropical Atlantic and cooler-than-average SST conditions over the southeastern subtropical Atlantic (e.g., Hagos and Cook 2008). This condition persisted throughout the summer, especially notable during August and then into September. El Niño, typically associated with dry conditions over the Sahel (Janicot et al. 1998), had relatively little impact this year.

(iii) Notable events

In northern Nigeria, torrential rain led to the failure of a dam in August. According to the UN Office for the Coordination of Humanitarian Affairs, 300 000 people were affected by the associated floods associated. Flash floods were also reported in some states. The floods led to 53 fatalities and destruction of property in about 11 states, and displaced about 100 000 people from their homes.

In early June, Togo, Benin, and Ghana experienced significant flooding; on 3 June, 84 mm of rain fell in Cotonou, Benin, in a 24-h period. Local media reported that flooding damaged several homes and blocked streets in the largest city and economic center of Benin.

The 2015 wet season (July–September) for The Gambia was characterized by several extreme events, including floods, lightning, and windstorms, resulting in loss of life and significant disruption in livelihood.

3) Eastern Africa—G. Mengistu Tsidu

Eastern Africa refers to countries located within 20°–50°E and 15°S–20°N. The region is comprised of the Sudan, South Sudan, Ethiopia, Eritrea, Dji-

bouti, and north and central Somalia, which are located north of 5°N, with the main rainfall season in June–September; southern Somalia, Kenya, northern Tanzania, Uganda, Rwanda, and Burundi, located between 5°N and 5°S, with the main rainfall season in March–May; and central and southern Tanzania, located south of 5°S, with the main rainfall season in December–February. Note also that Somalia, Kenya, northern Tanzania, Uganda, Rwanda, Burundi, and southern and southeastern Ethiopia receive a significant portion of their annual rainfall in autumn, with a peak rainfall shifting from October over Ethiopia and Somalia to November over the rest of the countries following the annual migration of the ITCZ. Therefore, rainfall analysis is also included for the extended September–December rainfall season.

The assessment for this region is based on rainfall from the latest version-2 Climate Hazards Group Infrared Precipitation with Stations (CHIRPS) data and European Centre for Medium-Range Weather Forecasts (ECMWF) Interim reanalysis (ERA-Interim) daily mean temperatures at a horizontal resolution of 0.25°.

(i) Temperature

The December–February 2014/15 mean temperature was above normal over Sudan, Eritrea, western Ethiopia, Djibouti, Uganda, Rwanda, Burundi, most parts of Kenya, and northwestern Tanzania (Fig. 7.18a). Near-normal temperatures over the eastern half of Ethiopia and cold anomalies of up to –2°C were observed over part of northern Tanzania. The warm anomalies observed in December–February expanded eastward to cover most parts of Ethiopia while cold anomalies over Tanzania during the same season expanded northeastward to cover Kenya, southeastern Ethiopia, and Somalia during March–May (Fig. 7.18b). During June–August, the whole region experienced warm anomalies exceeding +2°C, with the exception of some pockets over northern Tanzania, western Kenya, and southwestern Ethiopia, which reported normal to below-normal temperatures (Fig. 7.18c). The mean temperature remained above normal during September–November over most parts of the region, with the exception of below-normal temperatures at places in northern Tanzania and along the Ethiopia–Somalia border (Fig. 7.18d).

(ii) Precipitation

During December–February 2014/15, southern Uganda, Rwanda, Burundi, northern Tanzania, and southern Kenya received substantially below-normal rainfall. However, some places in Tanzania and southern Kenya along the coast received 110%–150% of their normal precipitation (Fig. 7.19a). Rainfall during March–May was normal to above normal

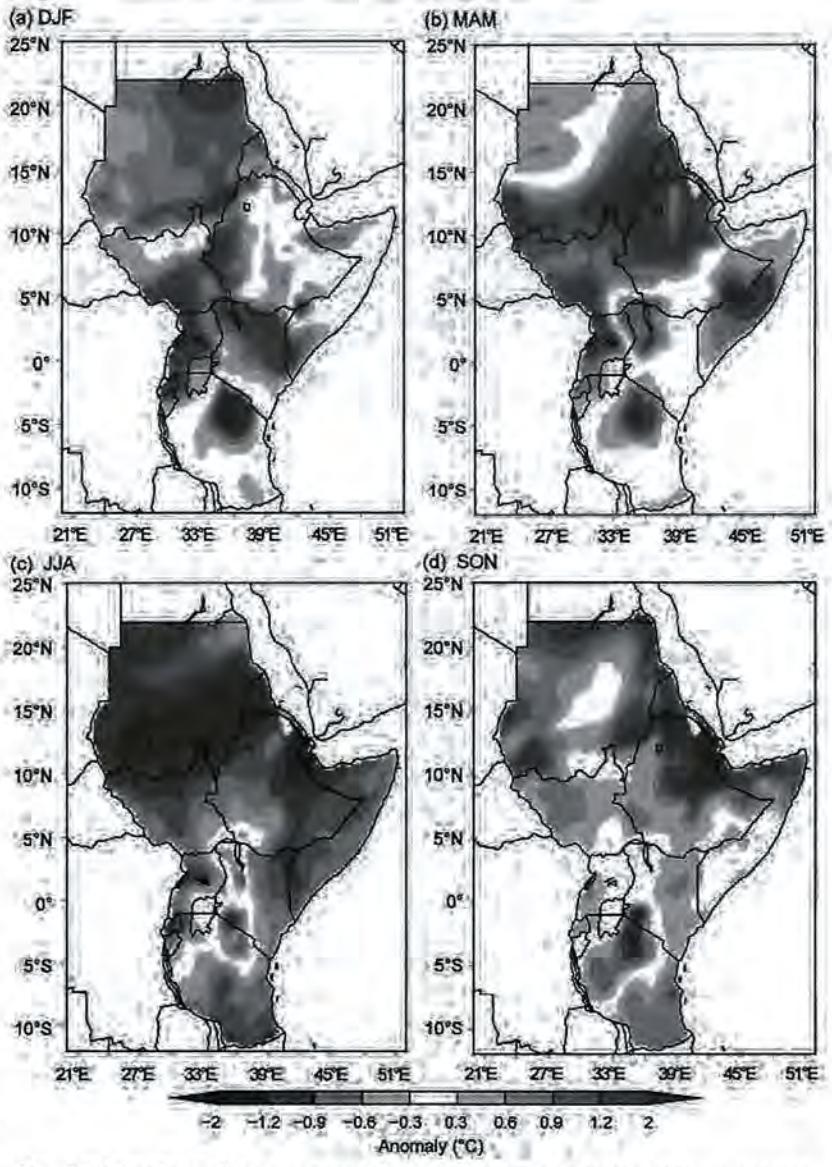

FIG. 7.18. Eastern Africa seasonally averaged mean temperature anomalies (°C) for (a) DJF 2014/15 and (b) MAM, (c) JJA, and (d) SON 2015, with respect to the 1981–2010 base period.

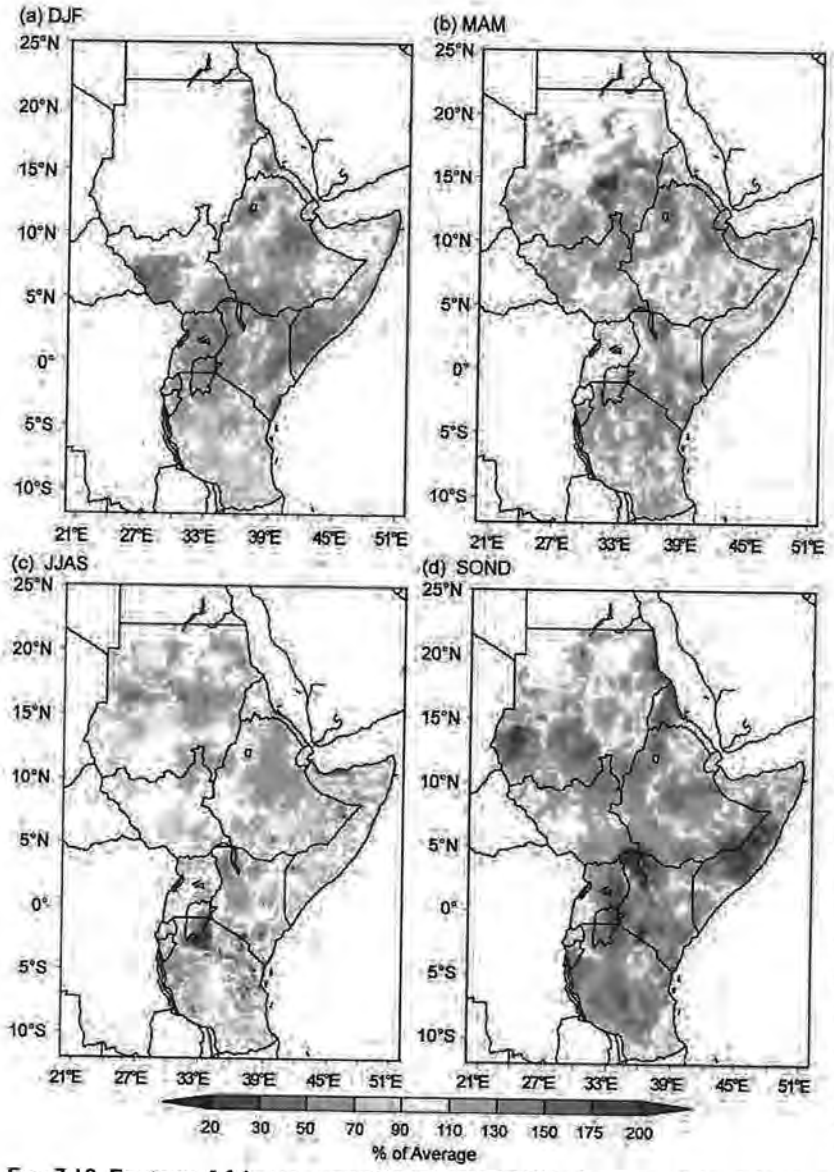

Fig. 7.19. Eastern Africa seasonal total rainfall (% of average) for (a) DJF 2014/15 and (b) MAM, (c) JJAS, and (d) SOND 2015, with respect to the 1981–2010 base period.

over southwestern and southeastern lowlands of Ethiopia, adjoining areas over South Sudan, most parts of Somalia, Kenya, and Tanzania except for small pockets over the southern tip of Tanzania, the southeastern highlands of Ethiopia and southeastern Ethiopia, and Somalia border areas, which received 50%–90% of normal rainfall (Fig. 7.19b). Most parts of Ethiopia, with the exception of southeastern lowlands, South Sudan, and southern parts of the Sudan, receive their main rainfall during June–September. However, below-average rainfall, associated with the strong El Niño event (see section 4b), dominated the region in 2015. As a result, northern, central, and southeastern Ethiopian highlands received 50%–90% of their normal rainfall. The most affected northeastern highlands of Ethiopia received as little as 30% of normal rainfall (Fig. 7.19c). The dry conditions persisted during the usual September–December rainfall season over central and southeastern highlands of Ethiopia (Fig. 7.19d).

(iii) Notable events

The failure of rainfall in Ethiopia in the summer of 2015, attributed to El Niño, led to the worst drought in decades, as reported by media outlets and later confirmed by the government of Ethiopia. According to the UN Office for the Coordination of Humanitarian Affairs, about 8.2 million people were in need of emergency food aid in Ethiopia.

The 2015 drought event can be illustrated using the standardized precipitation index (SPI) which provides a better representation of abnormal wetness and dryness than many other indices (Guttman 1998; McKee et al. 1993, 1995; Hayes et al. 1999). To account for the accumulation of drought effects over time, the SPI on 3-, 6-, 9-, and 12-month time scales during October 2014–September 2015 are considered based on the climatology of 1981–2015 for the region. Figure 7.20a shows 3-month SPIs from July to September 2015, which reveal moderate (SPI values between –1.0 and –1.49) to extreme (SPI values less than –2.0) drought over central, northern, and southeastern Ethiopian highlands as well as central Rift Valley of Ethiopia. Southern South Sudan and adjoining northern Uganda experienced moderate to severe (SPI values between –1.5 and –1.99) drought. However, the moderate to severe drought disappeared in the 6-month-SPI (April–September 2015) over these areas while the moderate to extreme drought over Ethiopia persisted (Fig. 7.20b). The moderate to extreme drought over Ethiopia continued to prevail in the 9-month (January–September 2015) and 12-month (October 2014–September 2015) SPIs (Figs. 7.20c,d) consistent with the prolonged observed rainfall anomalies in 2015 over Ethiopia. Thus, both the observed rainfall anomalies during the different seasons and the SPI confirm the failure of rains over a longer period of time.

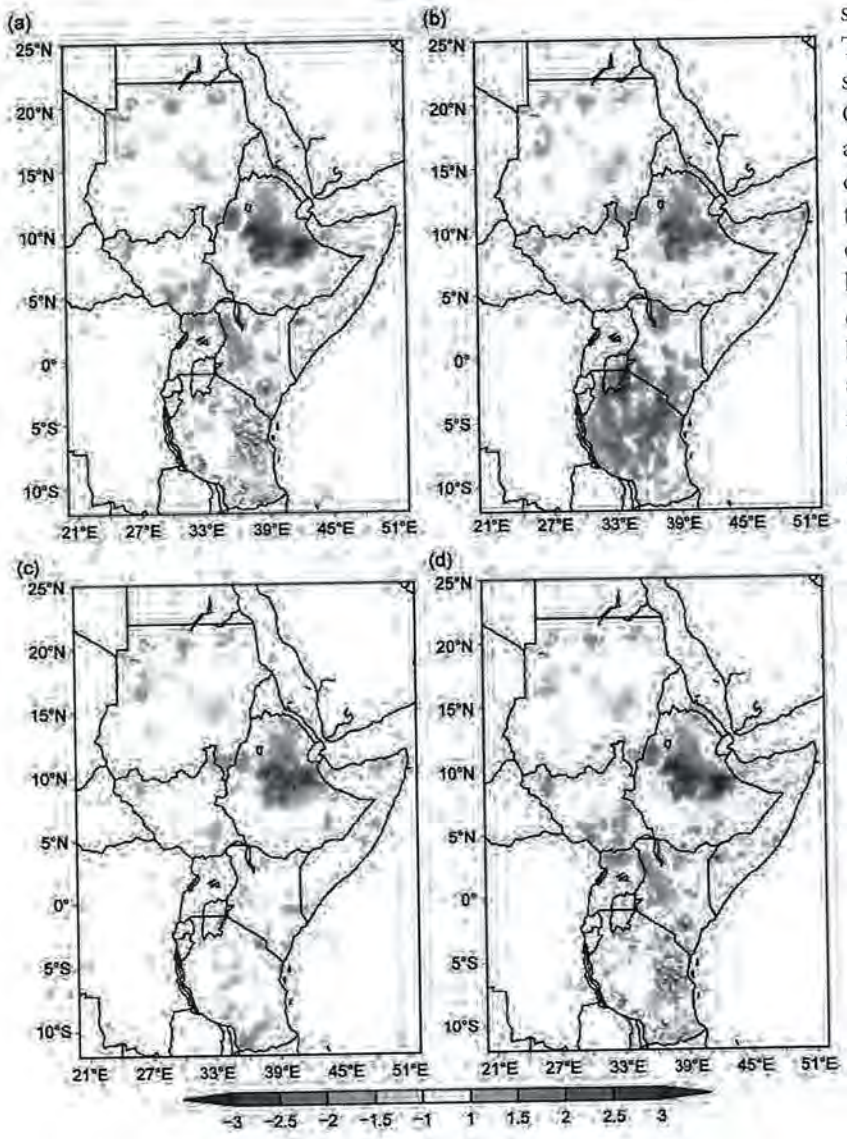

FIG. 7.20. SPI indices for eastern Africa for Oct 2014–September 2015 at (a) 3-month, (b) 6-month, (c) 9-month, and (d) 12-month times scales, based on 1981–2015 rainfall climatology.

4) SOUTHERN AFRICA BETWEEN 5° AND 30°S—G. Mengistu Tsidu

This region comprises countries bordering the Kalahari Desert within 5°–30°S and 10°–40°E, including Angola, Zambia, Botswana, Zimbabwe, and Namibia. The climate ranges from semiarid and subhumid in the east to arid in the west. Also included are Malawi and Mozambique, located in the east, with climate conditions ranging from dry to moist subtropical to midlatitude types. This region is located between two semipermanent high pressure systems over the South Atlantic and south Indian Oceans. The region is prone to frequent droughts and uneven rainfall distribution with two distinct seasons: a wet season from roughly November to April and a dry season roughly from May to October. The east coast is influenced by the southward-flowing Mozambique Current, which brings warm water and humid air from the equator and creates a humid, warm climate while the west coast is influenced by the cold Benguela Current from the Atlantic Ocean, which produces a drier climate. Total seasonal rainfall exhibits a strong spatial gradient along an axis oriented southwestward from above 700 mm over Zambia, Malawi, and Mozambique to below 25 mm over southern and eastern Namibia, southeastern Botswana, and eastern Angola during the peak rainy period of December–February (not shown).

Analyses are based on the same data sources as for section 7e3.

(i) Temperature

During December–February 2014/15, temperatures were well above normal over southern Angola, much of Namibia, and Botswana, and moderately above normal along the border between Malawi and Zambia (Fig. 7.21a). In contrast, the rest of the region had normal to below-normal temperatures. Warm anomalies exceeding +2°C were observed over the region bordering Namibia, Botswana, and Angola. The warm anomalies in the southwestern part of the region expanded eastward in March–May (Fig. 7.21b) and covered nearly the whole region in June–August (Fig. 7.21c) and September–November (Fig. 7.21d). The only exceptions were near-normal temperatures over areas that extended from the Mozambique–Zimbabwe border to close to the Mozambique–Malawi border during June–August and northern Angola and Zambia during September–November. Extreme warm anomalies exceeding +2°C during this period covered wider areas including the western half of Botswana, eastern half of Namibia, and southern part of Angola and Zambia (Fig. 7.21d).

(ii) Precipitation

In December–February, southern Africa received substantially lower-than-normal rainfall with the

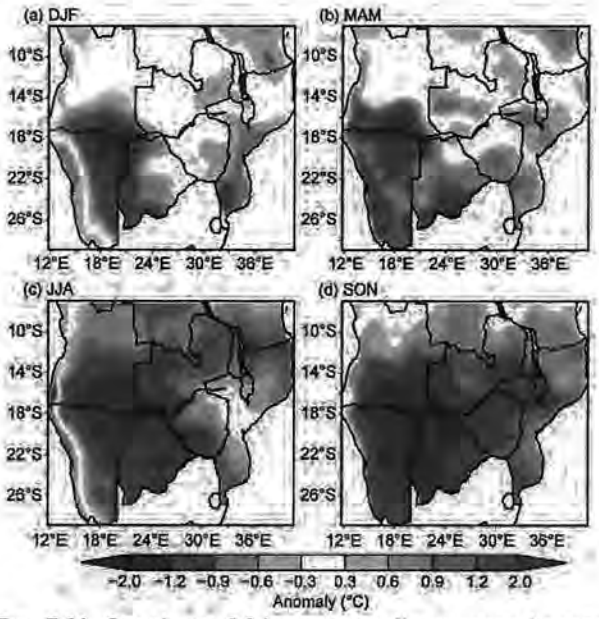

Fig. 7.21. Southern Africa seasonally-averaged mean temperature anomalies (°C) for (a) DJF 2014/15 and (b) MAM, (c) JJA, and (d) SON 2015, with respect to the 1981–2010 average.

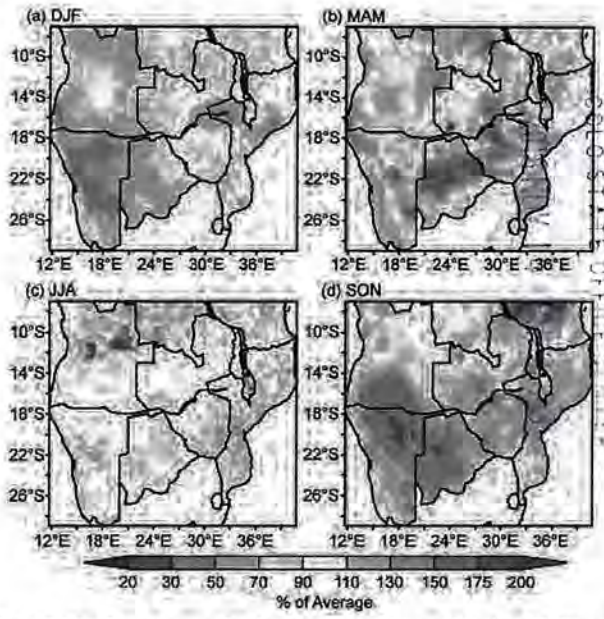

Fig. 7.22. Southern Africa seasonal total rainfall (% of normal) for (a) DJF 2014/15 and (b) MAM, (c) JJA, and (d) SON 2015, with respect to the 1981–2010 average.

exception of an isolated zonal band of normal to wet anomalies over northern Zimbabwe bordering Zambia and Mozambique, extending across Malawi to eastern Mozambique (Fig. 7.22a). Scattered normal-to-wet anomalies were observed in March–May (Fig. 7.22b) and June–August (Fig. 7.22c). The whole region received below-normal rainfall again during September–November (Fig. 7.22d). The deficit during this period is significant, as October and November constitute part of the extended climatological rainy period. Thus, overall rainfall over southern Africa was below normal in 2015.

(iii) Notable events

The below-normal rainfall was also investigated using the standardized precipitation index (SPI) on the 3-, 6-, 9-, and 12-month time scales from May 2014 to April 2015 which encompasses the peak rainy months over the region based on the climatology of 1981–2015 (not shown). The analyses revealed the presence of moderate to severe drought over the northern half of the region. On 10 November, the BBC reported that, as a result of the drought, significant portions of the population in Malawi and Zimbabwe needed food aid, citing a UNICEF assessment.

Southern Hemisphere heat waves were observed during SON over much of the region. The 90th percentile of heat wave duration (TXHW90, the maximum number of consecutive days with maximum temperatures higher than the 90th percentile calculated for each calendar day based on the 1981–2010 normal using running 5-day windows) is used (de Lima et al. 2013; Zhou and Ren 2011). In 2015, the longest period of consecutive days warmer than the 90th percentile of the normal maximum was, on average, more than 20 days over northern Namibia during September–November (Fig. 7.23d). Large parts of Botswana, Namibia, and southern Angola experienced 9- to 15-day periods warmer than the 90th percentile of normal maximum. There were warm anomalies of longer duration during other seasons over approximately the same areas (Figs. 7.23a–c).

5) South Africa—A. C. Kruger and C. McBride

The year 2015 was dominated by dry and abnormally hot conditions over most of the country.

(i) Temperature

In some parts of interior South Africa, mean maximum temperature deviations for January were more than 3°C above normal. Many areas in Western Cape, Free State, Limpopo Province, and Northern Cape had maximum temperature deviations in excess of +2° to +3°C during the first three months of the year.

The annual mean temperature anomaly for 2015 (based on data from 26 climate stations) was 0.86°C above the reference period (1981–2010), making it the warmest year for South Africa since records began in 1951 (Fig. 7.24). A warming trend of 0.14°C decade^{-1} is indicated by the data of these particular climate stations, statistically significant at the 5% level.

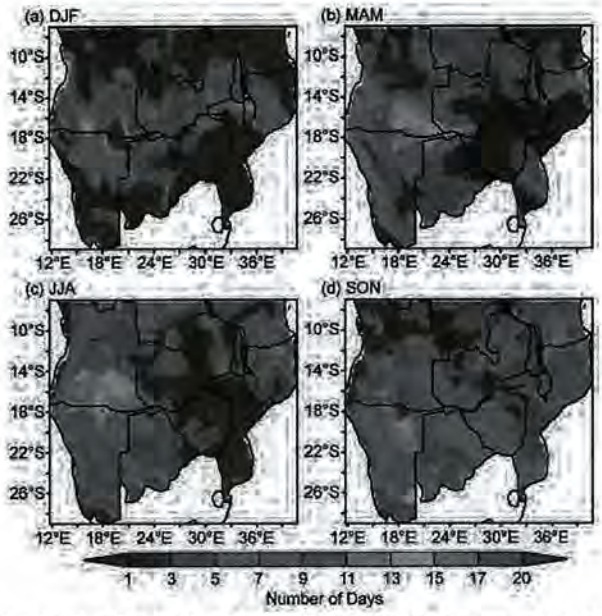

Fig. 7.23. The 90th percentile TXHW90 anomalies (in days) for Southern Africa during (a) DJF 2014/15 and (b) MAM, (c) JJA, and (d) SON 2015, with respect the 1981–2010 climatology.

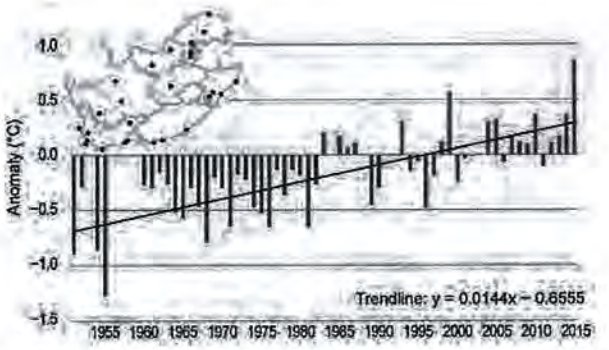

Fig. 7.24. Annual mean temperature anomalies (°C; base period 1981–2010) of 26 climate stations in South Africa, as indicated in the map, for the period 1951–2015. The linear trend is indicated. (Source: South African Weather Service.)

Fig. 7.25. Rainfall anomalies (% of normal; base period 1981–2010) for South Africa during 2015 (Source: South African Weather Service.)

(ii) Precipitation

Figure 7.25 presents the annual rainfall anomalies for 2015 compared to the 1981–2010 reference period. The most significant feature was below-normal rainfall across most of the country, with particularly dry conditions in northern KwaZulu-Natal province, the far northeast and western North West, and northeastern Northern Cape provinces.

The beginning of the year was characterized by dry conditions in the western and northwestern interior and, due to below-normal rainfall conditions during the 2014/15 austral summer rainfall season, the northern and northeastern parts were already classified as very dry.

In June and July, the western half of the country, as well as some parts in the east, got temporary relief from the dry conditions, with most places receiving more than double their average rainfall for the month. In September the rainy season in the summer-rainfall areas commenced well, with comparatively high rainfall totals reported in the northern interior. However, (austral) spring and beginning of summer of 2015 had dry conditions accompanied by recurring heat waves in many places.

The July–June 2014/15 period was on average the driest season for South Africa since 1991/92 and the third driest since 1932/33.

(iii) Notable events

With drought conditions firmly in place, by February some agricultural organizations requested that provinces, such as North West, be declared drought-stricken. In KwaZulu-Natal, a substantial loss in the sugarcane yield was expected, while water restrictions were in place over much of the province. By March, other provinces also considered applying to be declared drought-stricken areas, including the Western Cape, Free State, and Limpopo Province. The provinces of Northern Cape, North West, KwaZulu-Natal, Mpumalanga, and Limpopo, and the Free State were all declared drought disaster areas in November. By the end of (austral) summer, the prolonged drought conditions severely affected maize, sugar cane, and sorghum harvests.

In the spring, record high temperatures were broken on a regular basis, with Vredendal recording a temperature of 48.4°C on 27 October 2015, setting a new global record for the highest temperature ever observed for this month. The previous highest maximum temperature for this station was 42.5°C,

recorded on 30 October 1999. Extremely high maximum temperatures also occurred in Gauteng from 4 October, and resulted in prolonged heat wave conditions for 9 consecutive days in Pretoria and 8 consecutive days in Johannesburg. Lephalale in Limpopo Province also experienced heat wave conditions for 6 consecutive days. Heat wave conditions also occurred in November, beginning on the 7th and prevailing over four provinces: Gauteng Mpumalanga, the Limpopo Province, and North West.

An extensive dust storm occurred about 60 km north of Bloemfontein between Winburg and Verkeerdevlei on 11 November. According to reports, the wall of dust was estimated between 20 and 25 km wide and at least 3 km high. The dust storm was accompanied by strong winds blowing at 60–70 km hour^{-1}.

6) Western and central Indian Ocean island countries—G. Jumaux, L. Randriamarolaza, M. Belmont, and H. Zahid

This region consists of several island countries, namely Madagascar, La Réunion (France), Mayotte (France), Seychelles, and Maldives.

Overall, the 2015 mean temperature for the region was well above normal. Precipitation was also generally above normal, especially during the second half of the year in the Maldives and Réunion, but was below normal in Mayotte for the same period (Fig. 7.26).

(i) Temperature

In Madagascar, 2015 was the fourth warmest year since records began in 1971 (the warmest year was 2011). The overall annual mean temperature was 24.2°C, corresponding to an anomaly of about +0.5°C. All stations had positive anomalies, with the highest departure observed at Ambohitsilaozana (northeastern Madagascar; 1.8°C above average), except Antsiranana (northern Madagascar) station (0.1°C below; Fig. 7.27). During austral summer (January–March), the seasonal mean temperature was below the reference period. The mean temperature for July–August was above normal.

For Réunion Island, 2015 was the third warmest year since records began there in 1969, with an annual mean temperature anomaly (based on six stations) of +0.7°C. Only February and March were below or near-normal. Minimum and maximum annual temperatures were 0.5°C and 0.9°C above the 1981–2010 mean, respectively.

For Mayotte Island (Pamandzi Airport), 2015 was the warmest year since records began in 1961, with an annual mean temperature anomaly of +0.7°C (+0.6°C for maximum temperature and +0.8°C for minimum

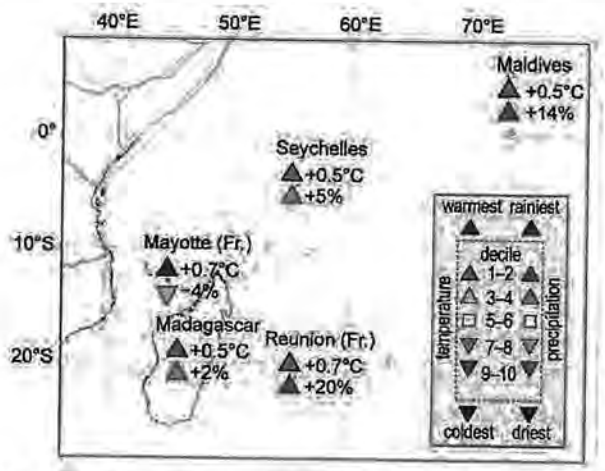

Fig. 7.26. Mean annual temperature anomalies (°C), annual rainfall anomalies (%), and their respective deciles for the Indian Ocean islands (Sources: Météo France; and Meteorological Services of Madagascar, Seychelles, and Maldives.)

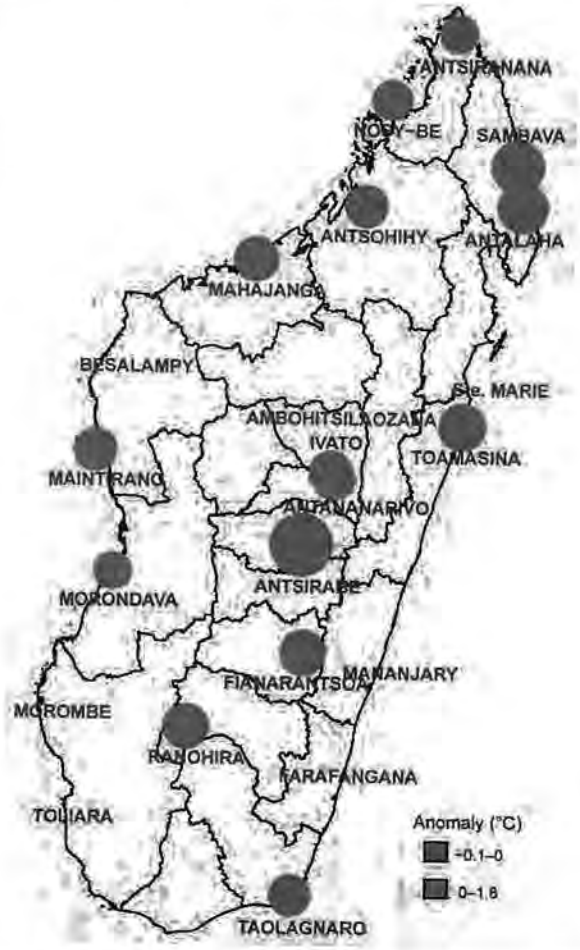

Fig. 7.27. Annual mean temperature anomalies (°C) based on 1981–2010 average. The circle dimension is related to the anomaly absolute values. (Source: Climate Change and Climatology Service, Meteorology of Madagascar.)

temperature, both highest on record). December was the warmest month of the year, with an average daily maximum temperature of 32°C.

For Seychelles, all months had above-normal mean maximum temperatures (at Seychelles International Airport) except January and February. The warmest month was April with a maximum temperature average of 32.3°C and a minimum temperature average of 26.2°C (respective anomalies of +0.7°C and +0.8°C). The annual mean temperature in 2015 was 0.5°C above average, marking the second warmest year since 2009.

For the Maldives, the annual mean temperature (based on two stations: Gan and Hulhule) in 2015 was 28.8°C, +0.5°C compared to normal. Mean temperatures were above average for all months, with the highest anomaly of +1.2°C observed in December (Fig. 7.28). These elevated temperatures are associated with the 2015 El Niño event. Overall, 2015 was the third warmest year since records began in 1981.

(ii) Precipitation

In Madagascar, annual accumulated precipitation was slightly above the 1981–2010 average. However, 10 of 22 stations indicated below-average annual total precipitation. The highest positive anomaly was recorded in Morombe (200% of normal) in southwestern Madagascar, while the lowest negative anomaly was observed in Sainte Marie (47% of normal) in northeastern Madagascar. In addition, more stations were drier than average in northern Madagascar than in the south (Fig. 7.29). During austral summer (January–March), rainfall was above average, but was below average from April to December. In addition, the number of dry days (rainfall < 0.1mm) were 12 on average during summer, compared with 22 days on average for April–December.

For Réunion Island, the annual rainfall was about 120% of average, marking the ninth rainiest year since records began in 1969. March was the wettest month of the year due to heavy rainfall in the wake of tropical storm Haliba's passage near Réunion on 9 March. The number of substantial rainy days (56 days compared with an average of 37) was the highest on record (followed by 1982, 1972, and 2008).

For Mayotte Island, the annual rainfall amount (based on two stations) was slightly below average. January was the wettest month of the year, especially on the eastern part of the island. Pamandzi airport recorded 510 mm, which is the rainiest January for this station since records began in 1961 (followed by 1971, 1986, and 2008).

In Seychelles, annual rainfall total in 2015 was 105% of normal. Below-normal rainfall and fewer-than-normal rain days were reported from January to April and in July. May–October is the dry season in Seychelles but, with the presence of an active

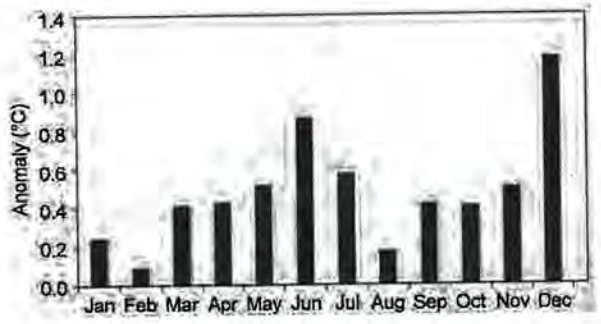

FIG. 7.28. Monthly mean temperature anomalies (°C) in 2015 in Maldives (average of two stations) with respect to the 1981–2010 base period. (Source: Maldives Meteorological Service.)

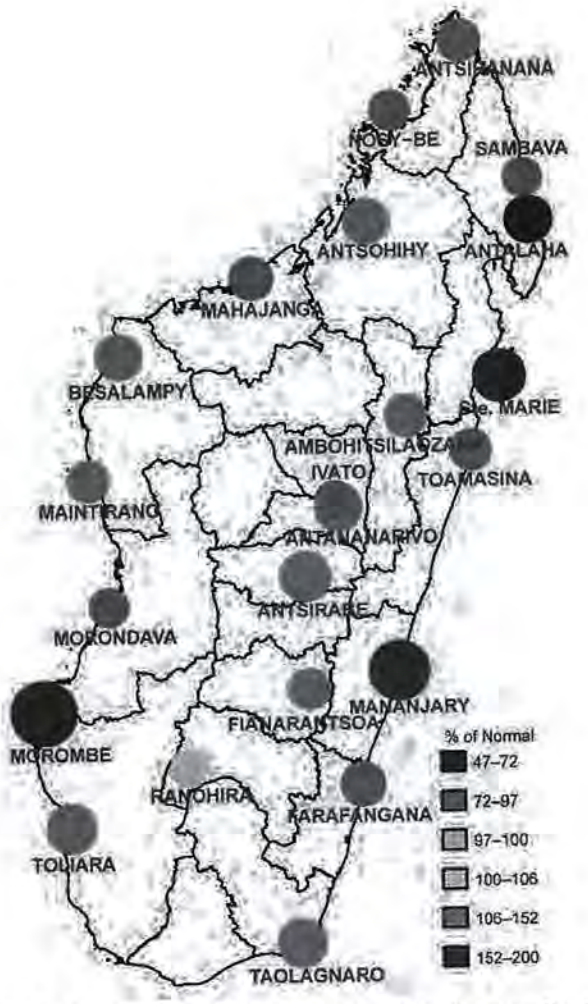

FIG. 7.29. Annual total precipitation (% of normal) with respect to the 1981–2010 period. The circle dimension is related to the anomaly absolute values. (Source: Climate Change and Climatology Service, Meteorology of Madagascar.)

El Niño, several months received abnormally high rainfall (Fig. 7.30). August received 298.3 mm (normal is 122.5 mm); October recorded 337.6 mm (normal is 177.7 mm); and November recorded 353.9 mm (normal is 192.5 mm). Many days with daily rainfall above 50 mm were recorded during the last five months of 2015. The highest daily value (122.6 mm) was recorded on 9 November at Seychelles Airport.

For the Maldives, the annual rainfall amount in 2015 was 2408 mm, 114% of average, making 2015 was the fourth wettest year since records began in 1981. August was the wettest month of the year, with an average rainfall of 370 mm over the Maldives (Fig. 7.31). As is typical, February was the driest month of the year, with average rainfall of 24 mm. On average, the Maldives experienced about 140 rainy days in 2015, 5 more than average. In 2015, the highest number of rainy days was recorded in August, September, and October (19 days each). On the other hand, the lowest number of rainy days (3) was experienced in January.

(iii) Notable events

The absolute maximum temperature was recorded at Antsohihy (northwestern Madagascar) on 13 October and 11 November (+38.7°C) and the absolute minimum temperature was recorded at Antsirabe (central Madagascar) on 21 July (−1.2°C).

The highest 24-h accumulated precipitation was 318 mm recorded in Maintirano (western Madagascar) on 2 February, which is a 12-year return period event. Grand-Ilet station (Salazie, in the highlands) recorded 1277 mm in 4 days (5-year return period).

Associated with cyclones and other systems in the region, the Maldives experienced rough sea conditions and flooding. Average winds of 24 km hour^{-1} prevailed in the central atolls from 10 January until the end of the month. Due to strong, sustained winds, moderate to rough seas prevailed in the area, which caused a passenger boat to run aground on a reef near Kaafu Maniyafushi. All 24 passengers were rescued, but the boat sank in the reef as the Coast Guard was unable to continue rescue efforts in the area due to the strong winds and rough seas. No cyclones directly impacted the Maldives in 2015.

On the other hand, Madagascar was affected by three tropical systems that formed in the Mozambican Channel on 13 January (Tropical Storm Chaedza), 5 February (Tropical Storm Fundi), and 3 March (a tropical depression). The persistence of the ITCZ amplified the conditions, leading to an event that had never occurred in February since records began in 1961. On 26 February, in Antananarivo, significant rainfall of 129.2 mm caused the destruction of a dam, which led to a major flooding event. Madagascar's disaster management agency, the Bureau National de Gestion des Risques et des Catastrophes (BNGRC), reported that 19 lives were lost, 36 956 residents displaced, and more than 60 000 people affected by the disaster. An estimated 517 houses were destroyed and 1698 were damaged in the floods. BNGRC also reported that the floods damaged 6339 hectares of rice fields.

Associated with a cloud cluster that formed south of the Maldives on 24 November, 228 mm of rain fell in the southernmost region in Addu City, the highest recorded 24-h rainfall for the Maldives, breaking the previous record of 188 mm. Three hours of torrential rain and more than 12 hours of incessant rainfall left most parts of Addu City under water, and flood water damaged household appliances and furniture in hundreds of households. It is estimated that more than 200 houses experienced flooding, and damage was estimated to be in excess of 200 000 U.S. dollars.

f. Europe and the Middle East

This section covers western Europe, from Scandinavia to the Mediterranean, and extends from Ireland and the United Kingdom to eastern Europe, European

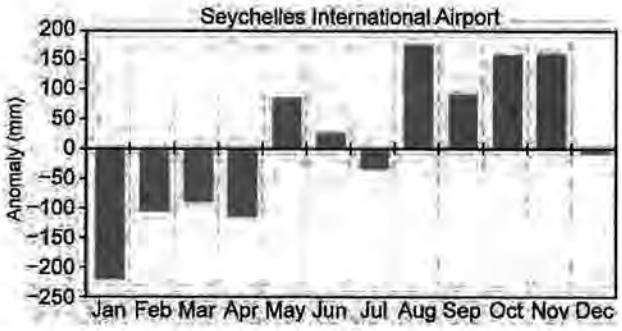

Fig. 7.30. 2015 monthly rainfall anomalies (mm) at Seychelles International Airport. (Source: Seychelles Meteorological Services.)

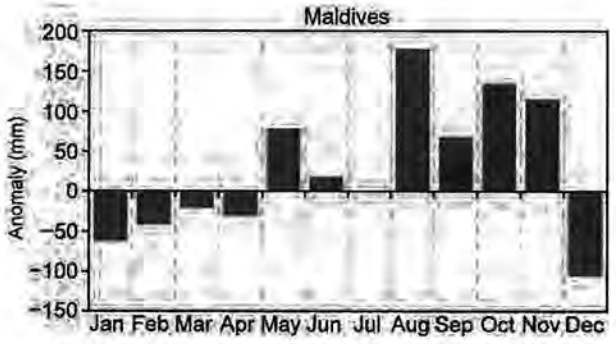

Fig. 7.31. 2015 monthly rainfall anomalies (mm) in Maldives (Source: Maldives Meteorological Services.)

Russia, and parts of the Middle East. While the entire region is covered in the Overview, not all countries provided input to this report, so some individual national details are not included.

Throughout this section, normal is defined as the 1961–90 average for both temperature and precipitation, unless otherwise specified. European countries conform to different standard base periods applied by their national weather services. All seasons mentioned in this section refer to the Northern Hemisphere. Significance implies an exceedance of 5th or 95th percentiles.

More detailed information, including monthly statistics, can be found in the Monthly and Annual Bulletin on the Climate in RA VI – European and the Middle East, provided by WMO RA VI Regional Climate Centre Node on Climate Monitoring (RCC Node-CM; www.dwd.de/rcc-cm). All statistics reported here are for three-month seasons.

1) Overview

Europe was, on average, much warmer than normal in 2015. The mean land surface air temperature for the European region (35°–75°N, 10°W–30°E) from the CRUTEM4 dataset (Jones et al. 2012) was +1.51°C above the 1961–90 normal, only 0.2°C short of the previous record set in 2014 (Fig. 7.32). According to the E-OBS dataset (van der Schrier et al. 2013b; Chrysanthou et al. 2014), which uses different meteorological stations over an area extending farther west and east (25°W–45°E), the European annual mean land surface temperature was the highest on record (+0.93°C above the 1981–2010 average; Fig. 7.33). However, differences between both datasets are within the level of uncertainty (allowing for the different base periods).

Across Europe and the Middle East, temperature anomalies ranged between +1°C in northwestern areas and +3°C in northeastern and Alpine regions (Fig. 7.34).

Precipitation totals in 2015 (Fig. 7.35) were below average across most of continental Europe and Iceland (60%–80% of normal). Parts of the British Isles, northern Europe, and the central and eastern Mediterranean recorded significantly above-average totals of 125% of normal and locally up to 170% of normal.

Winter 2014/15 (December–February) was exceptionally mild over Scandinavia and the eastern European region, with surface and 850-hPa temperature anomalies up to +4°C (Fig. 7.36a). The Icelandic low (negative anomalies of –12 hPa) and the Azores high (positive anomalies of +12 hPa) were well established as reflected by the North Atlantic Oscillation index

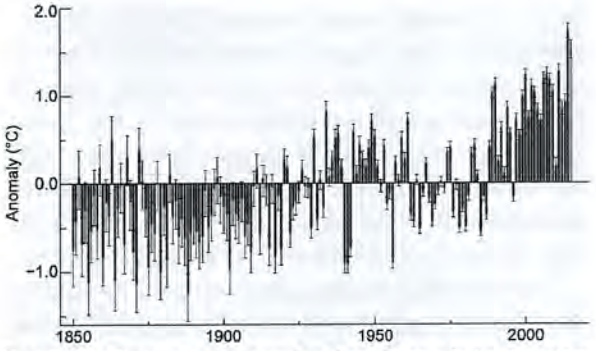

Fig. 7.32. Annual average land surface air temperature anomaly (°C) for the European region (35°–75°N, 10°W–30°E) relative to the 1961–90 base period. The blue bars show the annual average values and the black error bars indicate the 95% confidence range of the uncertainties. The green bar is the annual value for 2015. Data are from the CRUTEM4 dataset (Jones et al. 2012.)

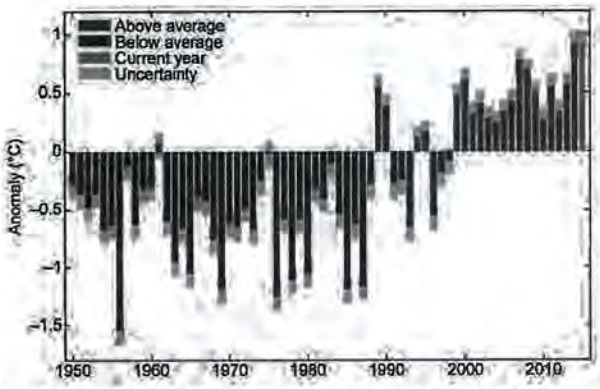

Fig. 7.33. Annual land surface air temperature anomaly (°C) for Europe, similar to Fig. 7.32, but based on the E-OBS dataset (van der Schrier et al. 2013b and Chrysanthou et al. 2014) from 1950 to 2015. [Source: KNMI (Royal National Meteorological Institute) Netherlands.]

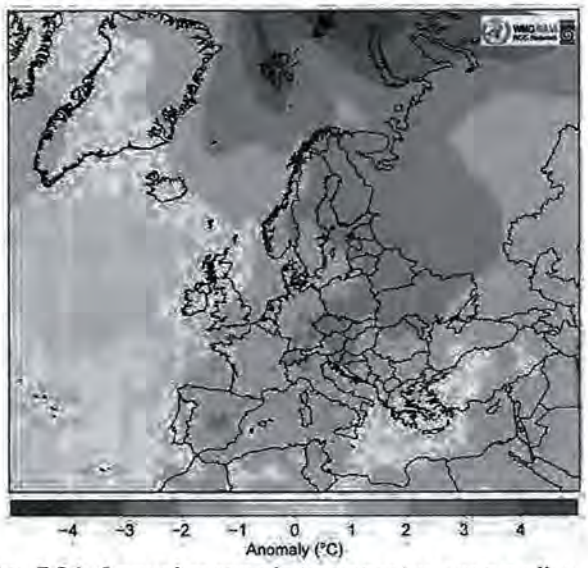

Fig. 7.34. Annual mean air temperature anomalies (°C; 1961–90 base period) in 2015. (Source: DWD.)

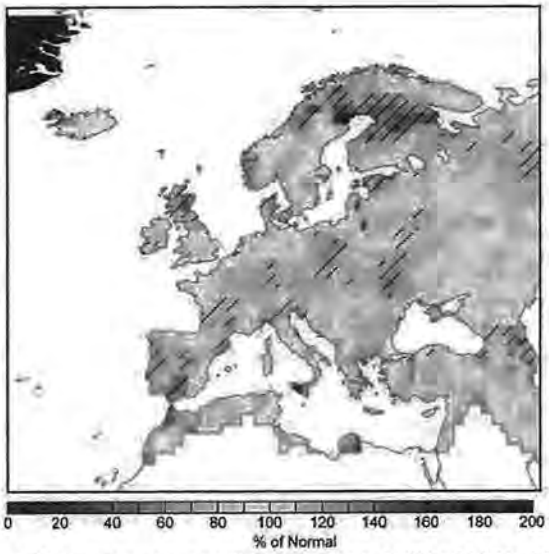

Fig. 7.35. European precipitation totals (% of 1951–2000 average) for 2015. Hatched areas indicate regions where precipitation is higher than the 95th percentile of the 1961–90 distribution. Only grid points with mean annual precipitation >15 mm month^{-1} are represented. [Source: Global Precipitation Climatology Centre (Schneider et al. 2015).]

[NAO +1.65, normalized pressure difference between the Azores High (Ponta Delgada, Azores) and the Icelandic Low (Reykjavík, Iceland)]. This synoptic pattern allowed for a frequent westerly flow of mild Atlantic air masses that brought precipitation totals of up to 170% of normal, particularly in northern parts of Europe and in the southeast (Fig. 7.37a, hatched). In contrast, the Iberian Peninsula and southwestern France had below-average surface temperature anomalies of up to −1°C due to the influence of high pressure and precipitation less than 40% of normal in places.

During spring (March–May) significant above-average 500-hPa heights centered over Iberia led to well-above-normal temperatures in southwestern Europe (Fig. 7.36c, dotted). March in particular contributed to the anomalous warmth. It was the third straight month of extensive westerlies and southwesterlies advancing over northeastern Europe where temperature anomalies exceeded +4°C.

Northern Europe was affected by frequent Atlantic cyclones throughout the season that caused a significant precipitation surplus of locally more than 180% of normal (Fig. 7.37b, hatched), whereas the western half of Europe, including most of the British Isles, had below-average totals.

The summer season (June–August) was characterized by a hot spell across western, central, and eastern Europe (see Sidebar 7.1) as a result of significant above-average 500-hPa heights (Fig. 7.36e, dotted). In

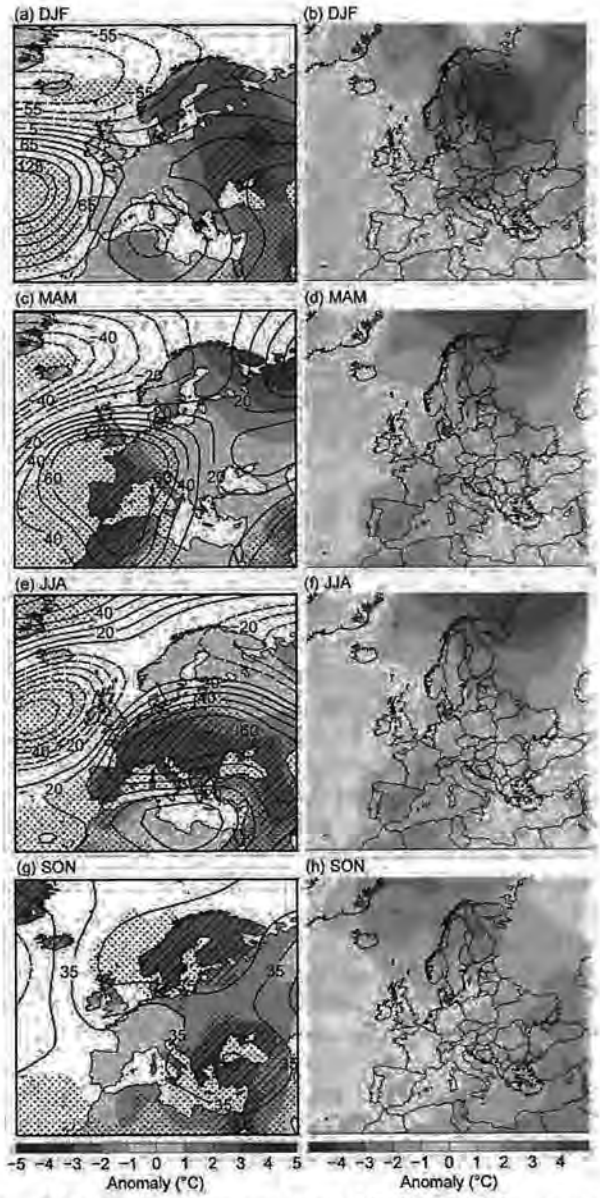

Fig. 7.36. Seasonal anomalies of (left) 500-hPa geopotential height (contour, gpm) and 850-hPa temperature (shading, °C) and (right) near-surface air temperature, using data from the NCEP–NCAR reanalysis for (a), (b) DJF (winter), (c), (d) MAM (spring), (e), (f) JJA (summer), and (g), (h) SON (autumn). In left column, dotted areas indicate regions where 500-hPa geopotential is above (below) the 95th percentile (5th percentile) of the 1961–90 distribution, while hatched areas represent the corresponding thresholds but for 850-hPa temperature. Base period used for both analyses is 1961–90. (Source: Deutscher Wetterdienst.)

contrast, the British Isles, Scandinavia, and northern European Russia were influenced by frequent low pressure systems. These regions recorded surface temperature anomalies of 0° to −1°C accompanied by above-average rain amounts of up to 170% of normal (Fig. 7.37c).

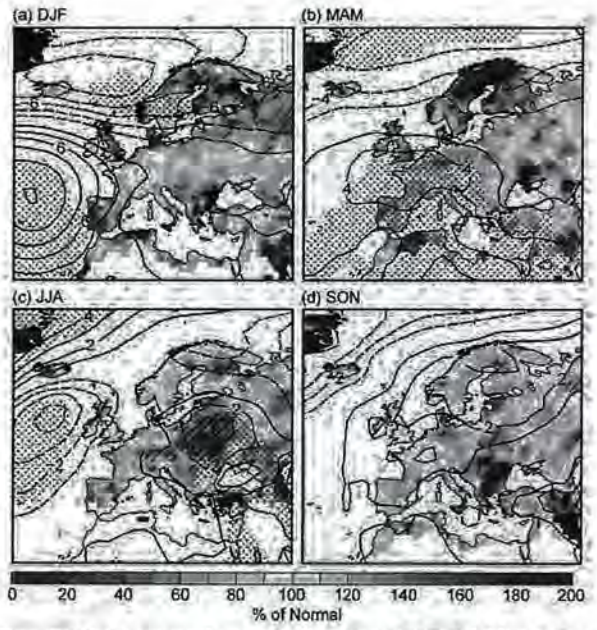

FIG. 7.37. Seasonal anomalies for 2015 (1961–90 base period) of sea level pressure (hPa) from NCAR–NCEP reanalysis (contours) for (a) DJF (winter); (b) MAM (spring); (c) JJA (summer); and (d) SON (autumn). Colored shading represents the percentage of seasonal mean precipitation for 2015 compared with the 1961–90 mean from the monthly Global Precipitation Climatology Centre (Schneider et al. 2015) dataset (only grid points with climatological mean seasonal precipitation above 15 mm month^{-1} are represented). Dotted areas indicate regions where SLP is higher (lower) than the 95th percentile (5th percentile) of the 1961–90 distribution, while hatched areas represent the corresponding thresholds but for precipitation.

In autumn the atmospheric circulation featured above-average 500-hPa heights (Fig. 7.36g), and temperatures were warmer than normal in nearly all regions. Scandinavia and the eastern Mediterranean, including the Black Sea region, were especially affected by high pressure conditions and recorded significantly positive surface and 850-hPa temperature anomalies of more than +3°C in places. According to the E-OBS dataset, it was the third warmest autumn since 1950 for the European region. Eastern Turkey and the Balkan States received localized precipitation totals of more than 200% of normal (Fig. 7.37d).

The year ended exceptionally warm, with a strong positive NAO (+2.24) phase in December. The synoptic pattern was associated with exceptionally widespread positive temperature anomalies that exceeded +4°C. Large parts of Europe recorded their warmest December since 1950. Only the eastern Mediterranean experienced below-average temperatures, with anomalies reaching –2°C.

2) Central and western Europe

This region includes Ireland, the United Kingdom, the Netherlands, Belgium, Luxembourg, France, Germany, Switzerland, Austria, Poland, Czech Republic, Slovakia, and Hungary.

(i) Temperature

Annual temperatures in central Europe were warmer than normal and nearly all areas of the region were around 2°C above their long-term means. Switzerland had its warmest year since national records began in 1864 (+2.1°C). Austria, Germany, Slovakia, and Hungary each experienced their second warmest year since 1767, 1881, 1961, and 1901, respectively, with anomalies ranging between +1.7°C and +2.2°C.

The winter season 2014/15 was exceptionally mild, particularly for the eastern part of the region, which was more often than normal under the influence of subtropical air masses. Spring was characterized by above-average temperatures except for most of Ireland, where deviations of –1°C were recorded. May in particular contributed to the cooler-than-normal conditions in Ireland, where deviations down to –1.7°C were recorded.

During summer, the atmospheric circulation featured significantly widespread anomalous high temperatures across continental Europe. Near the Alps, the blocking ridge led to positive temperature anomalies up to +4°C. In contrast, the British Isles were affected by frequent westerly flow of Atlantic air masses that led to a summer with mostly near-normal temperatures, although a brief heat wave occurred in early July, particularly affecting southern parts of the United Kingdom.

Temperature anomalies in autumn ranged between –1°C in parts of France to +2°C in the southern United Kingdom and eastern areas of the region. November was especially warm (2°–4°C above average), when many daily high temperature records were broken. Germany reported its warmest November on record (3.5°C above average). The United Kingdom and Switzerland reported deviations of +2.6°C and +2.7°C, respectively, with each having their third warmest November since 1910 and 1864, respectively.

The year ended with exceptionally warm December temperatures that were more than +4°C from the reference period across nearly the entire region. An exceptionally strong southwesterly flow associated with a strong positive phase of the NAO contributed to these spring-like temperatures.

(ii) Precipitation

Annual precipitation totals were mostly below the long-term mean. Only Ireland, Scotland, Benelux, and northern Germany had slightly above-normal precipitation.

Winter 2014/15 was characterized by below-average precipitation in central Europe, with locally less than 60% of normal. The United Kingdom was affected by frequent cyclonic conditions that gave rise to a surplus of up to 140% of normal precipitation.

Spring was drier than normal across the entire region, except in Scotland. France, central Germany, and western Poland each received 60%–80% of normal precipitation and locally even less, associated with areas of significantly above-average sea level pressure (SLP, dotted areas in Fig. 7.37b). Over the British Isles, below-average totals of 70% of normal in southern England contrasted with values in western Scotland of more than 150% of normal.

During summer, below-average precipitation totals continued, especially in eastern and central Europe and the Alpine region where totals as low as 40% of normal were registered. Hungary reported its sixth driest June since 1901.

Autumn precipitation was above normal in the eastern part of the region, while western areas, including the British Isles, experienced a rain deficit. High pressure over northern Europe during September and October brought dry conditions to the United Kingdom, with 54% and 65% of normal rain, respectively. The season ended with very wet conditions when the Icelandic low was well established. This synoptic pattern was associated with 250% of normal totals in most regions, except France and the Alpine region. Repeated low pressure systems continued to the end of the year, and precipitation remained well above normal.

(iii) Notable events

Two storms crossed the North Sea during 9–11 January. At the central German mountain station Brocken, wind gusts of more than 43 m s^{-1} were measured.

During July and August, Hungary reported a record 27 days of heat wave conditions, and Budapest experienced a record-breaking 34 tropical nights, the most since records began in 1901.

Two intense rainstorms crossed southeastern France during 12–13 September, bringing 200–242 mm rain within 6 hours. The latter amount is a new record at station Grospierres.

In November, many record high temperatures were measured. On 7 November, a station in Freiburg, southwest Germany, recorded 23.2°C, its highest daily maximum temperature for November.

Ireland reported its sixth wettest November since records began in 1866. Newport, on the west coast of Ireland, observed a record daily rainfall of 66.2 mm (190% of normal) on 14 November.

Several storms traversed central Europe in November. During the 17th and 18th, a core pressure below 985 hPa brought wind gusts of more than 48 m s^{-1}, causing traffic disturbance and damage to trees and buildings.

3) The Nordic and the Baltic countries

This region includes Iceland, Norway, Denmark, Sweden, Finland, Estonia, Latvia, and Lithuania.

(i) Temperature

Annual temperatures in 2015 were well above normal in the Nordic and Baltic countries. Finland and the Baltic States experienced anomalous temperatures of +2° to +3°C. Lithuania and Finland experienced their warmest year on record, with anomalies of +2.1°C and +2.6°C, respectively. Norway observed its third warmest year since records began in 1900, with an anomaly of +1.8°C. Iceland, however, recorded only slightly-above-average temperatures (0° to +1°C) and had its coldest year since 2000.

Winter 2014/15 was exceptionally mild in Scandinavia and the Baltic States, with the largest deviations of more than +4°C in Estonia, Finland, and central Sweden. The anomalous temperatures were caused by persistent southwesterly flow, which brought subtropical air far into Scandinavia. February in particular contributed to the anomalous warmth. Finland, on average, had temperatures 7°C above normal, marking its third warmest February, behind 1990 and 2014. Norway's average anomaly was +4.2°C, with anomalies at stations in southern and central regions up to +6°C and +9°C, respectively.

In spring, temperatures remained above the long-term mean, with anomalies between +3° and +4°C in northern Scandinavia (hatched areas in Fig. 7.36b). March was especially warm when mild subtropical air advanced far into the north. Lithuania reported positive anomalies of +4.9°C. Norway also experienced a mild March, at 3.8°C above average. Locally, in Finnmark and Troms (far northern Norway), deviations of +5° to +7°C were reported.

During summer, temperatures were near-normal on balance. Above-average temperatures of +1°C over the Baltic States contrasted with below-average conditions (–1°C) over Iceland and most of Scandinavia. June and July were cooler than normal, with anomalies as much as –2°C over the Scandinavian countries where below-average 500-hPa heights prevailed.

Temperatures in autumn were significantly warmer than normal throughout all regions due to dominant high pressure (dotted areas in Fig. 7.36g). The strongest deviations occurred in northern Scandinavia, at +2° to +3°C. In November, a strong positive NAO phase (+1.7) led to many locations in Scandinavia observing temperatures above their 90th percentile.

In December, a combination of prolonged high pressure over the central Mediterranean and warm air advection caused exceptionally mild conditions in the Nordic region. Widespread positive anomalies of more than +4°C were recorded across most regions, except for Iceland, where below-average temperatures in western areas contrasted with warmer conditions in the east.

(ii) Precipitation

With the exception of Iceland and the Baltic States, annual precipitation totals were above normal. Denmark reported its second wettest year since 1874, and Norway observed 125% of normal precipitation on average, which is third wettest in its 116-year record.

Winter 2014/15 was wetter than normal across nearly all of the Nordic countries due to a strong positive NAO phase (+1.65). Below-average 500-hPa heights were associated with frequent cyclonic conditions that brought up to 170% of normal precipitation to the region (hatched areas in Fig. 7.37a).

In spring, wetter-than-normal conditions remained, especially across Scandinavia where 125%–170% of normal totals were widely observed. Norway experienced its second wettest May on record (after 1949), with 175% of normal rainfall.

Precipitation in summer was close to normal except for the Baltic States. A persistent blocking ridge centered over continental Europe resulted in dry conditions, with only 60% of normal rainfall recorded (dotted in Fig. 7.37c). August was especially dry, with nearly all regions recording below-average totals. Exceptionally low rainfall of less than 20% of normal was recorded across the Baltic States. Lithuania reported just 16% of its normal rainfall.

During autumn, precipitation totals were mostly below the long-term mean, except for parts of north-central Finland and Denmark (>125% of normal totals). The Baltic States recorded a deficit between 40% and 60% of normal totals. Exceptionally strong southwesterlies in December brought well-above-normal precipitation totals to the Nordic countries. Denmark received up to 250% of normal precipitation. Only parts of central and northern Scandinavia registered a rain deficit, 60%–80% of normal.

(iii) Notable events

In January, Norway and Sweden experienced extreme precipitation totals. Some stations in Norway received up to 400% of normal; at Eikemo (coastal western Norway) 782.3 mm was measured, corresponding to 280% of normal. Station Piteå in northeast Sweden reported a monthly rain accumulation of 1346 mm, which is the most since the record began in 1890.

During 9–11 January, the Danish coast was hit by two successive storms. On the morning of 11 January, water in Lemvig (northwest Denmark) rose to 1.95 m above normal, breaking the previous record of 1.81 m.

During a period of strong westerlies in February, Norway reported record-breaking wind gusts of more than 46 m s^{-1} in southern mountainous areas; 70 000 people lost power. Givær, an island in Bodø (northern Norway), was evacuated during a spring high tide.

In September, Norway was hit by thunderstorms and accompanying extreme precipitation. In the south, station Gjerstad received monthly totals of 478 mm (330% of normal), and station Postmyr i Drangedal received 449.5 mm (350% of normal). On 2 September, the latter recorded its highest daily total of 117.8 mm.

On 2 October, a storm caused forest damage in central Finland and left over 200 000 households without power.

In November, two storms hit Denmark with record-breaking wind gusts. During 7–8 November, the first storm produced Hanstholm's (on the northwest coast) highest wind gust of 34.6 m s^{-1} and a record-breaking 10-minute mean wind of 27.3 m s^{-1}. On 29 November, the second storm passed with wind gusts up to 45.9 m s^{-1}.

4) Iberian Peninsula

This region includes Spain and Portugal. In this subsection, anomalies refer to a reference period of 1981–2010, with the exception of precipitation for Portugal, which the country reports with respect to a 1971–2000 reference period.

(i) Temperature

The Iberian Peninsula experienced a warmer-than-normal year in 2015. Spain recorded an annual anomaly of +0.9°C and tied with 2011 for its warmest year on record, which dates to 1961. Portugal reported positive anomalies compared to the 1981–2010 reference period between +0.6°C in southern regions and +1.7°C in east-central parts of the country.

Winter 2014/15 was colder than normal throughout Iberia due to cold air advection from the north. Spain and Portugal were 0.6°C and 1°C below average, re-

spectively. A colder-than-normal winter was followed by a very warm spring, and the entire Iberian Peninsula registered positive temperature anomalies and significantly above-average 500-hPa heights (dotted in Fig. 7.36a,c). Spain reported a mean anomaly of +1.5°C, with an extremely warm May (+2.4°C), which was the second warmest in its 55-year record.

Significantly anomalous above-normal temperatures remained in summer due to a blocking high pressure ridge over Europe, and anomalies exceeded +2.5°C in most areas. During July, Spain experienced its highest monthly average temperature on record. This month also featured unusually persistent heat wave conditions. In central and southeastern parts of the country, positive anomalies of +3°C were recorded; it was the second warmest summer season on record, behind 2003.

Autumn, overall, was also warmer than normal but with only slightly-above-average values. Very warm conditions in November remained in December, with monthly anomalies of +2°C as a result of an eastward extending Azores high (positive SLP anomalies of up to +10 hPa over the Iberian Peninsula).

(ii) Precipitation

Annual precipitation totals over Iberia were mostly below average (60%–80% of normal). For Portugal the year was extremely dry and only 68% of the normal rain was measured (25% of normal totals based on the 1971–2000 reference period used for precipitation in Portugal). Spain received 77% of its normal precipitation, mainly due to extremely dry conditions in April, May, November, and December.

Winter 2014/15 was characterized by a strong positive NAO, which was reflected in the precipitation distribution over the Iberian Peninsula. While the northernmost part was influenced by northerly flow bringing 125% of normal precipitation, the remaining region experienced a very dry season. Widespread below-average totals of less than 60% of normal were recorded.

During spring, the Azores high extended far into the European continent and led to well-below-normal precipitation totals. May brought an extreme rain deficit. Spain reported mean monthly precipitation totals just 25% of normal, its driest May on record. Portugal also observed extreme rain deficits, but mostly in the southern half of the country.

In summer, wetter-than-normal conditions in northeastern Spain contrasted with below-average totals in the remainder of the country. Southern Portugal received only 20%–40% of normal totals and locally even less.

Precipitation in autumn was below average throughout the Iberian Peninsula, with 60%–80% of normal rainfall over central to northeastern Spain. Only southeastern areas recorded a surplus, up to 125% of normal.

The year ended with very dry conditions, caused by a strengthening of the positive NAO phase (+2.2 in December). Spain reported December rainfall just 20% of normal, the driest December at many eastern stations (several reported no rain at all), and Portugal saw less than 50% of its normal precipitation in some regions.

(iii) Notable events

During the first 10 days of February, Spain recorded a significant cold spell due to an intrusion of continental cold air masses from central Europe. A minimum temperature of –11.9°C was measured at the station Molina de Aragon in central Spain.

In northern Spain along the coast of the Bay of Biscay, heavy rainfall in February set new record high totals, with precipitation 300% of the wintertime normal.

Although spring was overall drier than normal in Spain, heavy precipitation events occurred in March. Starting on 5 March, a week of heavy rain, combined with meltwater, led to flooding in the northeast. On 22 March, Castellón de la Plana-Almazora on the eastern coast recorded 133.8 mm within 24 hours.

In May, Spain and Portugal were affected by a heat wave with record-breaking high temperatures. Valencia Airport registered 42.6°C on 13 May, 6.6°C higher than the previous record. By 14 May, the southern station of Beja had already reported 19 days in 2015 with maximum temperatures above 30°C, which was 14 days more than normal.

In summer, Spain suffered from an extraordinarily long, intense heat wave (nearly continuous from 27 June to 22 July), particularly affecting the central and southern regions, where temperatures above 45°C were reported on 6 and 7 July.

On 4 September, Palma de Mallorca (island south of Barcelona) received 124.3 mm rain from thunderstorm activity within 24 hours, the highest for any time of year since the record began in 1973.

On 15–16 September, a low pressure system with a core pressure of 990 hPa delivered more than 100 mm precipitation to several stations in Portugal. Rainfall totals were 150%–200% of normal for September in northern Portugal. The highest accumulated rain was recorded at northern station Cabril (160.4 mm).

Intense rainfall occurred on 1 November at the Algarve in Portugal. Daily accumulated precipitation

SIDEBAR 7.1: UNUSUALLY STRONG AND LONG-LASTING HEAT WAVE IN EUROPE

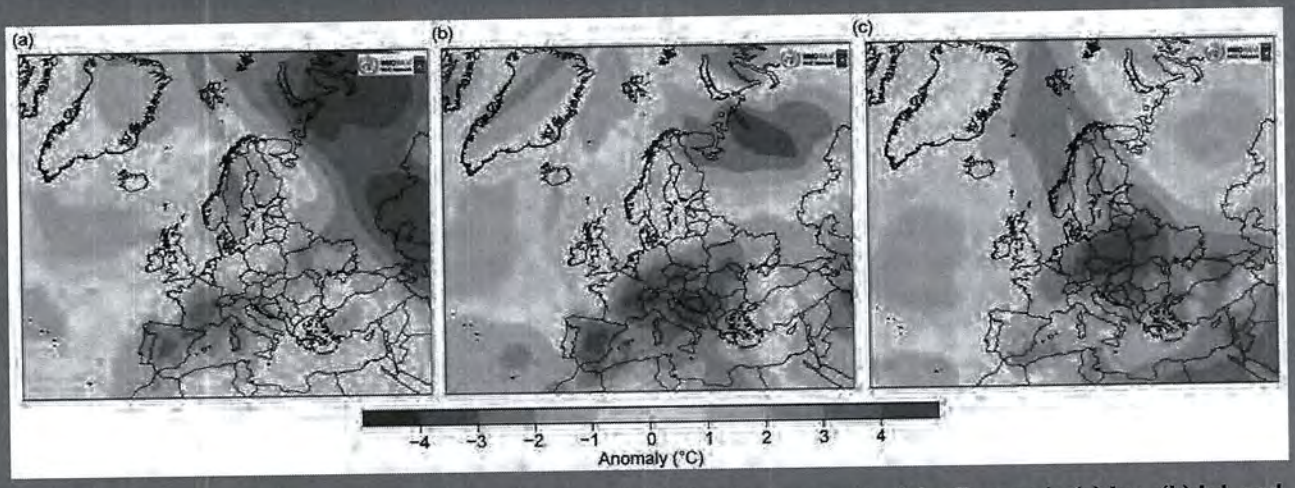

FIG. SB7.1. Monthly air temperature anomalies (°C, 1961–90 reference period) for Europe in (a) Jun, (b) Jul, and (c) Aug 2015. (Source: Deutscher Wetterdienst.)

From late June to early September 2015, much of Europe was under the influence of an unusually strong and long-lasting heat wave. Spain and Portugal also had well-above-normal temperatures in May. The heat was associated with an exceptional rain deficit that led to drought conditions in several regions from southwestern Iberia to eastern Europe, while at the same time heavy thunderstorms were recorded in the central and eastern Mediterranean.

The heat wave affected much of Europe during June, July, and August (Fig. SB7.1). At the end of June, a blocking high pressure system developed over southwest-to-central Europe, with a meandering upper level jet stream, allowing hot air to flow from Africa to Europe, where it became trapped. In mid-July, the Azores high extended farther into central Europe, and by the end of the month, it shifted eastward. The anticyclone caused large-scale subsidence, and western Europe recorded maximum temperatures up to around 40°C. By the end of August, two anticyclones developed over eastern Europe. The resulting southerly flow of hot air masses brought high temperatures to eastern and central Europe.

On an areal average, the European region experienced its third warmest summer season since 1910, behind 2003 and 2010, with temperatures +1.7°C above the 1961–90 mean. August contributed most to the anomalous warmth, with a record high anomaly of +2.3°C, while July was sixth warmest (+1.5°C); June was 15th warmest, with slightly-above-normal temperatures (+0.9°C).

For much of June, Iberia, France, and the western Alpine region observed high temperatures, with anomalies of +3° to +4°C. Portugal registered a monthly mean temperature of 21.8°C, its fifth highest on record, at +2.4°C above the 1961–90 mean. The absolute maximum of 43.2°C was measured on 29 June at Beja, in the south of the country. In France, many

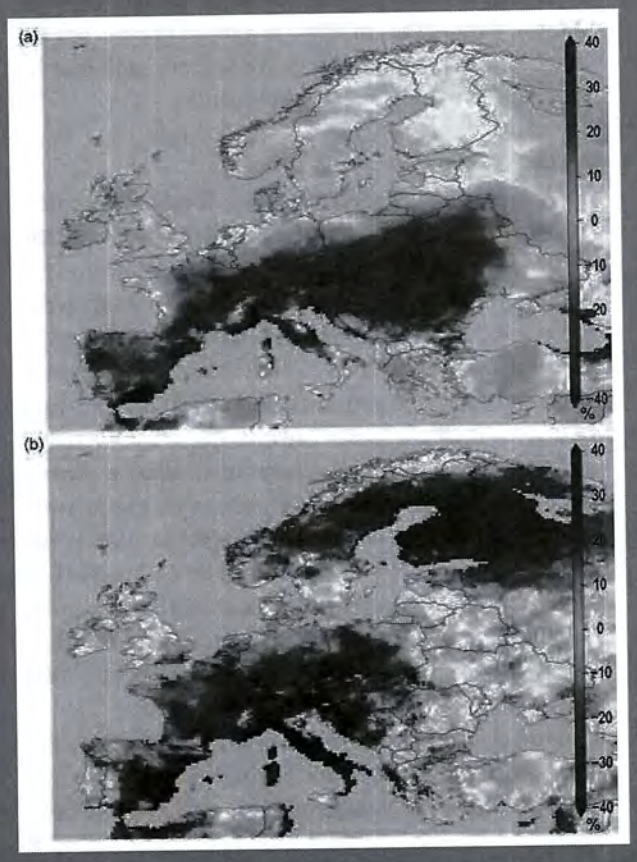

FIG. SB7.2. Percentages of (a) warm days and (b) warm nights for 2015. A warm day or night is defined as a day where the maximum or minimum temperature exceeds the 90th percentile of the values from the 1981–2010 average. (Source: E-OBS dataset, EURO4M.)

CONT. SIDEBAR 7.1: UNUSUALLY STRONG AND LONG-LASTING HEAT WAVE IN EUROPE

maximum temperature records were broken at the end of June. On the 30th, temperatures were as much as 12°C above the seasonal mean in western areas.

In July, the core region of the heat wave moved to central Europe, the Mediterranean, and the Balkan region. However, Spain still experienced its warmest July in its 55-year record, with anomalies of +2.5°C above the 1981–2010 mean. Germany observed a record-breaking maximum temperature of 40.3°C at Kitzingen (central region) on 5 July, and France had a new record maximum temperature, 41.1°C, at Brive-la-Gaillarde (central southern France). Austria recorded temperatures 3.1°C above normal, its warmest July since records began in 1767. In Vienna, a new record daily minimum temperature of 26.9°C was measured. August brought extremely high temperatures to eastern and central Europe, with anomalies exceeding +4°C. In Belarus (Brest) and Lithuania (Kaunas), record daily maximum temperatures of 36.7°C and 35.3°C, respectively, were observed.

The unusual and long-lasting high temperatures were reflected in the fact that warm days and nights (see section 2b5) were more than 40% more frequent than in a normal summer (Fig. SB7.2). High nighttime temperatures in particular can affect human health, and in Belgium and the Netherlands, strongly increased mortality was registered during this period. During July and August, Hungary reported a record 27 days of extremely warm conditions, and Budapest experienced a record-breaking 34 tropical nights, the most since records began in 1901.

The heat wave was also associated with sub-regional severe rain deficits. Southern Spain and Portugal each received only 10 mm rain per month during June, July, and August, which corresponds to less than 40% of their normal totals. After several weeks of persistent heat and continuous rain deficit, southern Portugal and northeastern continental Europe suffered from extreme drought conditions (Fig. SB7.3) in August. On 31 August, 74% of Portugal was categorized as severely or extremely dry. As a result, wildfires occurred in the Mediterranean from Iberia to Turkey and in the Balkan States. The rain deficit also caused low water of the rivers Elbe, Rhine, and Danube, which affected shipping. The river Dnjepr in Belarus had record low levels.

In contrast, several regions experienced well-above-normal precipitation during summer, especially in Greece, western Turkey, and Sicily. The rain surplus was generated by heavy thunderstorms induced by anomalous warm sea surface temperatures (anomalies up to +4°C) in the Tyrrhenian Sea.

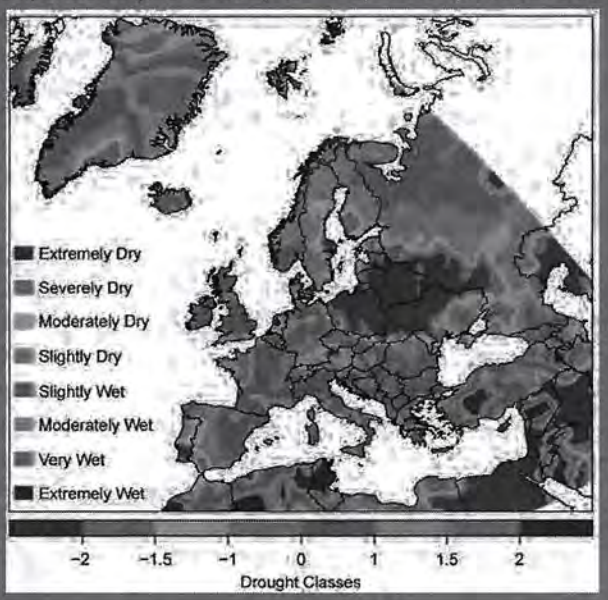

FIG. SB7.3. DWD standardized precipitation index (1961–90 average) for Augv 2015. (Source: Deutscher Wetterdienst.)

exceeded 100 mm. The highest amount of 144.8 mm was observed in Algoz, near the southern coast.

5) MEDITERRANEAN AND BALKAN STATES

This region includes Italy, Malta, Slovenia, Croatia, Serbia, Montenegro, Bosnia and Herzegovina, Albania, Macedonia, Greece, Bulgaria, and Turkey.

(i) Temperature

Averaged over the year, temperature anomalies in 2015 were between +1°C in the central and western Mediterranean and +2°C over the Balkans. Temperatures up to 3°C above normal occurred near the Alps. Much of Montenegro experienced its warmest year on record. Slovenia observed its third warmest year.

Winter 2014/15 was warmer than normal (+2° to +3°C) especially in northern parts of the region. Only some parts of southern Greece and southern Italy/Sicily had below-average temperatures, with anomalies up to −1°C. Croatia saw a mild season and registered positive anomalies up to +2.7°C in northeastern areas.

Above-average temperatures dominated almost the entire region in spring when the Azores high extended far into the European continent. Serbia recorded temperature anomalies of +2°C in northern areas. Croatia had positive anomalies of +1.8°C in its northern areas. During April, colder-than-normal conditions occurred over southeastern areas. In central Turkey, temperature anomalies ranged from −2° to −3°C.

Most of the region experienced a very warm summer, induced by prolonged anticyclonic conditions

centered over continental Europe. The northern Balkan States recorded large anomalies that ranged between +3°C and +4°C; Serbia and Croatia reported anomalies of +2.1°C to +3.8°C. In contrast, Greece's Peloponnese had only slightly-above-normal conditions.

During autumn, temperatures remained above the long-term mean. With the exception of northern Italy, which had only slightly-above-average temperatures, anomalies ranged between +1°C and +2°C. Southern Croatia reported temperature departures up to +2.8°C. The highest anomalies (+3°C to +4°C) occurred at the Bosporus, due to prevailing high pressure.

The year ended with contrasting conditions. While the northernmost areas of the region were under the influence of extremely strong westerlies and associated mild temperatures (3°–4°C above normal) during December, the southern Balkans experienced cool anomalies of –1°C.

(ii) Precipitation

With the exception of northern Italy, annual precipitation totals were above normal. The largest rainfall departures occurred in Sicily, eastern Greece, Bulgaria, and western Turkey, where 125%–170% of normal totals were observed. In the southern Alpine region, drier-than-normal conditions of 60%–80% of normal were recorded. Croatia reported just 63% of its normal precipitation in the northwest.

Winter 2014/15 was very wet for most regions (hatched in Fig. 7.37a). Over the Balkans, precipitation totals of 125%–170% of normal were measured. Southern Serbia had 175% of normal rainfall, and localized areas in Croatia observed 225% of normal.

Precipitation totals in spring mainly ranged between 60% and 125% of normal. While drier-than-normal conditions occurred near the Southern Alps and in Albania, central and southern Italy, as well as easternmost parts of the region, experienced a surplus of precipitation. In Serbia, totals ranged from 67% of normal in eastern areas to 180% of normal in localized spots. Croatia experienced dry conditions in northwestern parts of the country, with 45% of normal precipitation. In April, above-average 500-hPa heights over Europe led to well-below-average precipitation over southern regions. Sicily and southern Peloponnese had very dry conditions with rainfall less than 20% of normal.

During summer, below-average rain in the north of the region contrasted with wet conditions in the south. Greece and parts of Turkey recorded totals greater than 170% of normal, whereas most of the Balkans received below-average precipitation. Eastern Serbia and Croatia reported 25%–30% of normal rainfall. In June, heavy rains fell over northern and central Turkey, bringing totals up to 250% of normal, while July was exceptionally dry across the entire region. Most areas observed less than 40% of normal rainfall, except parts of Italy that received 125% of normal.

Autumn remained wet over the Balkans, whereas the Alpine region recorded below-normal precipitation. Serbia reported very wet conditions, with up to 230% of normal precipitation, and above-normal precipitation prevailed in Bulgaria and northern Greece. October contributed to the overall surplus of rain, when the dipole pattern associated with a split flow brought storms and above-average precipitation across southern Europe. Nearly all areas of the region received more than 170% of their normal precipitation. Croatia rainfall was 140%–410% of normal. In contrast, November was very dry in the Alpine region, with less than 20% of normal rain in northern Italy.

Dry conditions were also evident in December 2015, associated with an exceptionally strong southwesterly flow. Nearly all of Turkey, Italy, and the northern Balkans received less than 40% of their normal rainfall, with some areas observing less than 20% of normal.

(iii) Notable events

Southern Italy was hit by heavy thunderstorms on 5 September. The area surrounding Naples observed hail, the largest with a diameter of 11.5 cm and a weight of 350 g. The hail injured several people and animals, and caused damage to vehicles, houses, trees, and crops.

During 13–14 September, extremely intense precipitation over the Emilia Romania in central-north Italy caused a flood that destroyed roads and bridges. Record-breaking rainfall of 123.6 mm within 1 hour (189.0 mm within 3 hours) at Cabanne and 107.6 mm within 1 hour (201.8 mm within 3 hours) in Salsominore caused floods in the basin of the Aveto, Trebbia, and Nure Rivers. At Nure River, the water levels reached 7 m; the water entered the ground floors of nearby houses.

Bosnia and Herzegovina reported a nationwide heat wave that lasted six days, starting on 15 September. Many new September maximum temperature records were observed, for example, 38.0°C in Sarajevo and 40.9°C in Zenica, both on 18 September.

6) Eastern Europe

This region includes the European part of Russia, Belarus, Ukraine, Moldova, and Romania.

(i) Temperature

Averaged over the year, temperatures across eastern Europe were well above normal, with departures mostly in the +2° to +3°C range. Belarus had its warmest year on record, 2.6°C above normal, surpassing the previous record years of 1989 and 2008. Moldova had its second warmest year, after 2007, and recorded departures from +2.1° to +2.7°C across the country.

Temperatures in winter 2014/15 were extremely mild, especially in northwestern and eastern European Russia, where anomalies exceeded +4°C (hatched in Fig. 7.36a). Belarus reported a national temperature 3.8°C above average, its fifth warmest such period since records began in 1945. In February, above-average 500-hPa heights over central Siberia caused widespread anomalous mild conditions across eastern Europe (more than +4°C). At the end of February, Moldova observed daily temperatures 5°–6.5°C above the long-term mean, which, on average, occurs once every 10 years.

Spring remained warmer than normal, with a meridional gradient in the temperature anomalies due to prolonged high pressure over central Siberia. While northern European Russia experienced anomalies that exceeded +4°C, the Caucasus region had near-normal conditions.

Summer was characterized by high pressure over continental Europe, whereas northern areas were affected by frequent cyclones. In northeastern areas of the region, below-normal temperature anomalies as low as −1°C were registered, while positive anomalies up to +4°C were recorded in westernmost and southernmost places. July was very cool in northern European Russia (down to −4°C) as a result of SLP anomalies of −12 hPa over western Siberia.

During autumn, temperature departures of −1°C in eastern European Russia contrasted with positive anomalies between +1° and +2°C in the remaining regions. Southeastern Ukraine and southern European Russia observed temperatures up to +3°C due to advection of subtropical air masses.

The year ended with significant mild conditions. Moldova reported positive deviations of +2.7°C to +4.5°C in December. On the 27th, areas across Moldova set new records in maximum temperature that ranged from 14° to 18°C.

(ii) Precipitation

Annual precipitation totals in 2015 were above average (>125%) over northeastern areas of the region, while southwestern areas had near-normal conditions. Only the Caucasus region, western Ukraine, and northern Moldova recorded rainfall less than 80% of normal.

Winter 2014/15 was characterized by a strong Icelandic low associated with stronger-than-normal westerly winds that brought a precipitation surplus of more than 125% to most of European Russia (hatched in Fig. 7.37a). Along Romania's Black Sea coast, 170% of normal precipitation fell. Only southwestern Russia and Ukraine received below-average totals, less than 80% of normal.

In spring, precipitation was near normal for the westernmost areas but above average in the Black Sea region. The eastern half of Ukraine recorded totals more than 170% of normal. In contrast, parts of northern European Russia experienced drier-than-normal conditions.

During summer, prevailing high pressure conditions featured a strong rain deficit in western and southern areas of eastern Europe, where less than 60% of normal totals were observed (dotted in Fig. 7.37c). Northern and eastern European Russia were influenced by frequent low pressure systems that brought 125%–170% of normal totals to the region. August was dominated by exceptionally dry conditions in western and southern areas, with less than 20% of normal rainfall. Belarus reported just 16% of normal totals, experiencing its driest August on record since 1945.

Precipitation totals in autumn were unevenly distributed. While the majority of areas had near-normal precipitation, the western Black Sea region received more than 170% of normal, and Romania observed up to 250% of normal precipitation in places. In contrast, western European Russia recorded below-average totals, with some localized observations just 60% of normal.

In December, exceptionally strong westerlies brought well-above-average precipitation to most of the region, with more than 250% of normal totals measured in southern places.

(iii) Notable events

Belarus reported a thunderstorm on 14 June with hailstones measuring 3 cm in diameter. On 27 July, 34.5 mm of rain fell within 30 minutes at station Zhitkovichi in the south.

Moldova experienced high temperatures during 1–2 September. Record-breaking maximum air temperatures of 35.3°C and 38.6°C were measured.

7) Middle East

This region includes Israel, Cyprus, Jordan, Lebanon, Syria, West Kazakhstan, Armenia, Georgia, and Azerbaijan.

(i) Temperature

Annual temperatures were higher than normal, at +1° to +2°C above the long-term mean throughout the Middle East, except for Cyprus, where near-normal conditions prevailed. Armenia observed its third warmest year since records began in 1961 (+1.8°C) and Israel also had its third warmest year in its 65-year record.

Winter 2014/15 was characterized by anomalous temperatures between +2° and +3°C, associated with above-average 500-hPa heights and advection of subtropical air (Fig. 7.37a). Armenia reported significantly warmer conditions with positive anomalies of +2.6°C; locally, in January and February, temperatures were 4°–5°C above average.

In spring, temperatures were near to slightly below normal in the Caucasus region and western Kazakhstan, while the eastern Mediterranean countries experienced warmer-than-normal conditions (+1°C to +2°C). March contributed to the positive seasonal anomalies, due to a combination of high pressure over western Russia and warm air advection from subtropical regions. Armenia observed a national temperature 1.4°C above normal.

During summer, prevailing anticyclonic conditions induced positive temperature anomalies across the entire region (hatched and dotted areas in Fig. 7.36e). Western Kazakhstan and the Caucasus region had anomalies up to +3°C, and the eastern Mediterranean countries also experienced higher-than-normal temperatures of 1°–2°C above average. Armenia observed its second warmest summer, behind 2006, in its 55-year record, with anomalies of +2.4°C. The highest values were recorded in June, where most stations measured temperatures more than 3°C above the long-term mean. In Israel, colder-than-normal anomalies in June (–1°C) contrasted with well-above-average temperatures in August (+2°C).

Temperatures in autumn remained anomalously high in the Middle East. The eastern Mediterranean region experienced areawide anomalies of +3°C, whereas the Caucasus and western Kazakhstan were 1°–2°C above normal. Some places in northwestern Kazakhstan saw temperature anomalies down to –1°C. September was very warm, as a high pressure system associated with large subsidence developed over western Kazakhstan. Israel observed temperatures 2.5°–3°C above normal, marking its warmest September on record, while Cyprus reported its second warmest, with anomalies of +2°C. Armenia also had its second warmest September (2010 was warmer), exceeding the long-term mean by 3°C.

In December, colder-than-normal temperatures in the southern part of the region contrasted with exceptional positive anomalies in northern areas. Areawide anomalies exceeded +4°C in western Kazakhstan.

(ii) Precipitation

Averaged over the year, much of the region saw near-normal precipitation totals. Only western Kazakhstan and the Caucasus region experienced drier-than-normal conditions (< 80%), while much of Jordan received totals up to 125% of normal.

Winter 2014/15 was mostly drier than normal, with as little as 60% of normal precipitation. Only areas in the southern Caucasus region and parts of western Kazakhstan received above-average totals (more than 125% of normal). During February, westernmost Kazakhstan experienced very dry conditions, less than 20% of normal precipitation, whereas northern Israel saw 120%–170% of normal rainfall.

In spring, above-average precipitation in northern areas of the region contrasted with a rain deficit in the eastern Mediterranean countries due to significant above-average SLP. Locally, less than 40% of normal total precipitation was received in some places.

During summer, conditions changed when the region was under the influence of significantly above-average SLP (dotted in Fig. 7.37c). Azerbaijan reported a very dry summer, with less than 40% of normal precipitation. In contrast, the eastern Mediterranean countries mostly received an extreme surplus of rain, locally exceeding 500% of normal in some areas, despite its being the dry season.

In autumn, western Kazakhstan and much of the eastern Mediterranean recorded 60%–80% of normal precipitation, whereas the Caucasus region received 125% of normal. September was dry, whereas October was wet. Israel reported 130% of normal rainfall in the central and southern coastal plain.

In December, low pressure over central European Russia brought precipitation to western Kazakhstan that totaled more than 167% of normal. The Mediterranean region was affected by a high pressure ridge that caused a rain deficit, as little as 20% of normal, in the eastern half and parts of the Caucasus.

(iii) Notable events

Cyprus experienced heavy rainfall accompanied by floods during 5–6 January. Station Kelokedara received 276.6 mm of rain within 24 hours, the highest 1-day precipitation total during January since 1916.

On 7 January, Azerbaijan reported a daily maximum temperature of 15°C, the highest for January since records began in 1900.

During 6–8 January and 18–19 February, Cyprus received heavy snowfall, with 15 cm accumulation in the first event. In both events, schools in mountainous areas were closed.

On 13–14 June, Tbilisi, the capital of Georgia, was hit by heavy rain and thunderstorms. Flooding and an associated landslide led to 12 fatalities and damaged the local zoo, where many animals also perished.

From 25 to 30 October, Israel was hit by a major storm with strong winds of 13–20 m s^{-1} and maximum wind gusts of 36.6 m s^{-1}. Hailstones with diameters of 4–5 cm damaged agriculture crops. On 28 October, 80–85 mm rain fell within 2–3 hours and caused floods in central and eastern parts of the country. A station near Tel Aviv received a monthly accumulation of 246 mm, which is a national record.

g. *Asia*

This section covers Russia, East Asia, South Asia, and Southwest Asia. There is no information for Southeast Asia as no corresponding author was identified for the region. Throughout this section the normal periods used vary by region. The current standard is the 1981–2010 average for both temperature and precipitation, but earlier normal periods are still in use in several countries in the region. All seasons mentioned in this section refer to the Northern Hemisphere.

1) Overview

Based on data from WMO CLIMAT reports, annual mean surface air temperatures during 2015 were above normal across most of Asia and Siberia (Fig. 7.38). Annual precipitation amounts were above normal in eastern China, from southern Mongolia to northwestern China, and from western Siberia to northern India, and they were below normal in Southeast Asia (Fig. 7.39).

Figure 7.40 shows seasonal temperature and precipitation departures from the 1981–2010 average during the year. Seasonal mean temperatures were above normal across Siberia in all seasons, except for the east in spring and the south in autumn. Temperatures were also above normal in northern China in winter, in parts of central and Southeast Asia in spring, in Southeast Asia in summer, and across Southeast Asia and India in autumn. Temperatures were below normal from central China to India in winter, from the western part of central Asia to India in spring, from eastern China to central Pakistan and in European Russia in summer, and across central Asia in autumn.

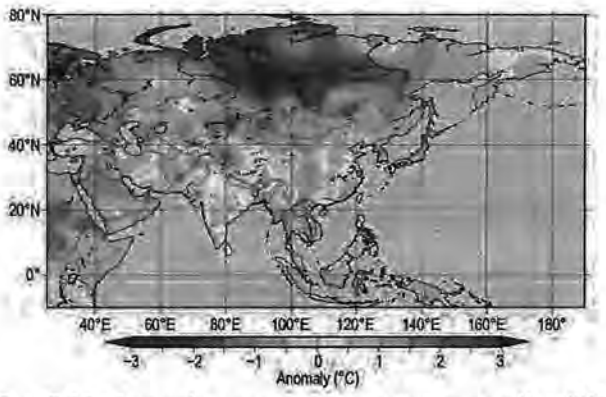

Fig. 7.38. Annual mean temperature anomalies (°C; 1981–2010 base period) over Asia in 2015. (Source: Japan Meteorological Agency.)

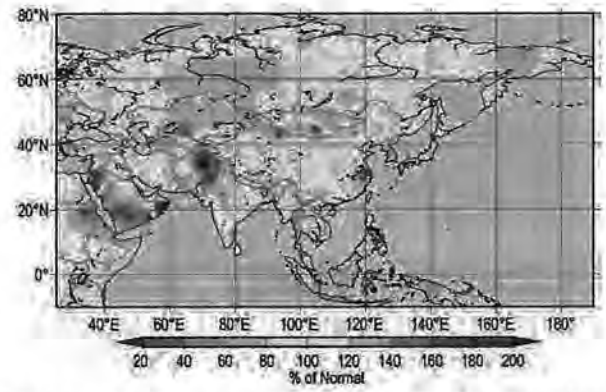

Fig. 7.39. Annual precipitation (% of normal; 1981–2010 base period) over Asia in 2015. (Source: Japan Meteorological Agency.)

Seasonal precipitation amounts were above normal in large areas from western to central Siberia in all seasons, especially in winter and summer. In contrast, they were below normal in Southeast Asia, especially in summer and autumn. They showed greater spatial variability across East, central, and South Asia.

Surface climate anomalies were associated with several distinct circulation features. Convective activity was suppressed over Southeast Asia except in winter (see Fig. 7.41), in association with El Niño conditions. In summer, the monsoon circulation over the Indian Ocean was weaker than normal (see Fig. 7.41c), and overall activity of the Asian summer monsoon was below normal. The northwestward seasonal extension of the northwest Pacific subtropical high was weaker than normal (see Fig. 7.42c), contributing to cool wet summer conditions from southeastern China to western Japan.

2) Russia—O. N. Bulygina, N. N. Korshunova, M. U. Bardin, and N. M. Arzhanova

Analyses are based on hydrometeorological observations conducted at Roshydromet Observa-

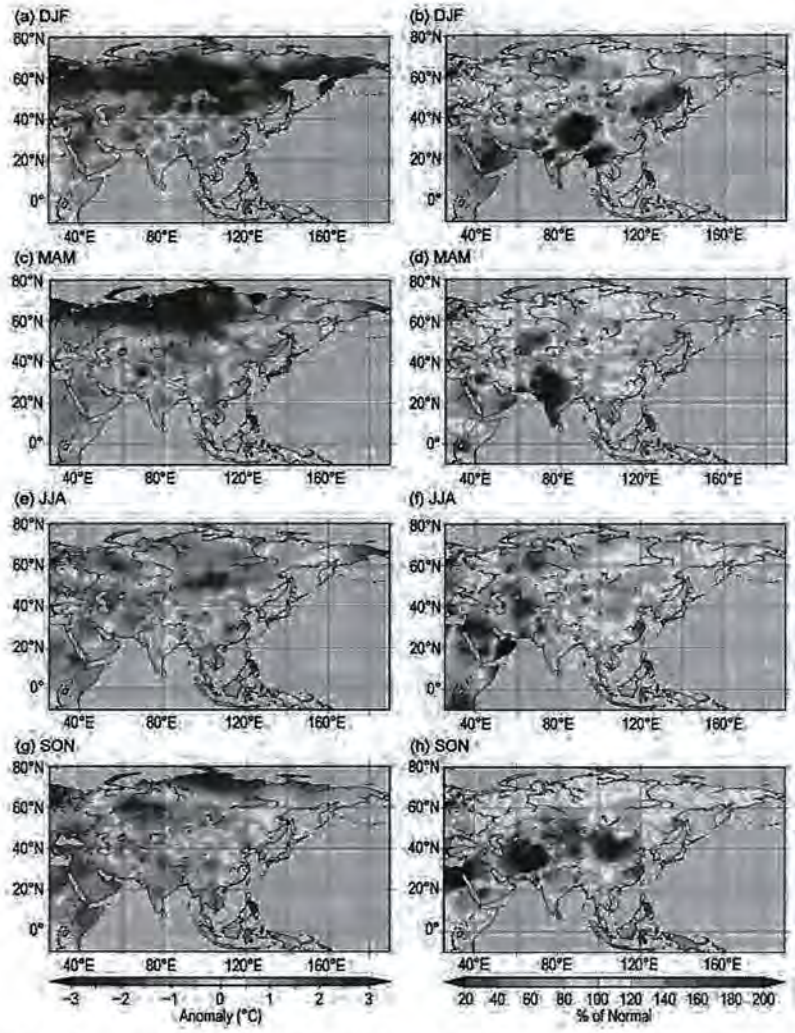

Fig. 7.40. Seasonal temperature anomalies (°C, left column) and precipitation ratios (%, right column) over Asia in 2015 for (a), (b) winter (Dec–Feb 2014/2015); (c), (d) spring (Mar–May); (e), (f) summer (Jun–Aug); and (g), (h) autumn (Sep–Nov), with respect to the 1981–2010 base period. (Source: Japan Meteorological Agency.)

tion Network. Datasets are officially registered and available at meteo.ru/english/climate/cl_data.php. The national average temperature and precipitation records began in 1935, while seasonal averages are considered reliable only since 1939.

(i) Temperature

The mean annual Russia-averaged air temperature was 2.2°C above the 1961–90 normal (Fig. 7.43), making 2015 the warmest year since records began in 1935. Positive mean annual air temperature anomalies were observed across all regions of Russia, with the largest anomalies in northern European Russia and western Siberia (Fig. 7.38).

For Russia as a whole, winter was record warm, with the mean temperature 3.6°C above normal (Fig. 7.43). Central European Russia experienced mean temperature anomalies of +4°–6°C, and +6°–8°C anomalies were observed across the Far East. Daily temperature records were exceeded many times across European Russia. Daily and monthly record-breaking air temperatures were repeatedly registered in many cities, including Moscow, St. Petersburg, Tambov, Voronezh, Tomsk, and Kemerovo.

Spring 2015 was also very warm, with a Russia-averaged mean seasonal air temperature anomaly of +2.3°C (Fig. 7.43), the fourth highest in the 77-year period of record. In northern European Russia and western Siberia, the spring mean air temperature anomaly reached a record-breaking value of +5.2°C.

Summer 2015 continued to be warmer-than-average across Russia, with a national seasonal air temperature anomaly of +1.2°C, the seventh warmest on record (Fig. 7.43).

Autumn was mild over most of Russia with a seasonal mean temperature anomaly of +0.9°C (Fig. 7.43). Positive anomalies were recorded in all regions, except southern West Siberia. From 11 to 30 September, all regions of European Russia experienced abnormally warm weather, and many meteorological stations, from Novaya Zemlya to northern Caucasia, registered several daily record-breaking maximum temperatures.

In December (Fig. 7.44), positive anomalies of mean monthly air temperature were recorded over a vast area, from the western boundaries to the Sea of Okhotsk coast. For the whole of Russia, the anomaly was +4.1°C, the second highest on record. The largest anomalies occurred in northwestern European Russia and in the central Krasnoyarsk Territory and southern West Siberia. In St. Petersburg, with nearly 200 years of meteorological observations, the December 2015 mean monthly air temperature of +2.1°C was the second highest for December on record (see inset in Fig. 7.44).

(ii) Precipitation

In 2015, Russia as a whole received slightly above-normal precipitation, 106% of the 1961–90 normal (Fig. 7.45).

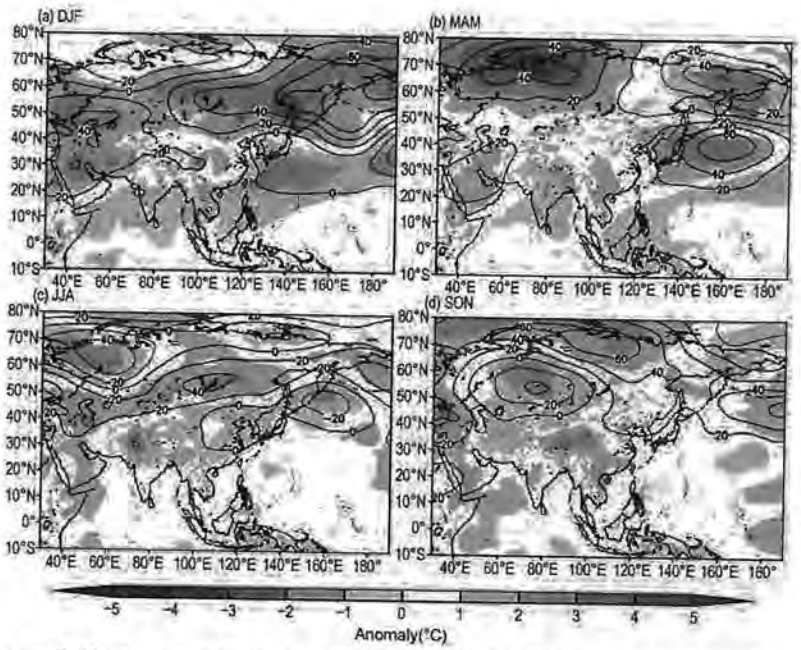

FIG. 7.41. Seasonal mean anomalies of 850-hPa stream function (contour, 1 × 10^6 m^2 s^{-1}) using data from the JRA-55 reanalysis and outgoing longwave radiation (OLR, shading, W m^{-2}) using data originally provided by NOAA for (a) winter (Dec–Feb 2014/15), (b) spring (Mar–May), (c) summer (Jun–Aug), and (d) autumn (Sep–Nov), with respect to the 1981–2010 base period. (Source: Japan Meteorological Agency.)

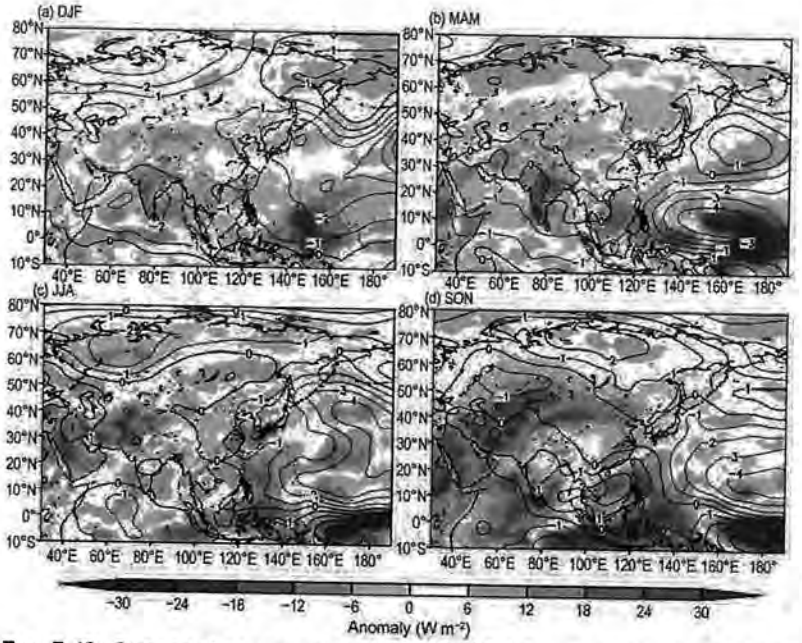

FIG. 7.42. Seasonal mean anomalies of 500-hPa geopotential height (contour, gpm) and 850-hPa temperature (shading, °C) for (a) winter (Dec–Feb 2014/15), (b) spring (Mar–May), (c) summer (Jun–Aug), and (d) autumn (Sep–Nov), with respect to the 1981–2010 base period. Data from the JRA-55 reanalysis. (Source: Japan Meteorological Agency.)

Winter precipitation was 119% of normal, tying (with 2007/08) as the second wettest since 1935 (the wettest winter was 1965/66, 136% of normal). In spring, Russia on average received 115% of normal precipitation. Over European Russia, a significant precipitation deficit was recorded in March.

The summer precipitation total averaged over Russia was normal (99%). Near-normal precipitation was also recorded in autumn, 101% of normal. In December, Atlantic cyclones brought heavy precipitation to northwestern European Russia, the Urals, southern western Siberia, and the central Krasnoyarsk Territory.

(iii) Notable events

On 14 January, Kazan reached +2.3°C, the warmest for this date since records began in 1880.

During the last five days of January, the city of Magadan received nearly five times its normal monthly precipitation.

On 12 April, strong winds (25–31 m s^{-1}) in Khakassia caused a rapid propagation of natural fires that killed five people and injured 121. The fire destroyed 1205 homes.

On 24–25 June, heavy rain fell in Sochi, with 122 mm of precipitation observed in less than 11 hours. As a result, roads, 2000 houses, and the railroad station were inundated. Damage was estimated to be 760 million rubles (~10 million U.S. dollars). In the city of Adler, 211 mm of precipitation fell in 18 hours; 200 houses, the local airport, and the railroad station were inundated. Damage was estimated to be 10–13 billion rubles (150–195 million U.S. dollars), mostly associated with the temporary closure of the airport.

On 11 July, heavy rain and hail fell in the Ulyanovsk Region, with 31 mm of precipitation falling in 48 minutes. Hail with diameters reaching 5.6 cm damaged roofs, glass panes, and 150 cars.

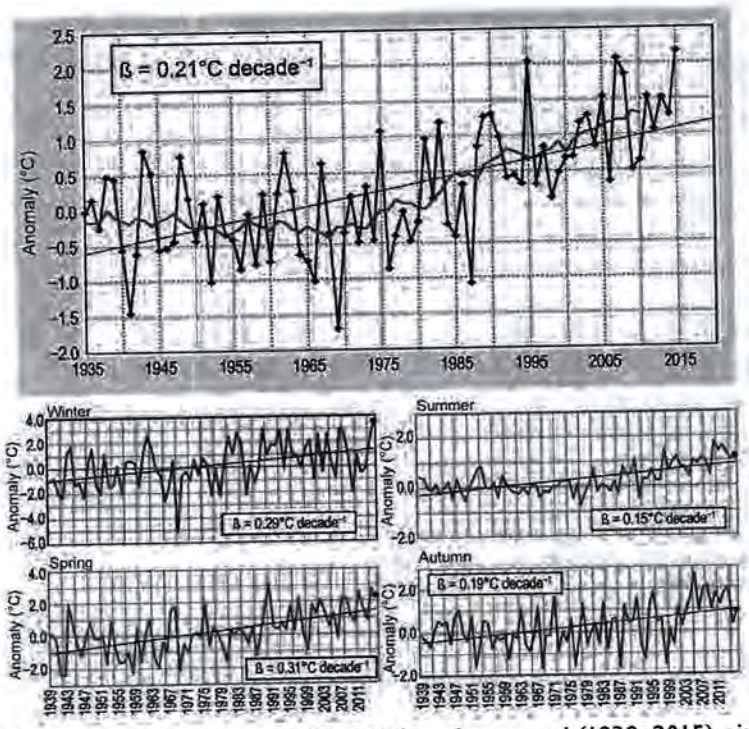

FIG. 7.43. Mean annual (1935–2015) and seasonal (1939–2015) air temperature anomalies (°C) averaged over the Russian territory for 1939–2015 (base period: 1961–90). Seasons are Dec–Feb (winter) 2014/15 and Mar–May (spring), Jun–Aug (summer), and Sep–Nov (autumn) 2015. The smoothed annual mean time series (11-point binomial filter) is shown in red in the top panel.

On 7–8 September, as a result of heavy rain (20 mm in 4 hours), large hail (2.0 cm in diameter), and strong winds (up to 24 m s^{-1}) in Tatarstan, 19 people were injured, 31 cars were damaged, trees were toppled, and roofs were damaged.

3) EAST ASIA—P. Zhang, A. Goto, S.-Y. Yim, and L. Oyunjargal

Countries considered in this section include: China, Japan, Korea, and Mongolia. Unless otherwise noted, anomalies refer to a normal period of 1981–2010.

(i) Temperature

The annual mean temperature over China was 10.5°C, 0.9°C above normal, the highest since records began in 1961. The seasonal mean surface temperature anomalies were +1.1°C, +1.0°C, +0.3°C, and +0.8°C for winter, spring, summer, and autumn, respectively. Annual mean temperatures were above normal across Japan, especially in northern Japan and Okinawa/Amami. In western Japan, temperatures were below normal in summer and autumn but above normal for the year as a whole.

The annual mean surface air temperature over the Republic of Korea was 13.4°C, 0.9°C above normal, the second warmest since national records began in 1973. In 2015, temperatures for most months except summer were higher than normal. May was the warmest on record, at 1.4°C above normal. The annual mean temperature over Mongolia for 2015 was 1.8°C, 1.3°C above normal, the second warmest since national records began in 1961 and 0.8°C warmer than 2014. Most monthly mean temperature anomalies for Mongolia were above normal, ranging from +0.2° to +4.4°C. January was the warmest month in 2015 with respect to departures from average, 4.4°C above normal and marking the warmest January for Mongolia in the 55-year record. Positive anomalies were as high as 5°–7°C in some areas.

(ii) Precipitation

The mean annual total precipitation in China was 648.8 mm, 103% of normal and 2% higher than 2014. The total seasonal precipitation was below normal in winter (94% of normal) and summer (91% of normal), and near-normal in spring but above normal in autumn (126% of normal). In 2015, the major rain belt of China lay south of its normal position, over areas from the middle and lower reaches of the Yangtze River to South China, especially during summer and autumn, associated with a weak East Asian monsoon. Regionally, total annual precipitation was significantly above normal in the Yangtze River basin (112% of normal, the wettest in 17 years) and in the Zhujiang River basin (111% of normal), and below normal in Northeast China (94% of normal), in the Liaohe River basin (86% of normal), and in the Yellow River basin (73% of normal, the driest in 13 years). The rainy season in the Meiyu region started approximately 16 days early on 26 May and ended around 17 days late on 27 July with about 169% of normal precipitation. The rainy season in North China started on 23 July (5 days later than normal) and ended on 17 August (slightly earlier than normal), and was the second driest season in the past 13 years.

In western Japan, annual precipitation amounts were above normal, especially on the Pacific side, since the seasonal northward expansion of the North Pacific subtropical high was weak and convection was often active in summer. On the Pacific side of eastern Japan, annual precipitation amounts were also above normal, including record-breaking rain in September.

SIDEBAR 7.2: EXTREMELY WET CONDITIONS IN JAPAN IN LATE SUMMER 2015

From mid-August to early September 2015, most of western to northern Japan experienced unseasonably wet conditions. Regional average precipitation totals in the 32 days starting on 11 August were 245% and 209% of normal for the Pacific side of western Japan and eastern Japan, respectively. Sunshine duration averaged over the Sea of Japan side of eastern Japan was nearly half the normal amount. Toward the end of the period, record-breaking torrential rainfalls led to large river overflows and flooding in parts of eastern Japan.

The lasting, extremely wet weather conditions were associated with low pressure systems repeatedly forming and migrating eastward along a frontal zone that persisted over the Japanese Archipelago. The persistence of the frontal zone in turn appears related to warm air and vorticity advection in the middle troposphere induced by nearly stationary cyclonic circulation anomalies to the west of Japan (Fif. SB7.4). Meanwhile the northwestern Pacific subtropical high, which would bring hot and sunny days during a normal summer, shifted far southward of its normal position and became a factor in enhancing southwesterly moist air inflow toward Japan in the lower troposphere. These anomalous atmospheric circulation patterns were sustained in connection with suppressed convective activity across the Asian summer monsoon area (Fig. SB7.5), which is consistent with that observed in past El Niño events. Upper tropospheric wave trains propagating from the west across the Eurasian continent may also have played a part in sustaining the cyclonic anomalies to the west of Japan.

A further contribution to the above-normal precipitation amount came from two tropical cyclones during the second week of September. Typhoon Etau made landfall on mainland Japan and Typhoon Kilo passed northward over the Pacific off the coast of Japan, both of which induced moist air inflow and set the environment conducive to torrential rainfalls observed in parts of eastern to northern Japan.

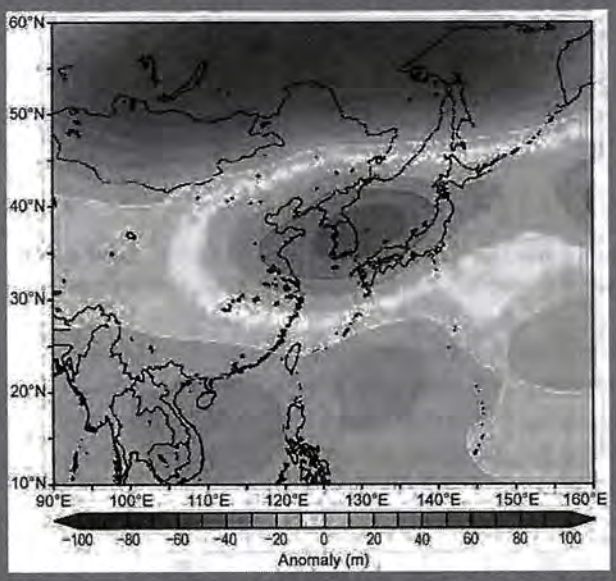

FIG. SB7.4. Geopotential height anomalies (m) at 500 hPa averaged over 11 Aug to 11 Sep, 2015 (base period: 1981–2010). (Source: Japanese 55-year reanalysis.)

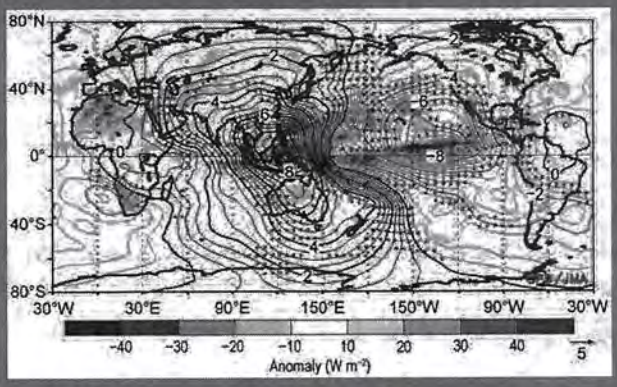

FIG. SB7.5. Velocity potential anomalies at 200 hPa (thick and thin contours at intervals of 2.0×10^6 and 0.5×10^6 m^2 s^{-1}, respectively) and outgoing longwave radiation (OLR; shading) anomalies averaged over the same period as Fig. SB7.4 (base period: 1981–2010). Arrows indicate associated divergent flow, where it is significantly different from climatology. [Source: Japanese 55-year reanalysis (velocity potential) and NOAA/CPC (OLR).]

In the Republic of Korea, the annual total precipitation was 948.2 mm, 72% of normal, the third lowest since national records began in 1973. In Mongolia, the annual average precipitation in 2015 was 202 mm, near normal. However, the temporal and spatial distribution of precipitation was unfavorable for agriculture. At the beginning of the growing season, late June was warmer and drier than normal in Mongolia, resulting in drought and economic losses in the agriculture sector. November was the wettest month of the year and wettest November on record (181% of normal) while July was the driest month of the year (80% of normal). The high November precipitation total included a lot of snowfall, with snow covering at least 80% of Mongolia during the month, making livestock husbandry difficult. Warm conditions in December helped alleviate this somewhat.

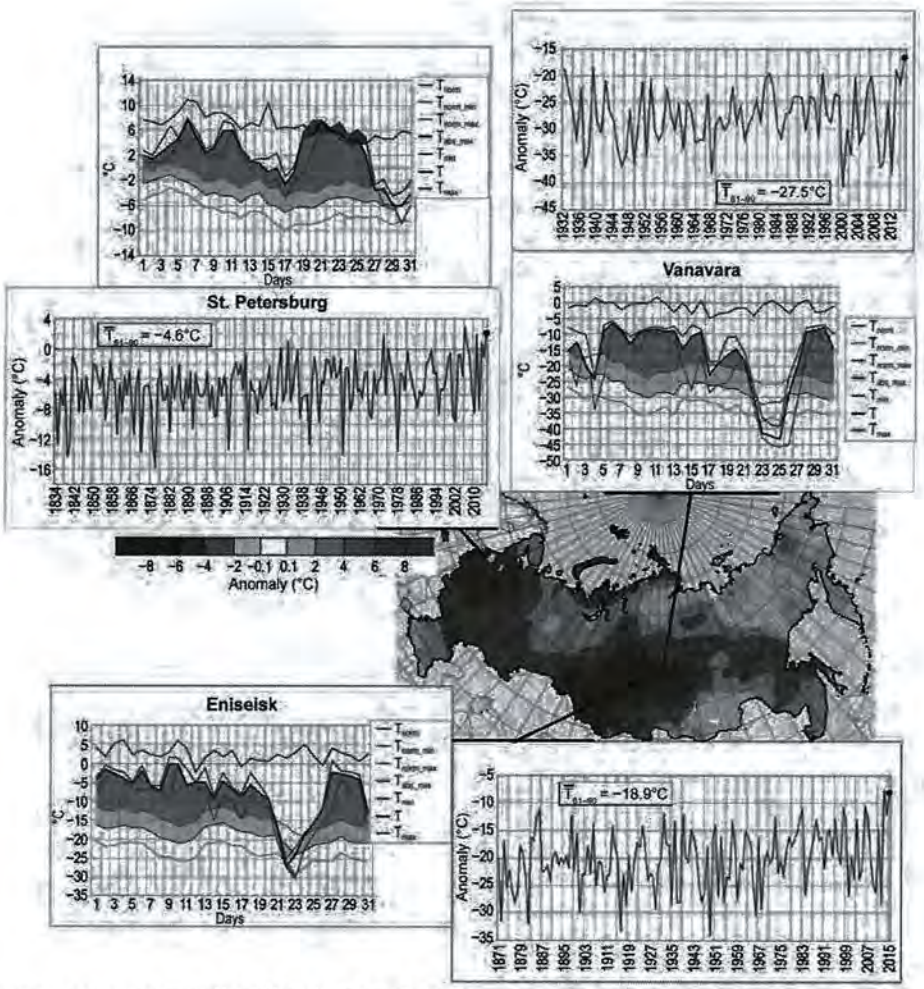

Fig. 7.44. Air temperature anomalies (°C) in Dec 2015. Insets show the time series of mean monthly and mean daily air temperatures (°C) for the month at meteorological stations St. Petersburg, Eniseisk, and Vanavara.

(iii) Notable events

Liaoning province in North China had its driest summer since records began in 1961, which contributed to severe drought in the area. Xinjiang had 25 days of daily maximum temperature exceeding 35°C (normal is 10 days).

In early September, the Kanto and Tohoku regions of Japan experienced record-breaking rainfall, due to warm, moist airflow associated with approaching typhoons Kilo and Etau. Total precipitation during 7–11 September was 647.5 mm at Imaichi in Tochigi Prefecture and 556.0 mm at Hippo in Miyagi Prefecture. Heavy rain caused large river overflows and serious damage.

Typhoon Mujigae in October was the strongest typhoon to make landfall in Guangdong province, China, since records began in 1949. The storm caused a major disaster, with 24 deaths and direct economic losses estimated at over 4.5 billion U.S. dollars (see section 4e4 for more details).

The worst large-scale and persistent haze event over China in 2015 occurred in Huanghuai and North China from late November to early December. It had a maximum extent of 41.7 km^2, with particulate matter smaller than 2.5 μm in diameter (PM2.5) exceeding 150 μg m^{-3} and visibility below 3 km.

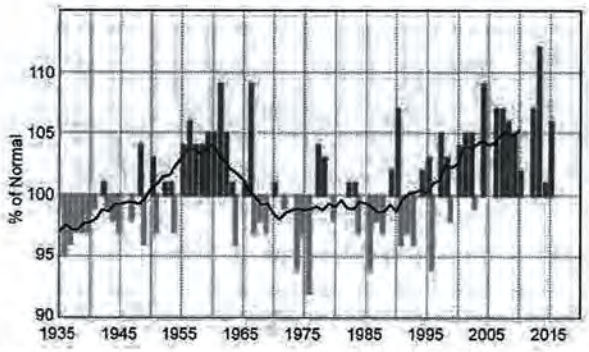

Fig. 7.45. Annual precipitation anomaly (% of normal) averaged over the Russian territory for the period 1935–2015. The smoothed time series (11-point binomial filter) is shown as a continuous line (base period: 1961–90).

4) South Asia—A. K. Srivastava, J. V. Revadekar, and M. Rajeevan

Countries in this section include: Bangaladesh, India, Pakistan, and Sri Lanka. Climate anomalies are relative to the 1961–90 normal. Monsoon precipitation is defined relative to a 50-year base period (1951–2000) because there is strong interdecadal variability in Indian monsoon precipitation (Guhathakurta et al. 2015). In the text below, this is referred to as the long-term average (LTA).

(i) Temperature

South Asia generally experienced well-above-normal temperatures in 2015. The annual mean land surface air temperature averaged over India was 0.7°C above the 1961–90 average, making 2015 the third warmest year since records commenced in 1901 (Fig. 7.46; 2009 and 2010 are warmest and second warmest, respectively). Record warmth was observed during July–September (+0.9°C) and October–December (+1.1°C).

(ii) Precipitation

The summer monsoon set in over Kerala (southern peninsular India) on 5 June, 4 days later than normal, but covered the entire country on 26 June, 20 days ahead of its normal date of 15 July. The pace of advance of the monsoon over different parts of the country was the third fastest in the 1950–2015 period.

Indian summer monsoon rainfall (ISMR) during 2015 was significantly below normal, 86% of its LTA of 890 mm. ISMR during 2015 was characterized by marked spatial and temporal variability. The eastern/northeastern region of the country received normal rainfall overall, with regional variability, while the central, peninsular, and northwestern regions of the country received below-normal rainfall (Fig. 7.47). Rainfall over many parts of northern, western, and central India was less than 70% of the LTA. Rainfall activity was also variable in time. During the first half of the season (1 June–31 July), the country received 95% of the LTA, falling to 77% of the LTA in the second half of the season (1 August–30 September).

During the monsoon season, only 1 meteorological subdivision (West Rajasthan) of 36 received excess rainfall. Eighteen subdivisions received normal rainfall, and the remaining 17 received below-normal rainfall. Except for June, rainfall averaged over the country was below normal on most days during the season (Fig. 7.48).

During winter (January–February), rainfall over the country was 92% of its LTA, while it was above normal (138% of the LTA) during the premonsoon season (March–May). During the post-monsoon season (October–December), it was 77% of the LTA.

The northeast monsoon (NEM) typically sets in over southern peninsular India during October and over Sri Lanka in late November. The NEM generally contributes 30%–50% of the annual rainfall over southern peninsular India and Sri Lanka as a whole. The 2015 NEM seasonal rainfall over southern pen-

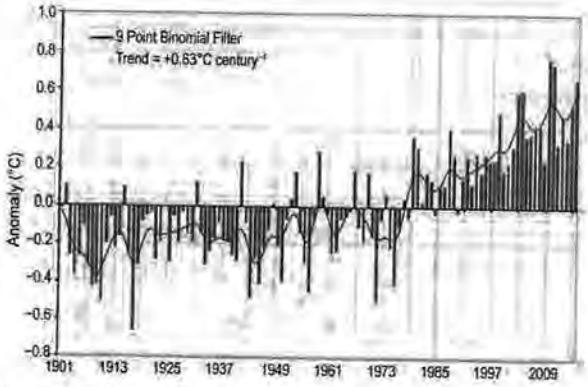

Fig. 7.46. Annual mean temperature anomalies (base period: 1961–90) averaged over India for the period 1901–2015. The smoothed time series (9-point binomial filter) is shown as a continuous line.

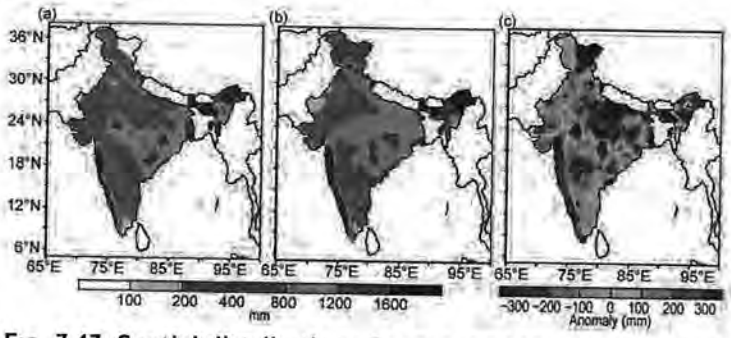

Fig. 7.47. Spatial distribution of monsoon seasonal (Jun–Sep) rainfall (mm) over India in 2015 for (a) observed rainfall, (b) normal rainfall, and (c) the difference between (a) and (b).

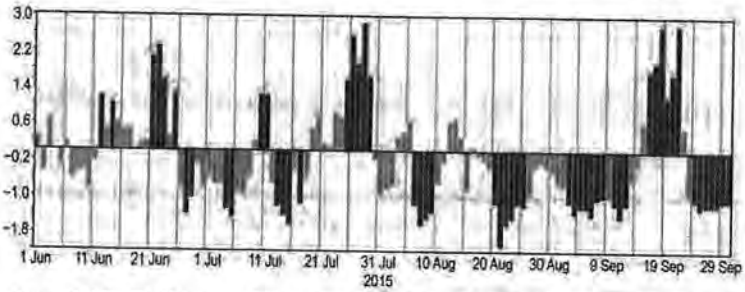

Fig. 7.48. Daily standardized rainfall time series averaged over the monsoon core zone over India (1 Jun–30 Sep).

insular India and Sri Lanka was above normal (132% of the LTA). Sri Lanka received below-normal rainfall during its summer monsoon season (May–September). However, northeast monsoon rainfall activity over the island nation during October–December was enhanced.

Pakistan, at the western edge of the pluvial region of the South Asian monsoon, generally receives 60%–70% of its annual rainfall during its summer monsoon season (July–September). In 2015, summer monsoon rainfall over Pakistan was 117% of the LTA and was marked by spatial and temporal variability. Southwestern/southern Pakistan received below-normal rainfall, while other regions received normal or above-normal rainfall during the season. Bangladesh also received above-normal rainfall overall during its summer monsoon season.

(iii) Notable events

A severe Nor'wester (a line of strong thunderstorms) affected 12 districts of Bihar (eastern India) during the nighttime/early morning hours of 22–23 April. Over 50 lives were lost.

Heat wave conditions prevailed over central, peninsular, and northern parts of India during the second half of May. Maximum temperatures were more than 5°C above normal at many eastern and central stations for several days. Some stations in Odissa and coastal Andhra Pradesh reported temperatures of near 47°C during 23–26 May. Overall, the intense heat over central and peninsular parts of the country during May took a toll of around 2500 lives, and more than 2000 deaths were reported in the south Indian states of Telangana and Andhra Pradesh.

One of the most severe heat waves since 1980 affected Karachi, Pakistan, during the second half of June and took a toll of more than 1000 lives. Temperatures reached 44°C for two days during the period. The heat wave coincided with the beginning of the holy month of Ramadan, when many Muslims do not eat or drink during daylight hours, increasing susceptibility to heat stroke.

During 25–26 June, heavy rain and floods associated with a deep depression over the Arabian Sea took a toll of more than 80 lives in Gujarat in western India.

Floods caused about 70 deaths in West Bengal (eastern India) during 30 July–5 August.

Many parts of Bangladesh experienced severe floods from late June through the first week of August. An estimated 30 people were killed and around one million were affected.

Very heavy rainfall during an active period of the NEM during 9–17 November and 2–5 December led to more than 350 fatalities in Tamil Nadu (southernmost India) and more than 50 deaths in the adjoining state of Andhra Pradesh. Heavy rainfall and flooding affected around 1.8 million people in Tamil Nadu. Tambaram (near Chennai) reported an all-time 24-h record rainfall of 490 mm on 2 December, while Chennai reported 345 mm of rain on the same day. Economic loss due to these events was estimated to be around 2 billion rupees (~29 million U.S. dollars).

Northeast monsoon activity during the first week of December also led to floods in Sri Lanka, which caused 40 deaths and displaced more than 1.2 million residents.

5) SOUTHWEST ASIA—F. Rahimzadeh, M. Khoshkam, S. Fateh, and A. Kazemi

This subsection currently covers only Iran. Turkey is incorporated in the Europe subsection. Climate anomalies are relative to the 1981–2010 normal.

(i) Temperature

Winter 2014/15 and spring 2015 were considerably warmer than normal, with anomalies up to +6.4°C during winter. Most of the country was also warmer than normal in summer and near-normal overall in autumn (Fig. 7.49).

(ii) Precipitation

Generally, in 2015, Iran experienced drier-than-normal conditions in winter and spring, while summer and autumn were wetter than normal (Fig. 7.50).

During winter 2014/15, 30%–90% of normal precipitation fell across most parts of the country. Areas with average or above-average rainfall (up to 170% of normal) were confined to a small part in the northwest of the country adjacent to the Turkish border and a small part in the southeast. During spring, precipitation amounts were 30%–90% of normal across most of the country. The middle of the country received more than 90% of normal precipitation.

In summer, most of the country experienced normal or above-normal precipitation (90%–170% of normal). During autumn, precipitation was more than 90% of normal in much of the northern and southern regions, while the rest of country received 30%–90% of normal.

(iii) Notable events

Significant dust storms during spring and summer spread over many parts of the country, especially southern and southwestern Iran.

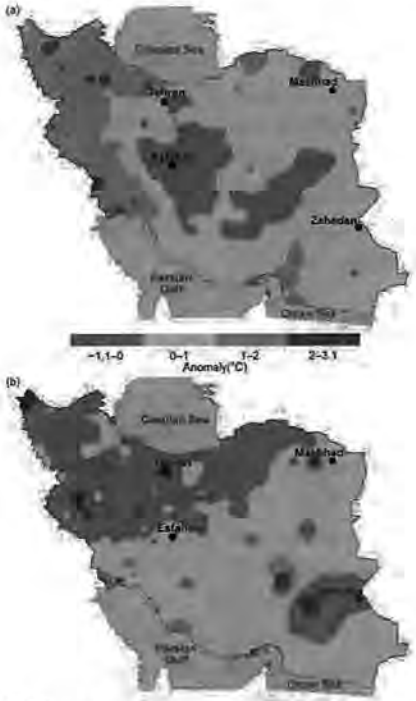

Fig. 7.49. Seasonal mean surface temperature anomalies (°C) in (a) summer (Jun–Aug) and (b) autumn (Sep–Nov). (Source: I.R. of Iran Meteorological Organization & National Center for Drought and Disaster Risk Management.)

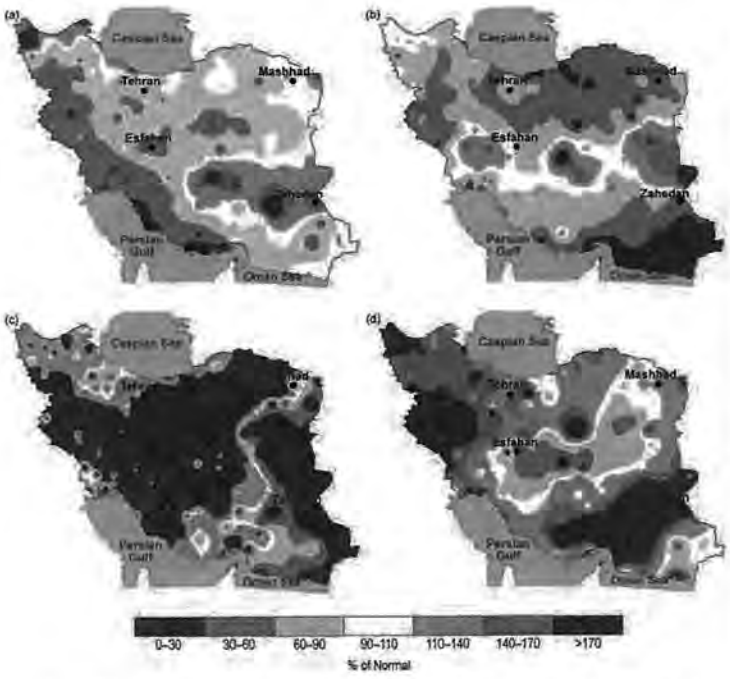

Fig. 7.50. Observed precipitation over Iran (% of normal) for (a) winter (Dec–Feb 2014/15), (b) spring (Mar–May), (c) summer (Jun–Aug), and (d) autumn (Sep–Nov). (Source: I.R. of Iran Meteorological Organization.)

h. Oceania

1) Overview—J. A. Renwick

During the first half of 2015, substantial warming of the equatorial Pacific sea surface and subsurface waters clearly signaled the arrival of El Niño. Extremes typical of El Niño onset were observed across the region, including rainfall extremes and an abundance of early-season tropical cyclones.

Following warm SSTs in the central and eastern equatorial Pacific in 2014 that almost reached El Niño thresholds (defined by NOAA as +0.5°C SST anomaly in the Niño-3.4 region for three consecutive months), El Niño became established in spring (March–May) 2015 and evolved into one of the strongest such events on record (alongside 1972/73, 1982/83, and 1997/98; see section 4b). El Niño–associated air temperature and rainfall patterns were observed across most of the South Pacific in 2015. A number of South Pacific countries experienced agricultural and/or hydrological drought.

Temperatures were generally above normal in Australasia, with Australia having another warm year, especially in the spring (Sidebar 7.3). Precipitation totals for 2015 were generally near-normal for both Australia and New Zealand. The southern annular mode (SAM) was generally positive through much of 2015, becoming strongly positive at the end of the year (www.cpc.ncep.noaa.gov/products/precip/CWlink/daily_ao_index/aao/month_aao_index.shtml). The base period used throughout this section is 1981–2010, unless otherwise indicated.

2) Northwest Pacific and Micronesia—M. A. Lander and C. P. Guard

This assessment covers the area from the international date line west to 130°E, between the equator and 20°N. It includes the U.S.-affiliated islands of Micronesia, but excludes the western islands of Kiribati and nearby northeastern islands of Indonesia.

(i) Temperature

Temperatures across Micronesia in 2015 were mostly above average. The warmth was persistent, with above-average temperatures occurring during most or all of the year. Only Yap Island had a substantial negative departure for any of the time periods summarized in Table 7.5. At islands located in the west of the region (e.g., Palau, Yap, Guam, and Saipan) there was a tendency for daytime maximum temperature anomalies to be greater than those of nighttime minima. In the east (Chuuk to Kosrae and Majuro), the reverse pattern was observed, as also seen in 2014. Average monthly maximum and minimum temperatures across most of Micronesia

have gradually increased for several decades, with a total rise in average temperature on par with the global average increase of +0.74°C in the last century (Guard and Lander 2012).

(ii) Precipitation

Dryness was observed across the Republic of the Marshall Islands (RMI) during early 2015, with very low rainfall totals reported at Utirik and Wotje in the northern RMI during January and February. However, rainfall throughout the RMI had a dramatic rebound to very wet conditions during March and April, even at the normally driest of the atolls in the north (e.g., Kwajalein, Utirik, and Wotje). Very wet conditions in the Marshall Islands typically occur in late winter and spring during years of El Niño onset. Dryness associated with El Niño typically begins earlier in the western bounds of Micronesia (e.g., Palau) and spreads eastward later in the year to the RMI. Meanwhile, locations in the far west of Micronesia experienced an early onset of dry conditions that became extreme late in the year.

Annual totals during 2015 were mostly higher than average, with early wetness outweighing dryness later in the year. The 2015 fourth quarter rainfall totals at Yap Island and at Palau were the lowest and second lowest in their ~65-year post-World War II historical record, respectively. By late December 2015, persistent dry conditions were becoming established at most of the islands of Micronesia. The 6-month and annual rainfall values for selected locations across Micronesia are summarized in Table 7.5.

(iii) Notable events

Micronesia was the overwhelming focus of the 2015 western North Pacific typhoon track distribution, with Guam at the primary nexus, by virtue of the passage of 12 named tropical cyclones within 550 km (see section 4e8 for more detail).

After nearly a decade of high values, sea level across Micronesia began to fall in 2014 and continued to fall dramatically in 2015 (Fig. 7.51). The maximum drop in monthly mean sea level (since 2013) at both Guam and at Kwajalein was approximately 40 cm (the drop in 12-month means was around 25 cm). A sharp drop in mean sea level typically occurs during El Niño, with the lowest sea level occurring in December of the year of the El Niño peak.

Table 7.5. Temperature and rainfall anomalies for selected Micronesia locations during 2015, (base period: 1981–2010). Latitudes and longitudes are approximate. "Kapinga" stands for Kapingamarangi Atoll in Pohnpei State, Federated States of Micronesia.

Location	Max/Min Temp Anomaly		Precipitation					
	Jan–Jun °C	Jul–Dec °C	Jan–Jun mm	Jan–Jun % of avg.	Jul–Dec mm	Jul–Dec %	Year mm	Year %
Saipan 15°N,146°E	+1.92 +1.04	+1.83 +1.46	570.0	126.9	**939.3**	71.0	**1509.3**	85.2
Guam 13°N,145°E	+0.40 −0.06	+0.58 +0.37	881.6	127.5	**2058.4**	115.1	**2940.1**	118.5
Yap 9°N,138°E	−1.44 −0.29	−0.30 +0.25	**1319.5**	112.8	**1818.9**	95.6	**3138.4**	102.2
Palau 7°N,134°E	+0.96 +0.03	+1.00 +0.31	**1185.2**	69.0	**1265.9**	62.3	**2451.1**	65.4
Chuuk 7°N,152°E	+0.31 +0.48	+0.28 +0.97	**2147.8**	135.6	**1823.0**	99.4	**3970.8**	116.2
Pohnpei 7°N,158°E	+0.18 +0.10	−0.10 +0.78	**3039.4**	134.1	**2470.9**	105.8	**5510.3**	119.7
Kapinga 1°N,155°E	N/A	N/A	**2411.7**	137.7	**1486.9**	98.4	**3261.4**	119.5
Kosrae 5°N,163°E	+0.38 +1.29	−0.21 +1.34	**2552.5**	99.4	**2007.6**	85.7	**4560.1**	92.9
Majuro 7°N,171°E	+0.01 +0.91	−0.03 +1.17	**1854.7**	135.5	**1713.5**	91.7	**3568.2**	110.2
Kwajalein 9°N,168°E	+0.37 +0.09	+0.22 +0.32	**1737.1**	216.8	**1593.6**	100.9	**3330.7**	139.9

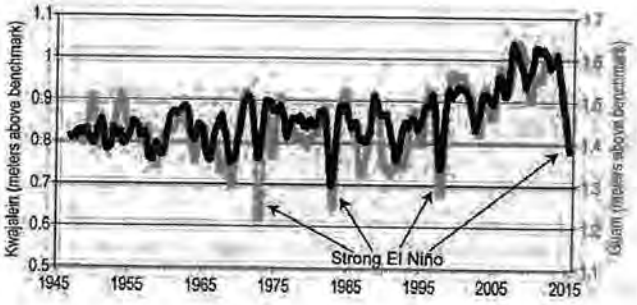

FIG. 7.51. Observed sea level rise/fall (12-month moving average) over the period 1945–2015 at Kwajalein (black, left vertical axis) and Guam (gray, right vertical axis).

3) SOUTHWEST PACIFIC—E. Chandler and S. McGree

Countries considered in this section include: American Samoa, Cook Islands, Fiji, French Polynesia, Kiribati, New Caledonia, Niue, Papua New Guinea (PNG), Samoa, Solomon Islands, Tokelau, Tonga, Tuvalu, and Vanuatu. Air temperature and rainfall anomalies are relative to the 1981–2010 period.

(i) Temperature

Mean air temperatures in 2015 (derived from NCEP–NCAR reanalysis) were strongly influenced by El Niño, which dominated the climate of the South Pacific during the year. Temperatures were near normal or above normal between January and March (Fig. 7.52a) across much of the southwest Pacific. Positive anomalies peaked at around +1.3°C near the equatorial date line. Below-average temperatures occurred near PNG, with anomalies up to −1.5°C over a small region covering the PNG Islands.

Positive temperature anomalies centered on the equator expanded westward towards the Solomon Islands and strengthened during the second quarter (Fig. 7.52b). The largest positive anomalies over central Kiribati exceeded +1.2°C. Negative anomalies persisted over the PNG Islands, while a large area of negative anomalies covered Vanuatu, Fiji, Tonga, and Niue during April–June, associated with cool surrounding ocean. Temperatures were within 0.3°C of average around the Solomon Islands, New Caledonia, Samoa, Tuvalu, and parts of French Polynesia.

The temperature anomaly pattern from April to June persisted into the third quarter with negative anomalies strengthening in the south (Fig. 7.52c). By the end of September, the characteristic El Niño signal was established: positive anomalies dominated the equatorial region, southwest of which was a band of negative anomalies aligned northwest–southeast. A narrow strip of near-average temperatures was sandwiched between the two major anomaly features.

Below-normal air temperatures near the PNG Islands persisted into the last three months of the year, although the band of negative anomalies stretching southeast from PNG through Fiji to the southern Cook Islands weakened considerably in the last quarter (Fig. 7.52d). In contrast, positive anomalies intensified along the equator and expanded southward to encompass northern French Polynesia.

(ii) Precipitation

In addition to ENSO, key climate features in the southwest Pacific are the west Pacific Monsoon (WPM), which lies over the west Pacific warm pool, the South Pacific convergence zone (SPCZ) aligned northwest–southeast in the southwest Pacific, and the subtropical high pressure belt which is part of the Hadley Circulation.

Due mainly to enhanced activity in the WPM and SPCZ, the year began with above-normal rainfall recorded during January–March in many western places and the Cook Islands (Table 7.6). High rainfall in central Vanuatu was associated with Tropical

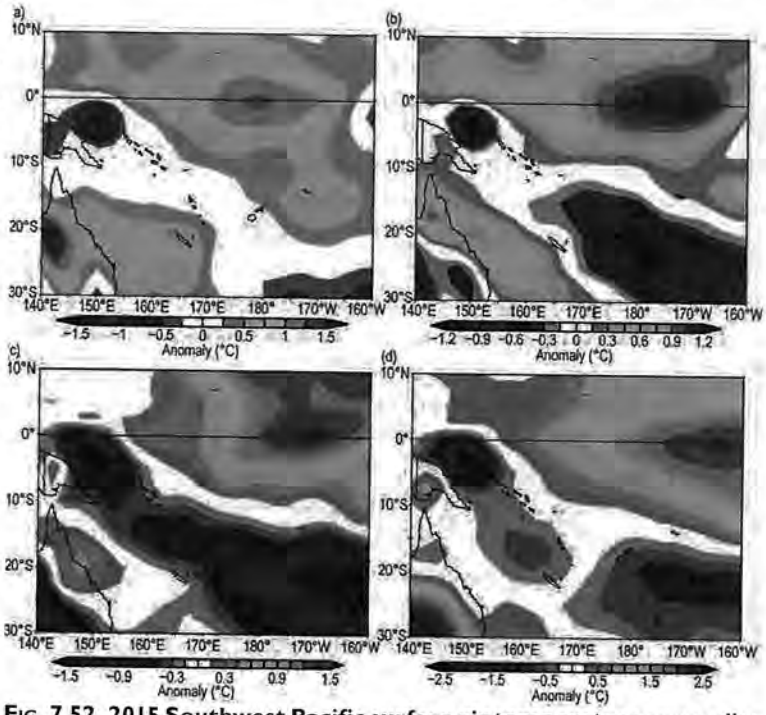

FIG. 7.52. 2015 Southwest Pacific surface air temperature anomalies from NCEP–NCAR reanalysis (°C; 1981–2010 base period); for (a) Jan–Mar, (b) Apr–Jun, (c) Jul–Sep, and (d) Oct–Dec.

Table 7.6. Observed 2015 rainfall relative to base period at capital towns/cities in the South Pacific.

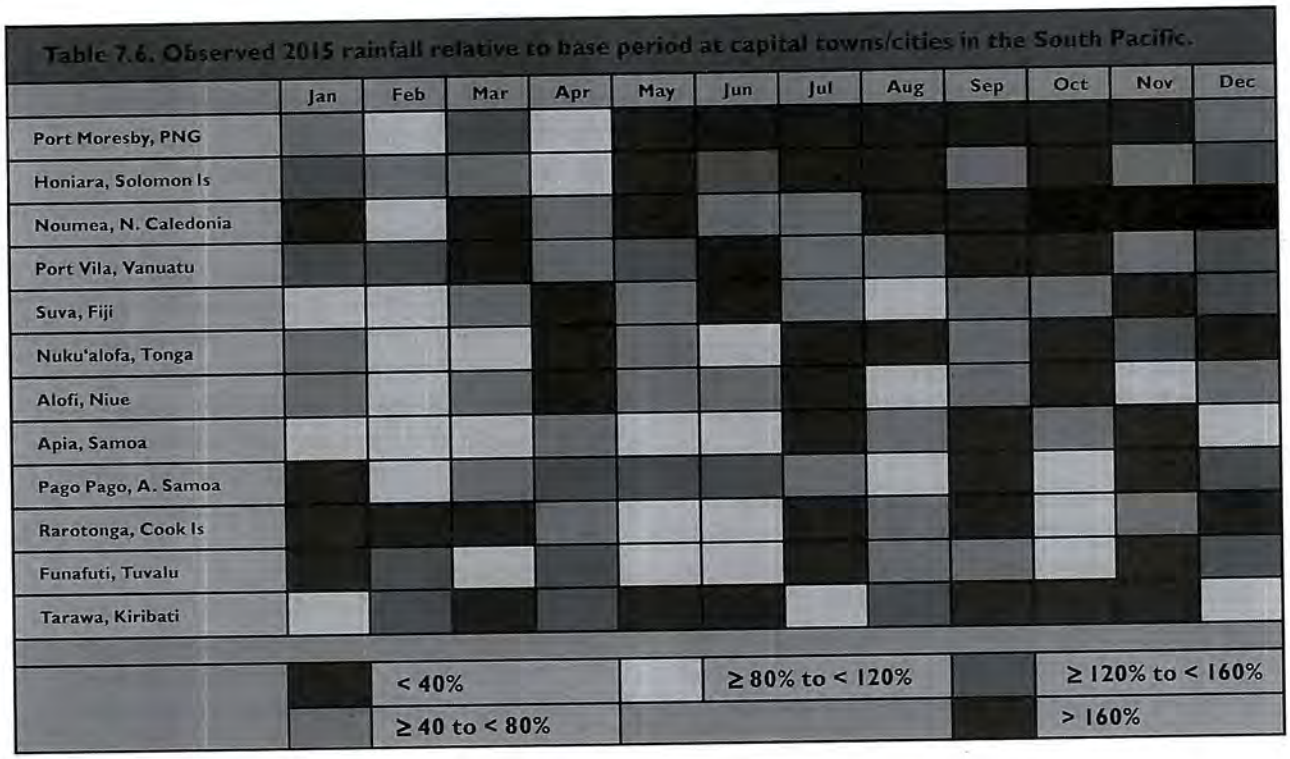

Cyclone Pam (see Notable events and section 4e8 for more details). Below-normal rainfall was recorded in the New Guinea Islands, northern and southern Vanuatu, southern Tuvalu, Fiji, northern Tonga, Niue, northern French Polynesia, and parts of Samoa. At Pekoa and Lamap in northern Vanuatu, January–March was second (out of 45 years of record) and fourth (out of 54 years of record) driest, respectively.

In the second quarter the SPCZ was displaced to the northeast. Rainfall was below normal in parts of PNG, Vanuatu, Fiji, Tonga, Niue, the Cook Islands, and French Polynesia. In contrast to typical El Niño conditions, the northern Cook Islands were drier than normal. At Suva (Fiji), April–June was the driest since 1942. Kiritimati (eastern) and Tarawa (western) Kiribati recorded their wettest and third wettest April–June respectively, with rainfall in excess of 1100 mm received across the country.

The extent of suppressed rainfall in the southwest Pacific expanded over the third quarter (July–September) to include most of PNG and most of the islands southwest of the SPCZ. Above-normal rainfall continued in the Kiribati, Tuvalu, and Tokelau region. Rainfall was strongly suppressed in the far western Pacific, with enhanced convection in the equatorial Pacific east of the Solomon Islands, a pattern typical of El Niño.

In the fourth quarter, the SPCZ continued to be displaced to the northeast. The central Pacific remained wetter or much wetter than average, with the region of enhanced rainfall extending to the northern Cook Islands and northern French Polynesia in November. Most islands between PNG and southern French Polynesia, with the exception of the Solomon Islands and Samoa, received below-normal rainfall. Rainfall for October–December at Garoka in the PNG highlands was the lowest in 45 years and second and third lowest at Momote and Wewak, respectively. Very low rainfall was also observed in western and southeastern Fiji, southern Cook Islands, and central Tonga.

(iii) Notable events

On 6 March, Tropical Disturbance 11F developed about 1140 km to the northwest of Nadi, Fiji. The disturbance was upgraded to a tropical depression two days later, then named Pam on 9 March. Located in an area of favorable conditions, Pam gradually intensified and became a Category 5 severe tropical cyclone on 12 March. Pam's 10-min maximum sustained winds peaked at 135 kt (69 m s^{-1}), along with a minimum pressure of 896 hPa, making Pam the most intense TC of the southwest Pacific basin since Zoe in 2002 (and third most intense storm in the Southern Hemisphere, after Zoe in 2002 and Gafilo in 2004). In addition, Pam had the highest 10-minute sustained wind speed recorded of any South Pacific TC. The center of Pam passed just east of Efate where the capital Port Vila is located (Fig. 7.53), and Erromango and Tanna suffered a direct hit, making Pam the single worst natural di-

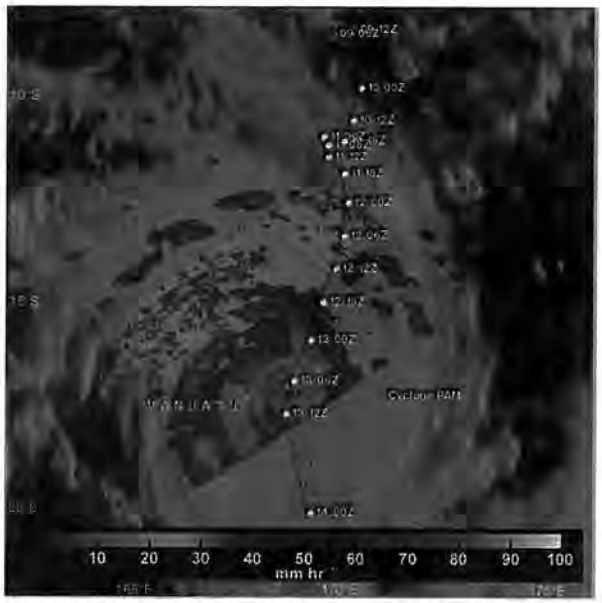

FIG. 7.53. Tropical Rainfall Measuring Mission (TRMM) satellite over Cyclone Pam on 13 March 2015 UTC. The image shows the cyclone track and a rainfall analysis from TRMM's Microwave Imager (TMI) and Precipitation Radar (PR) instruments. Rainfall in part of the cyclone was measured by TRMM PR at more than 119mmh^{-1}.(Source:trmm.gsfc.nasa.gov/trmm_rain/Events/pam_trmm_tmi_pr_13_march_2015_0923_utc.jpg.)

saster in the history of Vanuatu. The cyclone crippled infrastructure, with an estimated 90% of Vanuatu's buildings impacted by the storm. Communications were devastated and there was a shortage of water for several days following the storm. At least 132000 people were affected by Pam, including 54000 children. There were at least 15 fatalities.

4) AUSTRALIA—C. Ganter and S. Tobin

The information presented here has been prepared using the homogenized Australian temperature dataset (ACORN-SAT) for area-averaged temperature values and the observational dataset (AWAP) for area-averaged rainfall values and mapped analyses for both temperature and rainfall. See www.bom.gov.au/climate/change/acorn-sat/ and www.bom.gov.au/climate/maps/#tabs=About-maps-and-data for more information.

(i) Temperature

Australia's annual mean temperature for 2015 was 0.83°C above the 1961–90 average, making it the fifth warmest year since national observations commenced in 1910. Eight of Australia's ten warmest years have occurred since 2002, with the most recent three years among the five warmest. In 2015, Western Australia, Queensland, Victoria, South Australia, and New South Wales all observed one of their ten warmest years on record.

The Australian annual mean maximum temperature (Fig. 7.54) was 0.96°C above average, and annual mean minimum temperature (Fig. 7.55) was 0.69°C above average; both sixth highest on record. Several exceptional warm spells occurred during 2015, with an especially warm October–December (see Notable events and Sidebar 7.3 for more details). April and May were the only months in which national mean temperatures were below average.

Annual maxima were in the highest decile (top 10%) of the historical distribution (since 1900) for the north of the Northern Territory, most of Queensland and Victoria, southeast and western South Australia, and large areas of Western Australia (highest on record for part of southwest Western Australia). Annual anomalies of +1.5°C to +2.0°C were observed in the southwest and southern interior of Western Australia and over a large area of southwestern to central Queensland.

Annual minima were also in the highest 10% of historical observations for most of Western Australia, large parts of Queensland, western South Australia, areas of New South Wales, and far eastern Victoria. Annual minima were near-average for most of the Northern Territory, northeastern Western Australia, other smaller areas in western Tasmania, the northern Cape York Peninsula and near Rockhampton in Queensland, and pockets of the southern half of

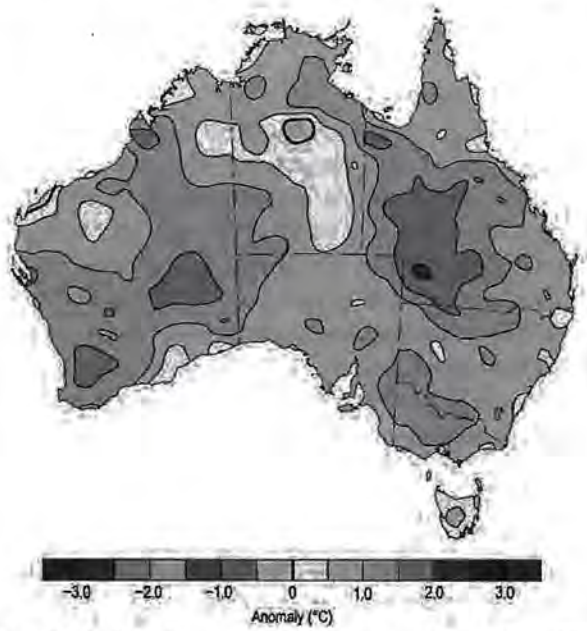

FIG. 7.54. Maximum temperature anomalies (°C) for Australia, averaged over 2015, relative to a 1961–90 base period. (Source: Australia Bureau of Meteorology.)

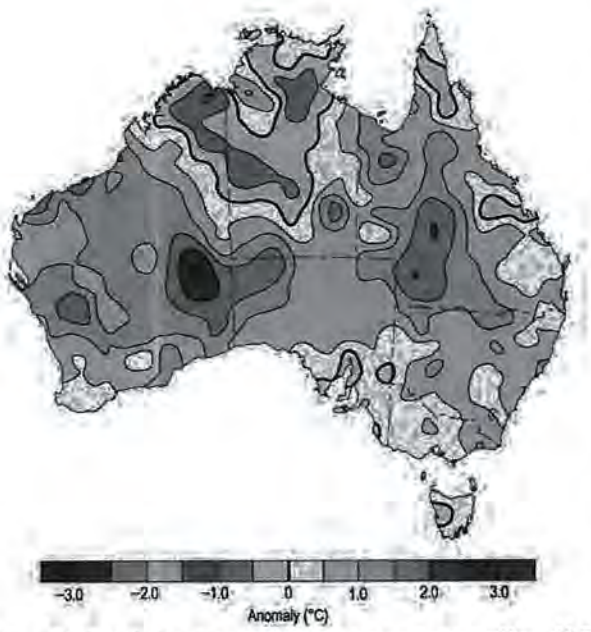

Fig. 7.55. Minimum temperature anomalies (°C) for Australia, averaged over 2015, relative to a 1961–90 base period. (Source: Australia Bureau of Meteorology.)

South Australia. They were cooler than average for some areas of the Northern Territory and northern Western Australia. Large areas of Western Australia and the western half of Queensland observed anomalies in excess of +1.0°C, rising to more than +2.0°C in the southeastern interior of Western Australia. Cool anomalies within 1°C of average were observed over the northern Kimberley and large parts of the Northern Territory.

(ii) Precipitation

Rainfall averaged across Australia for 2015 was 445.8 mm, or 96% of the 1961–90 average, the 59th driest year since records commenced in 1900 and close to the median. The near-average national total masks some regional differences. Notable areas of below-average rainfall were recorded in the southwest of Western Australia, large areas of southwest to central Queensland, and large areas of the southeast, extending from Tasmania through Victoria and into South Australia. Above-average precipitation was recorded in the Pilbara and Gascoyne regions of Western Australia, and across most of the Northern Territory extending into northern South Australia. Scattered parts of the eastern seaboard, extending from Victoria to southern Queensland, also had above-average precipitation for the year (Fig. 7.56).

State-wise, only Western Australia and the Northern Territory had above-average precipitation for the year, but within 20% of their annual total. All other states had below-average rainfall, with Victoria 14th driest and Tasmania 8th driest; both experiencing their driest year since the 2006 El Niño year. For Victoria, 16 of the last 19 years (1997–2015) have brought below-average rainfall with similar, though not quite as persistent, runs in other parts of southern Australia (e.g., southeastern Australia, 13 of the last 19 years).

Large parts of eastern Australia commenced the year with continuing long-term rainfall deficiencies (on the two- to three-year scale). These deficiencies persisted across much of inland Queensland in 2015, while drought increased through Victoria and southeast South Australia, and also emerged in Tasmania and southwest Western Australia. The deficiencies echo long-term declines in cool-season rainfall across southern Australia and poor wet-season rainfall in Queensland over three successive years.

After a wet January, much of northern and central Australia was very dry from February onwards, marking a dry end to the northern Australian wet season (October–April).

The combination of a strong El Niño and a record warm Indian Ocean (see section 4b) is an unusual set of climate drivers, and for Australia the presence of a very warm Indian Ocean appears to have limited the broad-scale rainfall anomalies in the cooler part of the year in inland southern and eastern Australia. However, southwest Western Australia recorded its second driest May–July while Victoria and southern South Australia were also dry, but to a lesser extent.

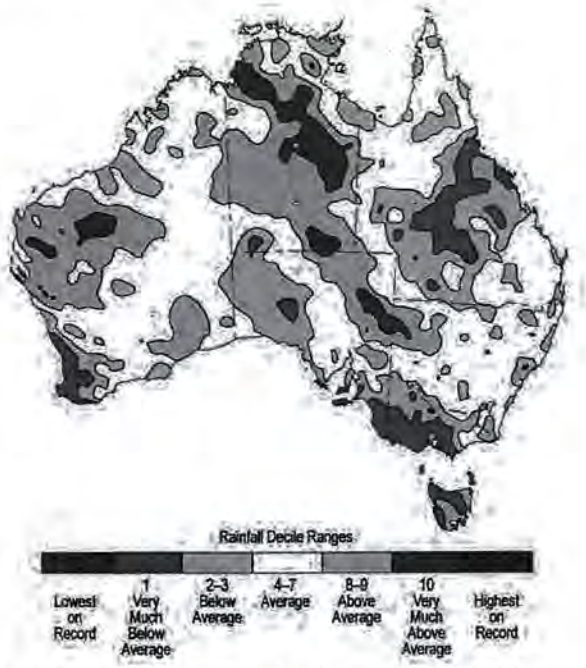

Fig. 7.56. Rainfall deciles for Australia for 2015, based on the 1900–2015 distribution. (Source: Australia Bureau of Meteorology.)

A late-developing positive Indian Ocean dipole was associated with a very dry September–October, which had significant impacts on agricultural production in southern areas. December closed the year with heavy rainfall over large parts of the north.

(iii) Notable events

An exceptional heat wave affected large parts of northern and central Australia during March, with prolonged heat peaking on the 19th and 20th. The other most notable heat waves occurred during the last three months of the year—record early-season heat across southern Australia in early October, contributing to Australia's warmest October on record and extreme heat in much of southeastern Australia in the third week of December (see Sidebar 7.3 for more detail).

Many significant bushfires occurred during the year. The most destructive, in terms of property loss or total area burned, are described below:

- Early January, South Australia's Mount Lofty Ranges, 27 houses destroyed and 20 000 hectares burned;
- Late January and early February, southwest Western Australia, 150 000 hectares burned—the most significant fires for the region in many decades;
- 15–21 November, around Esperance in Western Australia, 145 000 hectares burned;
- 25–27 November, South Australia's Mid North, at least 87 houses at Pinery (north of Adelaide) severely damaged or destroyed and 90 000 hectares burned;
- 25 December, near Lorne on Victoria's southwest coast, 116 homes and holiday houses destroyed at Wye River and Separation Creek.

Two east coast lows brought significant damage. The first caused severe weather and flooding in coastal New South Wales between 20 and 23 April, with 12 regions declared natural disaster areas and several deaths reported due to flash flooding at Dungog. The second low produced heavy rain and damaging winds over southeast Queensland and parts of New South Wales between 1 and 4 May.

A significant, but far from record-breaking, cold outbreak over southeastern Australia during 11–17 July brought widespread snow along the Great Dividing Range, extending from the hills east of Melbourne into southern Queensland. This was the most significant snow event in Queensland since 1984.

Four tropical cyclones made landfall in Australia during 2015: Lam, Marcia, Nathan, and Olwyn with a fifth, Quang, weakening below cyclone intensity just prior to landfall. Marcia was the strongest at landfall (Category 5) and the most intense known tropical cyclone so far south on the east coast [maximum 10-minute sustained winds of 110 kt (57 m s^{-1}), crossing near Yeppoon, and causing damage as far south as Bundaberg]. Lam made landfall in the eastern Top End on the same day, 20 February—the first time in recorded history that two severe tropical cyclones made landfall in Australia on the same day (see also section 4e7).

For further detail on these and other significant events please see the Monthly Weather Reviews, Annual Climate Statement, and Annual Climate Report available from www.bom.gov.au/climate/current/.

5) New Zealand—N. Fedaeff

In the following discussion, the base period is 1981–2010 for all variables, unless otherwise noted. The nation wide average temperature is based upon the National Institute of Water and Atmospheric Research (NIWA) seven-station temperature series that begins in 1909 (www.niwa.co.nz/our-science/climate/information-and-resources/nz-temp-record/seven-station-series-temperature-data). All statistics are based on data available as of 8 January 2016.

(i) Temperature

New Zealand had a relatively mild 2015, with annual mean temperatures within 0.5°C of the annual average across much of the country (Fig. 7.57).

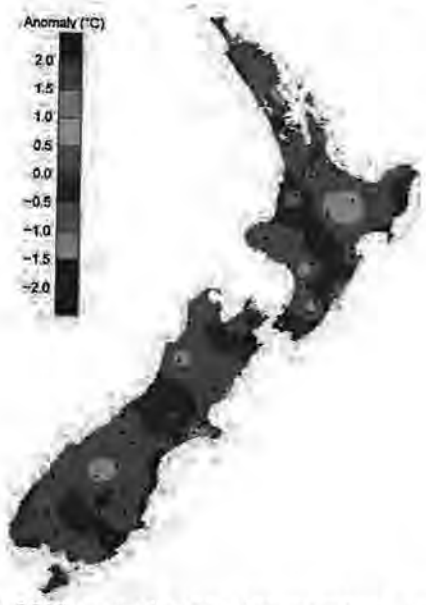

Fig. 7.57. 2015 annual mean temperature anomalies (°C) relative to 1981–2010 normal. Dots show observing station locations. (Source: NIWA.)

SIDEBAR 7.3: AUSTRALIA'S WARM RIDE TO END 2015

The last three months of 2015 saw a very warm end to the year for Australia. It was the warmest October on record with respect to both maximum and minimum temperatures, with the October mean temperature anomaly of +2.89°C the largest anomaly on record for Australia for any month in 106 years of records. Maximum temperatures for October in Victoria, South Australia, and New South Wales were close to values typical of an average December, with monthly anomalies of more than +5°C for the three states (Fig. SB7.6).

October's most significant daily extremes occurred in the first half of the month. Significantly high daytime temperatures occurred in southwest Western Australia beginning 1 October, spreading eastwards and peaking in extent during 4–6 October in the southeast; each day, some part of southern Australia had daily anomalies in excess of +12°C. Another bout of extreme heat occurred over southern Western Australia from 8 to 13 October. Later in the month, there were several other periods which had temperatures well above average, but no individual event in the latter part of October surpassed the extremes of the first 10 days (www.bom.gov.au/climate/current/statements/scs52.pdf).

November mean temperatures were the third warmest on record and, overall, spring 2015 was second warmest on record. The most recent three springs were the three warmest, with 2014 remaining the warmest on record.

The last notable warm period for the year occurred in December. Following a consistently warm first half of December for the southeast interior of Australia, a burst of more extreme warmth occurred in mid-December over South Australia. Adelaide reached 40°C each day during 16–19 December—the first time this has occurred in Adelaide in December (previous earliest run of four or more days of at least 40°C was 3–6 January in 1906). Heat peaked for this event on 19 December in South Australia and western Victoria ahead of a front, with the cool change passing through southeast Australia on 20 December. Individual daytime and nighttime December records were set on the 19th and 20th across South Australia, Victoria, New South Wales, and Tasmania (Fig. SB7.7). Mildura measured a minimum of 31.9°C on 20 December. This was a new record high minimum temperature for a Victorian site for any month, surpassing 30.9°C also at Mildura on 24 January 2001. A number of other locations in northern Victoria experienced their hottest night on record for any month (www.bom.gov.au/climate/current/statements/scs53.pdf).

Overall, October–December was the warmest such period on record, with a mean temperature anomaly of +1.93°C. It also tied with July–September 2013 for highest positive anomaly for any three month period.

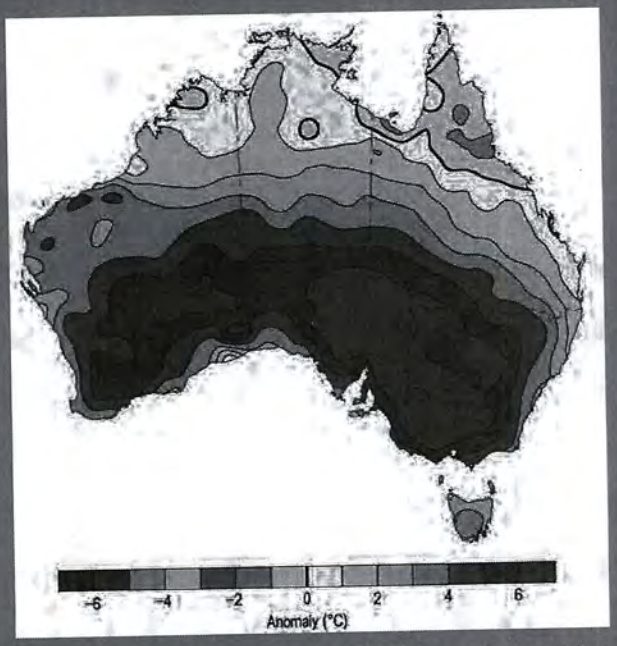

FIG. SB7.6. Maximum temperature anomalies for Oct 2015 for Australia (1961–90 base period). (Source: Australia Bureau of Meteorology.)

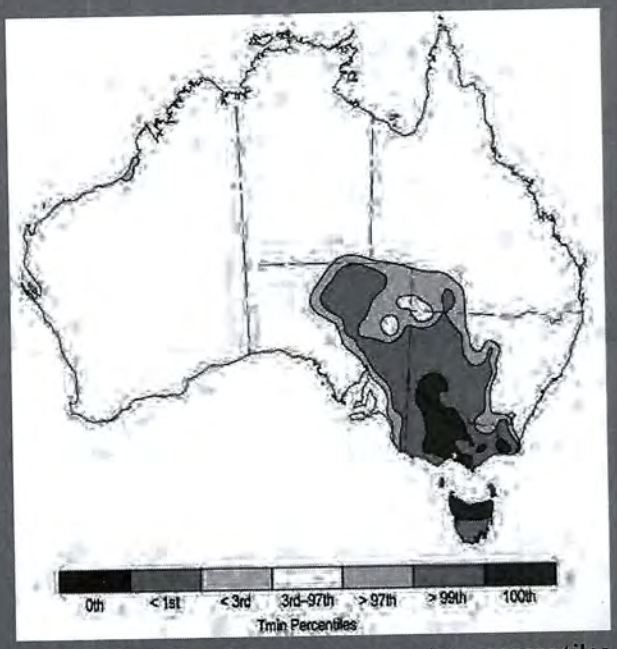

FIG. SB7.7. Daily minimum temperature percentiles for 20 Dec 2015 (1961–90 base period). (Source: Australia Bureau of Meteorology.)

The nation wide average temperature for 2015 was 12.7°C (0.1°C above average). According to NIWA's seven-station temperature series, 2015 was the 27th warmest year for New Zealand in the 107-year period of record. Above-average temperature anomalies were observed throughout many regions of the country in January and March, while below-average temperature anomalies were prominent in September.

(ii) Precipitation

Annual rainfall totals for 2015 were below normal (50%–79% of the annual normal) in the north and east of the country: Northland, Tasman, Nelson, and Canterbury as well as parts of eastern Waikato, Bay of Plenty, Gisborne, and Wellington—a pattern typically observed during El Niño. Rainfall was within 20% of the annual normal for the remainder of New Zealand (Fig. 7.58). It was the driest year on record for Kaitaia and Kerikeri (both located in Northland), which recorded 75% and 63% of their normal annual rainfall, respectively. There were no high total rainfall records or near-records set in 2015. January was a particularly dry month for New Zealand with rainfall totals well below normal (less than 50% of the January normal) or below normal (50%–79% of the January normal) for most parts of the country. Parts of Northland, Auckland, Taranaki, Manawatu-Whanganui, Kapiti Coast, Wellington, Marlborough, north Canterbury, and Central Otago each received less than 10% of their respective January normal rainfall. Conversely, rainfall during April and June was well above normal (greater than 149% of normal) in Taranaki and large parts of Manawatu-Whanganui.

Of all of the regularly reporting gauges, the wettest location in 2015 was Cropp River, in the Hokitika River Catchment (West Coast, South Island, 975 m a.s.l.) with an annual rainfall total of 11 632 mm. The driest of the regularly reporting rainfall sites in 2015 was Clyde (Central Otago), which recorded 267 mm of rainfall for the year. North Egmont (Taranaki) experienced the highest 1-day rainfall total in 2015 of 466 mm on 19 June.

(iii) Notable events

See Fig. 7.59 for a schematic of notable events. On 16 and 17 March, ex-Tropical Cyclone Pam passed east of New Zealand and was associated with strong winds and heavy rain in northern and eastern parts of the North Island. About 2200 Auckland and Northland properties lost power as strong winds brought down trees onto power lines. Over 100 people in the East Cape area were evacuated from their homes as a precaution, particularly in low lying coastal townships as high seas were expected to cause flooding and damage.

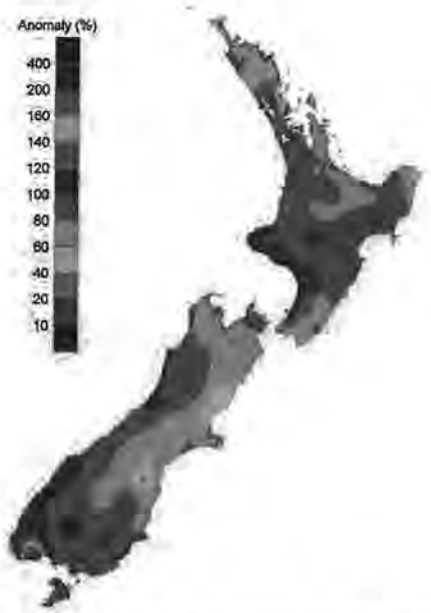

Fig. 7.58. 2015 annual total rainfall (%) relative to 1981–2010 normal. Distribution of observing station locations is as in Fig. 7.57. (Source: NIWA.)

On 3 June, Dunedin (Otago) was inundated by heavy and prolonged rainfall, which resulted in significant flooding, loss of electricity, evacuations, and road closures throughout the city and nearby areas. Dunedin (Musselburgh) received 113 mm of rainfall in the 24 hours to 9 a.m. on 4 June—its second-highest 1-day rainfall total on record for all months (records began in 1918).

Another sigificant flooding event occurred during 20–21 June in Whanganui. Heavy and prolonged rainfall caused evacuation of more than 100 households and the Whanganui River breached its banks, spilling floodwaters into Whanganui's central business district. This event was the worst flood on record for the area and led to the declaration of a state of emergency.

From 23 to 26 June, record-low temperatures were observed in many regions of the country. A high pressure system over and west of New Zealand combined clear skies with a southerly flow, resulting in very cold temperatures for many parts of the country. In particular, sites in the Mackenzie Country and Central Otago dropped to well below 0°C. The lowest recorded air temperature for 2015 (excluding high elevation alpine sites) was −21.0°C, observed at Tara Hills (Mackenzie Country) on 24 June. This was the fourth coldest temperature ever recorded in New Zealand.

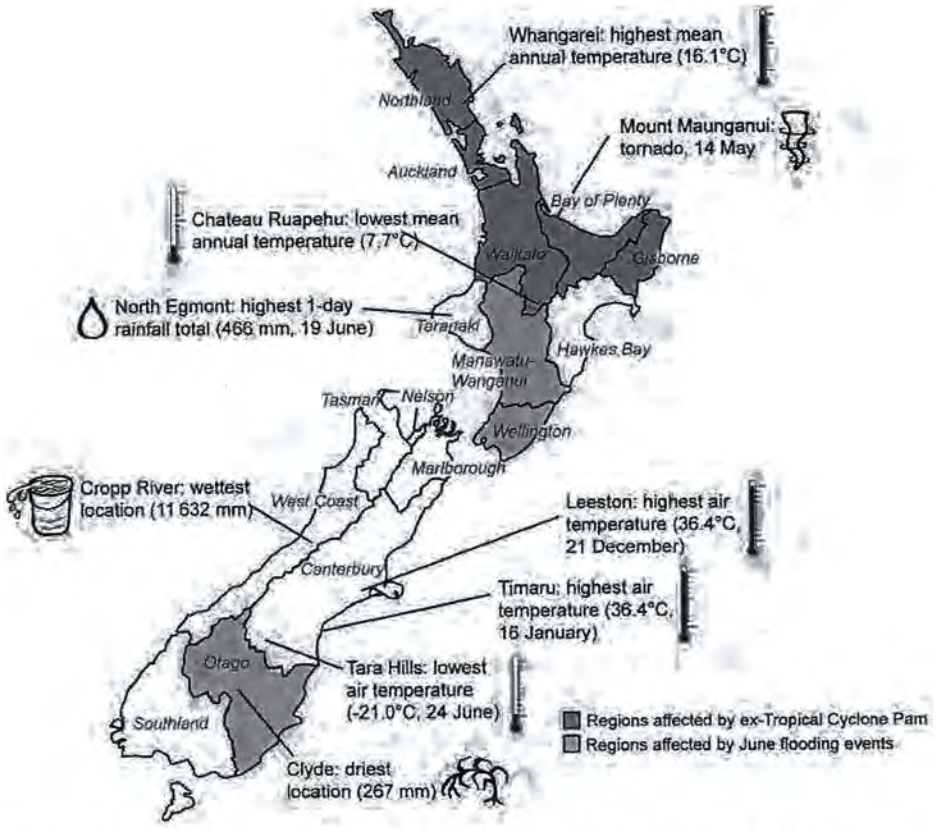

Fig. 7.59. Notable weather events and climate extremes for New Zealand in 2015. (Source: NIWA.)

APPENDIX 1: RELEVANT DATASETS AND SOURCES

General variable or phenomenon	Specific dataset or variable	Source	Section
Aerosols	Aerosol products	http://apps.ecmwf.int/datasets/data/macc-reanalysis	SB2.2
	CAMS Reanalysis	http://macc.copernicus-atmosphere.eu/catalogue/	2g3, SB2.2
Air-sea fluxes	Woods Hole Oceanographic Institute OAFlux project	http://oaflux.whoi.edu	3e
Albedo	MODIS	http://ladsweb.nascom.nasa.gov	2h1, 5e
Biomass burning	GFAS	http://atmosphere.copernicus.eu/documentation-fire-emissions	2h3, SB2.2
	GFEDv4	https://daac.ornl.gov/VEGETATION/guides/fire_emissions_v4.html	2h3
Clouds, cloudiness	*CALIPSO*	http://eosweb.larc.nasa.gov/PRODOCS/calipso/table_calipso.html	2d5
	CLARA-A2	https://climatedataguide.ucar.edu/climate-data/clara-a1-cloud-properties-surface-albedo-and-surface-radiation-products-based-avhrr	2d5
	HIRS	www.ssec.wisc.edu/~donw/PAGE/CLIMATE.HTM	2d5
	MISR	http://eosweb.larc.nasa.gov/PRODOCS/misr/level3/overview.html	2d5
	MODIS C6	http://ladsweb.nascom.nasa.gov	2d5
	NCEP CFSR	http://cfs.ncep.noaa.gov/cfsr/	d5
	PATMOS-x	www.ncdc.noaa.gov/cdr/operationalcdrs.html	2d5
	SatCORPS	No public archive	2d5
Evaporation, evapotranspiration, sublimation	ERA-Interim	www.ecmwf.int/en/research/climate-reanalysis/era-interim	SB2.1
	GLEAM	www.gleam.eu/	SB2.1
	Woods Hole Oceanographic Institute OAFlux project	http://oaflux.whoi.edu	3e2
FAPAR	FAPAR	http://fapar.jrc.ec.europa.eu	2h2
	MERIS	https://earth.esa.int/web/guest/missions/esa-operational-eo-missions/envisat/instruments/meris	2h2
	MODIS-TIP	http://modis.gsfc.nasa.gov/about/	2h2
Geopotential height	ERA-Interim	www.ecmwf.int/en/research/climate-reanalysis/era-interim	6b
	JRA-55	http://jra.kishou.go.jp/JRA-55/index_en.html	7g
	NCEP–NCAR reanalysis-1 pressure	www.esrl.noaa.gov/psd/data/gridded/data.ncep.reanalysis.pressure.html	5b, 7f
Glacier mass or volume	Glacier mass balance	http://dx.doi.org/10.5904/wgms-fog-2015-11	5f
	Randolph Glacier Inventory v3.2	www.glims.org/RGI/	2c3
	World Glacier Monitoring Service	www.wgms.ch/mbb/sum12.html	2c3, 5f

General variable or phenomenon	Specific dataset or variable	Source	Section
Humidity, (near) surface	Dai	By email to adai@ucar.edu	2d1
	ERA-Interim	www.ecmwf.int/research/era	2d1
	HadCRUH	www.metoffice.gov.uk/hadobs/hadcruh	2d1
	HadISDH	www.metoffice.gov.uk/hadobs/hadisdh	2d1
	HOAPS	wui.cmsaf.eu/safira/action/viewDoiDetails?acronym=HOAPS_V001	2d1
	JRA-55	http://jra.kishou.go.jp/JRA-55/index_en.html	2d1
	MERRA-2	http://gmao.gsfc.nasa.gov/reanalysis/MERRA-2/	2d1
	NOCS 2.0	www.noc.soton.ac.uk/noc_flux/noc2.php	2d1
Humidity, upper atmosphere	HIRS	www.ssec.wisc.edu/~donw/PAGE/CLIMATE.HTM	2d3
	UTH	By email to Viju.John@eumetsat.int	2d3
Ice sheet characteristics	DMSP-SSMIS	http://nsidc.org/data/docs/daac/nsidc0001_ssmi_tbs.gd.html	5e, 6e
	GRACE	http://podaac.jpl.nasa.gov/datasetlist?ids=Platform&values=GRACE	5e, 5f
	PROMICE (Greenland)	www.promice.dk/home.html	5e
Lake temperature	Institute of Meteorology and Water Management (Poland)	www.imgw.pl	2b4
	NOAA/GLERL	www.glerl.noaa.gov	2b4
Modes of variability	AMO	www.esrl.noaa.gov/psd/data/timeseries/AMO/	3h, 4e2
	AO	www.cpc.ncep.noaa.gov/products/precip/CWlink/daily_ao_index/teleconnections.shtml	2e1
	EQ-SOI	www.cpc.ncep.noaa.gov/data/indices	4b, 6d
	MEI	www.esrl.noaa.gov/psd/enso/mei/	3f
	MJO, real-time multivariate	http://monitor.cicsnc.org/mjo/current/rmm/	4c
	NAO	ftp://ftp.cpc.ncep.noaa.gov/wd52dg/data/indices/tele_index.nh	SB3.2, 3h
	NAO (summer)	Courtesy of Chris K. Folland	2e1
	NAO (winter)	https://climatedataguide.ucar.edu/climate-data/hurrell-north-atlantic-oscillation-nao-index-station-based	2e1
	ONI	www.cpc.ncep.noaa.gov/products/analysis_monitoring/ensostuff/ensoyears.shtml	4b
	PDO	http://research.jisao.washington.edu/pdo/	3b
	PDO	www.cpc.ncep.noaa.gov/products/GODAS/	3b
	SAM	www.antarctica.ac.uk/met/gjma/sam.html	6b, 6d
	SAM, AAO	www.cpc.ncep.noaa.gov/products/precip/CWlink/daily_ao_index/aao/aao.shtml	2e1
	SOI	ftp://ftp.bom.gov.au/anon/home/ncc/www/sco/soi/soiplaintext.html	2e1

General variable or phenomenon	Specific dataset or variable	Source	Section
Ocean carbon	CLIVAR/CO2 Repeat Hydrography Global Ocean Ship-Based Hydrographic Investigations Program	www.go-ship.org	3j
	pCO_2	www.socat.info	3j, 6g
Ocean circulation	Atlantic Meridional Overturning Circulation	www.noc.soton.ac.uk/rapidmoc	3h
Ocean heat content and temperature	Antarctic Bottom Water	https://portal.aodn.org.au/	6g
	CSIRO/ACE CRC/ IMAS-UTAS estimate	www.cmar.csiro.au/sealevel/thermal_expansion_ocean_heat_timeseries.html	3c
	MRI/JMA	www.data.jma.go.jp/gmd/kaiyou/english/ohc/ohc_global_en.html	3c
	NCEI	www.nodc.noaa.gov/OC5/3M_HEAT_CONTENT/	3c
	NCEP ocean reanalysis	www.cpc.ncep.noaa.gov/products/GODAS/	4h
	PMEL/JPL/JIMAR	http://oceans.pmel.noaa.gov	3c
	Roemmich and Gilson (2009) Argo monthly climatology	http://sio-argo.ucsd.edu/RG_Climatology.html	3c, SB3.2
	Met Office EN4.0.2	www.metoffice.gov.uk/hadobs/en4/download-en4-0-2-l09.html	3c
Ocean salinity	Antarctic Bottom Water	https://portal.aodn.org.au/	6g
	Argo	www.argo.ucsd.edu/	3d
	Blended Analysis for Surface Salinity	ftp://ftp.cpc.ncep.noaa.gov/precip/BASS	3d2
	NCEI global salinity anomalies	www.nodc.noaa.gov/OC5/3M_HEAT_CONTENT	3d3
	Roemmich and Gilson (2009) Argo monthly climatology	http://sio-argo.ucsd.edu/RG_Climatology.html	SB3.2
	World Ocean Atlas 2009	www.nodc.noaa.gov/OC5/WOA09/pr_woa09.html	3d2, 3d3
Ocean surface heat flux	CERES FLASHflux	https://eosweb.larc.nasa.gov/project/ceres/ebaf_surface_table	3e
Outgoing longwave radiation	CERES FLASHFlux Project	http://flashflux.larc.nasa.gov	3e, 4b2, 4c
	Daily OLR	https://www.ncdc.noaa.gov/cdr/atmospheric/outgoing-longwave-radiation-daily	4e3, 4e6

General variable or phenomenon	Specific dataset or variable	Source	Section
Ozone, total column and stratospheric	Bodeker Scientific	www.bodekerscientific.com/data/total-column-ozone	5j
	CALIPSO (polar stratospheric clouds)	http://eosweb.larc.nasa.gov/PRODOCS/calipso/table_calipso.html	6h
	GOME/SCIAMACHY/GOME2 (GSG) merged total ozone	www.iup.uni-bremen.de/gome/wfdoas/	2g4
	GOME/SCIAMACHY/GOME2 (GTO) merged total ozone	http://atmos.eoc.dlr.de/gome/gto-ecv.html www.esa-ozone-cci.org	2g4
	GOZCARDS ozone profiles	https://gozcards.jpl.nasa.gov http://mirador.gsfc.nasa.gov	2g4
	KNMI OMI	http://ozoneaq.gsfc.nasa.gov	6h
	Multisensor reanalysis of total ozone	www.temis.nl	2g4
	NASA *Aura* MLS	http://mls.jpl.nasa.gov/index-eos-mls.php	5j, 6h
	NASA BUV/SBUV v8.6 (MOD v8.6) merged ozone	http://acdb-ext.gsfc.nasa.gov/Data_services/merged	2g4
	NOAA BUV/SBUV v8.6 (MOD v8.6) merged ozone	ftp://ftp.cpc.ncep.noaa.gov/SBUV_CDR	2g4
	Ozonesonde	www.esrl.noaa.gov/gmd/dv/spo_oz	6h
	SAGE II/OSIRIS	Dataset linked to Bourassa et al. (2014)	2g4
	WOUDC ground-based ozone	ftp://ftp.tor.ec.gc.ca/pub/woudc/Project-Campaigns/ZonalMeans	2g4
Ozone, tropospheric	*Aura* OMI/MLS	http://acd-ext.gsfc.nasa.gov/Data_services/cloud_slice/new_data.html	2g6, SB2.2
Permafrost	Active layer thickness	http://nsidc.org/data/docs/fgdc/ggd313_calm/	5i
	GTN-P	http://gtnpdatabase.org	2cl
	Permafrost temperature	http://permafrost.gi.alaska.edu/sites_map	5i
	Permafrost temperature at French sites	http://edytem.univ-savoie.fr/	2cl
	Permafrost temperature at Norwegian sites	www.tspnorway.com, www.met.no	2cl
	Permafrost temperature at Swiss sites	www.permos.ch	2cl
Phytoplankton, ocean color	MODIS-*Aqua* Reprocessing R2014.0	http://oceancolor.gsfc.nasa.gov/cms/reprocessing/	3i
	SeaWiFS R2014.0	http://oceancolor.gsfc.nasa.gov/cms/reprocessing/	3i
	VIIRS R2014.0	http://oceancolor.gsfc.nasa.gov/cms/reprocessing/	3i

General variable or phenomenon	Specific dataset or variable	Source	Section
Precipitation	CMORPH	www.cpc.ncep.noaa.gov/products/janowiak/cmorph_description.html	4b3, 4d
	GHCN	www.ncdc.noaa.gov/temp-and-precip/ghcn-gridded-products.php	2d4
	GPCC	www.gpcc.dwd.de	2d4, 7f
	GPCPv23	http://precip.gsfc.nasa.gov	2d4, 3e, 4h
	NCEP–NCAR reanalysis	www.esrl.noaa.gov/psd/data/gridded/data.ncep.reanalysis.html	7e
	TRMM MI/PR	http://pmm.nasa.gov/TRMM/products-and-applications	7h
Precipitation (net)	JRA-55	http://jra.kishou.go.jp/JRA-55/index_en.html	6d
Pressure, sea level or near-surface	Antarctic Meteorological Research Center AWS	http://amrc.ssec.wisc.edu/data	6c
	ERA-Interim	www.ecmwf.int/en/research/climate-reanalysis/era-interim	6b, SB6.1
	HadSLP2r	www.metoffice.gov.uk/hadobs	2e1
	JRA-55	http://jra.kishou.go.jp/JRA-55/index_en.html	6d
	NCEP–NCAR reanalysis	www.esrl.noaa.gov/psd/data/gridded/data.ncep.reanalysis.html	7f
River discharge	ELSE	No public archive	2d6
Sea ice concentration	Near-Real-Time DMSP SSM/I-SSMIS Daily Polar Gridded	http://nsidc.org/data/nsidc-0081.html	6f
	Nimbus-7 SMMR and DMSP SSM/I (Bootstrap)	http://nsidc.org/data/docs/daac/nsidc0079_bootstrap_seaice.gd.html	6f
Sea ice duration	ESA CryoSat-2	https://earth.esa.int/web/guest/missions/esa-operational-eo-missions/cryosat	5c
	NASA Operation IceBridge	https://espo.nasa.gov/oib/content/OIB_1	5c
	Near-Real-Time DMSP SSM/I-SSMIS Daily Polar Gridded	http://nsidc.org/data/nsidc-0081.html	6f
	Nimbus-7 SMMR and DMSP SSM/I (Bootstrap)	http://nsidc.org/data/nsidc-0079.html	6f
Sea ice extent	Nimbus-7 SMMR and DMSP SSM/I (Bootstrap)	http://nsidc.org/data/docs/daac/nsidc0079_bootstrap_seaice.gd.html	5c,6f
Sea ice freeboard/thickness	CryoSat-2	https://earth.esa.int/web/guest/-/how-to-access-cryosat-data-6842	5c
Sea level/sea surface height	Ssalto/Duacs Multimission Altimeter Products	www.aviso.altimetry.fr	3f, 6g
	Tide gauge	http://uhslc.soest.hawaii.edu/	3f
	TOPEX/Jason	http://sealevel.colorado.edu/	3f

General variable or phenomenon	Specific dataset or variable	Source	Section
Sea surface temperature	ERSST.v3b and v4	www.esrl.noaa.gov/psd/data/gridded/data.noaa.ersst.html	3b, 4e2, 4e4 ,4g
	HadISST1	www.metoffice.gov.uk/hadobs/hadisst	3b
	HadSST3	www.metoffice.gov.uk/hadobs/hadsst3	2b1
	NOAA OISSTv2	www.esrl.noaa.gov/psd/data/gridded/data.ncep.oisst.v2.html	3b, 4b1, 4d2, 4e3, 4e6, 4h, 5d, 7d
Snow cover	NOAA daily Interactive Multisensor Snow and Ice Mapping System	http://nsidc.org/data/g02156	5g
	Snow cover extent and duration	www.snowcover.org	2c2, 5g
Snow depth	Canadian Meteorological Centre daily gridded global snow depth analysis	http://nsidc.org/data/nsidc-0447	5g
Soil moisture	ESA CCI SM	www.esa-soilmoisture-cci.org/node?page=3	2d8
Solar transmission	Mauna Loa solar transmission	www.esrl.noaa.gov/gmd/grad/mloapt.html	2f2
Stratospheric water vapor	Frost Point Hygrometer Data (Boulder, Hilo, Lauder)	ftp://aftp.cmdl.noaa.gov/data/ozwv/WaterVapor	2g5
	Frost Point Hygrometer Data (San Jose)	http://physics.valpo.edu/ozone/ticosonde.html	2g5
	MLS data	http://disc.sci.gsfc.nasa.gov/Aura/data-holdings/MLS/index.shtml	2g5
	NASA *Aura* MLS	http://aura.gsfc.nasa.gov/instruments/mls.html	2g5
Surface current	Brazil-Malvina Region Confluence Region	www.aoml.noaa.gov/phod/altimetry/cvar/mal/BM_anm.php	3g
	Long-term time series of surface currents: Agulhas Current	www.aoml.noaa.gov/phod/altimetry/cvar/agu/	3g
	Long-term time series of surface currents: North Brazil Current	www.aoml.noaa.gov/phod/altimetry/cvar/nbc	3g
	Long-term time series of surface currents: Yucatan Current	www.aoml.noaa.gov/phod/altimetry/cvar/yuc/transport.php	3g
	OSCAR	www.oscar.noaa.gov	3h

General variable or phenomenon	Specific dataset or variable	Source	Section
Temperature, (near) surface	Antarctic Meteorological Research Center AWS	http://amrc.ssec.wisc.edu/data	6c
	CRUTEM4	www.metoffice.gov.uk/hadobs/crutem4 www.cru.uea.ac.uk/cru/data/temperature	2b1, 5b, 7f
	ERA-Interim	www.ecmwf.int/en/research/climate-reanalysis /era-interim	2b1, 2b5, 6b
	EURO4m E-obs	www.ecad.eu/download/ensembles /ensembles.php	7f
	GHCNDEX	www.climdex.org/datasets.html	2b5
	HadCRUT4 global temperature	www.metoffice.gov.uk/hadobs/hadcrut4	2b1
	JMA global temperature	http://ds.data.jma.go.jp/tcc/tcc/products/gwp/temp /map/download.html	2b1, 7g
	JRA-55	http://jra.kishou.go.jp/JRA-55/index_en.html	2b1
	MERRA-2	http://gmao.gsfc.nasa.gov/reanalysis/MERRA-2/	2b1
	NASA/GISS global temperature	http://data.giss.nasa.gov/gistemp	2b1
	NCEP–NCAR reanalysis	www.esrl.noaa.gov/psd/data/gridded/data .ncep.reanalysis.html	5b, 5i, 7e, 7h
	NOAA/NCEI global temperature	www.ncdc.noaa.gov/monitoring-references /faq/anomalies.php	2b1
Temperature, upper atmosphere	Berkeley Earth surface temperature	www.berkeleyearth.org	2b1
	ERA-Interim	www.ecmwf.int/en/research/climate-reanalysis /era-interim	2b1, 2b2, 2b3, 6b
	JRA-55	http://jra.kishou.go.jp/JRA-55/index_en.html	2b2, 2b3
	MERRA-2	http://gmao.gsfc.nasa.gov/reanalysis/MERRA-2/	2b2, 2b3
	NCEP CFSR	http://cfs.ncep.noaa.gov/cfsr/	2b3
	NCEP–DOE Reanalysis 2	www.esrl.noaa.gov/psd/data/gridded /data.ncep.reanalysis2.html	6h
	NCEP–NCAR reanalysis	www.esrl.noaa.gov/psd/data/gridded /data.ncep.reanalysis.html	7f
	NOAA/NESDIS/ STAR	www.star.nesdis.noaa.gov/smcd/emb/mscat/	2b2, 2b3
	RAOBCORE, RICH	www.univie.ac.at/theoret-met/research /raobcore	2b2, 2b3
	RATPAC	www.ncdc.noaa.gov/oa/climate/ratpac	2b2, 2b3
	RSS	www.remss.com	2b2, 2b3
	UAH MSU	http://vortex.nsstc.uah.edu/public/msu	2b2, 2b3
	University of New South Wales	web.science.unsw.edu.au/~stevensherwood /radproj/index.html	2b2
	University of Washington	www.atmos.uw.edu/~pochedls/nobackup /share/	2b2, 2b3
Terrestrial groundwater storage	GRACE	http://podaac.jpl.nasa.gov/star/index.php	2d7
TOA earth radiation budget	CERES EBAF Ed2.8	http://ceres.larc.nasa.gov/products .php?product=EBAF-TOA	2f1
	CERES FLASHFlux	https://eosweb.larc.nasa.gov/project/ceres/ebaf _toa_table	2f1

General variable or phenomenon	Specific dataset or variable	Source	Section
Total column water vapor	COSMIC GPS-RO	www.cosmic.ucar.edu/ro.html	2d2
	ERA-Interim	www.ecmwf.int/en/research/climate-reanalysis/era-interim	2d2
	GNSS ground-based total column water vapor	http://rda.ucar.edu/datasets/ds721.1/	2d2
	JRA-55	http://jra.kishou.go.jp/JRA-55/index_en.html	2d2
	MERRA-2	http://gmao.gsfc.nasa.gov/reanalysis/MERRA-2/	2d2
	RSS SSM/I AMSR-E ocean total column water vapor	www.remss.com	2d2
Total solar irradiance	SORCE/TIM	http://science.nasa.gov/missions/sorce/	2f
Trace gases	AGGI	www.esrl.noaa.gov/gmd/aggi	2g1
	Carbon dioxide	www.esrl.noaa.gov/gmd/dv/iadv	2g1
	Carbon monoxide	https://www2.acom.ucar.edu/mopitt	2g7, SB2.2
	Chlorine monoxide, *Aura* MLS	http://mls.jpl.nasa.gov/products/clo_product.php	6h
	Hydrogen chloride, *Aura* MLS	http://disc.sci.gsfc.nasa.gov/datacollection/ML2HCL_V004.html	6h
	Methane	www.esrl.noaa.gov/gmd/dv/iadv	2g1
	Nitrous oxide	www.esrl.noaa.gov/gmd/hats/combined/N2O.html	2g1
	ODGI	www.esrl.noaa.gov/gmd/odgi	2g2
	Perfluorocarbons	http://agage.eas.gatech.edu	2g1, 2g2
	Sulfur hexafluoride	www.esrl.noaa.gov/gmd/hats/combined/SF6.html	2g1
Tropical cyclone data	IBTrACS	www.ncdc.noaa.gov/oa/ibtracs	4e
	JTWC best-track data (2011 preliminary)	www.usno.navy.mil/NOOC/nmfc-ph/RSS/jtwc/best_tracks	4e4, 4e5, 4e6
	RSMC-Tokyo, JMA best-track data	www.jma.go.jp/jma/jma-eng/jma-center/rsmc-hp-pub-eg/besttrack.html	4e4
	SPEArTC	http://apdrc.soest.hawaii.edu/projects/speartc	4e7, 4e8
Wind, (near) surface	Australian (McVicar)	http://doi.org/10.4225/08/56A85491DDED2	2e2
	ERA-Interim	www.ecmwf.int/en/research/climate-reanalysis/era-interim	2e2, SB6.1
	HadISD	www.metoffice.gov.uk/hadobs/hadisd/	2e2
	JRA-55	http://jra.kishou.go.jp/JRA-55/index_en.html	2e2, 4h
	MERRA-2	http://gmao.gsfc.nasa.gov/reanalysis/MERRA-2/	2e2
	RapidScat	winds.jpl.nasa.gov/missions/RapidScat/	SB4.2

General variable or phenomenon	Specific dataset or variable	Source	Section
Wind, upper atmosphere	Climate Forecast System	http://cfs.ncep.noaa.gov/	4b1
	ERA-Interim	www.ecmwf.int/en/research/climate-reanalysis/era-interim	2e3, 6b
	GRASP	http://doi.pangaea.de/10.1594/PANGAEA.823617	2e3
	JRA-55	http://jra.kishou.go.jp/JRA-55/index_en.html	2e3
	MERRA	http://gmao.gsfc.nasa.gov/research/merra/	2e3
	NCEP–NCAR reanalysis	www.esrl.noaa.gov/psd/data/gridded/data.ncep.reanalysis.html	4e3, 4e4, 4e6, 4g

ACKNOWLEDGMENTS

We wish to thank the AMS Journals' editorial staff, in particular Melissa Fernau, for facilitating the document. We thank the NCEI visual communications team for laying the document out and executing the countless number of technical edits needed. We also wish to express our sincere and deep gratitude to Dr. Rick Rosen, who served as the AMS special editor for this report. Dr. Rosen's handling of the reviews was at the same time rigorous and responsive, and greatly improved the document.

Chapter 2

- We thank David Parker for his excellent internal review.
- Kate Willett, Robert Dunn, Rob Allan, David Parker, Chris Folland, and Colin Morice were supported by the Joint U.K. DECC/Defra Met Office Hadley Centre Climate Programme (GA01101).
- Markus Donat received funding from Australian Research Council Grant DE150100456.
- Iestyn Woolway and Chris Merchant received funding from the European Union's Horizon 2020 Programme for Research and Innovation under Grant Agreement 640171.
- Sarah Perkins-Kirkpatrick was funded by Australian Research Council Grant DE140100952.
- The datasets used for sections 2d2 and 2d5 were provided from the JRA-55 project carried out by the Japan Meteorological Agency.
- We thank Paul Berrisford (European Centre for Medium-Range Weather Forecasts), Mike Bosilovich (NASA), and Shinya Kobayashi (Japan Meteorological Agency) for timely provision of reanalysis data.

Chapter 3

- Sandra Bigley (NOAA/Pacific Marine Environmental Laboratory) provided outstanding editorial assistance.
- Scott Cross, Toby Garfield, Jon Hare, Boyin Huang, Liqing Jiang, Kelly Kearney, and Dan Seidov imparted useful comments on an early draft of the chapter.
- Comments from three anonymous reviewers helped to improve the chapter.
- M. Baringer, G. Goni, R. Lumpkin, C. Meinen, and C. Schmid were supported by NOAA/AOML and the Climate Observation Division of NOAA/CPO.
- S. Dong, S. Garzoli, and D. Volkov were supported by NOAA/AOML, NOAA/CPO, and the Cooperative Institute for Marine and Atmospheric Studies, University of Miami.
- S. Billheimer and L. D. Tally acknowledge funding from US CLIVAR CLIMODE, NSF OCE-0960928.
- M. Ishii's work was supported by ERTDF [2-1506] of the Ministry of Environment, Japan.
- G. C. Johnson and J. M. Lyman were supported by NOAA/PMEL and the Climate Observations Division of the NOAA/CPO.
- R. Killick was supported by the joint U.K. DECC/Defra Met Office Hadley Centre Climate Programme (GA01101).
- S. W. Wijffels and D. Monselesan were supported by the Australian Climate Change Science Program.
- C. M. Domingues was supported by an Australian Research Council Future Fellowship (FT130101532).
- Computational resources and support from the NASA Advanced Supercomputing Division are gratefully acknowledged.

Chapter 4

- We thank Brenden Moses (NOAA/National Hurricane Center, Miami, Florida) for his timely inputs to sidebar 4.2.
- We thank Bill Ward (NOAA/NWS/Pacific Region Headquarters) who was involved with the internal review of the chapter.
- We thank Mark Lander (University of Guam) and Charles "Chip" Guard (NWS/Guam Weather Forecast Office) for providing valuable inputs related to section 4e4.

Chapter 5

- For support in coediting the chapter, Jackie Richter-Menge and Jeremy Mathis thank the NOAA/Arctic Research Office.
- We thank the authors for their contributions and the reviewers for their thoughtful and constructive comments.
- Jim Overland's contribution to section 5b was supported by the NOAA/Arctic Research Project of the Climate Program Office and by the Office of Naval Research, Code 322.

- Kit M. Kovacs and Christian Lydersen acknowledge the support of the Norwegian Polar Institute, while Patrick Lemons acknowledges the U.S. Fish and Wildlife Service, for the research programs that supported the creation of sidebar 5.1.
- For section 5f, B.Wouters was supported by the Netherlands Polar Program and the Marie Curie International Outgoing Fellowship within the 7th European Community Framework Programme (FP7-PEOPLE-2011-IOF-301260), and M. Sharp is supported by a Discovery Grant from NSERC Canada.
- Max Holmes and the coauthors of section 5h thank the USGS (Yukon), Water Survey of Canada (Mackenzie), and Roshydromet (Severnaya Dvina, Pechora, Ob', Yenisey, Lena, and Kolyma) for the discharge data.
- Vladimir Romanovsky and coauthors of section 5i acknowledge the support of the state of Alaska, the National Science Foundation (Grants PLR-0856864 and PLR-1304271 to the University of Alaska, Fairbanks, as well as PLR-1002119 and PLR-1304555 to the George Washington University), and the Geological Survey of Canada and Natural Resources Canada.
- Support for section 5i was also provided by the Russian Science Foundation (Projects RNF 16-17-00102, 13-05-41509 RGO, 13-05-00811, 13-08-91001, 14-05-00956, 14-17-00037, and 15-55-71004) and by the government of the Russian Federation.
- Germar Bernhard and coauthors of section 5j acknowledge the support of the U.S. National Science Foundation (Grant ARC-1203250), a Research Council of Norway Centres of Excellence award (Project 223268/F50) to the Norwegian Radiation Protection Authority, and the Academy of Finland for UV measurements by the FARPOCC and SAARA projects in Finland.

Chapter 6

- Special thanks to Dr. Marilyn Raphael and Dr. Florence Fetterer for their internal reviews of the chapter.
- The work of Rob Massom, Phil Reid, and Jan Lieser was supported by the Australian Government's Cooperative Research Centre program through the Antarctic Climate and Ecosystems CRC, and contributes to AAS Project 4116.
- Ted Scambos was supported under NASA Grant NNX10AR76G and NSF ANT 0944763, the Antarctic Glaciological Data Center.
- Sharon Stammerjohn was supported under NSF PLR 0823101.

Chapter 7

- We thank Peter Bissolli (Deutsche Wetterdienst) and David Parker (Met Office) for their excellent help with section 7f.
- Samson Hagos and Zhe Feng are supported by the U.S. Department of Energy Office of Science Biological and Environmental Research as part of the Regional and Global Climate Modeling Program; their institution, Pacific Northwest National Laboratory, is operated by Battelle for the U.S. Department of Energy under Contract DE-AC05-76RLO1830.

ACRONYMS AND ABBREVIATIONS

AAO	Antarctic Oscillation
ACE	NOAA's Accumulated Cyclone Energy Index
AGGI	NOAA's Annual Greenhouse Gas Index
ALT	active layer thickness
AMO	Atlantic multidecadal oscillation
AMSR-E	Advanced Microwave Scanning Radiometer for Earth Observing System
AMSU	Advanced Microwave Sounding Unit
AO	Arctic Oscillation
AOD	aerosol optical depth
ATSR	Along-Track Scanning Radiometers
AVHRR	Advanced Very High Resolution Radiometer
AVISO	Archiving, Validating, and Interpretation of Satellite Oceanographic data
CAMS	Climate Anomaly Monitoring System
CDR	climate data record
CERES	Clouds and the Earth's Radiant Energy System
CPC	NOAA's Climate Prediction Center
CPHC	NOAA's Central Pacific Hurricane Center
CRU	University of East Anglia's Climate Research Unit
DU	Dobson Unit
E–P	evaporation minus precipitation
ECMWF	European Centre for Medium-Range Weather Forecasts
ECV	essential climate variable
EECl	effective equivalent chlorine
EESC	effective equivalent stratospheric chlorine
EOS	Earth Observatory System
ERB	Earth radiation budget
ERBE	Earth Radiation Budget Experiment
ERSST	Extended Reconstructed Sea Surface Temperature
ESA	European Space Agency
ESRL	Earth System Research Laboratory
FAPAR	Fraction of Absorbed Photosynthetically Active Radiation
FLASHflux	Fast Longwave and Shortwave Radiative Fluxes
GCOS	Global Climate Observing System
GHCN	Global Historical Climatology Network
GHG	greenhouse gas
GISS	NASA's Goddard Institute of Space Studies
GOME	Global Ozone Monitoring Experiment
GPCC	Global Precipitation Climatology Centre
GPCP	Global Precipitation Climatology Project
GRACE	Gravity Recovery and Climate Experiment
GTN-P	Global Terrestrial Network on Permafrost
HadAT	Met Office Hadley Centre's radiosonde temperature product
HadCRUT	Met Office Hadley Centre/CRU gridded monthly temperatures dataset
HadISST	Met Office Hadley Centre's sea ice and SST dataset
HIRS-W	High Resolution Infrared Sounder
IBTrACS	International Best Track Archive for Climate Stewardship
ICD	ice cover duration
IOD	Indian Ocean dipole
ISCCP	International Satellite Cloud Climatology Project
JMA	Japanese Meteorological Agency
JPL	Jet Propulsion Laboratory
JRA	Japanese Reanalysis
JTWC	U.S. Navy's Joint Typhoon Warning Center
LHF	latent heat flux
LLGHG	long-lived greenhouse gas
MDR	Main Development Region
MEI	multivariate ENSO index
MERIS	Medium Resolution Imaging Spectrometer
MISR	Multiangle Imaging SpectroRadiometer
MLS	Microwave Limb Sounder
MOC	meridional overturning current
MOCHA	Meridional Overturning Circulation Heat Transport Array
MODIS	Moderate Resolution Imaging Spectroradiometer
MSLP	mean sea level pressure
MSU	Microwave Sounding Unit

NAO	North Atlantic Oscillation
NASA	National Aeronautics and Space Administration
NCAR	National Center for Atmospheric Research
NCDC	NOAA's National Climatic Data Center
NCEP	NOAA's National Center for Environmental Prediction
NERC	National Environmental Research Council
NOAA	National Oceanic and Atmospheric Administration
NSIDC	National Snow and Ice Data Center
OAFlux	Objectively Analyzed Air-Sea Fluxes
ODGI	Ozone-depleting Gas Index
ODS	ozone-depleting substance
OHCA	ocean heat content anomaly
OISST	Optimal Interpolation SST
OLR	outgoing longwave radiation
OMI	Ozone Monitoring Instrument
ONI	NOAA's Oceanic Niño index
OPI	OLR precipitation index
P–E	precipitation minus evaporation
PATMOS (-x)	Pathfinder Atmospheres (Extended Product)
PDO	Pacific decadal oscillation
PSC	polar stratospheric clouds
PSS	practical salinity scale
QBO	Quasi-biennial oscillation
QuikSCAT	Quick Scatterometer
RAOBCORE	Radiosonde Observation Correction
RATPAC	Radiosonde Atmospheric Temperature Products for Assessing Climate
RICH	Radiosonde Innovation Composite Homogenization
RSS	Remote Sensing Systems
SAM	Southern annular mode
SCD	snow covered duration
SCE	snow cover extent
SCIAMACHY	Scanning Imaging Absorption Spectrometer for Atmospheric Chartography
SeaWiFS	Sea-viewing Wide Field of View
SHF	Sensible heat flux
SLP	Sea level pressure
SOI	Southern Oscillation index
SPCZ	South Pacific convergence zone
SSM/I	Special Sensor Microwave Imager
SSH	Sea surface height
SSS	Sea surface salinity
SSTA	Sea surface temperature anomaly
SWE	Snow water equivalent
TCHP	Tropical cyclone heat potential
TCWV	Total column water vapor
TOA	Top of atmosphere
TOMS	Total Ozone Mapping Spectrometer
TRMM	Tropical Rainfall Measuring Mission
WBM	Water Balance Model
w.e.	water equivalent
WGMS	World Glacier Monitoring Service
WMO	World Meteorological Organization
WOA	World Ocean Atlas
WOCE	World Ocean Circulation Experiment

REFERENCES

Aagaard, K., and E. C. Carmack, 1989: The role of sea ice and other fresh water in the Arctic circulation. *J. Geophys. Res.*, **94**, 14 485–14 498, doi:10.1029/JC094iC10p14485.

Ackerman, S. A., R. E. Holz, R. Frey, E. W. Eloranta, B. C. Maddux, and M. McGill, 2008: Cloud Detection with MODIS. Part II: Validation. *J. Atmos. Oceanic Technol.*, **25**, 1073–1086, doi:10.1175/2007JTECHA1053.1.

Adler, R. F., and Coauthors, 2003: The version 2 Global Precipitation Climatology Project (GPCP) monthly precipitation analysis (1979–present). *J. Hydrometeor.*, **4**, 1147–1167, doi:10.1175/1525-7541(2003)004<1147:TVGPCP>2.0.CO;2.

Ahlstrøm, A. P., and Coauthors, 2008: A new programme for monitoring the mass loss of the Greenland ice sheet. *Geol. Surv. Denmark Greenl. Bull.*, **15**, 61–64.

Aiyyer, A., and J. Molinari, 2008: MJO and tropical cyclogenesis in the Gulf of Mexico and eastern Pacific: Case study and idealized numerical modeling. *J. Atmos. Sci.*, **65**, 2691–2704, doi:10.1175/2007JAS2348.1.

Albergel, C., and Coauthors, 2013: Skill and global trend analysis of soil moisture from reanalyses and microwave remote sensing. *J. Hydrometeor.*, **14**, 1259–1277, doi:10.1175/JHM-D-12-0161.1.

Allan, R. J., and R. D. D'Arrigo, 1999: 'Persistent' ENSO sequences: How unusual was the 1990–1995 El Niño? *Holocene*, **9**, 101–118, doi:10.1191/095968399669125102.

——, and T. Ansell, 2006: A new globally complete monthly historical gridded mean sea level pressure dataset (HadSLP2): 1850–2004. *J. Climate*, **19**, 5816–5842, doi:10.1175/JCLI3937.1.

——, G. Beard, A. Close, A. L. Herczeg, P. D. Jones and H. J. Simpson, 1996: Mean sea level pressure indices of the El Niño–Southern Oscillation: Relevance to stream discharge in southeastern Australia. CSIRO Division of Water Resources Rep. 96/1, 23 pp.

——, C. J. C. Reason, J. A. Lindesay, and T. J. Ansell, 2003: 'Protracted' ENSO episodes and their impacts in the Indian Ocean region. *Deep-Sea Res. II*, **50**, 2331–2347, doi:10.1016/S0967-0645(03)00059-6.

Allen, R. J., J. R. Norris, and M. Kovilakam, 2014: Influence of anthropogenic aerosols and the Pacific decadal oscillation on tropical belt width. *Nat. Geosci.*, **7**, 270–274, doi:10.1038/ngeo2091.

Amador, J. A., 1998: A climatic feature of the tropical Americas: The trade wind easterly jet. *Top. Meteor. Oceanogr.* **5**, 91–102.

——, E. J. Alfaro, O. G. Lizano, and V. O. Magaña, 2006: Atmospheric forcing of the eastern tropical Pacific: A review. *Progr. Oceanogr.*, **69**, 101–142, doi:10.1016/j.pocean.2006.03.007.

——, E. J. Alfaro, H. G. Hidalgo, and B. Calderón, 2011: Central America [in "State of the Climate 2010"]. *Bull. Amer. Meteor. Soc.*, **92** (6), S182–S183.

AMAP, 2015: Adaptation Actions for a Changing Arctic—Status report. Arctic Monitoring and Assessment Programme. [Available online at https://oaarchive.arctic-council.org/handle/11374/1439.]

Andela, N., and G. R. van der Werf, 2014: Recent trends in African fires driven by cropland expansion and El Niño to La Niña transition. *Nat. Climate Change*, **4**, 791–795, doi:10.1038/nclimate2313.

Anderson, M. C., J. M. Norman, G. R. Diak, W. P. Kustas, and J. R. Mecikalski, 1997: A two-source time-integrated model for estimating surface fluxes using thermal infrared remote sensing. *Remote Sens. Environ.*, **60**, 195–216, doi:10.1016/S0034-4257(96)00215-5.

——, and Coauthors, 2011: Mapping daily evapotranspiration at field to continental scales using geostationary and polar orbiting satellite imagery, *Hydrol. Earth Syst. Sci.*, **15**, 223–239, doi:10.5194/hess-15-223-2011.

Antonov, J. I., and Coauthors, 2010: *Salinity*. Vol. 2, *World Ocean Atlas 2009*, NOAA Atlas NESDIS 69, 184 pp. [Available online at http://www.nodc.noaa.gov/OC5/WOA09/pr_woa09.html.]

Aoki, S., 2002: Coherent sea level response to the Antarctic Oscillation. *Geophys. Res. Lett.*, **29**, 1950, doi:10.1029/2002GL015733.

Arguez, A., and S. Applequist, 2015: Understanding the statistical uncertainty of 2014's designation as the warmest year on record [in "State of the Climate in 2014"] *Bull. Amer. Meteor. Soc.*, **96** (7), S11–S12.

——, T. R. Karl, M. F. Squires, and R. S. Vose, 2013: Uncertainty in annual rankings from NOAA's global temperature time series. *Geophys. Res. Lett.*, **40**, 5965–5969, doi:10.1002/2013GL057999.

Arkin, P. A., 1982: The relationship between interannual variability in the 200 mb tropical wind field and the Southern Oscillation. *Mon. Wea. Rev.*, **110**, 1393-1404.

Armstrong, R. L., K. W. Knowles, M. J. Brodzik, and M. A. Hardman, 1994 (updated annually): DMSP SSM/I-SSMIS pathfinder daily EASE-grid brightness temperatures, version 2. Southern Hemisphere data, National Snow and Ice Data Center, accessed 2016. [Available online at http://nsidc.org/data/docs/daac/nsidc0032_ssmi_ease_tbs.gd.html.]

Aschmann, J., J. P. Burrows, C. Gebhardt, A. Rozanov, R. Hommel, M. Weber, and A. M. Thompson, 2014: On the hiatus in the acceleration of tropical upwelling since the beginning of the 21st century. *Atmos. Chem. Phys.*, **14**, 12803–12814, doi:10.5194/acp-14-12803-2014.

Ashok, K., S. K. Behera, S. A. Rao, H. Weng, and T. Yamagata, 2007: El Niño Modoki and its possible teleconnection. *J. Geophys. Res.*, **112**, C11007, doi:10.1029/2006JC003798.

Azorin-Molina, C., and Coauthors, 2014: Homogenization and assessment of observed near-surface wind speed trends over Spain and Portugal, 1961–2011. *J. Climate*, **27**, 3692–3712, doi:10.1175/JCLI-D-13-00652.1.

——, J. A. Guijarro-Pastor, T. R. McVicar, S. M. Vicente-Serrano, S. Jerez, and F. Espírito-Santo, 2016: Trends of daily peak wind gusts in Spain and Portugal, 1961–2014. *J. Geophys. Res.*, **121**, 1059–1078, doi:10.1002/2015JD024485.

Bakker, D. C. E., and Coauthors, 2014: An update to the Surface Ocean CO_2 Atlas (SOCAT version 2). *Earth Syst. Sci. Data*, **6**, 69–90, doi:10.5194/essd-6-69-2014.

Balks, M., K. Seybold and M. Gugliemin, 2016: Thermal snapshot of McMurdo Dry Valley, continental Antarctica. *Proc. 11th Int. Conf. on Permafrost (ICOP)*, Potsdam, Germany, Alfred Wegener Institute, in press.

Banzon, V. F., and R. W. Reynolds, 2013: Use of WindSat to extend a microwave-based daily optimum interpolation sea surface temperature time series. *J. Climate*, **26**, 2557–2562, doi:10.1175/JCLI-D-12-00628.1.

Baringer, M. O., and Coauthors, 2013: Meridional overturning circulation and heat transport observations in the Atlantic [in "State of the Climate in 2012"]. *Bull. Amer. Meteor. Soc.*, **94** (8), S65–S68.

——, W. E. Johns, W. R. Hobbs, S. Garzoli, S. Dong, and J. Willis, 2015a: Meridional oceanic heat transport in the Atlantic Ocean [in "State of the Climate in 2014"]. *Bull. Amer. Meteor. Soc.*, **96** (7), S81–S82.

——, and Coauthors, 2015b: Meridional overturning circulation observations in the North Atlantic Ocean [in "State of the Climate in 2014"]. *Bull. Amer. Meteor. Soc.*, **96** (7), S78–S80.

Barnston, A., 2015: Why are there so many ENSO indexes, instead of just one? [Available online at https://www.climate.gov/news-features/blogs/enso/why-are-there-so-many-enso-indexes-instead-just-one.]

Barrett, J. E., R. A. Virginia, D. H. Wall, P. T. Doran, A. G. Fountain, K. A. Welch, and W. B. Lyons, 2008: Persistent effects of a discrete warming event on a polar desert ecosystem. *Global Change Biol.*, **14**, 2249–2261, doi:10.1111/j.1365-2486.2008.01641.x.

Bastos, A., S. W. Running, C. Gouveia, and R. M. Trigo, 2013: The global NPP dependence on ENSO: La Niña and the extraordinary year of 2011. *J. Geophys. Res. Biogeosci.*, **118**, 1247–1255, doi:10.1002/jgrg.20100.

Bauer-Marschallinger, B., W. A. Dorigo, W. Wagner, and A. I. J. M. van Dijk, 2013: How oceanic oscillation drives soil moisture variations over mainland Australia: An analysis of 32 years of satellite observations. *J. Climate*, **26**, 10159–10173, doi:10.1175/JCLI-D-13-00149.1.

Baxter, S., S. Weaver, J. Gottschalck, and Y. Xue, 2014: Pentad evolution of wintertime impacts of the Madden–Julian Oscillation over the contiguous United States. *J. Climate*, **27**, 7356–7367, doi:10.1175/JCLI-D-14-00105.1.

Beal, L. M., V. Hormann, R. Lumpkin, and G. R. Foltz, 2013: The response of the surface circulation of the Arabian Sea to monsoonal forcing. *J. Phys. Oceanogr.*, **43**, 2008–2022, doi:10.1175/JPO-D-13-033.1.

Becker, A., P. Finger, A. Meyer-Christoffer, B. Rudolf, K. Schamm, U. Schneider, and M. Ziese, 2013: A description of the global land-surface precipitation data products of the Global Precipitation Climatology Centre with sample applications including centennial (trend) analysis from 1901–present. *Earth Syst. Sci. Data*, **5**, 71–99, doi:10.5194/essd-5-71-2013.

Behrenfeld, M. J., and Coauthors, 2006: Climate-driven trends in contemporary ocean productivity. *Nature*, **444**, 752–755, doi:10.1038/nature05317.

——, and Coauthors, 2016: Revaluating ocean warming impacts on global phytoplankton. *Nat. Climate Change*, **6**, 323–330, doi:10.1038/nclimate2838.

Behringer, D. W., M. Ji, and A. Leetmaa, 1998: An improved coupled model for ENSO prediction and implications for ocean initialization. Part I: The ocean data assimilation system. *Mon. Wea. Rev.*, **126**, 1013–1021, doi:10.1175/1520-0493(1998)126<1013:AICMFE>2.0.CO;2.

Bell, G. D., and M. S. Halpert, 1998: Climate assessment for 1997. *Bull. Amer. Meteor. Soc.*, **79**, S1–S51, doi:10.1175/1520-0477(1998)079<1014:CAF>2.0.CO;2.

——, and M. Chelliah, 2006: Leading tropical modes associated with interannual and multi-decadal fluctuations in North Atlantic hurricane activity. *J. Climate*, **19**, 590–612, doi:10.1175/JCLI3659.1.

——, and Coauthors, 2000: The 1999 North Atlantic and eastern North Pacific hurricane season [in "Climate Assessment for 1999"]. *Bull. Amer. Meteor. Soc.*, **81** (6), S19–S22, doi:10.1175/1520-0477(2000)081<1328:CAF>2.3.CO;2.

——, and Coauthors, 2011: Tropical cyclones; Atlantic basin [in "State of the Climate in 2010"]. *Bull. Amer. Meteor. Soc.*, **92** (7), S115–S121.

——, and Coauthors, 2012: Tropical cyclones; Atlantic basin [in "State of the Climate in 2011"]. *Bull. Amer. Meteor. Soc.*, **93** (7), S99–S105.

——, and Coauthors, 2014: Tropical cyclones; Atlantic basin [in "State of the Climate in 2013"]. *Bull. Amer. Meteor. Soc.*, **95** (7), S86–S90.

——, and Coauthors, 2015: The 2014 North Atlantic hurricane season: A climate perspective [in "State of the Climate in 2014"]. *Bull. Amer. Meteor. Soc.*, **96** (7), S101–S107.

Benedetti, A., and Coauthors, 2009: Aerosol analysis and forecast in the European Centre for Medium-Range Weather Forecasts Integrated Forecast System: 2. Data assimilation. *J. Geophys. Res.*, **114**, D13205, doi:10.1029/2008JD011115.

Beniston, M., 2004: The 2003 heat wave in Europe: A shape of things to come? An analysis based on Swiss climatological data and model simulations. *Geophys. Res. Lett.*, **31**, L02202, doi:10.1029/2003GL018857.

Berg, R., 2016: Hurricane Joaquin (AL112015). National Hurricane Center tropical cyclone report. [Available online at http://www.nhc.noaa.gov/data/tcr/AL112015_Joaquin.pdf.]

Bernhard, G., and Coauthors, 2015: Comparison of OMI UV observations with ground-based measurements at high northern latitudes. *Atmos. Chem. Phys.*, **15**, 7391–7412, doi:10.5194/acp-15-7391-2015.

Berrisford, P., I. Tobin, R. J. H. Dunn, R. Vautard, and T. R. McVicar, 2015: Land surface winds [in "State of the Climate in 2014"]. *Bull. Amer. Meteor. Soc.*, **96** (7), S33–S34.

Berry, D. I., and E. C. Kent, 2009: A new air–sea interaction gridded dataset from ICOADS with uncertainty estimates. *Bull. Amer. Meteor. Soc.*, **90**, 645–656, doi:10.1175/2008BAMS2639.1.

——, and ——, 2011: Air–sea fluxes from ICOADS: The construction of a new gridded dataset with uncertainty estimates. *Int. J. Climatol.*, **31**, 987–1001, doi:10.1002/joc.2059.

Bestelmeyer, B. T., and Coauthors, 2011: Analysis of abrupt transitions in ecological systems. *Ecosphere*, **2**, 1–26, doi:10.1890/ES11-00216.1.

Bhartia, P. K., and C. W. Wellemeyer, 2002: TOMS-V8 total O_3 algorithm. OMI Algorithm Theoretical Basis Document, Vol II, NASA Goddard Space Flight Center, 15–31.

Bichet, A., M. Wild, D. Folini, and C. Schär, 2012: Causes for decadal variations of wind speed over land: Sensitivity studies with a global climate model. *Geophys. Res. Lett.*, **39**, L11701, doi:10.1029/2012GL051685.

Billheimer, S., and L. D. Talley, 2013: Near cessation of Eighteen Degree Water renewal in the western North Atlantic in the warm winter of 2011–2012. *J. Geophys. Res. Oceans*, **118**, 6838–6853, doi:10.1002/2013JC009024.

Biskaborn, B. K., J.-P. Lanckman, H. Lantuit, K. Elger, D. A. Streletskiy, W. L. Cable, and V. E. Romanovsky, 2015: The new database of the Global Terrestrial Network for Permafrost (GTN-P). *Earth Syst. Sci. Data*, **7**, 245–259, doi:10.5194/essd-7-245-2015.

Bjerknes, J., 1969: Atmospheric teleconnections from the equatorial Pacific. *Mon. Wea. Rev.*, **97**, 163–172, doi:10.1175/1520-0493(1969)097<0163:ATFTEP>2.3.CO;2.

Blake, E., and Coauthors, 2009: *Tropical Cyclones of the Eastern North Pacific Basin, 1949–2006*. Historical Climatology Series 6-5, NOAA/National Climatic Data Center, 162 pp.

Bliss, A., R. Hock and V. Radić, 2014: Global response of glacier runoff to twenty-first century climate change. *J. Geophys. Res. Earth Surf.*, **119**, 717–730, doi:10.1002/2013JF002931.

Boden, T. A., G. Marland, and R. J. Andres, 2015: Global, regional, and national fossil-fuel CO_2 emissions. Carbon Dioxide Information Analysis Center, Oak Ridge National Laboratory, doi:10.3334/CDIAC/00001_V2015.

Bodhaine, B. A, B. G. Mendonca, J. M. Harris, and J. M. Miller, 1981: Seasonal variations in aerosols and atmospheric transmission at Mauna Loa Observatory. *J. Geophys. Res.*, **86** (C6), 7395–7398, doi:10.1029/JC086iC08p07395.

Boeckli, L., A. Brenning, S. Gruber, and J. Noetzli, 2012: Permafrost distribution in the European Alps: Calculation and evaluation of an index map and summary statistics. *Cryosphere*, **6**, 807–820, doi:10.5194/tc-6-807-2012.

Boening, C., J. K. Willis, F. W. Landerer, R. S. Nerem, and J. Fasullo, 2012: The 2011 La Niña: So strong, the oceans fell. *Geophys. Res. Lett.*, **39**, L19602, doi:10.1029/2012GL053055.

Boitsov, V. D., A. L. Karsakov, and A. G. Trofimov, 2012: Atlantic water temperature and climate in the Barents Sea, 2000–2009. *ICES J. Mar. Sci.*, **69**, 833–840, doi:10.1093/icesjms/fss075.

Bojinski, S., M. Verstraete, T. C. Peterson, C. Richter, A. Simmons, and M. Zemp, 2014: The concept of essential climate variables in support of climate research, applications, and policy. *Bull. Amer. Meteor. Soc.*, **95**, 1431–1443, doi:10.1175/BAMS-D-13-00047.1.

BoM, 2016: Annual climate report 2015. Bureau of Meteorology Australia. [Available online at http://www.bom.gov.au/climate/current/annual/aus/2015/.]

Bond, N. A., M. F. Cronin, H. Freeland, and N. Mantua, 2015: Causes and impacts of the 2014 warm anomaly in the NE Pacific. *Geophys. Res. Lett.*, **42**, 3414–3420, doi:10.1002/2015GL063306.

Bonjean, F., and G. Lagerloef, 2002: Diagnostic model and analysis of the surface currents in the tropical Pacific Ocean. *J. Phys. Oceanogr.*, **32**, 2938–2954, doi:10.1175/1520-0485(2002)032<2938:DMAAOT>2.0.CO;2.

Bosilovich, M. G., and Coauthors, 2015: MERRA-2: Initial evaluation of the climate. NASA/TM-2015-104606, Vol. 43, 136 pp. [Available online at http://gmao.gsfc.nasa.gov/reanalysis/MERRA-2/docs/.]

Boucher, O., and Coauthors, 2013: Clouds and aerosols. *Climate Change 2013: The Physical Science Basis*, T. F. Stocker et al. Eds., Cambridge University Press, 573–657.

Bourassa, A. E., D. A. Degenstein, W. J. Randel, J. M. Zawodny, E. Kyrölä, C. A. McLinden, C. E. Sioris, and C. Z. Roth, 2014: Trends in stratospheric ozone derived from merged SAGE II and Odin-OSIRIS satellite observations. *Atmos. Chem. Phys.*, **14**, 6983–6994, doi:10.5194/acp-14-6983-2014.

Box, J. E., and K. Hansen, 2015: Survey of Greenland glacier area changes. *PROMICE Newsletter*, Vol. 8, Geological Survey of Denmark and Greenland, Copenhagen, Denmark, 1–2. [Available online at http://promice.org/Newsletter_08.pdf.]

——, X. Fettweis, J. C. Stroeve, M. Tedesco, D. K. Hall, and K. Steffen, 2012: Greenland ice sheet albedo feedback: Thermodynamics and atmospheric drivers. *Cryosphere*, **6**, 821–839, doi:10.5194/tc-6-821-2012.

Boyd, P. W., and M. J. Ellwood, 2010: The biogeochemical cycle of iron in the ocean. *Nat. Geosci.*, **3**, 675–682, doi:10.1038/ngeo964.

Boyer, T. P., S. Levitus, J. I. Antonov, J. R. Reagan, C. Schmid, and R. Locarnini, 2012: Subsurface salinity [in "State of the Climate in 2011"]. *Bull. Amer. Meteor. Soc.*, **93** (7), S72–S75.

——, and Coauthors, 2013: *World Ocean Database 2013*. S. Levitus, Ed., NOAA Atlas NESDIS 72, 209 pp.

Brasnett, B., 1999: A global analysis of snow depth for numerical weather prediction. *J. Appl. Meteor.*, **38**, 726–740, doi:10.1175/1520-0450(1999)038<0726:AGAOSD>2.0.CO;2.

Bromwich, D. H., and S.-H. Wang, 2014: Net precipitation ($P - E$) [in "State of the Climate in 2013"]. *Bull. Amer. Meteor. Soc.*, **95** (7), S147–S149, doi:10.1175/2014BAMSStateoftheClimate.1.

——, and S.-H. Wang, 2015: Net precipitation ($P - E$) [in "State of the Climate in 2014"]. *Bull. Amer. Meteor. Soc.*, **96** (7), S153–S159, doi:10.1175/2015BAMSStateoftheClimate.1.

——, A. J. Monaghan, and Z. Guo, 2004: Modeling the ENSO modulation of Antarctic climate in the late 1990s with Polar MM5. *J. Climate*, **17**, 109–132, doi:10.1175/1520-0442(2004)017<0109:MTEMOA>2.0.CO;2.

——, R. L. Fogt, K. E. Hodges, and J. E. Walsh, 2007: A tropospheric assessment of the ERA-40, NCEP, and JRA-25 global reanalyses in the polar regions. *J. Geophys. Res.*, **112**, D10111, doi:10.1029/2006JD007859.

——, J. P. Nicolas, and A. J. Monaghan, 2011: An assessment of precipitation changes over Antarctica and the Southern Ocean since 1989 in contemporary global reanalyses. *J. Climate*, **24**, 4189–4209, doi:10.1175/2011JCLI4074.1.

Brown, J., Hinkel K. and Nelson F., 2000: The Circumpolar Active Layer Monitoring (CALM) program: Research designs and initial results. *Polar Geogr.*, **24**, 166–258, doi:10.1080/10889370009377698.

Butchart, N., and E. E. Remsberg, 1986: The area of the stratospheric polar vortex as a diagnostic for tracer transport on an isentropic surface. *J. Atmos. Sci.*, **43**, 1319–1339, doi:10.1175/1520-0469(1986)043<1319:TAOTSP>2.0.CO;2.

Callaghan, T., and Coauthors, 2011: The changing face of Arctic snow cover: A synthesis of observed and projected changes. *Ambio*, **40**, 17–31, doi:10.1007/s13280-011-0212-y.

Camargo, S. J., and A. H. Sobel, 2005: Western North Pacific tropical cyclone intensity and ENSO. *J. Climate*, **18**, 2996–3006, doi:10.1175/JCLI3457.1.

——, K. A. Emanuel, and A. H. Sobel, 2007: Use of a genesis potential index to diagnose ENSO effects on tropical cyclone genesis. *J. Climate*, **20**, 4819–4834, doi:10.1175/JCLI4282.1.

——, M. C. Wheeler, and A. H. Sobel, 2009: Diagnosis of the MJO modulation of tropical cyclogenesis using an empirical index. *J. Atmos. Sci.*, **66**, 3061–3074, doi:10.1175/2009JAS3101.1.

Cappelen, J., Ed., 2015. Greenland—DMI Historical Climate Data Collection 1784–2014. Danish Meteorological Institute Tech. Rep. 15-04, 97 pp. [Available online at www.dmi.dk/fileadmin/user_upload/Rapporter/TR/2015/tr15-04.pdf.]

Carpenter, L. J., and Coauthors, 2014: Ozone-depleting substances (ODSs) and other gases of interest to the Montreal Protocol. *Scientific Assessment of Ozone Depletion: 2014*, Global Ozone Research and Monitoring Project Rep. 55, World Meteorological Organization, 1.1–1.101.

Carrer, D., X. Ceamanos, B. Six, and J.-L. Roujean, 2014: AERUS-GEO: A newly available satellite-derived aerosol optical depth product over Europe and Africa. *Geophys. Res. Lett.*, **41**, 7731–7738, doi:10.1002/2014GL061707.

Carton, J. A., G. A. Chepurin, J. Reagan, and S. Häkkinen, 2011: Interannual to decadal variability of Atlantic Water in the Nordic and adjacent seas. *J. Geophys. Res.*, **116**, C11035, doi:10.1029/2011JC007102.

——, A. Cunningham, E. Frajka-Williams, Y.-O. Kwon, D. Marshall, and R. Msadek, 2014: The Atlantic overturning circulation: More evidence of variability and links to climate. *Bull. Amer. Meteor. Soc.*, **95**, ES163–ES166, doi:10.1175/BAMS-D-13-00234.1.

Carturan, L., F. Cazorzi, F. De Blasi, and G. Dalla Fontana, 2015: Air temperature variability over three glaciers in the Ortles–Cevedale (Italian Alps) effects of glacier fragmentation, comparison of calculation methods, and impacts on mass balance modeling. *Cryosphere*, **9**, 1129–1146, doi:10.5194/tc-9-1129-2015.

Cassou, C., 2008: Intraseasonal interaction between the Madden Julian Oscillation and the North Atlantic Oscillation. *Nature*, **455**, 523–527, doi:10.1038/nature07286.

Cavalieri, D. J., C. L. Parkinson, P. Gloersen, and H. Zwally, 1996 (updated yearly): Sea ice concentrations from Nimbus-7 SMMR and DMSP SSM/I-SSMIS passive microwave data, version 1 [1981–2011]. National Snow and Ice Data Center Distributed Active Archive Center, accessed 2016, doi:10.5067/8GQ8LZQVL0VL.

Cavicchia, L., H. von Storch, and S. Gualdi, 2014: S. Mediterranean tropical-like cyclones in present and future climate. *J. Climate*, **27**, 7493–7501, doi:10.1175/JCLI-D-14-00339.1.

Chandra, S., J. R. Ziemke, W. Min, and W. G. Read, 1998: Effects of 1997–1998 El Niño on tropospheric ozone and water vapor. *Geophys. Res. Lett.*, **25**, 3867–3870, doi:10.1029/98GL02695.

——, ——, B. N. Duncan, T. L. Diehl, N. Livesey, and L. Froidevaux, 2009: Effects of the 2006 El Niño on tropospheric ozone and carbon monoxide: Implications for dynamics and biomass burning. *Atmos. Chem. Phys.*, **9**, 4239–4249, doi:10.5194/acp-9-4239-2009.

Chehade, W., M. Weber, and J. P. Burrows, 2014: Total ozone trends and variability during 1979–2012 from merged data sets of various satellites. *Atmos. Chem. Phys.*, **14**, 7059–7074, doi:10.5194/acp-14-7059-2014.

Chelton, D. B., and R. E. Davis, 1982: Monthly mean sea-level variability along the West Coast of North America. *J. Phys. Oceanogr.*, **12**, 757–784, doi:10.1175/1520-0485(1982)012<0757:MMSLVA>2.0.CO;2.

Chen, Y., D. C. Morton, Y. Jin, G. J. Collatz, P. S. Kasibhatla, G. R. van der Werf, R. S. DeFries, and J. T. Randerson, 2013: Long-term trends and interannual variability of forest, savanna and agricultural fires in South America. *Carbon Manage.*, **4**, 617–638, doi:10.4155/cmt.13.61.

Chepurin, G. A., and J. A. Carton, 2012: Subarctic and Arctic sea surface temperature and its relation to ocean heat content 1982–2010. *J. Geophys. Res.*, **117**, C06019, doi:10.1029/2011JC007770.

Chia, H. H., and C. F. Ropelewski, 2002: The interannual variability in the genesis location of tropical cyclones in the northwest Pacific. *J. Climate*, **15**, 2934–2944, doi:10.1175/1520-0442(2002)015<2934:TIVITG>2.0.CO;2.

Chiou, E. W., and Coauthors, 2014: Comparison of profile total ozone from SBUV (v8.6) with GOME-type and ground-based total ozone for a 16-year period (1996 to 2011). *Atmos. Meas. Tech.*, **7**, 1681–1692, doi:10.5194/amt-7-1681-2014.

Christiansen, H. H., and Coauthors, 2010: The thermal state of permafrost in the Nordic area during the International Polar Year 2007–2009. *Permafr. Periglac. Process.*, **21**, 156–181, doi:10.1002/ppp.687.

Christiansen, J. S., C. W. Mecklenburg, and O. V. Karamushko, 2014: Arctic marine fishes and fisheries in light of global change. *Global Change Biol.*, **20**, 352–359, doi:10.1111/gcb.12395.

Christy, J., 2014: Lower tropospheric temperature [in "State of the Climate in 2013"]. *Bull. Amer. Meteor. Soc.*, **95** (7), S10–S11.

——, 2015: Lower tropospheric temperature [in "State of the Climate in 2014"]. *Bull. Amer. Meteor. Soc.*, **96** (7), S9–S10.

——, R. W. Spencer, W. B. Norris, W. D. Braswell, and D. E. Parker, 2003: Error estimates of version 5.0 of MSU-AMSU bulk atmospheric temperatures. *J. Atmos. Oceanic Technol.*, **20**, 613–629, doi:10.1175/1520-0426(2003)20<613:EEOVOM>2.0.CO;2.

Chrysanthou, A., G. Van der Schrier, E. J. M. Van den Besselaar, A. M. G. Klein Tank, and T. Brandsma, 2014: The effects of urbanization on the rise of the European temperature since 1960. *Geophys. Res. Lett.*, **41**, 21, 7716–7722, doi:10.1002/2014GL061154

Chu, J. H., C. R. Sampson, A. S. Levine, and E. Fukada, 2002: The Joint Typhoon Warning Center tropical cyclone best-tracks, 1945–2000. Ref. NRL/MR/7540-02-16, Naval Research Laboratory. [Available online at http://www.usno.navy.mil/NOOC/nmfc-ph/RSS/jtwc/best_tracks/TC_bt_report.html.]

Chung, E.-S., B. J. Soden, and V. O. John, 2013: Intercalibrating microwave satellite observations for monitoring long-term variations in upper- and midtropospheric water vapor. *J. Atmos. Oceanic Technol.*, **30**, 2303–2319, doi:10.1175/JTECH-D-13-00001.1.

——, ——, X. Huang, L. Shi, and V. O. John, 2016: An assessment of the consistency between satellite measurements of upper tropospheric water vapour, revised. *J. Geophys. Res. Atmos.*, **121**, 2874–2887, doi:10.1002/2015JD024496.

Ciais, P., and Coauthors, 2013: Carbon and other biogeochemical cycles. *Climate Change 2013: The Physical Science Basis*, T. F. Stocker, et al. Eds., Cambridge University Press, 465–570.

Coelho, C. A. S., D. H. F. Cardoso, and M. A. F. Firpo, 2016a: Precipitation diagnostics of an exceptionally dry event in São Paulo, Brazil. *Theor. Appl. Climatol.*, doi:10.1007/s00704-015-1540-9, in press.

——, and Coauthors, 2016b: The 2014 southeast Brazil austral summer drought: Regional scale mechanisms and teleconnections. *Climate Dyn.*, **46**, 3737–3752, doi:10.1007/s00382-015-2800-1.

Coldewey-Egbers, M., D. Loyola, P. Braesicke, M. Dameris, M. van Roozendael, C. Lerot, and W. Zimmer, 2014: A new health check of the ozone layer at global and regional scales. *Geophys. Res. Lett.*, **41**, 4363–4372, doi:10.1002/2014GL060212.

——, and Coauthors, 2015: The GOME-type Total Ozone Essential Climate Variable (GTO-ECV) data record from the ESA Climate Change Initiative. *Atmos. Meas. Tech.*, **8**, 3923–3940, doi:10.5194/amt-8-3923-2015.

Cooper, O. R., and J. R. Ziemke, 2013: Tropospheric ozone [in "State of the Climate in 2012"]. *Bull. Amer. Meteor. Soc.*, **94** (8), S38–S39.

——, and ——, 2014: Tropospheric ozone [in "State of the Climate in 2013"]. *Bull. Amer. Meteor. Soc.*, **95** (7), S42.

——, and ——, 2015: Tropospheric ozone [in "State of the Climate in 2014"]. *Bull. Amer. Meteor. Soc.*, **96** (7), S48–S49.

——, and Coauthors, 2014: Global distribution and trends of tropospheric ozone: An observation-based review. *Elementa Sci. Anthropocene*, **2**, 000029, doi:10.12952/journal.elementa.000029.

Cross, J. N., and Coauthors, 2014: Annual sea–air CO_2 fluxes in the Bering Sea: Insights from new autumn and winter observations of a seasonally ice-covered continental shelf. *J. Geophys. Res. Oceans*, **119**, 6692–6708, doi: 10.1002/2013JC009579.

Curtis, S., and R. Adler, 2000: ENSO indexes based on patterns of satellite-derived precipitation. *J. Climate*, **13**, 2786–2793, doi:10.1175/1520-0442(2000)013<2786:EIBOPO>2.0.CO;2.

Dai, A., 2006: Recent climatology, variability, and trends in global surface humidity. *J. Climate*, **19**, 3589–3606, doi:10.1175/JCLI3816.1.

——, 2013: Increasing drought under global warming in observations and models. *Nat. Climate Change*, **3**, 52–58, doi:10.1038/nclimate1633.

Dalpadado, P., R. B. Ingvaldsen, L. C. Stige, B. Bogstad, T. Knutsen, G. Ottersen, and B. Ellertsen, 2012: Climate effects on Barents Sea ecosystem dynamics. *ICES J. Mar. Sci.*, **69**, 1303–1316, doi:10.1093/icesjms/fss063.

——, and Coauthors, 2014: Productivity in the Barents Sea—Response to recent climate variability. *PLoS One*, **9**, e95273, doi:10.1371/journal.pone.0095273.

Daniel, J. S., S. Solomon, and D. L. Albritton, 1995: On the evaluation of halocarbon radiative forcing and global warming potentials. *J. Geophys. Res.*, **100**, 1271–1285, doi:10.1029/94JD02516.

Davis, S. M., D. F. Hurst, and K. H. Rosenlof, 2015: Stratospheric water vapor [in "State of the Climate in 2014"]. *Bull. Amer. Meteor. Soc.*, **96** (7), S46–S48.

De Jeu, R., W. Dorigo, W. Wagner, and Y. Liu, 2011: Soil moisture [in "State of the Climate in 2010"]. *Bull. Amer. Meteor. Soc.*, **92** (6), S52–S53.

——, ——, R. M. Parinussa, W. Wagner, and D. Chung, 2012a: Soil moisture [in "State of the Climate in 2011"]. *Bull. Amer. Meteor. Soc.*, **93** (7), S30–S34.

——, ——, ——, ——, Y. Y. Liu, D. Chung, and D. Fernández-Prieto, 2012b: Building a climate record of soil moisture from historical satellite observations [in "State of the Climate in 2011"]. *Bull. Amer. Meteor. Soc.*, **93** (7), S32–S33.

de Laat, A. T. J., R. J. van der A, and M. van Weele, 2015: Tracing the second stage of ozone recovery in the Antarctic ozone-hole with a "big data" approach to multivariate regressions. *Atmos. Chem. Phys.*, **15**, 79–97, doi:10.5194/acp-15-79-2015.

de Lima, M. I., F. E. Santo, A. M. Ramos, and J. L. M. P. de Lima, 2013: Recent changes in daily precipitation and surface air temperature extremes in mainland Portugal, in the period 1941–2007. *Atmos. Res.*, **127**, 195–209, doi:10.1016/j.atmosres.2012.10.001.

de Pablo, M. A., M. Ramos, and M. Molina, 2014: Thermal characterization of the active layer at the Limnopolar Lake CALM-S site on Byers Peninsula (Livingston Island), Antarctica. *Solid Earth*, **5**, 721–739, doi:10.5194/se-5-721-2014.

de Ronde, C. E. J., and Coauthors, 2002: Discovery of active hydrothermal venting in Lake Taupo, New Zealand. *J. Volcanol. Geotherm.*, **115**, 257–275, doi:10.1016/S0377-0273(01)00332-8.

Dee, D. P., and Coauthors, 2011: The ERA-Interim reanalysis: Configuration and performance of the data assimilation system. *Quart. J. Roy. Meteor. Soc.*, **137**, 553–597, doi:10.1002/qj.828.

Deeter, M. N., and Coauthors, 2013: Validation of MOPITT Version 5 thermal-infrared, near-infrared, and multispectral carbon monoxide profile retrievals for 2000–2011. *J. Geophys. Res.*, **118**, 6710–6725, doi:10.1002/jgrd.50272.

Deser, M., A. Alexander, S. P. Xie, and A. S. Phillips, 2010: Sea surface temperature variability: Patterns and mechanisms. *Annu. Rev. Mar. Sci.*, **2**, 115–143, doi:10.1146/annurev-marine-120408-151453.

DeVries, T., 2014: The oceanic anthropogenic CO_2 sink: Storage, air–sea fluxes, and transports over the industrial era. *Global Biogeochem. Cycles*, **28**, 631–647, doi:10.1002/2013GB004739.

Dewitte, S., D. Crommelynck, and A. Joukof, 2004: Total solar irradiance observations from DIARAD/VIRGO. *J. Geophys. Res.*, **109**, A02102, doi:10.1029/2002JA009694.

Di Girolamo, L., A. Menzies, G. Zhao, K. Mueller, C. Moroney, and D. J. Diner, 2010: Multi-angle imaging spectroradiometer level 3 cloud fraction by altitude algorithm theoretical basis document. JPL Publ. D-62358, Jet Propulsion Laboratory, 23 pp.

Diamond, H. J., Ed., 2013: Tropics [in "State of the Climate in 2012"]. *Bull. Amer. Meteor. Soc.*, **94** (8), S79–S110.

——, Ed., 2014: Tropics [in "State of the Climate in 2013"]. *Bull. Amer. Meteor. Soc.*, **95** (8), S81–S114.

——, Ed., 2015: Tropics [in "State of the Climate in 2014"]. *Bull. Amer. Meteor. Soc.*, **96** (7), S91–S126.

——, A. M. Lorrey, K. R. Knapp, and D. H. Levinson, 2012: Development of an enhanced tropical cyclone tracks database for the southwest Pacific from 1840 to 2011. *Int. J. Climatol.*, **32**, 2240–2250, doi:10.1002/joc.2412.

Dickson, R., J. Lazier, J. Meincke, P. Rhines, and J. Swift, 1996: Long-term coordinated changes in the convective activity of the North Atlantic. *Prog. Oceanogr.*, **38**, 241–295, doi:10.1016/S0079-6611(97)00002-5.

Dlugokencky, E. J., E. G. Nisbet, R. Fisher, and D. Lowry, 2011: Global atmospheric methane: Budget, changes and dangers. *Philos. Trans. Roy. Soc. London*, **369A**, 2058–2072, doi:10.1098/rsta.2010.0341.

Dohan, K., G. Goni, and R. Lumpkin, 2015: Surface currents [in "State of the Climate in 2014"]. *Bull. Amer. Meteor. Soc.*, **96** (7), S64–S66, S68.

Doherty, R. M., D. S. Stevenson, C. E. Johnson, W. J. Collins, and M. G. Sanderson, 2006: Tropospheric ozone and El Niño–Southern Oscillation: Influence of atmospheric dynamics, biomass burning emissions, and future climate change. *J. Geophys. Res.*, **111**, D19304, doi:10.1029/2005JD006849.

Dokulil, M. T., A. Herzig, B. Somogyi, L. Vörös, K. Donabaum, L. May, and T. Nõges, 2014: Winter conditions in European shallow lakes: A comparative synopsis. Est. *J. Ecol.*, **63**, 111–129, doi:10.3176/eco.2014.3.01.

Domingues, C. M., J. A. Church, N. J. White, P. J. Gleckler, S. E. Wijffels, P. M. Barker, and J. R. Dunn, 2008: Improved estimates of upper-ocean warming and multi-decadal sea-level rise. *Nature*, **453**, 1090–1093, doi:10.1038/nature07080.

Domingues, R., and Coauthors, 2015: Upper ocean response to Hurricane Gonzalo (2014): Salinity effects revealed by targeted and sustained underwater glider observations. *Geophys. Res. Lett.*, **42**, 7131–7138, doi:10.1002/2015GL065378.

Donat, M. G., L. V. Alexander, H. Yang, I. Durre, R. Vose, and J. Caesar, 2013: Global land-based datasets for monitoring climatic extremes. *Bull. Amer. Meteor. Soc.*, **94**, 997–1006, doi:10.1175/BAMS-D-12-00109.1.

Doney, S. C., and Coauthors, 2012: Climate change impacts on marine ecosystems. *Annu. Rev. Mar. Sci.*, **4**, 11–37, doi:10.1146/annurev-marine-041911-111611.

Dong, S., S. L. Garzoli, M. O. Baringer, C. S. Meinen, and G. J. Goni, 2009: The Atlantic meridional overturning circulation and its northward heat transport in the South Atlantic. *Geophys. Res. Lett.*, **36**, L20606, doi:10.1029/2009GL039356.

——, G. Goni, and F. Bringas, 2015: Temporal variability of the meridional overturning circulation in the South Atlantic between 20°S and 35°S. *Geophys. Res. Lett.*, **42**, 7655–7662, doi:10.1002/2015GL065603.

Dorigo, W., R. De Jeu, D. Chung, R. Parinussa, Y. Liu, W. Wagner, and D. Fernández-Prieto, 2012: Evaluating global trends (1988–2010) in harmonized multi-satellite surface soil moisture. *Geophys. Res. Lett.*, **39**, L18405, doi:10.1029/2012GL052988.

——, and Coauthors, 2014: Soil moisture [in "State of the Climate in 2013"]. *Bull. Amer. Meteor. Soc.*, **95** (7), S25–S26.

——, C. Reimer, D. Chung, R. M. Parinussa, T. Melzer, W. Wagner, R. A. M. de Jeu, and R. Kidd, 2015a: Soil moisture [in "State of the Climate in 2014"]. *Bull. Amer. Meteor. Soc.*, **96** (7), S28–S29.

——, and Coauthors, 2015b: Evaluation of the ESA CCI soil moisture product using ground-based observations. *Remote Sens. Environ.*, **162**, 380–395, doi:10.1016/j.rse.2014.07.023.

——, and R. De Jeu, 2016: Satellite soil moisture for advancing our understanding of Earth system processes and climate change. *Int. J. Appl. Earth Obs. Geoinf.*, **48**, 1–4, doi:10.1016/j.jag.2016.02.007.

Douville, H., A. Ribes, B. Decharme, R. Alkama, and J. Sheffield, 2013: Anthropogenic influence on multidecadal changes in reconstructed global evapotranspiration. *Nat. Climate Change*, **3**, 59–62, doi:10.1038/nclimate1632.

Drozdov, D., and Coauthors, 2015: Monitoring of permafrost in Russia and the international GTN-P project. *Proc. 68th Canadian Geotechnical Conf. (GEOQuébec 2015)*, Québec, Canada, GEOQuébec.

Duchesne, C., S. L. Smith, M. Ednie, and P. P. Bonnaventure, 2015: Active layer variability and change in the Mackenzie Valley, Northwest Territories. *Proc. 68th Canadian Geotechnical Conf. and Seventh Canadian Conf. on Permafrost (GEOQuébec 2015)*, Québec, Canada, GEOQuébec, Paper 117.

Duchez, A., and Coauthors, 2014: A new index for the Atlantic meridional overturning circulation at 26°N. *J. Climate*, **27**, 6439–6455, doi:10.1175/JCLI-D-13-00052.1.

Ducklow, H., and Coauthors, 2013: West Antarctic Peninsula: An ice-dependent coastal marine ecosystem in transition. *Oceanography*, **26**, 190–203, doi:10.5670/oceanog.2013.62.

Dunn, R. J. H., K. M. Willett, P. W. Thorne, E. V. Woolley, I. Durre, A. Dai, D. E. Parker, and R. S. Vose, 2012: HadISD: A quality-controlled global synoptic report database for selected variables at long-term stations from 1973–2011. *Climate Past*, **8**, 1649–1679, doi:10.5194/cp-8-1649-2012.

——, M. G. Donat, and T. Peterson, 2015: Temperature extreme indices [in "State of the Climate in 2014"]. *Bull. Amer. Meteor. Soc.*, **96** (7), S15–S16.

Durack, P. J., S. E. Wijffels, and P. J. Gleckler, 2014: Long-term sea-level change revisited: The role of salinity. *Environ. Res. Lett.*, **9**, 114017, doi:10.1088/1748-9326/9/11/114017.

Dutton, E. G., 1992: A coherence between the QBO and the amplitude of the Mauna Loa atmospheric transmission annual cycle. *Int. J. Climatol.*, **12**, 383–396, doi:10.1002/joc.3370120406.

——, and B. A. Bodhaine, 2001: Solar irradiance anomalies caused by clear-sky transmission variations above Mauna Loa: 1958–1999. *J. Climate*, **14**, 3255–3262, doi:10.1175/1520-0442(2001)014<3255:SIACBC>2.0.CO;2.

——, J. J. Deluisi and A. P. Austring, 1985: Interpretation of Mauna Loa atmospheric transmission relative to aerosols, using photometric precipitable water amounts. *J. Atmos. Chem.*, **3**, 53–68, doi:10.1007/BF00049368.

Dvortsov, V., and S. Solomon, 2001: Response of the stratospheric temperatures and ozone to past and future increases in stratospheric humidity. *J. Geophys. Res.*, **106**, 7505–7514, doi:10.1029/2000JD900637.

Ebita, A., and Coauthors, 2011: The Japanese 55-year Reanalysis "JRA-55": An interim report. *SOLA*, **7**, 149–152, doi:10.2151/sola.2011-038.

Ednie, M., and S. L. Smith, 2015: Permafrost temperature data 2008–2014 from community based monitoring sites in Nunavut. Geological Survey of Canada Open File 7784, doi:10.4095/296705.

Edson, J., and Coauthors, 2013: On the exchange of momentum over the open ocean. *J. Phys. Oceanogr.*, **43**, 1589–1610, doi:10.1175/JPO-D-12-0173.1.

Ellis, H. T., and R. F. Pueschel, 1971: Solar radiation: Absence of air pollution trends at Mauna Loa. *Science*, **172**, 845–846.

Emanuel, K. A., 1988: The maximum intensity of hurricanes. *J. Atmos. Sci.*, **45**, 1143–1155, doi:10.1175/1520-0469(1988)045<1143:TMIOH>2.0.CO;2.

——, 1995: Sensitivity of tropical cyclones to surface exchange coefficients and a revised steady-state model incorporating eye dynamics. *J. Atmos. Sci.*, **52**, 3969–3976, doi:10.1175/1520-0469(1995)052<3969:SOTCTS>2.0.CO;2.

——, and D. S. Nolan, 2004: Tropical cyclone activity and the global climate system. *Proc. 26th Conf. on Hurricanes and Tropical Meteorology*, Miami, FL, Amer. Meteor. Soc., 10A.2. [Available online at https://ams.confex.com/ams/26HURR/techprogram/paper_75463.htm.]

Enfield, D. B., and J. S. Allen, 1980: On the structure and dynamics of monthly mean sea level anomalies along the Pacific coast of North and South America. *J. Phys. Oceanogr.*, **10**, 557–578, doi:10.1175/1520-0485(1980)010<0557:OTSADO>2.0.CO;2.

——, and A. M. Mestas-Nuñez, 1999: Multiscale variabilities in global sea surface temperatures and their relationships with tropospheric climate patterns. *J. Climate*, **12**, 2719–2733, doi:10.1175/1520-0442(1999)012<2719:MVIGSS>2.0.CO;2.

——, ——, and P. J. Trimble, 2001: The Atlantic multidecadal oscillation and its relationship to rainfall and river flows in the continental US. *Geophys. Res. Lett.*, **28**, 2077–2080, doi:10.1029/2000GL012745.

England, M. H., and Coauthors, 2014: Recent intensification of wind-driven circulation in the Pacific and the ongoing warming hiatus. *Nat. Climate Change*, **4**, 222–227, doi:10.1038/nclimate2106.

Esaias, W. E., and Coauthors, 1998: An overview of MODIS capabilities for ocean science observations. *IEEE Trans. Geosci. Remote Sens.*, **36**, 1250–1265, doi:10.1109/36.701076.

Estilow, T., and Coauthors, updated 2013: The climate data guide: Snow cover extent (Northern Hemisphere) climate data record, by Rutgers. Data accessed 2015. [Available online at https://climatedataguide.ucar.edu/climate-data/snow-cover-extent-northern-hemisphere-climate-data-record-rutgers.]

Evans, W., and Coauthors, 2015: Sea–air CO_2 exchange in the western Arctic coastal ocean. *Global Biogeochem. Cycles*, **29**, 1190–1209, doi:10.1002/2015GB005153.

Falkowski, P. G., R. T. Barber, and V. Smetacek, 1998: Biogeochemical controls and feedbacks on ocean primary production. *Science*, **281**, 200–206, doi:10.1126/science.281.5374.200.

Farbrot, H., K. Isaksen, B. Etzelmüller, and K. Gisnås, 2013: Ground thermal regime and permafrost distribution under a changing climate in northern Norway. *Permafrost Periglacial Process.*, **24**, 20–38, doi:10.1002/ppp.1763.

Fasullo, J. T., C. Boening, F. W. Landerer, and R. S. Nerem, 2013: Australia's unique influence on global sea level in 2010–2011. *Geophys. Res. Lett.*, **40**, 4368–4373, doi:10.1002/grl.50834.

Fausto, R. S., and Coauthors, 2012: Ablation observations for 2008–2011 from the Programme for Monitoring of the Greenland Ice Sheet (PROMICE). *Geol. Surv. Denmark Greenl. Bull.*, **26**, 73–76.

Fay, F. H., 1982: Ecology and biology of the Pacific walrus, *Odobenus rosmarus divergens* Illiger. *North Amer. Fauna*, **74**, 1–279, doi:10.3996/nafa.74.0001.

——, B. P. Kelly, and J. L. Sease, 1989: Managing the exploitation of Pacific walruses: A tragedy of delayed response and poor communication. *Mar. Mamm. Sci.*, **5**, 1–16, doi:10.1111/j.1748-7692.1989.tb00210.x.

Fekete, B. M., 2013: [Global Climate] River discharge [in "State of the Climate in 2012"]. *Bull. Amer. Meteor. Soc.*, **94** (8), S22–S23.

——, U. Looser, and R. D. Robarts, 2012: Rationale for monitoring discharge on the ground. *J. Hydrometeor.*, **13**, 1977–1986, doi:10.1175/JHM-D-11-0126.1.

Feng, W., M. Zhong, J.-M. Lemoine, R. Biancale, H.-T. Hsu, and J. Xia, 2013: Evaluation of groundwater depletion in North China using the Gravity Recovery and Climate Experiment (GRACE) data and ground-based measurements. *Water Resour. Res.*, **49**, 2110–2118, doi:10.1002/wrcr.20192.

Fennig, K., A. Andersson, S. Bakan, C.-P. Klepp, and M. Schröder, 2012: Hamburg Ocean Atmosphere Parameters and Fluxes from Satellite Data–HOAPS 3.2–Monthly means/6-hourly composites. Satellite Application Facility on Climate Monitoring, doi:10.5676/EUM_SAF_CM/HOAPS/V001.

Field, C. B., M. J. Behrenfeld, J. T. Randerson, and P. Falkowski, 1998: Primary production of the biosphere: Integrating terrestrial and oceanic components. *Science*, **281**, 237–240, doi:10.1126/science.281.5374.237.

Field, R. D., Y. Wang, O. Roswintiarti, and Guswanto, 2004: A drought-based predictor of recent haze events in western Indonesia. *Atmos. Environ.*, **38**, 1869–1878, doi:10.1016/j.atmosenv.2004.01.011.

——, G. R. van der Werf, and S. S. P. Shen, 2009: Human amplification of drought-induced biomass burning in Indonesia since 1960. *Nat. Geosci.*, **2**, 185–188, doi:10.1038/ngeo443.

Fioletov, V. E., G. E. Bodeker, A. J. Miller, R. D. McPeters, and R. Stolarski, 2002: Global and zonal total ozone variations estimated from ground-based and satellite measurements: 1964–2000. *J. Geophys. Res.*, **107**, 4647, doi:10.1029/2001JD001350.

——, and Coauthors, 2008: The performance of the ground-based total ozone network assessed using satellite data. *J. Geophys. Res.*, **113**, D14313, doi:10.1029/2008JD009809.

Fischbach, A. S., D. H. Monson, and C. V. Jay, 2009: Enumeration of Pacific walrus carcasses on beaches of the Chukchi Sea in Alaska following a mortality event, September 2009. U.S. Geological Survey Open-File Rep. 2009–1291, 10 pp. [Available online at http://pubs.usgs.gov/of/2009/1291/.]

Fisher, J. B., K. P. Tu, and D. D. Baldocchi, 2008: Global estimates of the land–atmosphere water flux based on monthly AVHRR and ISLSCP-II data, validated at 16 FLUXNET sites. *Remote Sens. Environ.*, **112**, 901–919, doi:10.1016/j.rse.2007.06.025.Fishman, J., C. E. Watson, J. C. Larsen, and J. A. Logan, 1990: Distribution of tropospheric ozone determined from satellite data. *J. Geophys. Res.*, **95**, 3599–3617, doi:10.1029/JD095iD04p03599.

Flemming, J., and A. Inness, 2015: Carbon monoxide [in "State of the Climate in 2014"]. *Bull. Amer. Meteor. Soc.*, **96** (7), S49–S52.

——, and Coauthors, 2015: Tropospheric chemistry in the Integrated Forecasting System of ECMWF. *Geosci. Model Dev.*, **8**, 975–1003, doi:10.5194/gmd-8-975-2015.

Fofonoff, N. P., and E. L. Lewis, 1979: A practical salinity scale. *J. Oceanogr. Soc. Japan*, **35**, 63–64, doi:10.1007/BF02108283.

Fogt, R. L., D. H. Bromwich, and K. M. Hines, 2011: Understanding the SAM influence on the South Pacific ENSO teleconnection. *Climate Dyn.*, **36**, 1555–1576, doi:10.1007/s00382-010-0905-0.

Folland, C. K., J. Knight, H. W. Linderholm, D. Fereday, S. Ineson, and J. W. Hurrell, 2009: The summer North Atlantic Oscillation: Past, present and future. *J. Climate*, **22**, 1082–1103, doi:10.1175/2008JCLI2459.1.

Font, J., and Coauthors, 2013: SMOS first data analysis for sea surface salinity determination. *Int. J. Remote Sens.*, **34**, 3654–3670, doi:10.1080/01431161.2012.716541.

Foreman, C. M., C. F. Wolf, and J. C. Priscu, 2004: Impact of episodic warming events. *Aquat. Geochem.*, **10**, 239–268, doi:10.1007/s10498-004-2261-3.

Fossheim, M., R. Primicerio, E. Johannesen, R. B. Ingvaldsen, M. M. Aschan, and A. V. Dolgov, 2015: Recent warming leads to a rapid borealization of fish communities in the Arctic. *Nat. Climate Change*, **5**, 673–677, doi:10.1038/nclimate2647.

Fountain, A. G., G. L. Dana, K. J. Lewis, B. H. Vaughn, and D. M. McKnight, 1998: Glaciers of the McMurdo Dry Valleys, southern Victoria Land, Antarctica. *Ecosystem Dynamics in a Polar Desert: The McMurdo Dry Valleys, Antarctica*. J. C. Priscu, Ed., Antarctic Research Series, Vol. 72, Amer. Geophys. Union, 65–75.

——, J. L. Campbell, E. A. G. Schuur, S. E. Stammerjohn, M. W. Williams, and H. W. Ducklow, 2012: The disappearing cryosphere: Impacts and ecosystem responses to rapid cryosphere loss. *BioScience*, **62**, 405–415, doi:10.1525/bio.2012.62.4.11.

Frajka-Williams, E., 2015: Estimating the Atlantic overturning at 26°N using satellite altimetry and cable measurements. *Geophys. Res. Lett.*, **42**, 3458–3464, doi:10.1002/2015GL063220.

Frank, W. M., and P. E. Roundy, 2006: The role of tropical waves in tropical cyclogenesis. *Mon. Wea. Rev.*, **134**, 2397–2417, doi:10.1175/MWR3204.1.

Frankignoul, C., and K. Hasselmann, 1977: Stochastic climate models, Part II: Application to sea-surface temperature anomalies and thermocline variability. *Tellus*, **29A**, 289–305, doi:10.1111/j.2153-3490.1977.tb00740.x.

Franz, B. A., M. J. Behrenfeld, D. A. Siegel, and P. J. Werdell, 2015: [Global Oceans] Phytoplankton [in "State of the Climate in 2014"]. *Bull. Amer. Meteor. Soc.*, **96**, S85–S87.

Fraser, W. R., and E. E. Hofmann, 2003: A predator's perspective on causal links between climate change, physical forcing and ecosystem response. *Mar. Ecol. Prog. Ser.*, **265**, 1–15, doi:10.3354/meps265001.

——, D. L. Patterson-Fraser, C. A. Ribic, O. Schofield, and H. Ducklow, 2013: A nonmarine source of variability in Adélie penguin demography. *Oceanography*, **26**, 207–209, doi:10.5670/oceanog.2013.64.

Freckman, D. W., and R. A. Virginia, 1997: Low-diversity Antarctic soil nematode communities: Distribution and response to disturbance. *Ecology*, **78**, 363–369, doi:10.1890/0012-9658(1997)078[0363:LDASNC]2.0.CO;2.

Free, M., D. J. Seidel, J. K. Angell, J. R. Lanzante, I. Durre, and T. C. Peterson, 2005: Radiosonde Atmospheric Temperature Products for Assessing Climate (RATPAC): A new dataset of large-area anomaly time series. *J. Geophys. Res.*, **110**, D22101, doi:10.1029/2005JD006169.

Friis, K., A. Körtzinger, J. Pätsch, and D. Wallace, 2005: On the temporal increase of anthropogenic CO_2 in the subpolar North Atlantic. *Deep-Sea Res. I*, **52**, 681–698, doi:10.1016/j.dsr.2004.11.017.

Frith, S. M., N. A. Kramarova, R. S. Stolarski, R. D. McPeters, P. K. Bhartia, and G. J. Labow, 2014: Recent changes in total column ozone based on the SBUV version 8.6 Merged Ozone Data Set. *J. Geophys. Res. Atmos.*, **119**, 9735–9751, doi:10.1002/2014JD021889.

Froidevaux, L., and Coauthors, 2015: Global Ozone Chemistry and Related Trace Gas Data Records for the Stratosphere (GOZCARDS): Methodology and sample results with a focus on HCl, H_2O, and O_3. *Atmos. Chem. Phys.*, **15**, 10 471–10 507, doi:10.5194/acp-15-10471-2015.

Fung, I., J. John, J. Lerner, E. Matthews, M. Prather, L. P. Steele, and P. J. Fraser, 1991: Three-dimensional model synthesis of the global methane cycle. *J. Geophys. Res.*, **96**, 13 033–13 065, doi:10.1029/91JD01247.

Gardner, A. S., and Coauthors, 2011: Sharply increased mass loss from glaciers and ice caps in the Canadian Arctic Archipelago. *Nature*, **473**, 357–360, doi:10.1038/nature10089.

——, and Coauthors, 2013: A reconciled estimate of glacier contributions to sea level rise: 2003 to 2009. *Science*, **340**, 852–857, doi:10.1126/science.1234532.

Garzoli, S. L., M. O. Baringer, S. Dong, R. C. Perez, and Q. Yao, 2013: South Atlantic meridional fluxes. *Deep-Sea Res. I*, **71**, 21–32, doi:10.1016/j.dsr.2012.09.003.

Gergis, J., and A. M. Fowler, 2009: A history of ENSO events since A.D. 1525: Implications for future climate change. *Climatic Change*, **92**, 343–387, doi:10.1007/s10584-008-9476-z.

Ghilain, N., A. Arboleda, and F. Gellens-Meulenberghs, 2011: Evapotranspiration modelling at large scale using near-real time MSG SEVIRI derived data. *Hydrol. Earth Syst. Sci.*, **15**, 771–786, doi:10.5194/hess-15-771-2011.

Gobron, N., and M. Robustelli, 2013: Monitoring the state of the global terrestrial surfaces. *Proc. 2013 ESA Living Planet Symp.*, Edinburgh, United Kingdom, European Space Agency, SP-722.

——, A. S. Belward, B. Pinty, and W. Knorr, 2010: Monitoring biosphere vegetation 1998–2009. *Geophys. Res. Lett.*, **37**, L15402, doi:10.1029/2010GL043870.

Goddard, P., J. Yin, S. M. Griffies, and S. Zhang, 2015: An extreme event of sea-level rise along the northeast coast of North America in 2009–2010. *Nat. Commun.*, **6**, 6346, doi:10.1038/ncomms7346.

Goldenberg, S. B., and L. J. Shapiro, 1996: Physical mechanisms for the association of El Niño and West African rainfall with Atlantic major hurricane activity. *J. Climate*, **9**, 1169–1187, doi:10.1175/1520-0442(1996)009<1169:PMFTAO>2.0.CO;2.

——, C. W. Landsea, A. M. Mestas-Nuñez, and W. M. Gray, 2001: The recent increase in Atlantic hurricane activity: Causes and implications. *Science*, **293**, 474–479, doi:10.1126/science.1060040.

Gong, T., S. B. Feldstein, and D. Luo, 2010: The impact of ENSO on wave breaking and southern annular mode events. *J. Atmos. Sci.*, **67**, 2854–2870, doi:10.1175/2010JAS3311.1.

——, ——, and ——, 2013: A simple GCM study on the relationship between ENSO and the southern annular mode. *J. Atmos. Sci.*, **70**, 1821–1832, doi:10.1175/JAS-D-12-0161.1.

Goni, G. J., and J. A. Trinanes, 2003: Ocean thermal structure monitoring could aid in the intensity forecast of tropical cyclones. *Eos, Trans. Amer. Geophys. Union*, **84**, 573–578, doi:10.1029/2003EO510001.

——, and J. A. Knaff, 2009: Tropical cyclone heat potential [in "State of the Climate in 2008"]. *Bull. Amer. Meteor. Soc.*, **90** (8), S54–S56.

——, S. Kamholz, S. Garzoli, and D. Olson, 1996: Dynamics of the Brazil-Malvinas confluence based on inverted echo sounders and altimetry. *J. Geophys. Res.*, **101** (C7), 16 273–16 289, doi:10.1029/96JC01146.

——, and Coauthors, 2009: Applications of satellite-derived ocean measurements to tropical cyclone intensity forecasting. *Oceanography*, **22**, 190–197, doi:10.5670/oceanog.2009.78.

——, F. Bringas, and P. N. DiNezio, 2011: Observed low frequency variability of the Brazil Current front. *J. Geophys. Res.*, **116**, C10037, doi:10.1029/2011JC007198.

——, J. A. Knaff, and I.-I. Lin, 2015: Tropical cyclone heat potential [in "State of the Climate in 2013"]. *Bull. Amer. Meteor. Soc.*, **96** (7), S121–S122.

Gozzo, L. F., R. P. da Rocha, M. S. Rebotia, and S. Sugahara, 2014: Subtropical cyclones over the southwestern South Atlantic: Climatological aspects and case study. *J. Climate*, **27**, 8543–8562, doi:10.1175/JCLI-D-14-00149.1.

Granier, C., and Coauthors, 2011: Evolution of anthropogenic and biomass burning emissions of air pollutants at global and regional scales during the 1980–2010 period. *Climatic Change*, **109**, 163–190, doi:10.1007/s10584-011-0154-1.

Gray, W. M., 1968: Global view of the origin of tropical disturbances and storms. *Mon. Wea. Rev.*, **96**, 669–700, doi:10.1175/1520-0493(1968)096<0669:GVOTOO>2.0.CO;2.

Grebmeier, J. M., and Coauthors, 2006: A major ecosystem shift in the northern Bering Sea. *Science*, **311**, 1461–1464, doi:10.1126/science.1121365.

——, S. E. Moore, J. E. Overland, K. E. Frey, and R. Gradinger, 2010: Biological response to recent Pacific Arctic sea ice retreats. *Eos, Trans. Amer. Geophys. Union*, **91**, 161–162, doi:10.1029/2010EO180001.

Guard, C. P., and M. A. Lander, 2012: Northwest Pacific, Micronesia [in "State of the Climate in 2011"]. *Bull. Amer. Meteor. Soc.*, **93**, S215–S218.

Gugliemin, M., M. R. Worland and N. Cannone, 2012: Spatial and temporal variability of ground surface temperature and active layer thickness at the margin of maritime Antarctica, Signy Island. *Geomorphology*, **155**, 20–33, doi:10.1016/j.geomorph.2011.12.016.

——, M. Dalle Fratte, and N. Cannone, 2014: Permafrost warming and vegetation changes in continental Antarctica. *Environ. Res. Lett.*, **9**, 045001, doi:10.1088/1748-9326/9/4/045001.

Guhathakurta, P., M. Rajeevan, D. R. Sikka, and A. Tyagi, 2015: Observed changes in southwest monsoon rainfall over India during 1901–2011. *Int. J. Climatol.*, **35**, 1881–1898, doi:10.1002/joc.4095.

Guo, Y., X. Jiang, and D. E. Waliser, 2014: Modulation of the convectively coupled Kelvin waves over South America and the tropical Atlantic Ocean in association with the Madden–Julian oscillation. *J. Atmos. Sci.*, **71**, 1371–1388, doi:10.1175/JAS-D-13-0215.1.

Guttman, N. B., 1998: Comparing the Palmer Drought Index and the Standardized Precipitation Index. *J. Amer. Water Res. Assoc.*, **34**,113–121, doi:10.1111/j.1752-1688.1998.tb05964.x.

Hagos, S. M., and K. H. Cook, 2008: Ocean warming and late-twentieth-century Sahel drought and recovery. *J. Climate*, **21**, 3797–3814, doi:10.1175/2008JCLI2055.1.

Haimberger, L., 2015: Upper air wind speed [in "State of the Climate in 2014"]. *Bull. Amer. Meteor. Soc.*, **96** (7), S35–S37.

——, C. Tavolato, and S. Sperka, 2012: Homogenization of the global radiosonde temperature dataset through combined comparison with reanalysis background series and neighboring stations. *J. Climate*, **25**, 8108–8131, doi:10.1175/JCLI-D-11-00668.1.

Hansen, J., R. Ruedy, M. Sato, and K. Lo, 2010: Global surface temperature change. *Rev. Geophys.*, **48**, RG4004, doi:10.1029/2010RG000345.

Hardy, A., 1967: Great Waters. Collins, 542 pp.

Harris, I., P. D. Jones, T. J. Osborn, and D. H. Lister, 2014: Updated high-resolution grids of monthly climatic observations—The CRU TS3.10 dataset. *Int. J. Climatol.*, **34**, 623–642, doi:10.1002/joc.3711.

Harris, N. R. P., and D. J. Wuebbles, 2014: Scenarios and information for policymakers. *Scientific Assessment of Ozone Depletion: 2014*, Global Ozone Research and Monitoring Project Rep. 55, World Meteorological Organization, 5.1–5.58. [Available online at http://www.esrl.noaa.gov/csd/assessments/ozone/2014/chapters/2014OzoneAssessment.pdf.]

——, and Coauthors, 2015: Past changes in the vertical distribution of ozone—Part 3: Analysis and interpretation of trends. *Atmos. Chem. Phys.*, **15**, 9965–9982, doi:10.5194/acp-15-9965-2015.

Hart, R. E., 2003: A cyclone phase space derived from thermal wind and thermal asymmetry. *Mon. Wea. Rev.*, **131**, 585–616, doi:10.1175/1520-0493(2003)131<0585:ACPSDF>2.0.CO;2.

Hartmann, D. L., and Coauthors, 2013: Observations: Atmosphere and surface. *Climate Change 2013: The Physical Science Basis*, T. F. Stocker et al., Eds., Cambridge University Press, 159–254.

Hawkings, J. R., and Coauthors, 2014: Ice sheets as a significant source of highly reactive nanoparticulate iron to the oceans. *Nat. Commun.*, **5**, 3929, doi:10.1038/ncomms4929.

Hayes, M. J., M. D. Svoboda, D. A. Wilhite, and O. V. Varnyarkho, 1999: Monitoring the 1996 drought using the Standardized Precipitation Index. *Bull. Amer. Meteor. Soc.*, **80**, 429–438, doi:10.1175/1520-0477(1999)080<0429:MTDUTS>2.0.CO;2.

Heidinger, A. K., M. J. Foster, A. Walther, and X. Zhao, 2014: The Pathfinder Atmospheres–Extended AVHRR climate dataset. *Bull. Amer. Meteor. Soc.*, **95**, 909–922, doi:10.1175/BAMS-D-12-00246.1.

Helfrich, S., D. McNamara, B. Ramsay, T. Baldwin, and T. Kasheta, 2007: Enhancements to, and forthcoming developments in the Interactive Multisensor Snow and Ice Mapping System (IMS). *Hydrol. Processes*, **21**, 1576–1586, doi:10.1002/hyp.6720.

Hendon, H., C. Zhang, and J. Glick, 1999: Interannual variation of the Madden–Julian oscillation during austral summer. *J. Climate*, **12**, 2538–2550, doi:10.1175/1520-0442(1999)012<2538:IVOTMJ>2.0.CO;2.

Hess, P. G., and R. Zbinden, 2013: Stratospheric impact on tropospheric ozone variability and trends: 1990–2009. *Atmos. Chem. Phys.*, **13**, 649–674, doi:10.5194/acp-13-649-2013.

Hills, S., and J. R. Gilbert, 1994: Detecting Pacific walrus population trends with aerial surveys. *Transactions of the 59th North American Wilderness and Natural Resources Conference*, Wildlife management Institute, 201–210.

Hirschi, M., B. Mueller, W. A. Dorigo, and S. I. Seneviratne, 2014: Using remotely sensed soil moisture for land–atmosphere coupling diagnostics: The role of surface vs. root-zone soil moisture variability. *Remote Sens. Environ.*, **154**, 246–252, doi:10.1016/j.rse.2014.08.030.

Ho, D. T., and R. Wanninkhof, 2016: Air–sea gas exchange in the North Atlantic: $^{3}He/SF_{6}$ Experiment during GasEx-98. *Tellus*, **68B**, 30198, doi:10.3402/tellusb.v68.30198.

Ho, S. P., X. Zhou, Y. H. Kuo, D. Hunt, and J. H. Wang, 2010: Global evaluation of radiosonde water vapor systematic biases using GPS radio occultation from COSMIC and ECMWF analysis. *Remote Sens.*, **2**, 1320–1330, doi:10.3390/rs2051320.

Hobbs, W., and J. K. Willis, 2012: Midlatitude North Atlantic heat transport: A time series based on satellite and drifter data. *J. Geophys. Res.*, **17**, C01008, doi:10.1029/2011JC007039.

Hoegh-Guldberg, O., and J. F. Bruno, 2010: The impact of climate change on the world's marine ecosystems. *Science*, **328**, 1523–1528, doi:10.1126/science.1189930.

Hofmann, D. J., and S. A. Montzka, 2009: Recovery of the ozone layer. *Eos, Trans. Amer. Geophys. Union*, **90**, 1–2, doi:10.1029/2009EO010001.

——, J. H. Butler, E. J. Dlugokencky, J. W. Elkins, K. Masarie, S. A. Montzka, and P. Tans, 2006: The role of carbon dioxide in climate forcing from 1979 to 2004: introduction of the Annual Greenhouse Gas Index. *Tellus*, **58B**, 614–619, doi:10.1111/j.1600-0889.2006.00201.x.